Experimental and geochemical studies of terrestrial and lunar magmatic processes

by

Thomas Paul Wagner
B.S. Geology, Binghamton University, 1989

Submitted to the Department of Earth, Atmospheric and Planetary Sciences in partial fulfillment of the requirements for the

Degree of

Doctor of Philosophy in Geology

at the Massachusetts Institute of Technology
May 1995

Signature of author_____
Department of Earth, Atmospheric and Planetary Sciences

Certified by_____
Professor Timothy Grove
Thesis Supervisor

Accepted by_____
Professor Thomas Jordan
Department Head

Experimental and geochemical studies of terrestrial and lunar magmatic processes

by Thomas Paul Wagner

Submitted to the Department of Earth, Atmospheric and Planetary Sciences at the Massachusetts Institute of Technology on May 26, 1995 in partial fulfillment of the requirements for the degree of

Doctor of Philosophy in Geology

Abstract

Experimental and geochemical studies were performed to understand the formation of certain terrestrial and lunar igneous rocks. Chapter one is a study of convergent margin magmatism at Medicine Lake Volcano, California. The petrogenesis of a suite of variably porphyritic, high-alumina lavas was inferred from field relations, hydrous melting experiments and geochemical modeling. I conclude that phenocryst-poor lavas formed by hydrous differentiation, while phenocryst-rich lavas formed by a combination of hydrous differentiation and crystal accumulation. Chapters two and three discuss the origin of oceanic island tholeiite at Kilauea volcano, Hawaii. Chapter two reports the results of phase equilibria experiments on an estimated tholeiite primary magma. The results show that tholeiite primary magmas are in equilibrium with depleted harzburgite at lithospheric depths beneath Hawaii. I propose that Hawaiian tholeiite forms by melting of garnet lherzolite in deep parts of a mantle plume and that these melts equilibrate with depleted harzburgite in the plume top. Chapter three is an ion-microprobe study of picritic glass grains from Kilauea volcano, Hawaii. These glasses have the highest MgO-contents of any glass found in Hawaii and were used to make the primary magma estimate studied in chapter two. The glasses have trace element abundances similar to other Hawaiian lavas and show variation consistent with derivation by partial melting of garnet lherzolite. Chapter four models the origin of lunar high-Ti magmas using the results of two experimental studies. First, the phase relations of the most Ti-rich lunar ultramafic glass, Apollo 14 black glass, were determined to 2.5-GPa. Second, the dissolution rate of ilmenite was measured in both high- and low-Ti lunar magmas. The experimental results support the generation of the high-Ti lunar ultramafic glasses by assimilation of ilmenite and clinopyroxene into low-Ti primary magmas. This model allows the generation of high-Ti lunar magmas without overturn of the lunar mantle. The thesis also contains two appendices that discuss the construction and calibration of the piston-cylinder device used to perform the experiments.

Thesis Supervisor: Dr. Timothy L. Grove, Professor of Geology

Acknowledgments: Many people have contributed to my education and the completion of this thesis. First and foremost among those is Tim Grove, my mentor and friend, who put an exceptional amount of time and energy into teaching me about igneous rocks. Tim provides a very stimulating environment to work in by constantly pushing students to try new things and allowing us the freedom to explore any area we choose to work in. Fred Frey was always willing to discuss my work and his help enabled me to work on Hawaiian volcanism. Fred's 'Trace Element Geochemistry' course was one of the most important classes I have ever taken. Aside from the knowledge I gained, it was the place I learned to read and understand scientific papers. Rosamond Kinzler deserves a small monument for selflessly giving of her time. Ro taught me most of the techniques used in this thesis. Glenn Gaetani has been a great officemate and has provided thoughtful insight into all of my work. Alberto 'Bandito' Saal, Eiichi '5' Takazawa and Huai-Jen 'Wyman' Yang have continually helped me through discussion, reading of manuscripts and aiding in research. Steve Recca, Mike Jercinovic, and Nilanjan Chatterjee expertly maintained the MIT electron microprobe and contributed to these works through discussion of the analytical technique, as well as reviewing abstracts and manuscripts. Steve helped me write my first general exam paper by placing a pen in my hand, putting a pad in front of me and ordering me to write! Julie Donnelly-Nolan and Tom Sisson were instrumental in the completion of chapter one. Julie provided the samples, patiently explained the field relations and helped me rewrite the manuscript. Tom trained me in the experimental technique and intensively reviewed the manuscript. Discussions with Ro Kinzler greatly aided the development of the melting models in chapter two. Ro and Mike Walter generously allowed me to use their unpublished data on the composition of garnet lherzolite melts. David Clague provided the samples studied in chapter three, reviewed the manuscript and has given me a number of lessons on Hawaiian volcanism. Erik Hauri has become a good friend and collaborator on a number of projects, including chapters two and three. Even when busy moving from WHOI to DTM, Erik made time to help me on the ion-probe. Brian Evans and Nobu Shimizu served on my thesis committee and provided thought provoking discussions of my research. It was a pleasure talking with Nobu about the importance of the contribution of geoscience to society.

Peter Kelemen's talks on melt/wall rock reaction given during the Keck Geodynamics seminar at WHOI inspired the assimilation models developed for both the Hawaiian and Lunar chapters. Discussions with Henry Dick and others during that seminar and its field trips were very valuable educational experiences. MIT colleagues and friends Drew Coleman, Beverly Saylor, Karen Bartels, Tom Juster, Alan Brandon and the Reverend Billy Jones helped in ways too numerous to list. Thanks also go to Derek Hirst, who machined many exact things from my inexact drawings and Karen Campbell who cheerfully provided critical assistance in library research.

I've made a lot of great friends at MIT outside of EAPS who in no small part helped me finish. Special thanks go to the MIT men's and women's Rugby football clubs for great times and helping to keep me sane in the early years. I'd especially like to thank my housemates: Jon 'Dingo' Suber, Inpachelvan 'Chevy' Vithianithan, T.J. Craddick, and

other rugby friends: Rachael Berman, Brigette Tannian, Eik, Stracher, EMO, Elmo, Paul, Killer, Leo, Greg T., Jaco, Fife, Hoss, Kiwi, Hyena, Ben Paul, Murph, Jeff, Pat M., Brian T., Jim Culliton, and the most inspirational leader I have ever met, Marthinus 'Tienie' van Schoor. I'd also like to thank all the students of D-Entry, MacGregor House for their friendship and for making graduate school a lot of fun! I wish I could list everybody, but in particular I want to thank: Leslie 'in-charge' Compton, Becky 'CEO-bound' Foster, John 'Control-Freak' Robinson, Art 'Prince of Cambridge' Min, Tan 'Gunjan' Bhatnagar, Vince 'Big-Mouth' Rose, Hemant 'Haji-Jordan' Taneja, Anand 'is a-nal' Radhakrishnan, Jon '2-tall' Hsiao, Dave 'Twitcher' Hully, Brian 'Baden Powell' Blatnik, Brian 'Rainbow Head' Zabel, Adel 'Rikers bound' Rophaiel, Diana 'Banana' Chiang, Zvonimir 'Z' Turcinov, Pratip 'the double E in Geek' Banerji, Mark 'Jedhi' Ribick, Maggie 'Betty Crocker' Raphael and last but not least, Brad Spiers, the most intense human being on earth and my personal career counseler. Thanks also go out to other MITers: Lynn Roberson, one of the most interesting people to discuss the meaning of life with I've ever met; Dave Custer, who has recently been teaching me about both writing and rock climbing; and Megan Jasek who commiserated with me on finishing a thesis!

My professors and friends at SUNY Binghamton turned me on to geology and encouraged me to go on. Tim Lowenstein, through his outstanding course, Introduction to Geologic Processes, inspired myself and many other fortunate undergraduates to study geology. Great classes and discussions were also had with Bob Demicco, Dick Naslund, Dave Jenkins, Bill MacDonald, Erik Johnson, Julieanne Turko and Jim Kradyna. Important thanks go to all my classmates, including: Dave Winslow, Sara Marcus, Jen Montieth, and Becky Soble. We had a lot of fun and learned a lot together. I'd also like to thank Bernadette Kamin, Dan Abernethy and Kevin and Nancy Nazca for encouragement along the way.

Some of the most important skills I used in performing this research I learned while working at Engelbosch bicycles with Mr. Charles Sulc, who was also my most excellent high school geometry teacher. Thank you Chuck! I'd like to thank all the teachers I've ever had, and in particular: Mr. Case, who taught us that learning was fun; Ms. Diane Yaris who started science-oriented extracurricular activities including the 'learn-at-lunch' computer course and the 'Robotics and Electronics' course; Mr. Rizzi, who combined learning the Spanish language with an intensive literature appreciation course; Mr. Danley, whose european history class was so well taught I still think of it often; Mr. Griffith, my engine mechanics teacher who taught a great class on the fundamental use of tools; and Mr. Moore, my high school coach who was good coach, an excellent teacher and a great man.

Finally, I'd like to thank my family: Mom, Dad, John, Christine, Granny and Poppy for the love and support they have given me over the years. This thesis is dedicated to you!

Table of Contents

Chapter 1

Chapter 2

Chapter 3

Chapter 4

Appendix A

Appendix B

INTRODUCTION

Each of the four chapters of this thesis is written as a stand-alone paper with a comprehensive abstract at its beginning. This introduction points out the problems addressed in each chapter and outlines how solutions were developed. In all cases, the techniques of experimental petrology and geochemistry were used to discern the physical processes that lead to melt generation and/or melt modification. The thesis also contains two appendices that discuss the construction and calibration of the piston-cylinder device used to perform the experiments of chapters 2 and 4.

Chapter one addresses issues related to convergent margin magmatism through a comprehensive study of the Lake Basalt; a suite of variably porphyritic, low-MgO, high-Al_2O_3 lavas from Medicine Lake Volcano. This study provides an estimate of pre-eruptive magmatic water contents and explores the role of crystal accumulation as a magmatic process. It was performed in conjunction with Dr. J. M. Donnelley-Nolan of the USGS, who is co-author of the manuscript. The liquid line of descent of the most primitive lava was determined in a series of 1-kbar, H_2O-saturated melting experiments. These results are used to infer pre-eruptive magmatic H_2O-contents. The lavas of the Lake Basalt vary in phenocryst content from nearly aphyric to highly-porphyritic. Highly porphyritic lavas are common to convergent margin settings and questions have been raised as to whether they represent liquid compositions or crystal cumulates. The relative contributions of crystal fractionation and accumulation to the formation of the Lake Basalt is determined through modeling of major and trace element concentrations.

Chapter two addresses the origin of tholeiitic basalt in oceanic hotspots. The melting relations of a tholeiite primary magma were determined to 2.2-GPa. The results indicate that tholeiite primary magmas are in equilibrium with harzburgite at lithospheric depths beneath Hawaii. Geochemical studies of Hawaiian tholeiite conclude that it forms by partial

melting of garnet lherzolite (Chapter 3). It is proposed that Hawaiian tholeiite forms by melting of garnet lherzolite in deeper regions of a mantle plume and that these melts ascend and equilibrate with depleted harzburgite in the plume top. The experimental results are used to constrain the chemical and thermal aspects of the equilibration reaction.

Chapter three is a ion-microprobe study of the trace element abundances of picritic glass grains from Kilauea volcano, Hawaii. It was conducted in conjunction with Dr. D.A. Clague of the USGS, who is co-author of the manuscript. These glasses have the highest MgO contents of any glasses reported in Hawaii and were used to make the primary magma estimate studied in Chapter 2. The uniqueness of these glasses and their implications for the composition of tholeiite primary magmas requires that their relationship to more typical, Hawaiian shield lavas be established, which this chapter accomplishes through comparison of trace element abundances. The variations in glass trace abundances are also used to determine the residual mineralogy of their source. The effect of the equilibration reaction proposed in Chapter 2 on trace element abundances is also determined.

Chapter four explores the origin of the high-Ti lunar ultramafic glasses. It has been proposed that their formation requires overturn of the moon's outer cumulate pile. This chapter proposes an alternative model that produces high-Ti ultramafic magmas by in situ assimilation of ilmenite and clinopyroxene into low-Ti primary magmas. The assimilation reaction is determined by modeling the compositional variation in the lunar ultramafic glasses. Thermal and kinetic aspects of the reaction are constrained by experimental determination of 1) the liquidus relations of the most Ti-rich lunar ultramafic glass and 2) the dissolution rate of ilmenite in lunar magmas. Assimilation takes place at the depth at which ilmenite and clinopyroxene are thought to have precipitated during crystallization of the lunar magma ocean (~100-km), and allows the formation of high-Ti magmas without overturn of the cumulate pile.

Chapter 1

Evidence of hydrous differentiation and crystal accumulation in the low-MgO, high-Al_2O_3 Lake Basalt from Medicine Lake Volcano, California

Abstract

The late Pleistocene Lake Basalt of Medicine Lake volcano, California is comprised of variably porphyritic basalt and basaltic andesite flows and scoria. These eruptives are similar in composition and phenocryst abundance to the low-MgO, high-Al_2O_3 mafic magmas common in convergent margin settings. The petrogenesis of the magmas that produced the Lake Basalt has been inferred from field relations, melting experiments and subsequent major and trace element modeling. Their formation involved both hydrous differentiation and plagioclase accumulation and thus the Lake Basalt can be used to constrain the relative contributions of these processes to the production of high-Al_2O_3 arc basalt. Phenocryst-poor lavas of the Lake Basalt formed by hydrous differentiation; their compositions and observed phenocrysts were reproduced in 1-kbar, H_2O-saturated melting experiments. Anorthite-rich plagioclase compositions of the lavas of the Lake Basalt necessitate crystallization from melts with between 4 and 6 wt.% dissolved H_2O. Phenocryst-rich lavas of the Lake Basalt, with 18 modal-% phenocrysts and greater, formed by plagioclase accumulation in magmas similar to the phenocryst-poor lavas. This interpretation is supported by the depleted incompatible element abundances and enriched Sr/Zr ratio of the more porphyritic lavas relative to the phenocryst-poor lavas. We model the formation of the Lake Basalt as a two-stage process that combines the differentiation model of Sisson and Grove (1993b) and the plagioclase accumulation model of Crawford et al (1987). Stage one involved hydrous fractionation, granitic assimilation and mixing with undifferentiated parent magma. This process generated lavas with up to 19.2 wt.% Al_2O_3 and 7 modal-% phenocrysts. In stage two, plagioclase accumulated in these liquids and produced more aluminous and porphyritic lavas with up to 21.8 wt.% Al_2O_3 and 33 modal-% phenocrysts.

Introduction

Low-MgO high-Al_2O_3 basalt (low-MgO HAB) and basaltic andesite (BA) are among the dominant products of arc volcanism. They are thought to be derived from melts of the mantle wedge located above subducted oceanic slabs (Boettcher 1973; Ringwood 1974). Melting of the wedge is fluxed by dehydration of the down-going slab, which produces magmas that are notably more water-rich than those generated in other tectonic settings. Mantle melts are more magnesian and less aluminous than low-MgO HABs and BAs and must undergo significant compositional modification prior to eruption. Modification by differentiation is supported by some studies of the lavas' compositional variation and hydrous experimental work. The melting experiments of Sisson and Grove (1993a,b) show that typical low-MgO HABs and BAs can be produced by crystallization of mantle melts with dissolved H_2O contents of 4 to 6 wt.%. There are, however, good reasons to question whether all low-MgO HABs and BAs are liquids. These lavas can have very high abundances of phenocrysts that have textures and compositional zonation indicative of disequilibrium conditions. Noting these and other geochemical characteristics of HABs, Crawford et al. (1987) propose that these lavas have accumulated plagioclase phenocrysts and are not liquid compositions produced by crystallization.

The Lake Basalt of Medicine Lake volcano (MLV) falls within the compositional range of typical low-MgO HABs and BAs from the Aleutian Islands, Central America and elsewhere. Lavas of the Lake Basalt offer insight into the question of liquid versus cumulate origin of low-MgO HABs and BAs because they are variably porphyritic and show clear genetic relationships between nearly aphyric and phenocryst-rich lavas. We have combined an experimental melting study with major and trace element modeling to constrain the roles of crystal-fractionation and crystal-accumulation in their formation.

Geologic Setting and Field Relations

Medicine Lake volcano is a large Pleistocene and Holocene shield volcano in the southern Cascade Range with an estimated volume of 750 km^3 (Donnelly-Nolan et al., 1990; Dzurisin et al., 1991). The eruptive products range from primitive high-alumina basalt to rhyolite. The Lake Basalt was identified by Powers (1932, p. 262-263) as a coherent group of eruptive materials and later mapped and described by Anderson (1941, p. 364-365, 388). Remapping combined with chemical analyses and paleomagnetic measurements (J. Donnelly-Nolan and D.E. Champion, unpublished data 1980-1993) shows that the unit includes porphyritic and less phyric lavas that cover a large area of the volcano's eastern rampart and southeastern flank, as well as the type locality within the caldera of MLV. Late Pleistocene glaciation and subsequent eruptions have covered and obscured some of the contact relations making a detailed discrimination of flow units and an eruptive sequence impossible. Lavas comprising the Lake Basalt cover an area of approximately 150 km^2 (Fig. 1); assuming an average thickness of 20 m, their estimated volume is 3 km^3. Outcrops of the Lake Basalt are commonly scoriaceous and even where massive are purplish in hue because of pervasive oxidation. The lavas erupted from multiple vents, most forming a 15-km-long NNW-trending array that is similar to other regional vent and fault trends. These are among the highest cinder cones at MLV, including 500-m-high Border Mountain. Three vents lie within the caldera and form an approximate E-W trend, intersecting the NNW-trend at its northern end (Fig. 1).

The lavas are subdivided by mapping into four major groups: Caldera, North, South and less porphyritic (Fig. 1). The Caldera, North and South group lavas are highly porphyritic and contain 7 to 33 modal-% phenocrysts. The less porphyritic lavas contain less than 3 modal-% phenocrysts and are relatively rare. Field relations and paleomagnetic data indicate that the events which formed the Lake Basalt began with the eruption of the Caldera group. The lavas of the Caldera group stratigraphically underlie

the rest of the lavas of the Lake Basalt with flows exposed both inside and outside of the caldera rim. The lavas erupted from the E-W trend of vents and one or more sources (now buried) in the vicinity of Red Shale Butte and Lyons Peak. The eruption of the Caldera group was followed by a hiatus of geologically short duration, after which the NNW-trending vents opened and erupted the lavas of the North and South groups. In the area of the North group, the event began and ended with eruption of the less porphyritic lavas that are exposed within and on its boundaries. The less porphyritic lavas are here subdivided into two subgroups based on their location and inferred eruptive sequence, early or late. The early less porphyritic lavas form flows exposed along the eastern and southwestern margin of the North group. The late less porphyritic magmas erupted as spatter at the top of three vents for the North group: Red Shale Butte, Lyons Peak and the vent SE of Lyons Peak. Each of these three vents has a base of more porphyritic spatter which grades upward into the less porphyritic facies with no observable discontinuity. This sequence of alternating more and less porphyritic magma facies is similar to that described by Rose et al. (1978) for Fuego volcano in Guatemala.

Analytical Methods

Whole rock samples were ground to powders in alumina and analyzed for major elements by X-ray fluorescence at the U. S. Geological Survey laboratory in Lakewood, Colorado. Analytical methods and estimates of precision are discussed in Taggart et al. (1987). Splits of selected samples were analyzed for the rare earth elements, Cr, Co, Cs, Hf, Ta, Th and U concentrations by INAA at the U. S. Geological Survey laboratories at Lakewood, Colorado and Reston, Virginia. Rb, Sr, Y, Zr, Nb, Ba, Ni, Cu, Zn and Cr concentrations were measured by energy dispersive X-ray fluorescence techniques at the U. S. Geological Survey in Menlo Park, California. See Baedecker (1987) for description of analytical technique. All data are reported in Table 1.

Lava phenocrysts and the experimental products were analyzed by electron microprobe at MIT on a JEOL 733 Superprobe using wavelength-dispersive techniques. Data were reduced using the correction scheme of Bence and Albee (1968) with the modifications of Albee and Ray (1970). Crystalline phases in the lavas and experiments were analyzed at 15 kV accelerating potential, 10 nA beam current and a spot size on the order of 2 μm. Spot size was increased to 30 μm to analyze the hydrous glasses in the experiments. The large spot sizes and low beam currents were used to minimize diffusion of alkali elements away from the region of interest during the analysis. The H_2O content of the experimental glasses was estimated from the electron microprobe analyses by summation deficit. This technique has been shown to produce results within ±0.2-0.3 wt.% to those obtained by ion microprobe techniques (Sisson and Layne 1993). Electron microprobe analyses were corrected for analytical bias relative to the XRF major element data, +5% for TiO_2 and -9.6% for Na_2O. Values were determined by comparing the concentration of these elements in experiment 15 to the XRF analysis of 1471M-B.

Petrography and chemical composition of the lavas

The lavas show a complete gradation in phenocryst abundance and range from nearly aphyric to highly porphyritic with 33 modal-% phenocrysts. Highly porphyritic lavas grade into nearly aphyric lavas with no observable discontinuity at a number of vent areas for the North group. Anorthite-rich plagioclase is the most abundant phenocryst, followed by much less common olivine (Table 2). Minor amounts of high-chromium spinel and titano-magnetite phenocrysts are present in most samples, while clinopyroxene phenocrysts are found in only one sample. Groundmass in all samples is completely crystalline and contains microphenocrysts of plagioclase, olivine, clinopyroxene and magnetite.

Plagioclase phenocrysts vary from large equant laths to broken and resorbed crystals and range in size from 0.2 to 3.5 mm. Some phenocrysts have sieve-like textures due to

large numbers of inclusions of groundmass material. Many phenocrysts have rims of more albitic plagioclase up to 10 μm thick. Phenocryst core compositions are both normally and inversely zoned and vary from An_{62} to An_{87} with rims from An_{43} to An_{47} (Table 3, Anderson 1941; Gerlach and Grove 1982). Olivine phenocrysts have broken, sharp edges and range in size from 0.2 to 0.9 mm. Olivines are generally homogeneous in composition within each sample, though some cores are slightly normally zoned. Phenocryst core compositions throughout the suite vary from Fo_{70} to Fo_{82}. Thin rims (<5 μm) of more fayalitic olivine (Fo_{64} to Fo_{77}) are present on some phenocrysts. Spinels are found as individual phenocrysts and inclusions in olivine and plagioclase and range in size from 0.04 to 0.18 mm. They vary in composition from titano-magnetite to high-chromium spinel (Cr-sp). Titano-magnetites are generally equant in shape and are found as phenocrysts and inclusions. Cr-sp are rarer than titano-magnetites and have rounded and embayed edges where present in the groundmass but can be equant as inclusions. Their molar $^{Cr}/_{Cr+Al}$ varies from 40 to 74, the most chromium-rich spinels are present only as inclusions. Clinopyroxene forms phenocrysts in only one sample (1709M), where it is present in glomerocrystic intergrowths with olivine and plagioclase.

The map units comprising the Lake Basalt (Fig. 1) correlate with compositional and modal phenocryst abundance differences (Fig. 2 and Table 2). Whole-rock Al_2O_3 contents correlate with plagioclase phenocryst abundances, as observed by Ewart (1982) and Crawford et al. (1987) for other arcs. The less porphyritic units have the lowest Al_2O_3 contents (17.4 to 18.2 wt.%) and the lowest plagioclase phenocryst abundances (<2.3 modal-%). The Caldera and South group lavas have the highest Al_2O_3 contents (>20 wt.%) and the highest plagioclase phenocryst contents. The South group lavas have higher MgO contents than the Caldera group lavas due to their greater abundance of olivine phenocrysts. The North group lavas have the largest compositional variation and correspondingly show the largest variations in phenocryst abundance, ranging from the least to most porphyritic.

Experimental Methods

Starting composition A sample of the less porphyritic lavas with the highest Mg# (100*molar $^{MgO}/_{MgO+FeO}$=54), 1471M-B, was chosen as a starting composition. It contains only trace amounts of olivine and plagioclase phenocrysts and is thus likely to represent a liquid composition. A split of the powder used for chemical analysis was reground under ethyl alcohol in an agate mortar to reduce the grain size.

Experiments All experiments were performed in a TZM rapid quench pressure vessel using the assembly and techniques described in Sisson and Grove (1993a). Sample powder was placed in a 0.25" x 0.15" cylindrical Au sample capsule which was crimped and welded closed on one end and simply crimped and left unsealed on the other. This sample capsule was loaded into a 1"x 0.20" cylindrical Au outer capsule with 2 or 3 Pt buffer capsules and approximately 18 μL of H_2O. The Pt buffer capsules contained a mixture of Ni and NiO. The outer capsule was sealed by welding at each end. The sample and Pt buffer capsules were left unsealed to allow for O_2 exchange. The highest temperature experiment exceeded the melting point of Au; in this case, Au_{80}-Pt_{20} and Ag-Pd alloys were substituted for the outer capsule and sample capsules respectively. Fe loss to the Au and Ag-Pd sample capsules is negligible; mass balance of all observed phases against the starting composition showed Fe to balance within 1% relative.

All experiments were performed at 1 kbar, using a mixture of argon and methane (CH_4) gas added in the proportion of 2000 psi : 20 psi as the pressure medium. The breakdown of CH_4 to graphite and H_2(gas) slows H_2 diffusion out of the outer capsule and helps maintain its H_2O content. An experiment was judged successful on the basis of the following criteria: 1) liquid H_2O was present upon puncture of the outer capsule, 2) buffer capsules contained both Ni and NiO and 3) silicate liquid formed a glass free of quench growth. Individual run conditions and phase proportions are reported in Table 4. Phase compositions for each experiment are reported in Table 5.

Matrix separates The matrix material in two of the more porphyritic samples, 1443M (South group) and 79-3g (Caldera group) was separated for chemical analysis. Rocks were coarsely crushed (0.5 to 2 mm in size) in a platener mortar and the least phyric pieces were hand separated under a binocular microscope. The samples were ground in an agate mortar and completely melted in gold capsules under H_2O saturated conditions at 1.75 kbar and 1050°C. Compositions of the resultant glasses were determined by electron microprobe. Higher pressures were used than in the experiments to increase the sample water content and ensure complete melting.

Experimental Results

The liquid phase in all experiments quenched to a hydrous, homogeneous glass with approximately 4-5 wt.% H_2O. The glass compositions define a differentiation trend that ranges from low-MgO HAB to andesite, characterized by increasing SiO_2, Na_2O and TiO_2 with decreasing Al_2O_3, CaO and MgO contents (Fig. 2). These trends are similar to those defined by the less porphyritic lavas of the Lake Basalt. Al_2O_3 contents of the experimental liquids range from 17.1 to 18.1 wt.% and are thus distinctly lower than many low-MgO HAB. Olivine (ol) is the liquidus phase near 1075° C, joined within a 25° reduction in temperature by plagioclase (pl) and chrome-spinel (Cr-sp). Cr-sp is only present in trace amounts. Ol, pl and Cr-sp crystallize together until 1030°C, where high-calcium pyroxene (cpx) joins the assemblage at the expense of Cr-sp. Titano-magnetite appears at 1000° C.

Olivine The olivines in all experiments are homogeneous in composition and equant in shape. The Fe/Mg exchange K_D [$K_D=(Fe_{ol}/Mg_{ol})/(Fe_{liq}/Mg_{liq})$] ranged from 0.27 to 0.30 with an average value of 0.29±0.01, assuming all Fe is Fe^{2+}. Sisson and Grove (1993a) measured $Fe^{3+}/(Fe^{2+} + Fe^{3+})$ to be 0.137 by Mossbauer spectroscopy in 2-kbar H_2O-saturated, Ni-NiO buffered basaltic liquids. Using this ratio to calculate the Fe^{2+} in our experiments and recalculating our exchange K_Ds gives an average value of 0.33. This

is similar to the average value of 0.34 determined for the 1-kbar, H_2O-saturated experiments of Sisson and Grove (1993b) and within the range of K_Ds (0.26-0.36) determined by Roeder and Emslie (1970) for dry basaltic liquids.

Plagioclase Phenocrysts generally grew as equant, homogeneous laths. Plagioclase present in the starting composition did not completely re-equilibrate in the two lowest temperature experiments but grew homogeneous reaction rims (>10 μm) that were analyzed. The Ca/Na exchange K_D for plagioclase [$K_D=(Ca_{pl}/Na_{pl})/(Ca_{liq}/Na_{liq})$] in the experiments ranged from 2.5 to 4.4 with an average value of 3.1 and was inversely correlated with temperature. This is similar to the average value of 3.3 determined for the 1-kbar, H_2O-saturated experiments of Sisson and Grove (1993b).

Spinel Oxide phases are either Cr-sp or titano-magnetite, similar in composition to those present in the lavas. Spinel crystals are on the order of 2-3 μm in size, making quantitative analysis difficult. Cr-sp is present in experiments from 1050 to 1035° C, but was only large enough for quantitative analysis in the 1035° C experiment where a single large equant Cr-sp was analyzed. Spinel in the lower temperature experiments (run #'s 1 and 8) is titano-magnetite. The loss of Cr-sp from the liquidus in the experiments concurs with the resorbed habit of Cr-sp surrounded by groundmass in the lavas.

High-calcium pyroxene Cpx is not present as a phenocryst phase in 1471M-B and where present in the experiments grew from liquid. Assuming all Fe is FeO, the Fe/Mg exchange K_D ranged from 0.20 to 0.25 with an average value of 0.21±0.02. This is similar to the average value of 0.22 determined for the 1-kbar, H_2O-saturated experiments of Sisson and Grove (1993b) as well as in the 1 atm anhydrous experiments of Grove and Bryan (1983).

Discussion

Models of low-MgO HAB and BA genesis

The petrologic complexity of low-MgO HABs and BAs indicate that a variety of processes led to their origin. Low-MgO HABs and BAs often have very high plagioclase phenocryst contents, some in excess of 50 modal-%, which can be correlated with bulk rock Al_2O_3 (Ewart 1982). The phenocrysts commonly have disequilibrium textures and variable compositions, indicating crystallization under a variety of conditions. These observations and other geochemical evidence led Crawford et al. (1987) to conclude that HABs with >18 wt.% Al_2O_3 form by plagioclase accumulation. They argue that liquids produced by differentiation contain <17.5 wt.% Al_2O_3 and are produced through olivine- and clinopyroxene-controlled differentiation of less aluminous mantle melts. Many other studies (e.g. Kay et al. 1982; Gust and Perfit 1987) conclude that the compositional variation in HABs is consistent with an origin by differentiation. Nevertheless, anhydrous experimental studies have been unable to produce typical low-MgO HAB and BAs by crystallization of either high- or low-Al_2O_3 parent compositions at any pressure (Gust and Perfit 1987; Bartels et al. 1991; Draper and Johnston 1993). Hydrous experimental studies, on the other hand, have shown that differentiation with dissolved water contents of 4 to 6 wt.% can produce liquids with compositions similar to typical low-MgO HABs and BAs (Sisson and Grove 1993b ; Gaetani et al. 1993). Water contents of this magnitude have been observed in melt inclusions from arc environments (Anderson 1979; Sisson and Layne 1993). Sisson and Grove (1993b) propose that high dissolved water contents produce the high phenocryst contents of low-MgO HABs and BAs; as rising magmas degas, the corresponding rise in liquidus temperature and shift of phase boundaries would cause plagioclase crystallization.

Magmatic H_2O contents of lavas of the Lake Basalt

Though magmas can have significant dissolved H_2O contents at crustal pressures, they undergo rapid devolatilization during eruption. Unaltered lavas generally have less than 0.1 wt.% dissolved H_2O. Pre-eruptive H_2O contents can be estimated based on plagioclase phenocryst composition since melt H_2O content is positively correlated with the anorthite content of coexisting plagioclase (e.g. Yoder 1969; Arculus and Wills 1980; Housh and Luhr 1991). The plagioclase-liquid Ca/Na exchange K_D has a value of ~1 under anhydrous conditions, increasing to ~3.1 at dissolved water contents of 4 wt.% (this study) and further increasing to ~5.5 at water contents of 6 wt.% (Sisson and Grove 1993a). These values were used to calculate the plagioclase compositions that would coexist with the less porphyritic lavas and the experimental glasses (Fig. 3). Calculations using the more porphyritic lavas as melts yield similar results. The anorthite contents of the plagioclase phenocryst cores of the more and less porphyritic lavas are similar to those predicted to coexist with melts containing 4 to 6 wt.% dissolved H_2O (1-to 2-kbar H_2O saturated conditions). These are the same conditions predicted by Sisson and Grove (1993b) for formation of low-MgO HABs and BAs by differentiation. The plagioclase phenocryst rim compositions approach those predicted for dry conditions and indicate that rim growth continued after degassing, probably during eruption or shallow level storage. Olivine core compositions of 79-3g and 1709M have Mg#s much lower than would be in equilibrium with the matrix separates or the less porphyritic lavas, but are similar to the lowest temperature experimental liquids. Olivine cores of 1471M-A, 1366M and 1443M indicate crystallization in magmas with higher Mg#s than the most primitive sampled lava.

The liquid line of descent followed by a magma will also vary as a function of dissolved H_2O content. Figures 4a and 4b show the anhydrous and hydrous crystallization paths for 1471M-B, the most primitive less porphyritic lava and

experimental starting composition. The 1-kbar anhydrous ol-cpx-pl crystallization boundary has been predicted using the equations of Yang et al. (Unpublished, 1993) that parameterize 175 ol-cpx-pl saturated basaltic liquids in the 1-atm to 10-kbar range from the experimental literature. The anhydrous boundary reduces to a point in the Ol-Pl-Cpx projection (Fig.4a) since it is nearly perpendicular to the ol-cpx-pl plane. In the Cpx-Pl-Qtz (Fig. 4b) projection the boundary projects as a line. 1471M-B projects in the anhydrous plagioclase liquidus phase volume. If 1471M-B liquid underwent anhydrous crystallization, residual liquids would move towards ol-cpx-pl saturation by crystallizing plagioclase until intersection with the ol-pl cotectic (point 1 in Fig. 4a). None of the lavas plot along the anhydrous path in either projection.

The addition of water changes the direction of crystallization and generates a path that parallels the shape of the field defined by the less porphyritic lavas. Hydrous differentiation, as initially determined by Yoder (1965) in the system diopside-anorthite, expands the diopside primary phase volume at the expense of anorthite. The hydrous ol-cpx-pl boundary is redirected in the Ol-Cpx-Pl projection to trend towards the Pl apex. For hydrous crystallization of 1471M-B, olivine becomes the liquidus phase. A small amount of olivine crystallization, followed by Cr-sp and pl, leads to ol-cpx-pl multiple saturation. The less porphyritic lava samples plot near the 1-kbar H_2O saturated boundaries in both projections, while the more porphyritic lavas are displaced towards the plagioclase apex in the Cpx-Pl-Qtz projection (Fig. 4b).

Petrogenesis of the less porphyritic lavas

The less porphyritic lavas show major element compositional variation broadly similar to the liquid line of descent followed by the experiments. However, CaO, FeO and TiO_2 contents of the lavas are lower while SiO_2 contents are higher than the experimental liquids at corresponding MgO contents (Fig. 2). Trace element concentrations in the experimental liquids were calculated for a simple fractional crystallization model (Table 6, Fig. 5). The

trace element abundances of the calculated fractionation path are not similar to the less porphyritic lava samples for several key elements. K_2O, Ba and Rb abundances are progressively enriched in the less porphyritic lava samples relative to the calculated fractionation path. Although the variations in the major element concentrations of the less porphyritic lavas resemble those of the experiments, fractionation of the most commonly observed phenocrysts (ol and pl) can not be solely responsible for the observed chemical variations. We conclude that open system processes operated in the magma system. Many studies (Eichelberger 1975; Anderson 1976; Grove et al. 1988; Baker et al. 1991; Donnelly-Nolan et al. 1991) have concluded that magmatic systems at MLV experienced complex, open-system processes including assimilation and magma mixing. The resorbed textures and common reverse compositional zonation of plagioclase phenocrysts in the lavas of the Lake Basalt led Anderson (1941) and Gerlach and Grove (1982) to conclude that these lavas formed by open system processes. Baker et al. (1991) recognized such complexities as the FARM process (Fractionation, Assimilation, Replenishment and Mixing) for the Giant Crater lava field.

Major element FARM models The major element compositions of all of the less porphyritic lava samples were modeled using a FARM model (Table 7, Fig. 2) following the method of Baker et al. (1991). A unit of parent liquid differentiates and supplies heat to melt granitic crust. The magma system is subsequently replenished with undifferentiated parent liquid which mixes with the melted crust and differentiated liquid. The glass compositions from experiments 13 and 14 were chosen as the differentiated liquids. These experiments contained little to no cpx (Table 4) which is consistent with the lack of cpx in the lavas. Using lower temperature experiments did not improve the fit of any models. A partially melted granitic xenolith from the Lake Basalt, (561M, Grove et al. 1988) was chosen as the assimilant composition. There are a variety of other granitic inclusions found at MLV (Grove et al. 1988), but varying the composition of granitic assimilant did not result in significantly better fits to the lava compositions.

Sample 1471M-B, the most primitive less porphyritic lava sample, was used for the replenishing liquid. Proportions of each of the components were determined by multiple linear regression for each less porphyritic lava composition. Complete FARM models generally result in a significantly better fit to the data set than assimilation and fractional crystallization (AFC) models. Two (1344M and 313M) lavas can be equally well reproduced using only AFC and one (1444M) can be reproduced using only FRM. Major element contents of most samples were reproduced to better than 2% relative and minor elements (TiO_2 and K_2O) were well reproduced for most samples.

Trace Element FARM models The proportions of FARM components from the major element regressions of Table 7 were used in trace element modeling of the less porphyritic lavas (Table 8, Fig. 5). The Sr abundances of the less porphyritic lavas form two distinct trends that have similar slopes, but are offset in concentration by approximately 25% (Fig. 5). The low-Sr trend was well reproduced by the FARM model used for the major elements, which uses 1471M-B as the parent for the fractionating and replenishing liquid (denoted Model-1 in Table 8 and Fig. 5). A second model was developed to reproduce the high-Sr trend. Model-2 uses the most primitive lava of the late less porphyritic group, 1281M, for the fractionating and replenishing liquid. It has undergone some assimilation of granitic crust based on the FARM model calculation for major elements. It was corrected to its pre-assimilation trace element abundance levels based on the proportions from the major element model (Table 7), 6 wt.% of 561M was subtracted from it. Recalculating the major element FARM models using the 1281M-based parent reproduces some of the minor element abundances better than Model-1, but does not make a significant difference for the other major elements. Most of the variations in abundances shown by the less porphyritic lavas fall within the trends defined by Model-1 and -2. Model-1 abundances define the lower limit of variation in Sr, Ba and Nd and the upper limit of variation in the Rb and Zr variation diagrams. Model-2 forms

complementary trends that define the upper limit of variation on the Sr, Ba and Nd and the lower limit in the Rb and Zr variation diagrams.

The low-Sr trend contains early less porphyritic lavas and is similar in concentration and slope to Model-1. The high-Sr trend contains two of the early and all of the late less porphyritic samples and is overlapped in concentration and slope by Model-2. In other words, using the most primitive early lava (1471M-B) as a parent generally reproduces the early lavas (Model-1), while using the most primitive late lava (1281M) as a parent reproduces some of the early and all of the late lavas (Model-2).

Petrogenesis of the more porphyritic lavas

Moderately porphyritic lavas The North group lavas with < or =19.2 wt.% Al_2O_3 (1471M-A, 1669M, 1670M and 1725M) have the lowest phenocryst contents of the porphyritic samples. With the exception of their higher Al_2O_3 contents, they are chemically similar to the less porphyritic lavas (Figs. 2, 5 and 6) and form trends consistent with either an accumulation or a differentiation origin. 1471M-A has approximately 7-modal % phenocrysts and was collected from the same outcrop as less porphyritic lava 1471M-B, which is nearly aphyric. Addition of 7 wt.% plagioclase to 1471M-B can nearly produce the bulk composition of 1471M-A. The experiments of Sisson and Grove (1993a) show that the plagioclase phase volume shrinks with increasing dissolved H_2O, resulting in increased liquid Al_2O_3 contents during differentiation. Ol-pl-cpx-H_2O saturated liquids at 2-kbar contain approximately 20 wt.% Al_2O_3. The moderately porphyritic North group lavas could represent liquids that differentiated at 2-kbar with dissolved water contents of up to 6 wt.%, which led to their higher Al_2O_3 contents. Their higher phenocryst contents relative to the less porphyritic lavas could reflect in situ phenocryst growth during degassing of higher water content magma that occurred during decompression and eruption.

Highly porphyritic lavas The majority of the more porphyritic lavas have >20 wt. % Al_2O_3 and >18 modal-% phenocrysts. Liquids with Al_2O_3 contents of this magnitude might be produced by H_2O-saturated differentiation at pressures >2-kbar, however the plagioclase phenocrysts found in these lavas have anorthite contents consistent with crystallization under H_2O-saturated conditions of only 1- or 2-kbar (Fig. 3). Furthermore, these porphyritic lavas plot away from the differentiation trend and lie along a plagioclase addition line (Fig. 4b). The major and trace elements incompatible in ol, cpx and pl (Na_2O and TiO_2 and Ba, K_2O, Ce, Zr and Rb) are depleted in the more porphyritic South group and most of the North group lavas relative to the less porphyritic lavas (Figs. 2 and 5). Therefore these more porphyritic lavas cannot be related to the less porphyritic lavas through differentiation.

Variations in the Sr/Zr ratio also indicate that the most porphyritic lavas are not related to each other or the less porphyritic lavas through differentiation. The Sr/Zr ratios (Fig. 6) of the more porphyritic lavas are highly variable and enriched relative to the less porphyritic lavas, which form trends consistent with the FARM model. Olivine and cpx fractionation increases the residual liquid's Al_2O_3 content, but has little effect on its Sr/Zr ratio (partition coefficients in Table 6). Plagioclase crystallization would decrease the Sr/Zr ratio and retard any Al_2O_3 increases during crystallization so it was left out to maximize differentiation effects. Crystallization of ol and cpx defines nearly horizontal lines in Fig. 6. Twenty-four percent crystallization of 15% olivine and 85% clinopyroxene from 1471M-B only changes the Sr/Zr ratio from 4.67 to 4.72. The Al_2O_3 content of the liquid rises from 17.9 to 22 wt.%, the lava maximum, but lowers the MgO content from 5.98 to 2.50, well below that observed in the lavas. MgO/Al_2O_3 ratio drops from 0.33 to 0.11. The other major element concentrations of the liquid are significantly different than those observed in the more porphyritic lavas. The South group and most of the North group lavas have Sr/Zr>6, while all of the less porphyritic lavas have Sr/Zr<6. Therefore, the Sr/Zr ratios of the most of the North and South group lavas are too high to

be related to any of the less porphyritic lavas through crystallization. Production of the more porphyritic lavas by differentiation could have involved an unsampled parent with a high Sr/Zr ratio. However, the variability in the Sr/Zr ratio of the more porphyritic lavas at nearly constant MgO/Al_2O_3 ratio is difficult to explain by a differentiation process. We conclude that the more porphyritic North and South group lavas with >19.7 wt.% Al_2O_3 are not related to each other or the less porphyritic lavas through a differentiation mechanism and are likely produced through a process of phenocryst accumulation at a pressure/depth similar to the one that generated the less and moderately porphyritic lavas. The accumulation model is also supported by the composition of the matrix separate of 1443M (Table 9), which is very similar to the less porphyritic lava compositions.

Accumulation constraints To estimate the proportions and compositions of the entrained phenocrysts in the more porphyritic lavas, the bulk rock compositions of samples 1443M (South group) and 79-3g (Caldera group) were mass balanced against their groundmass separates and phenocryst compositions (Table 9). All of the observed phenocryst phases with a complete range of plagioclase compositions were included in the mass balances, but only the most anorthite-rich plagioclase and some olivine was required to reproduce the bulk rocks. Olivine and spinel phenocrysts are much smaller in size than plagioclase phenocrysts and hence may not have been as effectively removed during matrix separation. More albitic plagioclase did not significantly improve the models of either sample.

Accumulation models The mass balance proportions from Table 9 were used to model the effects of phenocryst accumulation on the Sr/Zr and MgO/Al_2O_3 ratios of various less porphyritic lavas (Fig. 6). Plagioclase accumulation increases the Sr/Zr ratio and decreases the MgO/Al_2O_3 ratio. The relatively minor amount of olivine accumulation has little effect on the Sr/Zr ratio, but somewhat counters the effect of plagioclase on the MgO/Al_2O_3 ratio. The models of plagioclase and olivine accumulation (Fig. 6) use the proportions estimated for phenocryst accumulation in 1443M of the South group. Three

wt.% olivine and 19 wt.% plagioclase were added to the less porphyritic lavas with MgO contents near that of the 1443M matrix separate, 1281M of the high-Sr series and 1444M of the low-Sr series. Trace element abundances of accumulated phenocrysts are in equilibrium with a 1471M-B liquid composition from Table 6 that has an MgO content nearest to that of the matrix separate. The accumulation lines approximately define the field of South group lavas in Fig. 6. A model of plagioclase-only accumulation (Fig. 6) uses the proportions estimated for accumulation in sample 79-3g of the Caldera group. It adds 18 wt.% plagioclase (Table 9) to less porphyritic sample 1762M, which has a similar MgO content to the matrix separate of sample 79-3g. The accumulation line ends right in the field of the Caldera group lavas, though based on other constraints it is not clear that the Caldera group is chemically related to the other lavas of the Lake Basalt. It is clear from Fig. 6 that pl and ol addition models can reproduce the entire spectrum of more porphyritic lavas from the less porphyritic lavas and we conclude that plagioclase accumulation is viable mechanism.

Caldera group lavas The lavas of the Caldera group differ from the more and less porphyritic lavas in having FeO and TiO_2 concentrations similar to the less porphyritic lavas (Fig. 2). This similarity might support a differentiation origin, but all of the incompatible element abundances of the Caldera group lavas are depleted with respect to the less porphyritic lavas and in this regard they resemble the other more porphyritic lavas (Fig. 5). Field constraints show that the Caldera group erupted before the other lavas of the Lake Basalt and from the E-W vent trend rather than the much larger NNW trend that vented the North and South groups. Therefore the Caldera group may sample a different magmatic system of which a less porphyritic member is either not erupted or not exposed. The phenocryst textures and compositions found in the Caldera group are identical to the those of the North and South groups and likely formed by the same hydrous fractionation and plagioclase accumulation mechanisms.

Conclusions

We conclude that the lavas of the Lake basalt were formed by a combination of hydrous FARM differentiation and phenocryst accumulation. Plagioclase phenocrysts found in the lavas crystallized from magmas with dissolved H_2O contents of 4 to 6 wt.%. The less porphyritic lavas formed by FARM differentiation with dissolved water contents of approximately 4 wt.%, while the most porphyritic lavas formed by plagioclase crystal accumulation in these magmas. These conclusions combine the hydrous differentiation model of Sisson and Grove (1993b) with the plagioclase accumulation model of Crawford et al. (1987). Moderately porphyritic lavas fall in a crossover region where differentiation and accumulation cannot be uniquely constrained. Thus, liquids in the Lake Basalt magmatic system had at least 18.2 wt.% Al_2O_3 and possibly up to 19.2 wt.%, significantly higher than the limits proposed by Crawford et al. (1987), but slightly lower than the Al_2O_3 solubility limit determined by Sisson and Grove (1993a,b) 1- to 2- kbar H_2O saturated liquids.

The magmatic system that produced these lavas preferentially segregated and concentrated plagioclase phenocrysts into the more porphyritic lavas. Brophy (1989b) propose that simultaneous crystallization and convection in magma chamber could cause such sorting. There is evidence of at least 1 km^3 sized magma chambers beneath MLV (Baker et al. 1991). A multiply recharged magma chamber is consistent with the FARM model we developed. The most differentiated liquids used in the FARM modeling crystallized approximately 10 wt.% plagioclase. The most porphyritic lavas have almost twice that amount and hence there should twice as much less porphyritic than more porphyritic material, which is not supported by the mapped area. This unaccounted for less porphyritic component could be trapped at depth or simply buried beneath the more porphyritic lavas. Alternatively, the plagioclase phenocrysts could be related to the formation of andesites that are present in abundance in the older eruptive sequence at MLV. The differentiating liquids that produced these lavas may have remained hot enough to be entrained by the magmas of the Lake Basalt.

Acknowledgments: A. Brandon, D.E. Champion, N. Chatterjee, F.A. Frey, G.A. Gaetani, A. Saal and E. Takazawa are thanked for helpful discussion and reading of earlier versions of the manuscript. H.J. Yang is thanked for the use of his equations for predicting the anhydrous phase boundaries. S.I. Recca and M.J. Jercinovic expertly maintained the MIT electron microprobe facility during the course of this study. The geo-artistic talents of E.B. Lougee created Fig. 1. The senior author wishes to thank T.W. Sisson for helpful direction early on in the project and two rounds of formal review. This paper also benefited from reviews by C. Bacon and anonymous reviewer. This work was supported by NSF grant # EAR-9204661 and EAR-9406177.

Figure Captions

Figure 1. Location map shows distribution of the Lake Basalt. Dashed lines are inferred or approximate boundaries. Inset map shows location within state of California, USA.

Figure 2. MgO variation diagrams of major oxides for the lava samples of the Lake Basalt, experimental glasses and models of the less porphyritic lava samples. All values are in wt.%. Data for the lava samples (Table 1) and the experimental glasses (Table 5) is normalized to 100%, volatile free. Arrows show compositional variation of the less porphyritic Lake Basalt models from Table 7, arrow-tails begin at 1471M-B. Two-sigma error bars for experimental glasses are smaller than their symbol. The two lowest temperature experiments are not plotted because their MgO contents are significantly lower than that of the Lake Basalt.

Figure 3. Comparison of measured phenocryst compositions of lavas of the Lake Basalt with those predicted as a function of magmatic water content, Mg# of olivine against An# of plagioclase. Dashed lines connect cores to measured phenocryst rim compositions. Predicted phenocryst compositions are based on the less porphyritic lava samples, the experimental glasses and the matrix separates of the more porphyritic lava samples (Table 9). Plagioclase Ca/Na exchange K_D varies from 1 ("Predicted Anhydrous") to 3.1 ("Predicted 1-kbar H_2O") to 5.5 ("Predicted 2-kbar H_2O"). Fe/Mg exchange K_D for olivine was held constant at 0.29. Rim compositions were not analyzed on 1443M or 1709M, but were present in each sample.

Figure 4. Normative projections using the equations of Grove (1993). Arrows point in down temperature directions. *a.* Pl-Cpx-Ol projection (critical plane of silica undersaturation). Solid curve represents 1-kbar water-saturated ol-cpx-pl crystallization boundary as determined by the experiments in this study. Dashed lines schematically show phase boundaries and 1-kbar anhydrous crystallization path. Point 1 shows the beginning of ol-pl cosaturation during 2-kbar anhydrous crystallization, point 2 shows ol-pl-cpx saturation as predicted by the equations of Yang et al. (Unpublished, 1993). *b.* Pl-Cpx-Qtz projection. Solid curves represent 1-kbar ol-cpx-pl boundaries.

Figure 5. Selected trace element and K_2O abundances plotted against MgO for lavas and models. K_2O and MgO in wt.%. Sr, Rb, Ba, Ce and Yb in ppm. "Fract. Cryst." points are from Table 6. Arrows are FARM model compositions from Table 8 that employ fractional crystallization, assimilation and mixing. Tails of Model-1 arrows begin at 1471M-B, tails of Model-2 arrows begin at calculated 1281M-pre-assimilation points from Tables 8 and 9.

Figure 6. Plagioclase compatible/incompatible vs. incompatible/compatible trace and major element ratio plot to illustrate the relationship between more and less porphyritic lavas.

Footnotes to Tables

Table 1a. Major oxides are in wt.%, normalized to 100 excluding LOI. Total is the original total with Fe as Fe_2O_3 plus LOI (loss on ignition at 900°C). FeO* is total Fe calculated as FeO. Major elements analyzed at USGS, Lakewood, CO. Analysts: J. Baker, A. Bartel, J. Mee, D. Siems, J. Taggart and J. Wahlberg.

Table 1b. Trace elements are in ppm, determined by INAA at USGS; Lakewood, CO (Analysts: J. Budahn and R. Knight) and Reston, VA. Analysts: P. Baedecker, J. Mee and G. Wandless. '-' indicates elemental abundance not determined.

Table 1c. Trace elements are in ppm, determined by energy dispersive XRF at USGS, Menlo Park, CA. Analyst: P. Bruggman. Values followed by an * were determined by wavelength dispersive XRF at USGS, Reston, VA. Analysts: D. Burgi and R. Johnson. '-' indicates elemental abundance not determined.

Table 2. Normalized to 100%, vesicle free.

Table 3. Spinel: Fe_2O_3, FeO and total are based on 3 cation, 4 oxygen stoichiometry. 'nd' indicates element not detected. '-' indicates elemental abundance not determined.

Table 4. Analyses of all phases were mass balanced against the bulk composition 1471M-B.

Table 5. All analyses by electron microprobe, reported in wt.%. Values in parentheses are the two sigma deviations based on replicate analysis. The number of analyses of individual phases are reported in "Pts." column. Glass analyses are normalized to 100% on a volatile free basis; the original total is reported in "Total" column. * indicates phase detected, but is not of sufficient size for quantitative analysis. 'nd' indicates element not detected. '-' indicates elemental abundance not determined. For spinel analyses all Fe was originally determined as FeO. Reported Fe_2O_3, FeO, and Total for spinels are recalculations based on a stoichiometry of 3 cations and 4 Oxygens.

Table 6. All abundance values in ppm. Data sources for partition coefficients: Sr, Rb, Ba, Th, Ta and Nb from - Gill (1981); REE, Hf and Zr from Fujimaki et al. (1984). Bulk partition coefficients determined using the experimental phase proportions from Table 4. Elemental abundances for 1471M-B from Table 1. 1281M was corrected to its pre-assimilation abundances of trace elements based on the proportions determined in Table 7, 6 wt.% of 561M was subtracted from 1281M. Fractionation calculation for differentiated liquids calculated using the equations of Allegre and Minster (1978).

Table 7. FARM models are calculated by least squares multiple linear regression of the differentiated liquid, primitive liquid, and assimilant against the bulk composition of each sample. All compositions normalized to 100% without Cr_2O_3, MnO and P_2O_5. Differentiated liquids are the experimental glasses (Table 5) with TiO_2 and Na_2O concentrations corrected for analytical bias as discussed in text. Primitive liquid is sample 1471M-B. Granitic assimilant is 561M reported in Grove et al (1988).

Table 8. All values in ppm. Mixing models are based on the proportions calculated from the major element mass balances in Table 7. Elemental abundances for lavas from Table 1. Model-1 uses 1471M-B as parent composition for differentiated liquids (Table 6) and the primitive liquid recharge. Model-2 uses the pre-assimilation corrected 1281M as parent composition for differentiated liquids (Table 6) and the primitive liquid recharge.

Table 9. All analyses in wt.%, normalized to 100 without P_2O_5 and MnO. Matrix is analyzed glass from melted matrix separates described in text. Phenocryst compositions are from Table 3. Proportions were calculated by least squares multiple linear regression.

References

Albee AL, Ray L (1970). Correction factors for electron microprobe microanalysis of silicates, oxides, carbonates, phosphates and sulfates. Anal Chem 42: 1408-1418

Allegre CJ, Minster JF (1978). Quantitative models of trace element behavior in magmatic processes. Earth Plan Sci Lett 38: 1-25

Anderson AT (1976). Magma mixing: petrological processes and volcanological tools. Journal of Volcanology and Geothermal Research 1: 3-33

Anderson AT (1979). Water in some hypersthenic magmas. J Geol 87: 509-531

Anderson CA (1941). Volcanoes of the Medicine Lake Highland, California. University of California Publications, Bulletin of Department of Geological Sciences. 25, no. 7: 347-422

Arculus RJ, Wills KJ (1980). The petrology of igneous blocks and inclusions from the lesser Antilles island arc. J Petrol 21: 143-168

Baedecker PA (1987). Methods for geochemical analysis. USGS Bulletin 1770

Baker MB, Grove TL, Kinzler RJ, Donnelly-Nolan JM, Wandless GA (1991). Origin of compositional zonation (high-alumina basalt to basaltic andesite) in the Giant Crater lava field, Medicine Lake volcano, northern California. J Geophys Res 96(B13): 21819-21842

Bartels KS, Kinzler RJ, Grove TL (1991). High pressure phase relations of primitive high-alumina basalts from Medicine Lake volcano, northern California. Contrib Mineral Petrol 108: 253-270

Bence AB, Albee AL (1968). Empirical corrections factors for the electron microanalysis of silicates and oxides. J Geol 76: 382-403

Boettcher AL (1973). Volcanism and orogenic belts- the origin of andesites. Tectonophysics 17: 223-240

Brophy JG (1989a). Can high-alumina arc basalt be derived from low alumina arc basalt? Evidence from Kanaga island, Aleutian arc, Alaska. Geol 17: 333-336

Brophy JG (1989b). Basalt convection and plagioclase retention: a model for the generation of high-alumina arc basalt. J Geol 97: 319-329

Crawford AJ, Falloon TJ, Eggins S (1987). The origin of island arc high-alumina basalts. Contrib Mineral Petrol 97: 417-430

Donnelly-Nolan JM (1988). A magmatic model of Medicine Lake Volcano, California. J Geophys Res 93: 4412-4420

Donnelly-Nolan JM, Champion DE, Grove TL, Baker MB, Taggart JE, Bruggman PE (1991). The Giant Crater lava field: geology and geochemistry of a compositionally zoned, high-alumina basalt to basaltic andesite eruption at Medicine Lake volcano, California. J Geophys Res 96(B13): 21843-21863

Donnelly-Nolan JM, Champion DE, Miller CD, Grove TL, Trimble DA (1990). Post-11,000-year volcanism at Medicine Lake Volcano, Cascade Range, northern California. J Geophys Res 95: 19693-19704

Draper DS, Johnston AD (1992). Anhydrous PT phase relations of an Aleutian high-MgO basalt: An investigation of the role of olivine-liquid reaction in the generation of arc high-alumina basalts. Contrib Mineral Petrol 112(4): 501-519

Dzurisin D, Donnelly-Nolan JM, Evans JR, Walter SR (1991). Crustal Subsidence, Seismicity and Structure near Medicine Lake volcano, California. J Geophys Res 96: 16319-16333

Eichelberger JC (1975). Origin of andesite and dacite: evidence of mixing at Glass Mountain in California and other circum-Pacific volcanoes. Geol Soc Am Bull 86: 1381-1391

Ewart A (1982). The mineralogy and petrology of Tertiary-recent orogenic volcanic rocks with special reference to the andesitic-basaltic compositional range. Andesites Ed. R. S. Thorpe. New York, Wiley. 25-95

Fujimaki H, Tatsumoto M, Aoki K (1984). Partition coefficients of Hf, Zr and REE between phenocrysts and groundmass. J Geophys Res 89: 662-672

Gaetani GA, Grove TL, Bryan WB (1993). The influence of water on the petrogenesis of subduction related igneous rocks. Nature 365: 332-334

Gerlach DC, Grove TL (1982). Petrology of Medicine Lake Highland volcanics: Characterization of the endmembers of magma mixing. Contrib Mineral Petrol 80: 147-159

Gill JB (1981). Orogenic Andesites and Plate Tectonics. Berlin-Heidelberg, Springer-Verlag

Grove TL (1993). Corrections to expressions for calculating mineral components in "Origin of calc-alkaline series lavas at Medicine Lake volcano by fractionation, assimilation and mixing" and "Experimental petrology of normal MORB near the Kane Fracture Zone: 22°-25°N, mid-Atlantic ridge". Contrib Mineral Petrol 114: 422-424

Grove TL, Bryan WB (1983). Fractionation of pyroxene-phyric MORB at low pressure: an experimental study. Contrib Mineral Petrol 84: 293-309

Grove TL, Kinzler RJ, Baker MB, Donnelly-Nolan JM, Lesher CE (1988). Assimilation of granite by basaltic magma at Burnt Lava flow, Medicine Lake volcano, northern California. Contrib Mineral Petrol 99: 320-343

Gust DA, Perfit MR (1987). Phase relations of a high-Mg basalt from the Aleutian Island arc: Implications for primary island arc basalts and high-Al basalts. Contrib Mineral Petrol 97: 7-18

Housh TB, Luhr JF (1991). Plagioclase-melt equilibria in hydrous systems. Am Min 76: 477-492

Kay SM, Kay RW, Citron GP (1982). Tectonic controls on tholeiitic and calc-alkaline magmatism in the Aleutian arc. J Geophys Res 87: 4051-4072

Powers HA (1932). The lavas of the Modoc Lava-Bed Quadrangle. Am Min 17: 253-294

Ringwood AE (1974). The petrological evolution of island arc systems. J Geol Soc London 130: 183-204

Roeder PL, Emslie RF (1970). Olivine liquid equilibrium. Contrib Mineral Petrol 29: 275-289

Rose WI, Anderson AT Jr, Woodruff LG, Bonis SB (1978). The October 1974 basaltic tephra from Fuego volcano: description and history of the magma body. Journal of Volcanology and Geothermal Research 4: 3-53

Sisson TW, Grove TL (1993a). Experimental investigations of the role of H2O in calc-alkaline differentiation and subduction zone magmatism. Contrib Mineral Petrol 113: 143-166

Sisson TW, Grove TL (1993b). Temperatures and H2O contents of low-MgO high-alumina basalts. Contrib Mineral Petrol 113: 167-184

Sisson TW, Layne GD (1993). H_2O in basalt and basaltic andesite glass inclusions from four subduction-related volcanoes. Earth Plan Sci Lett 117: 619-635

Taggart JEJ, Lindsay JR, Scott BA, Vivit DV, Bartel AJ, Stewart KC (1987). Analysis of geologic materials by a wavelength dispersive X-ray fluorescence spectrometry. U.S. Geologic Survey Bulletin 1170: E1-E9

Yang HJ, Grove TL, Kinzler RJ (Unpublished, 1993). The compositions of olivine-plagioclase-high calcium pyroxene saturated basalts: constraints from experimental studies.

Yoder HS (1965). Diopside-anorthite-water at five and ten kilobars and its bearing on explosive volcanism. Yearb Carnegie Inst Wash 64: 82-89

Yoder HSJ (1969). Calc-alkaline andesites: experimental data bearing on the origin of their assumed characteristics. Proceedings of the Andesite Conference Ed. A. R. McBirney. Oregon Department of Geology and Mineral Resources (Bulletin). 77-91

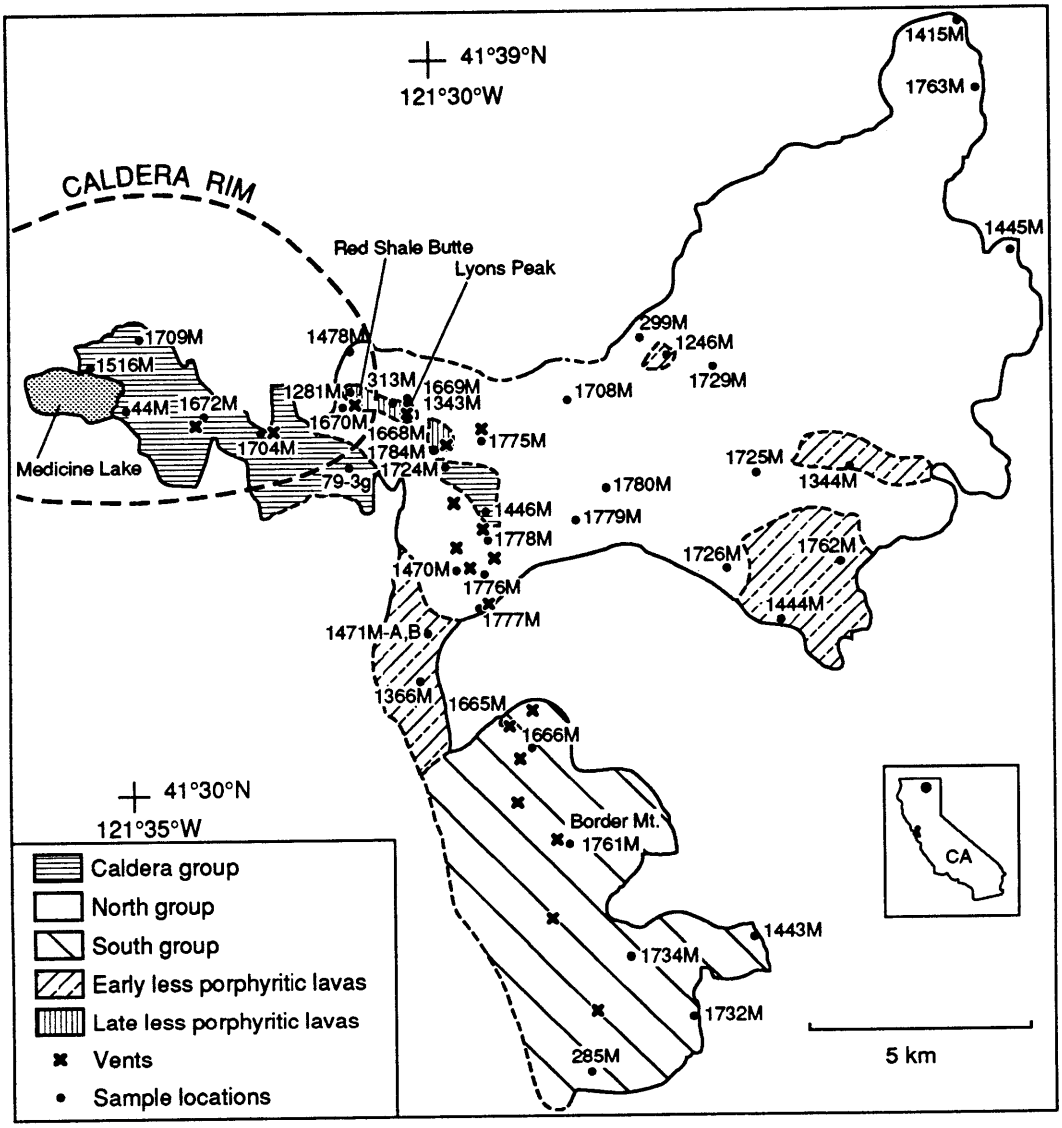
41°39°N
121°30°W
CALDERA RIM
Red Shale Butte
Lyons Peak
1415M
1763M
1445M
1709M
1516M
1478M
313M
1669M
1343M
1281M
1672M
1670M
1668M
1704M
1784M
1724M
79-3g
Medicine Lake
299M
1246M
1729M
1708M
1775M
1725M
1344M
1780M
1446M
1779M
1778M
1726M
1762M
1470M
1776M
1444M
1777M
1471M-A,B
1366M
1665M
1666M
41°30°N
121°35°W
Border Mt.
1761M
CA
1443M
1734M
1732M
285M
5 km
Caldera group
North group
South group
Early less porphyritic lavas
Late less porphyritic lavas
Vents
Sample locations

Figure 1

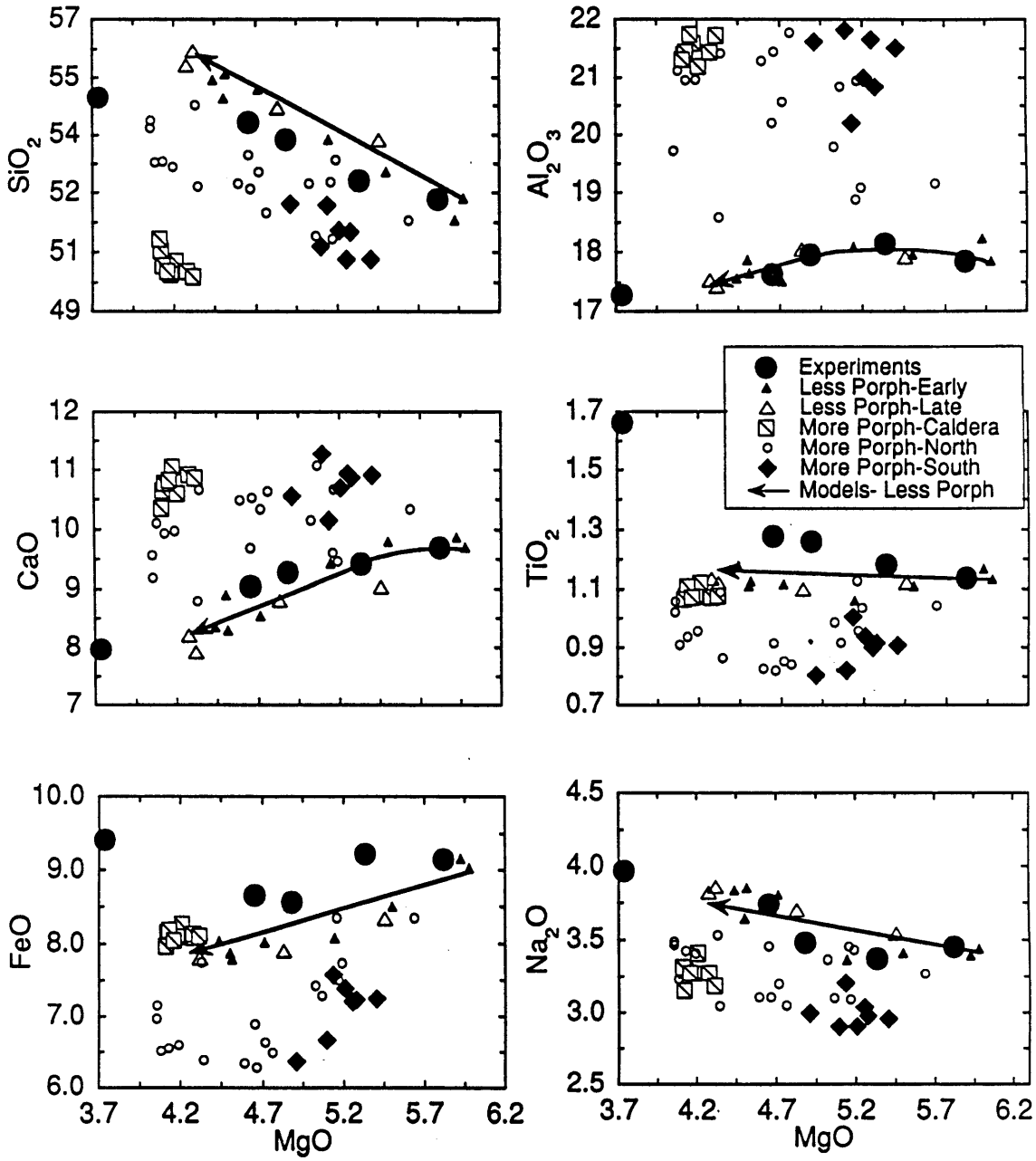
SiO2
Al2O3
CaO
TiO2
FeO
Na2O
MgO
MgO
Experiments
Less Porph-Early
Less Porph-Late
More Porph-Caldera
More Porph-North
More Porph-South
Models- Less Porph

Figure 2

Figure 3

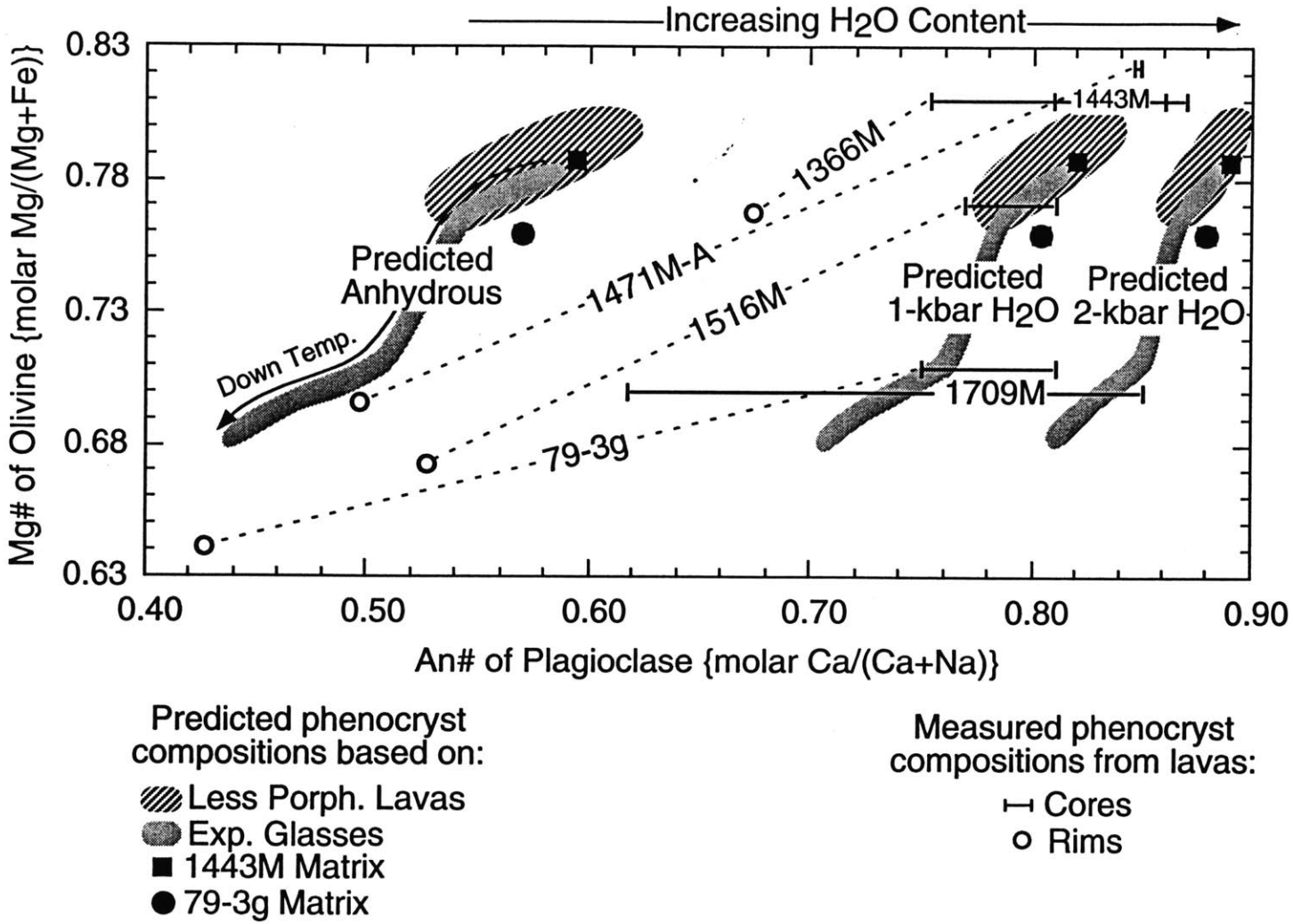
Increasing H2O Content
Mg# of Olivine {molar Mg/(Mg+Fe)}
0.83
0.78
0.73
0.68
0.63
0.40
0.50
0.60
0.70
0.80
0.90
An# of Plagioclase {molar Ca/(Ca+Na)}
Predicted Anhydrous
Down Temp.
1471M-A
1366M
1516M
79-3g
1443M
1709M
Predicted 1-kbar H2O
Predicted 2-kbar H2O
Predicted phenocryst compositions based on:
Less Porph. Lavas
Exp. Glasses
1443M Matrix
79-3g Matrix
Measured phenocryst compositions from lavas:
Cores
Rims

Figure 4a

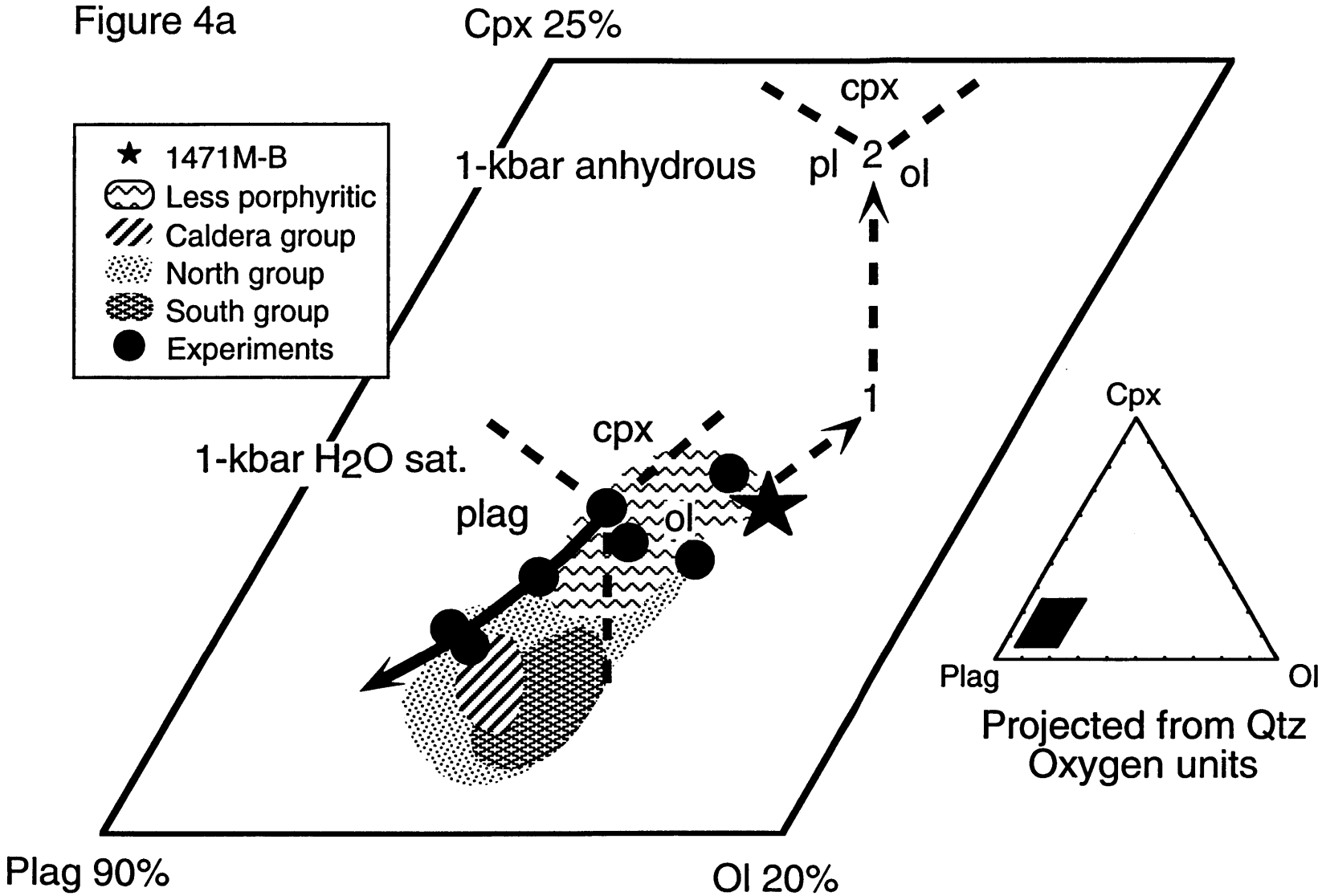
Cpx 25%
1471M-B
Less porphyritic
Caldera group
North group
South group
Experiments
1-kbar anhydrous
cpx
pl
2
ol
1
1-kbar H2O sat.
cpx
plag
ol
Plag 90%
Ol 20%
Cpx
Plag
Ol
Projected from Qtz
Oxygen units

Figure 4b

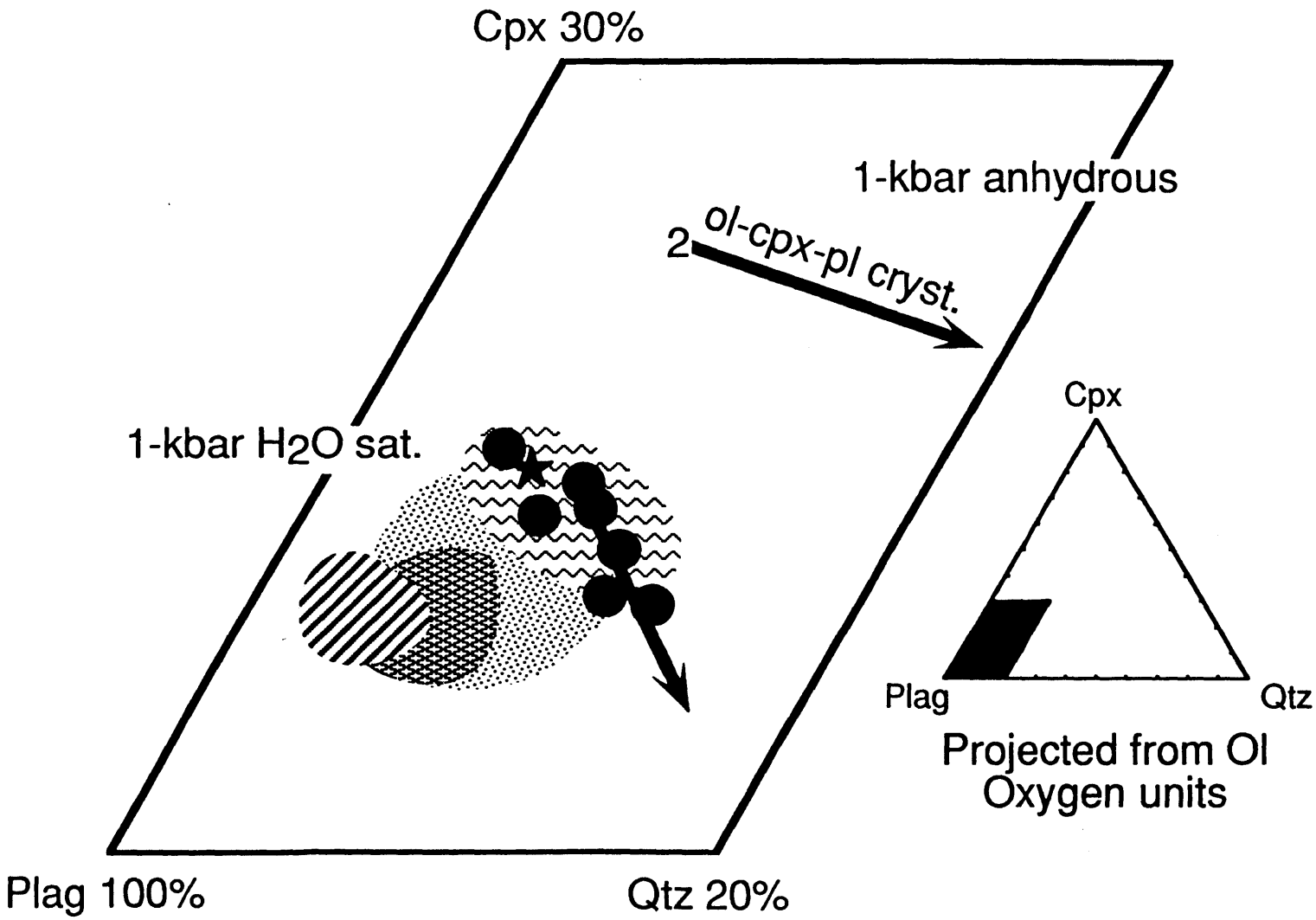
Cpx 30%
1-kbar anhydrous
2 ol-cpx-pl cryst.
1-kbar H2O sat.
Cpx
Plag
Qtz
Projected from Ol
Oxygen units
Plag 100%
Qtz 20%

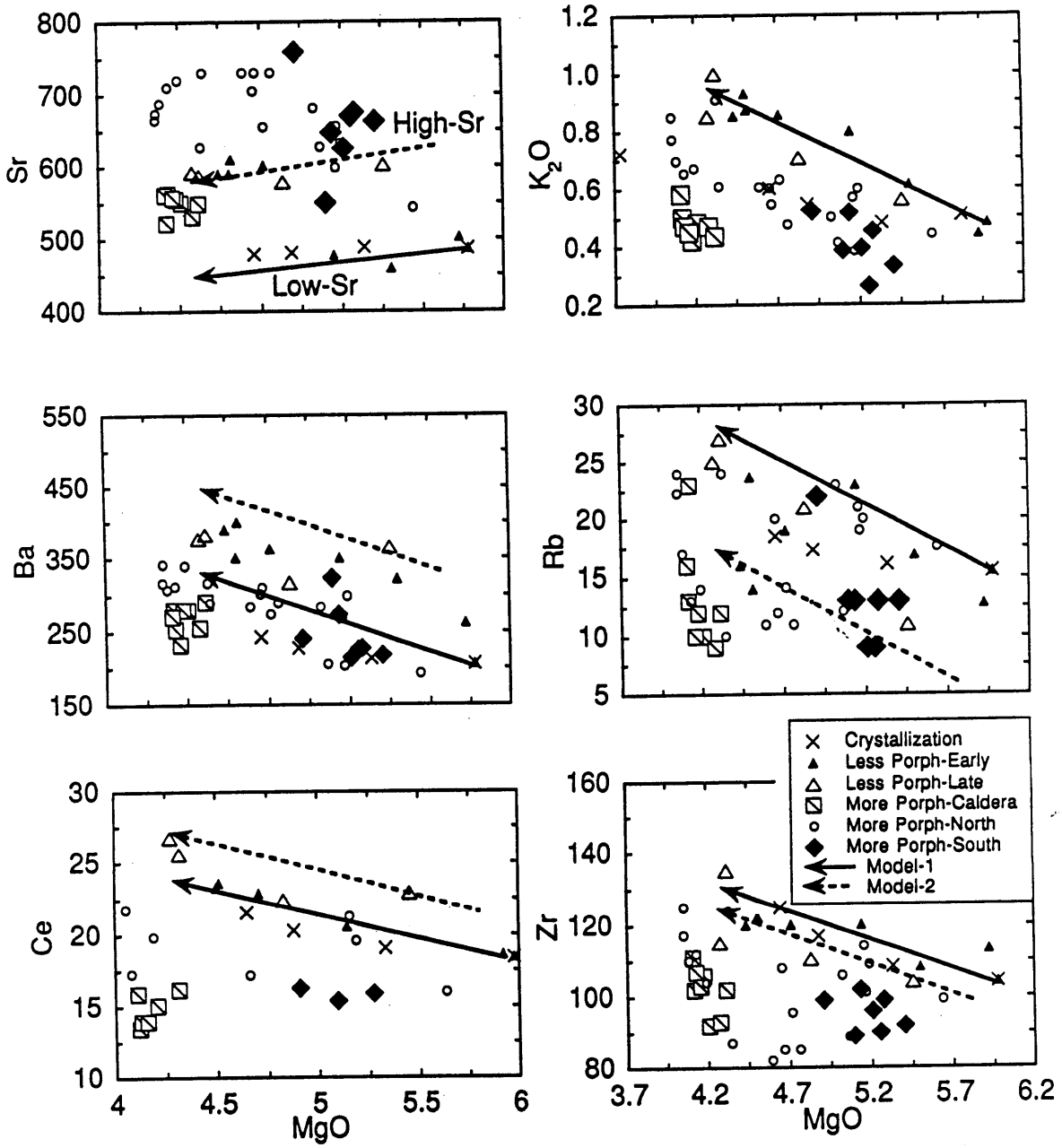
Sr
High-Sr
Low-Sr
K_2O
Ba
Rb
Ce
Zr
MgO
MgO
Crystallization
Less Porph-Early
Less Porph-Late
More Porph-Caldera
More Porph-North
More Porph-South
Model-1
Model-2

Figure 5

Figure 6

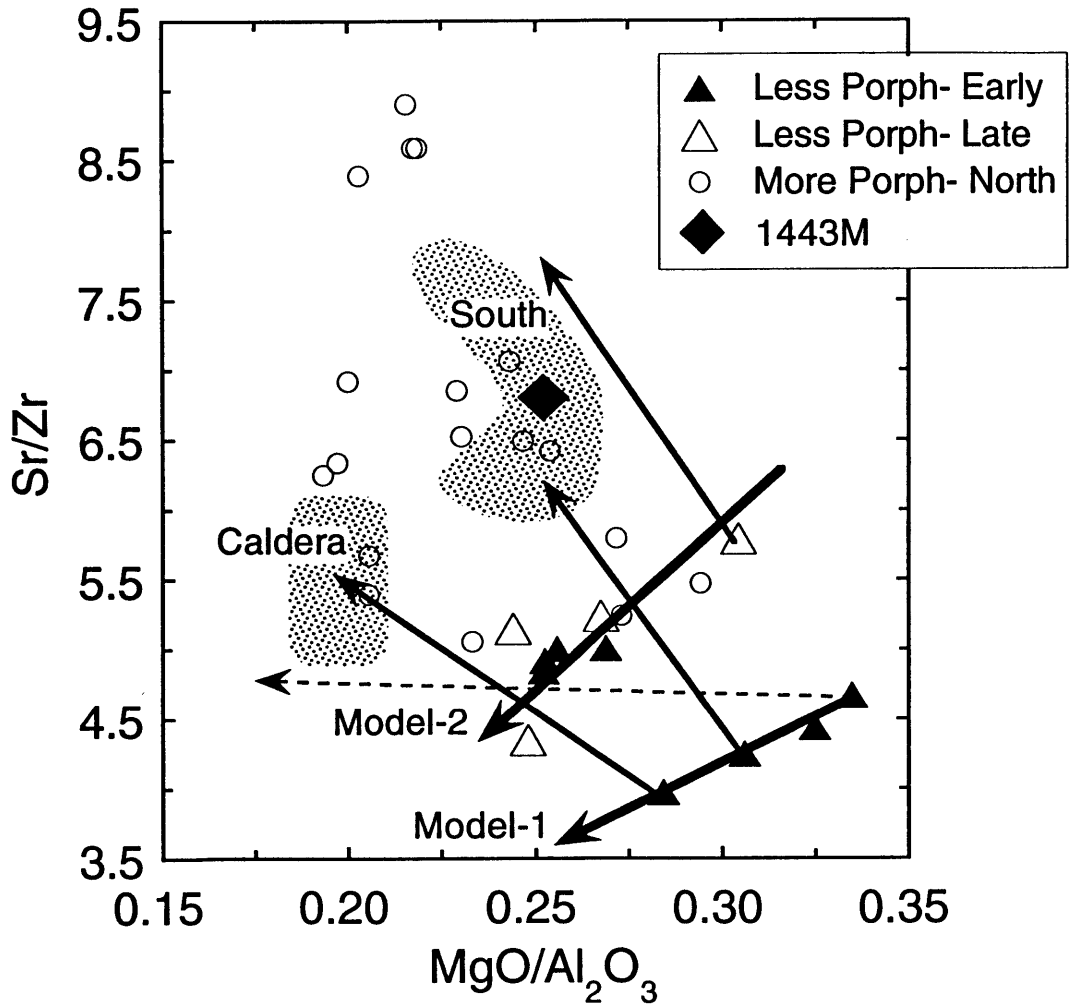
Less Porph- Early
Less Porph- Late
More Porph- North
1443M
South
Caldera
Model-2
Model-1
Sr/Zr
MgO/Al2O3
9.5
8.5
7.5
6.5
5.5
4.5
3.5
0.15
0.20
0.25
0.30
0.35

Table 1a. Major element contents of the lavas of the Lake Basalt.

Sample	SiO_2	Al_2O_3	FeO*	MgO	CaO	Na_2O	K_2O	TiO_2	P_2O_5	MnO	Total	LOI
Less porphyritic - Early												
1246 M	55.1	17.5	8.02	4.71	8.54	3.80	0.86	1.12	0.24	0.14	100.2	0.27
1344 M	54.8	17.9	7.88	4.50	8.90	3.64	0.93	1.11	0.23	0.14	100.0	0.39
1366 M	51.5	18.2	9.16	5.92	9.87	3.39	0.44	1.17	0.18	0.16	100.3	0.10
1444 M	52.8	18.0	8.50	5.50	9.80	3.41	0.62	1.11	0.18	0.15	100.0	0.44
1471 M-B	52.1	17.9	9.03	5.98	9.70	3.44	0.48	1.13	0.18	0.16	100.7	< 0.01
1762 M	53.7	18.1	8.08	5.14	9.43	3.37	0.80	1.06	0.21	0.15	99.8	0.16
1778 M	55.3	17.6	8.04	4.44	8.36	3.84	0.85	1.18	0.25	0.14	99.4	0.25
1784 M	55.5	17.7	7.80	4.51	8.30	3.86	0.87	1.13	0.24	0.14	99.4	0.34
Less porphyritic - Late												
313 M	55.7	17.5	8.06	4.28	8.21	3.82	0.85	1.14	0.23	0.14	99.6	0.31
1281 M	53.7	17.9	8.34	5.46	9.04	3.54	0.56	1.12	0.22	0.15	100.8	0.13
1343 M	54.5	18.0	7.90	4.83	8.80	3.70	0.71	1.10	0.23	0.14	100.1	0.25
1668 M	56.1	17.4	7.81	4.32	7.93	3.86	1.00	1.12	0.25	0.14	99.0	0.35
More porphyritic - Caldera group												
44 M	50.6	21.4	8.16	4.12	10.65	3.15	0.50	1.08	0.17	0.13	100.4	0.14
79 3g	50.4	21.2	8.27	4.21	10.60	3.41	0.48	1.12	0.21	0.14	100.0	<0.01
1446 M	50.0	21.6	8.10	4.18	11.05	3.27	0.42	1.07	0.17	0.13	100.5	0.03
1516 M	50.1	21.4	8.13	4.28	10.92	3.28	0.47	1.07	0.18	0.13	100.7	< 0.01
1672 M	50.0	21.7	8.11	4.32	10.86	3.19	0.44	1.08	0.18	0.14	99.4	<0.01
1704 M	50.3	21.5	8.18	4.13	10.78	3.29	0.47	1.11	0.19	0.14	100.2	<0.01
1709 M	51.0	21.3	7.97	4.11	10.35	3.32	0.58	1.07	0.20	0.14	100.4	0.09
1724 M	50.1	21.7	8.04	4.16	10.82	3.28	0.45	1.07	0.20	0.14	100.7	<0.01
More porphyritic - North group												
299 M	53.0	21.1	6.51	4.08	10.10	3.23	0.70	0.91	0.19	0.11	99.7	0.05
1415 M	54.0	19.7	6.97	4.05	9.56	3.49	0.85	1.02	0.23	0.12	99.7	0.34
1445 M	52.8	20.6	6.64	4.71	10.33	3.20	0.63	0.85	0.19	0.11	100.4	0.30
1470 M	51.0	20.8	7.28	5.06	11.07	3.10	0.41	0.92	0.16	0.12	100.2	0.10
1471 M-A	51.5	19.2	8.35	5.64	10.33	3.27	0.44	1.04	0.17	0.15	100.6	< 0.01
1478 M	52.4	19.8	7.42	5.02	10.15	3.37	0.50	0.98	0.18	0.13	100.4	0.22
1669 M	53.1	19.1	7.74	5.19	9.46	3.43	0.60	1.04	0.21	0.14	99.3	0.19
1670 M	52.5	18.9	8.35	5.16	9.60	3.45	0.57	1.13	0.21	0.15	99.4	0.15
1708 M	53.1	20.9	6.55	4.13	9.93	3.42	0.65	0.94	0.23	0.12	100.0	<0.01
1725 M	54.6	18.6	7.75	4.33	8.79	3.53	0.91	1.09	0.25	0.14	99.9	0.39
1726 M	51.0	20.9	7.50	5.17	10.67	3.09	0.38	0.96	0.19	0.14	100.1	<0.01
1729 M	53.3	20.2	6.89	4.65	9.69	3.46	0.60	0.91	0.22	0.13	100.3	<0.01
1763 M	54.2	19.7	7.15	4.06	9.19	3.47	0.77	1.06	0.25	0.13	99.1	0.51
1775 M	52.9	21.0	6.59	4.19	9.97	3.41	0.67	0.96	0.21	0.12	99.0	0.25
1776 M	52.3	21.5	6.28	4.66	10.52	3.11	0.55	0.82	0.18	0.11	99.5	0.2
1777 M	52.4	21.4	6.39	4.34	10.66	3.05	0.61	0.86	0.18	0.11	99.2	0.34
1779 M	52.5	21.3	6.34	4.59	10.49	3.11	0.61	0.83	0.19	0.11	99.8	0.11
1780 M	51.7	21.8	6.49	4.76	10.64	3.05	0.48	0.84	0.19	0.12	99.4	0.3
More porphyritic - South group												
285 M	51.2	21.0	7.39	5.21	10.70	2.91	0.39	0.94	0.16	0.13	99.9	0.28
1443 M	51.1	20.8	7.23	5.28	10.87	2.98	0.45	0.92	0.17	0.12	100.1	0.28
1665 M	50.8	21.8	6.67	5.10	11.27	2.90	0.39	0.82	0.14	0.12	99.2	0.36
1666 M	51.9	20.2	7.58	5.14	10.15	3.21	0.52	1.00	0.20	0.14	99.4	0.09
1732 M	50.4	21.7	7.21	5.25	10.93	3.04	0.26	0.90	0.19	0.13	99.6	0.12
1734 M	50.4	21.5	7.25	5.40	10.91	2.96	0.33	0.91	0.18	0.13	99.8	0.04
1761 M	51.9	21.6	6.36	4.91	10.56	3.00	0.52	0.80	0.19	0.12	100.1	0.19

Table 1b. Neutron activation trace element contents of the lavas of the Lake Basalt.

Sample	Sc	Cr	Co	Cs	La	Ce	Nd	Sm	Eu	Tb	Yb	Lu	Hf	Ta	Th	U
Less porphyritic - Early																
1246 M	28.4	64	26.5	0.72	11.1	22.9	13.0	3.54	1.200	0.530	1.90	0.280	2.3	0.24	1.70	< 1.20
1344 M	28.9	66	26.3	0.74	10.8	23.3	13.0	3.47	1.240	0.540	1.97	0.290	2.4	0.25	1.65	0.420
1366 M	35.0	104	35.4	0.42	8.20	18.6	12.1	3.41	1.170	0.600	2.41	0.350	2.4	0.18	0.86	< 0.80
1471 M-B	33.6	101	34.6	-	7.9	18.4	10.5	3.29	1.170	0.582	2.76	0.398	2.37	0.205	0.99	0.350
1762 M	33.7	109	31.1	0.75	9.97	20.6	11.3	3.52	1.190	0.567	2.11	0.327	2.5	<0.3	1.89	0.550
1784 M	28.5	63	25.7	0.75	10.8	23.6	13.2	3.62	1.230	0.568	1.96	0.278	2.62	0.339	1.90	0.640
Less porphyritic - Late																
313 M	28.3	49	24.5	0.77	10.8	26.7	14.8	3.55	1.270	0.551	1.77	0.315	2.58	0.235	1.73	-
1281 M	30.2	85	30.4	0.54	11.1	22.9	15.0	3.66	1.250	0.570	2.00	0.320	2.2	0.20	1.20	< 1.40
1343 M	27.9	72	27.6	0.66	10.5	22.4	13.5	3.40	1.210	0.530	1.80	0.258	2.34	0.24	1.55	0.450
1668 M	28.1	55	25.4	0.95	12.4	25.6	14.4	3.56	1.310	0.620	2.16	0.312	2.88	0.342	2.32	0.740
More porphyritic - Caldera group																
44 M	22.7	46	26.3	0.36	6.2	13.5	9.0	2.31	1.060	0.449	1.79	0.278	1.70	0.160	0.82	-
79 3g	25.9	55	29.0	0.24	7.12	15.1	10.2	3.09	1.140	0.513	1.92	0.281	2.05	0.194	0.74	0.310
1672 M	26.3	57	31.3	0.32	7.33	16.2	10.8	3.07	1.180	0.551	1.98	0.286	2.09	0.2	0.84	0.250
1704 M	24.2	51	27.7	0.24	6.56	14	8.7	2.76	1.080	0.480	1.72	0.252	1.8	0.18	0.83	0.184
1709 M	24.0	53	28.0	0.59	7.45	15.9	9.4	3.12	1.110	0.510	1.84	0.280	2.07	0.208	1.17	0.430
1724 M	23.8	53	27.8	0.23	6.25	14	9.1	2.86	1.090	0.498	1.72	0.244	1.84	0.185	0.66	0.252
More porphyritic - North group																
299 M	19.7	59	21.4	0.56	7.6	17.3	10.7	2.59	1.020	0.417	1.39	0.214	1.90	0.231	1.21	
1471 M-A	30.4	98	32.0	0.28	7.4	16.0	11.3	2.98	1.080	0.520	2.14	0.298	2.05	0.178	0.83	0.240
1669 M	28.6	86	30.1	0.41	8.8	19.6	11.9	3.21	1.160	0.533	1.87	0.264	2.13	0.221	1.20	0.390
1670 M	32.4	82	31.9	0.51	9.3	21.3	13.0	3.29	1.260	0.593	2.24	0.319	2.45	0.224	1.23	0.320
1763 M	23.7	59	23.5	0.64	10.5	21.8	12.5	3.39	1.150	0.494	1.65	0.252	2.34	0.306	1.65	0.660
1775 M	21.6	72	23.4	0.51	9.48	19.9	12.4	2.96	1.080	0.446	1.52	0.222	2.14	0.289	1.37	0.500
1776 M	20.9	81	25.2	0.45	7.84	17.2	10.8	2.54	0.947	0.388	1.39	0.191	1.69	0.182	1.11	0.330
More porphyritic - South group																
1443 M	25.4	89	29.5	0.28	7.26	15.9	9.4	2.82	1.008	0.432	1.63	0.243	1.73	0.179	0.83	0.260
1665 M	25.0	141	28.2	0.4	7.42	15.4	9.1	2.67	0.937	0.446	1.63	0.233	1.81	0.193	1.33	0.450
1761 M	20.7	84	26.3	0.35	7.59	16.3	9.7	2.45	0.955	0.362	1.29	0.185	1.62	0.145	1.11	0.330

Table 1c. XRF trace element contents of the lavas.

Sample	Rb	Sr	Y	Zr	Nb	Ba	Ni	Cu	Zn	Cr
				Less porphyritic - Early						
1246 M	19	601	23	120	6	363	25	80	80	
1344 M	24	590	24	122	4	351	26	72	54	67
1366 M	13	502	27	113	5	262	48	84	59	109
1444 M	17	459	30	108	6	322	45	95	68	104
1471 M-B	15	487	29	104	5	206	51	77	67	86
1762 M	23	477	32	120	8	350	32	72	72	103
1778 M	16	590	18	120	-	390	24	85	78	64
1784 M	14	610	17	122	-	400	18	77	72	66
				Less porphyritic - Late						
313 M	25*	592*	19*	115*	5*	377*				
1281 M	11	602	21	104	2	365	40	65	80	
1343 M	21	578	23	110	6	317	36	46	59	71
1668 M	27	587	29	135	7	383	26	74	84	69
				More porphyritic - Caldera group						
44 M	13	522	20	102	4	281	33	59	43	38
79 3g	10	550	20	92	-	280				
1446 M	12	555	28	106	6	280	45	57	52	49
1516 M	9	531	20	93	2	256	28	62	63	34
1672 M	12	549	21	102	3	291	34	72	67	68
1704 M	23	563	29	107	5	254	27	79	66	51
1709 M	16	561	25	111	6	271	32	65	66	55
1724 M	10	557	25	103	4	233	25	54	71	48
				More porphyritic - North group						
299 M	17	688	17	110	5	308	23	-	59	-
1415 M	22	665	28	117	5	317	32	54	58	50
1445 M	14	655	24	96	5	274	49	48	57	82
1470 M	12	627	27	89	6	205	51	55	52	79
1471 M-A	18	543	26	99	5	192	50	74	53	79
1478 M	23	681	27	106	6	284	48	61	48	72
1669 M	20	632	26	109	6	299	38	57	66	88
1670 M	21	598	26	114	6	268	44	72	71	93
1708 M	13	710	22	112	8	312	34	64	61	70
1725 M	24	627	26	124	6	317	28	81	67	63
1726 M	19	656	30	101	6	203	46	74	67	78
1729 M	20	705	25	108	4	302	37	58	59	74
1763 M	24	674	25	125	8	342	20	63	69	58
1775 M	14	720	18	104	-	340	31	61	61	345
1776 M	12	730	15	85	-	310	38	53	54	83
1777 M	10	730	14	87	-	290	29	60	52	81
1779 M	11	730	15	82	-	285	36	57	58	62
1780 M	11	730	15	85	-	290	46	56	53	79
				More porphyritic - South group						
285 M	9	625	15	96	7	214	65	57	47	84
1443 M	13	675	26	99	6	228	63	57	44	82
1665 M	13	550	21	89	2	323	52	76	50	119
1666 M	13	647	22	102	4	274	43	73	67	88
1732 M	9	670	21	90	4	226	59	63	60	87
1734 M	13	663	23	92	4	218	64	62	56	106
1761 M	22	759	24	99	6	241	55	54	55	82

Table 2. Modal abundances (vol.%)

Group	Sample	Groundmass	Plagioclase	Olivine	Spinel	# of Points
Less Porph.	1366M	97.7	2.3	tr	tr	1143
North	1471MA	93.5	5.9	0.5	0.1	2140
North	1763M	82.7	16.4	1.0	tr	1065
Caldera	1516M	66.7	32.7	0.5	tr	1808
Caldera	79-3g	70.0	29.4	0.6	tr	1183
South	1443M	74.1	24.2	1.7	tr	1112

Table 3. Phenocryst compositions of the lavas of the Lake Basalt.

Phase	Pts.	SiO_2		TiO_2		Al_2O_3		Cr_2O_3		FeO		MgO		MnO		CaO		K_2O		Na_2O		Fe_2O_3	Sum	Mg# or An#
1366M	Less porphyritic																							
Ol-core	8	39.2	0.1	nd		0.06	0.01	0.04	0.01	17.5	0.08	42.7	0.1	0.29	0.01	0.21	0.01	-		-		-	100.0	0.81
Ol-rim	1	38.5		0.01		0.04		0.06		21.3		39.4		0.34		0.27		-		-		-	99.9	0.77
Pl-core	1	46.5		-		34.6		-		0.42		0.13		-		17.8		0.02		1.54		-	101.0	0.87
Pl-core	4	49.3	0.8	-		31.8	0.35	-		0.62	0.04	0.16	0.01	-		15.7	0.54	0.05	0.00	2.79	0.33	-	100.4	0.76
Pl-rim	1	51.5		-		31.0		-		0.65		0.17		-		14.0		0.06		3.73		-	101.2	0.67
Sp	1	nd		1.34		25.5		28.4		17.9		12.4		0.33		0.15		-		-		15.0	101.0	
Sp	1	nd		17.7		0.89		0.48		43.0		2.28		0.53		0.36		-		-		34.2	99.5	
1516M	Caldera group																							
Ol-core	2	38.7	0.2	nd		0.03	0	0.12	0.01	21.0	0.03	40.3	0.1	0.38	0.01	0.23	0.04	-		-		-	100.8	0.77
Ol-rim	1	37.1		0.10		0.02		0.14		29.2		33.6		0.45		0.29		-		-		-	101.0	0.67
Pl-core	1	48.0		-		32.8		-		0.69		0.11		-		16.7		0.02		2.10		-	100.4	0.81
Pl-core	1	48.8		-		31.7		-		0.74		0.12		-		15.9		0.04		2.60		-	99.9	0.77
Pl-rim	1	55.7		-		27.5		-		0.74		0.14		-		10.8		0..249		5.33		-	100.2	0.53
Sp	1	nd		2.01		20.9		27.8		19.4		11.1		0.38		0.16		-		-		18.5	100.3	
Sp	1	nd		16.1		1.62		3.40		40.8		3.31		0.57		0.12		-		-		34.9	100.8	
1709M	Caldera group																							
Ol-core	6	37.1	0.2	0.09	0.01	0.04	0.02	0.07	0.03	26.7	0.5	35.3	0.6	0.43	0.02	0.22	0	-		-		-	100.0	0.70
Pl-core	1	47.2		-		33.2		-		0.56		0.11		-		17.1		0.03		1.67		-	100.0	0.85
Pl-core	1	53.8		-		29.3		-		0.85		0.11		-		12.5		0.11		4.24		-	100.9	0.62
Sp	1	0.16		11.9		4.74		1.22		41.2		0.07		0.33		0.02		-		-		36.2	95.9	
Cpx-Core	6	50.9	0.4	0.76	0.04	3.0	0.3	0.08	0.08	8.8	0.3	15.1	0.2	0.21	0.01	20.8	0.2	-		0.31	0.04	-	100.0	0.75
79-3g	Caldera group																							
Ol-core	1	36.5		0.03		0.01		nd		26.5		36.24		0.52		0.22		-		-		-	100.0	0.71
Ol-rim	1	36.3		0.05		0.15		nd		31.6		31.8		0.7		0.19		-		-		-	100.9	0.64
Pl-core	1	48.4		-		33.4		-		0.75		0.01		-		16.3		0.07		2.14		-	101.1	0.81
Pl-core	1	49.7		-		31.7		-		0.70		0.03		-		15.2		0.11		2.76		-	100.2	0.75
Pl-rim	1	58.2		-		25.8		-		0.96		0.10		-		8.6		0.59		6.34		-	100.6	0.43
Sp	1	nd		6.63		8.37		11.7		32.7		4.0		0.4		0.06		-		-		37.7	101.5	
Sp	1	nd		27.5		0.66		0.10		52.9		1.1		0.3		0.23		-		-		12.3	95.1	
1443M	South group																							
Ol-core	2	39.2	0.3	nd		0.03	0.01	0.01	0.02	17.9	0.6	43.5	0.3	0.27	0.04	0.19	0.00	-		-		-	101.1	0.81
Pl-core	7	46.7	0.3	-		33.0	0.3	-		0.46	0.03	0.10	0.01	-		17.4	0.2	0.02	0.00	1.60	0.2	-	99.3	0.86
Pl-core	1	48.0		-		33.7		-		0.55		0.11		-		16.8		0.03		2.12		-	101.4	0.81
Sp	1	0.02		1.73		21.6		26.5		24.1		8.37		0.31		0.02		-		-		18.8	101.5	
Sp	1	nd		11.6		2.90		12.2		37.0		3.48		0.39		0.06		-		-		33.4	101.1	
Sp	1	nd		18.2		1.66		0.17		43.3		2.69		0.50		0.23		-		-		33.2	100.0	
1471M-A	North group																							
Ol-core	4	39.4	0.1	0.02	0.02	0.02	0	0.04	0.02	16.9	0.2	43.7	0.3	0.23	0.04	0.19	0.01	-		-		-	100.5	0.82
Ol-rim	1	37.5		0.02		0.04		0.08		27.09		34.81		0.39		0.3		-		-		-	100.2	0.70
Pl-core	5	47.0	0.4	-		33.82	0.65	-		0.50	0.05	0.12	0.02	-		17.38	0.36	0.03	0.01	1.72	0.2	-	100.6	0.85
Pl-rim	1	56.0		-		26.69		-		0.98		0.11		-		10.31		0.29		5.77		-	100.1	0.50

Table 4. Run conditions, observed phases and their proportions.

Exp. #	T (C°)	Dur (h)	Phases Present	Phase Proportions	Σr^2
15	1075	10	gl, ol	1:tr	0.2
12	1050	18	gl, ol, pl, Cr-sp	0.96:0.02:0.02:tr	0.2
14	1045	20	gl, ol, pl, Cr-sp	0.89:0.04:0.06:tr	0.5
13	1035	24	gl, ol, pl, Cr-sp, aug	0.83:0.05:0.10:tr:0.02	0.6
2	1015	38	gl, ol, pl, aug	0.63:0.08:0.23:0.06	0.2
1	1000	36	gl, ol, pl, aug,mt	0.56:0.07:0.26:0.10:0.02	0.01
8	985	23	gl, ol, pl, aug, mt	0.53:0.08:0.28:0.10:0.01	0.03

Table 5. Experimental Phase Compositions.

Exp #	Phase	Pts.	SiO_2	TiO_2	Al_2O_3	Cr_2O_3	FeO	MgO	MnO	CaO	K_2O	Na_2O	P_2O_5	Fe_2O_3	Total
15	gl	11	51.8(3)	1.08(4)	17.8(2)	0.04(3)	9.1(2)	5.80(4)	0.18(5)	9.7(1)	0.51(3)	3.8(1)	0.23(3)	-	94.55
	ol	4	38.7(3)	0.00(1)	0.06(1)	0.05(1)	18.9(2)	41.7(1)	0.30(3)	0.29(3)	-	-	-	-	99.7
12	gl	15	52.3(2)	1.12(4)	18.1(1)	0.04(3)	9.2(1)	5.31(7)	0.14(3)	9.4(1)	0.48(2)	3.7(1)	0.24(3)	-	96.19
	ol	7	38.6(3)	0.03(7)	0.07(5)	nd	19.5(3)	41.4(3)	0.27(3)	0.32(3)	-	-	-	-	99.9
	pl	4	46.6(5)	-	33.3(4)	-	0.76(5)	0.16(5)	-	17.4(3)	0.03(1)	1.6(2)	-	-	99.8
	Cr-sp	*													
14	gl	11	53.5(4)	1.19(3)	17.9(1)	0.04(3)	8.5(2)	4.86(4)	0.18(3)	9.2(1)	0.54(2)	3.8(2)	0.24(3)	-	95.46
	ol	5	38.6(4)	0.11(1)	0.09(3)	0.04(0)	20.3(0)	40.1(4)	0.35(5)	0.33(2)	-	-	-	-	99.6
	pl	4	47.9(7)	-	32.8(9)	-	0.8(2)	0.2(2)	-	16.7(6)	0.03(2)	2.0(3)	-	-	100.3
	Cr-sp	*													
13	gl	11	53.9(2)	1.21(3)	17.6(1)	nd	8.6(1)	4.63(3)	0.08(4)	9.0(1)	0.60(2)	4.1(1)	0.22(2)	-	94.97
	ol	5	38.1(5)	0.05(1)	0.07(3)	0.04(1)	21.7(6)	39.5(7)	0.37(2)	0.29(2)	-	-	-	-	100.2
	pl	8	48.2(8)	-	31.8(7)	-	0.8(2)	0.2(1)	-	16.0(6)	0.00(1)	2.3(3)	-	-	99.3
	aug	5	51(1)	0.7(1)	3.5(6)	0.4(2)	7(1)	15.6(4)	0.14(3)	21.3(5)	-	0.3(1)	-	-	99.9
	Cr-sp	1	0	3.57	14.3	25.4	23.8	8.05	0.46	0.47	-	-	-	23.7	99.8
2	gl	10	54.6(3)	1.58(6)	17.2(7)	0.05(3)	9.4(3)	3.7(2)	0.19(4)	7.9(2)	0.72(4)	4.4(1)	0.29(2)	-	95.57
	ol	6	37.2(5)	0.03(2)	0.06(1)	0.02(2)	25.7(2)	36.1(6)	0.43(4)	0.32(1)	-	-	-	-	99.3
	pl	8	50.8(4)	-	30.3(7)	-	0.85(7)	0.22(7)	-	14.5(4)	0.08(1)	3.2(3)	-	-	100.0
	aug	12	51.6(5)	0.82(9)	3.0(6)	0.29(7)	7.8(3)	15.3(4)	0.20(4)	21.0(3)	-	0.31(9)	-	-	99.8
1	gl	15	56.0(3)	1.58(5)	17.1(3)	nd	8.9(2)	3.3(1)	0.15(3)	7.3(2)	0.80(3)	4.6(2)	0.28(2)	-	95.97
	ol	12	36.9(3)	0.06(4)	0.06(2)	nd	27.2(4)	35.3(4)	0.45(4)	0.29(3)	-	-	0.02(1)	-	99.8
	pl	4	51.5(7)	-	30.8(4)	-	0.8(1)	0.14(4)	-	14.0(4)	0.08(2)	3.4(3)	-	-	100.7
	aug	9	51.4(5)	0.84(9)	3.4(5)	0.23(8)	8.3(6)	15.0(5)	0.21(7)	20.9(7)	-	0.28(6)	-	-	100.1
	mt	*													
8	gl	14	55.9(3)	1.64(4)	17.1(2)	0.05(3)	8.9(1)	3.12(7)	0.20(3)	7.0(1)	0.87(3)	4.9(1)	0.32(3)	-	95.40
	ol	15	36.6(3)	0.04(5)	0.1(1)	0.07(1)	28.9(4)	33.3(5)	0.46(4)	0.34(4)	-	-	-	-	99.4
	pl	9	50.7(7)	-	30.2(8)	-	0.83(6)	0.15(4)	-	14.1(6)	0.08(3)	3.4(3)	-	-	99.5
	aug	10	50.8(6)	0.9(1)	3.1(3)	0.17(5)	9.0(7)	15.2(5)	0.21(6)	20(1)	-	0.33(5)	-	-	99.7
	mt	5	0.1(1)	15.6(4)	4.9(1)	2.9(2)	38.7(3)	4.3(1)	0.43(1)	0.4(1)	-	-	-	31.6	99.0

Table 6. Calculated trace element abundances of liquids following the experimental crystallization sequence.

Phase		La	Ce	Nd	Sm	Eu	Yb	Lu	Hf	Ta	Th	Rb	Sr	Zr	Nb	Ba
		Partition coefficients														
Olivine		0.008	0.008	0.006	0.005	0.005	0.009	0.009	0.004	0.010	0.01	0.010	0.010	0.005	0.010	0.010
Plagioclase		0.302	0.221	0.149	0.102	1.214	0.041	0.039	0.015	0.025	0.010	0.070	1.800	0.013	0.025	0.160
Augite		0.105	0.125	0.287	0.477	0.562	0.601	0.560	0.121	0.300	0.010	0.020	0.080	0.131	0.300	0.020
Experiment	F	*Bulk distribution coefficients for experimental liquids*														
12	0.96	0.155	0.115	0.077	0.054	0.610	0.025	0.024	0.009	0.018	0.010	0.040	0.905	0.009	0.018	0.085
14	0.89	0.205	0.151	0.102	0.070	0.815	0.030	0.029	0.011	0.020	0.010	0.050	1.209	0.010	0.020	0.111
13	0.83	0.202	0.162	0.166	0.193	0.850	0.193	0.180	0.043	0.100	0.010	0.047	1.050	0.045	0.100	0.098
		Calculated abundances for 1471M-B liquids														
12		8.18	19.1	10.9	3.42	1.19	2.87	0.41	2.47	0.21	1.03	16.1	488	109	5.36	214
14		8.68	20.3	11.7	3.67	1.21	3.09	0.45	2.66	0.23	1.11	17.3	481	117	5.78	229
13		9.18	21.6	12.4	3.88	1.22	3.27	0.47	2.84	0.24	1.19	18.5	479	125	6.15	244

Table 7. Major element FARM models for less porphyritic lavas.

Model = Differentated liquid (from experiments) + Primitive liquid (1471M-B) + Granitic assimilant (561M)

Sample		Results									Components			
		SiO_2	Al_2O_3	FeO	MgO	CaO	Na_2O	K_2O	TiO_2	Σr^2	Diff. lq	wt.% Diff. lq	wt.% 1471M-B	wt.% 561M
Less Porphyritic - Early														
1246M	Composition	55.3	17.6	8.05	4.73	8.57	3.82	0.86	1.12					
	Model	55.3	17.5	8.14	4.73	8.58	3.68	0.87	1.14	0.04	Exp 13	0.53	0.36	0.11
1344M	Composition	55.0	17.9	7.90	4.52	8.93	3.66	0.93	1.11					
	Model	55.0	17.8	8.11	4.59	8.77	3.53	0.77	1.20	0.1	Exp 14	0.92	-	0.07
1444M	Composition	52.9	18.0	8.53	5.52	9.83	3.42	0.62	1.11					
	Model	52.9	17.9	8.85	5.52	9.54	3.47	0.51	1.19	0.2	Exp 14	0.44	0.56	-
1762M	Composition	53.9	18.2	8.11	5.16	9.46	3.38	0.80	1.07					
	Model	54.0	17.9	8.56	5.11	9.25	3.50	0.61	1.20	0.4	Exp 14	0.68	0.29	0.03
1778M	Composition	55.6	17.6	8.07	4.45	8.39	3.85	0.86	1.18					
	Model	55.6	17.5	8.10	4.44	8.48	3.75	0.87	1.18	0.04	Exp 13	0.78	0.12	0.10
1784M	Composition	55.7	17.7	7.83	4.53	8.33	3.87	0.88	1.13					
	Model	55.7	17.6	7.84	4.52	8.45	3.56	0.92	1.13	0.1	Exp 14	0.72	0.15	0.13
Less Porphyritic - Late														
313M	Composition	55.9	17.6	8.09	4.29	8.24	3.83	0.85	1.14					
	Model	55.9	17.5	8.06	4.28	8.40	3.79	0.88	1.20	0.05	Exp 13	0.90	-	0.10
1281M	Composition	53.9	18.0	8.37	5.48	9.07	3.56	0.56	1.13					
	Model	53.9	17.8	8.54	5.41	9.17	3.51	0.69	1.13	0.1	Exp 14	0.25	0.69	0.06
1343M	Composition	54.7	18.1	7.93	4.85	8.83	3.71	0.71	1.10					
	Model	54.8	17.8	8.23	4.78	8.88	3.53	0.74	1.18	0.2	Exp 14	0.77	0.16	0.07
1668	Composition	56.4	17.5	7.84	4.34	7.96	3.88	1.00	1.13					
	Model	56.4	17.4	7.79	4.30	8.16	3.76	1.01	1.13	0.08	Exp 13	0.68	0.17	0.15

Table 8. Trace element FARM models for less porphyritic lavas.

Sample	La	Ce	Nd	Sm	Eu	Yb	Lu	Hf	Ta	Th	Rb	Sr	Zr	Nb	Ba
						Less porphyritic - Early									
1246M	11.1	22.9	13.0	3.54	1.20	1.90	0.28	2.30	0.24	1.70	19.0	601	120	6.00	363
model 1	10.1	22.6	12.4	3.70	1.17	2.93	0.43	2.90	0.31	2.15	25.3	455	124	5.66	299
model 2	12.5	25.8	16.6	4.03	1.26	2.19	0.35	2.54	0.25	1.71	15.4	579	118	2.32	421
1344M	10.8	23.3	13.0	3.47	1.24	1.97	0.29	2.40	0.25	1.65	23.7	590	122	3.62	351
1	9.7	21.9	12.2	3.70	1.18	2.99	0.43	2.83	0.29	1.82	22.8	461	122	5.71	277
2	12.1	25.2	16.5	4.04	1.28	2.22	0.35	2.45	0.22	1.37	12.5	590	116	2.23	404
1444M	-	-	-	-	-	-	-	-	-	-	16.9	459	108	5.54	322
1	8.2	19.2	11.0	3.45	1.18	2.90	0.42	2.50	0.22	1.04	16.3	484	110	5.42	216
2	10.8	22.6	15.4	3.81	1.29	2.12	0.34	2.12	0.15	0.58	5.8	623	104	1.89	345
1762M	10.0	20.6	11.3	3.52	1.19	2.11	0.33	2.50	<0.3	1.89	23.0	477	120	8.00	350
1	8.9	20.4	11.6	3.58	1.19	2.96	0.43	2.64	0.24	1.35	18.9	476	115	5.58	241
2	11.4	23.8	16.0	3.93	1.29	2.17	0.35	2.26	0.18	0.89	8.4	612	109	2.04	370
1778M	-	-	-	-	-	-	-	-	-	-	16.0	590	120	-	390
1	10.3	23.2	12.8	3.83	1.18	3.06	0.45	2.99	0.31	2.10	25.3	456	128	5.91	301
2	12.8	26.5	17.2	4.18	1.28	2.28	0.37	2.61	0.25	1.63	14.8	581	122	2.38	430
1784M	10.8	23.6	13.2	3.62	1.23	1.96	0.28	2.62	0.34	1.90	14.0	610	122	-	400
1	10.3	22.8	12.5	3.67	1.16	2.87	0.42	2.91	0.32	2.34	26.7	449	123	5.57	310
2	12.6	25.8	16.4	3.99	1.25	2.16	0.35	2.57	0.27	1.92	17.1	569	118	2.36	427
						Less porphyritic - Late									
313M	10.8	26.7	14.8	3.55	1.27	1.77	0.32	2.58	0.24	1.73	25.0	592	115	5.00	377
1	10.5	23.6	13.0	3.91	1.19	3.12	0.45	3.05	0.32	2.13	25.7	455	131	6.04	307
2	13.0	27.0	17.5	4.26	1.28	2.33	0.37	2.66	0.25	1.66	15.0	579	125	2.42	438
1281M	11.1	22.9	15.0	3.66	1.25	2.00	0.32	2.20	0.20	1.20	11.0	602	104	2.00	365
1	9.0	20.4	11.4	3.45	1.17	2.79	0.40	2.61	0.26	1.65	20.8	470	113	5.31	255
2	11.4	23.5	15.4	3.77	1.26	2.06	0.33	2.27	0.20	1.22	11.2	601	107	2.06	375
1343M	10.5	22.4	13.5	3.40	1.21	1.80	0.26	2.34	0.24	1.55	21.0	578	110	6.31	317
1	9.5	21.5	12.0	3.64	1.18	2.95	0.43	2.77	0.28	1.76	22.2	464	119	5.62	270
2	11.9	24.8	16.3	3.98	1.28	2.18	0.35	2.40	0.22	1.31	12.0	593	114	2.18	396
1668M	12.4	25.6	14.4	3.56	1.31	2.16	0.31	2.88	0.34	2.32	27.0	587	135	7.00	383
1	10.9	24.1	13.1	3.82	1.17	2.96	0.43	3.09	0.35	2.60	29.0	443	130	5.80	334
2	13.3	27.2	17.2	4.15	1.25	2.23	0.36	2.73	0.29	2.17	19.2	561	125	2.51	454

Table 9. Mass Balance Models for the More Porphyritic Lavas

Sample	SiO_2	TiO_2	Al_2O_3	FeO*	MgO	CaO	K_2O	Na_2O	Total	Proportions	$\sum r^2$
79-3g	50.8	1.12	21.1	8.30	4.12	10.7	0.48	3.32	100.0		
Model	50.8	1.15	21.1	8.21	4.15	10.6	0.47	3.31	99.8		0.02
Matrix	51.6	1.39	18.7	9.78	5.02	9.46	0.55	3.57	100.0	0.83	
high-An Pl	47.9	0.00	33.0	0.74	0.01	16.1	0.07	2.12	100.0	0.17	
1443M	51.3	0.92	20.9	7.26	5.30	10.9	0.45	2.99	100.0		
Model	51.3	0.94	21.0	7.32	5.28	10.8	0.40	2.83	99.8		0.05
Matrix	52.9	1.21	18.7	8.66	5.20	9.51	0.51	3.24	100.0	0.78	
Ol	38.9	0.00	0.03	17.8	43.1	0.19	0.00	0.00	100.0	0.03	
high-An Pl	47.0	0.00	33.2	0.46	0.10	17.5	0.02	1.61	100.0	0.19	

Chapter Two

Origin of Hawaiian tholeiite

ABSTRACT

The liquidus relations of a Hawaiian tholeiite primary magma (Clague et al., 1991) have been determined to 2.2-GPa. The studied composition is based on tholeiitic picritic glass grains from Kilauea volcano, Hawaii, which show variation in trace element abundances consistent with derivation by partial melting of garnet lherzolite (Chapter 3). At no point on or below the liquidus is this composition near multiple saturation with the phases present in garnet lherzolite. This composition is cosaturated with olivine and orthopyroxene on its liquidus at 1.4 GPa and 1425°C. This result is consistent with the composition's higher normative silica content than melts of garnet lherzolite. We infer that liquidus saturation with olivine and orthopyroxene reflects equilibration with harzburgite in the plume top and conclude that Hawaiian tholeiites form in a two step process. Liquids initially form by melting of garnet lherzolite from 130- to 75-km depth in a mantle plume (Step 1). These liquids ascend, aggregate and equilibrate with depleted harzburgite in the plume top or lower lithosphere by assimilating orthopyroxene and crystallizing olivine (Step 2). This reaction will enrich the liquid's silica content (Fisk, 1986) and is consistent with the shift of liquidus phase boundaries during ascent and decompression. The proportions of reactants were determined by mass balance. Orthopyroxene is assimilated and olivine crystallized in a ratio of ~2:1. Magma mass increases by 10 to 20% during reaction. Heat for assimilation is provided by olivine crystallization and superheat of the liquid due to adiabatic ascent. Osmium isotopic constraints (Hauri et al., 1994) require harzburgite equilibration take place within plume, not lithospheric, material. The shallow cosaturation point from the experiments requires the plume to erode ~45-km of lithosphere, consistent with some models of plume-lithosphere interaction.

INTRODUCTION

Tholeiitic lavas from the Hawaiian islands show variations in trace element abundances consistent with derivation by low-degree partial melting of garnet-lherzolite (e.g. Hofmann et al., 1984; Budahn and Schmitt, 1985). Experimental studies, however, find that tholeiite primary magma estimates are only in equilibrium with the phases present in harzburgite (e.g. Green and Ringwood, 1967; Eggins, 1992a), a result which supports tholeiite derivation from a much more depleted source than garnet lherzolite. This contradiction in results may be related to the complexities involved in estimating primary magma composition. Hawaiian shield lavas are derived from magmas that pass through shallow-level plumbing systems where they are affected by crystal fractionation, crystal entrainment, magma mixing and assimilation. Major element concentrations are strongly fractionated by these processes, making it difficult to estimate primary magma composition. For example, estimates of tholeiite primary magma MgO content range from 7 to 22 wt.% (Wright, 1984; Feigenson, 1986). Experimental results are strongly dependent on starting composition and the uncertainties involved in estimating tholeiite primary magma composition raise questions about the relevance of the experimental results. Abundances of incompatible trace elements are not as strongly fractionated by shallow level processing and hence the trace element-based, garnet-lherzolite source model has come into general acceptance.

This paper reports the results of high-pressure melting experiments on a new tholeiite primary magma estimate based on picritic glass grains from Kilauea's eastern rift zone (Clague et al., 1991; 1995). These samples are unique in that they contain up to 15 wt.% MgO and, as glasses, definitely represent liquid compositions. Equally magnesian shield lavas typically have accumulated olivine phenocrysts and are not representative of liquids. The glasses are similar to typical Hawaiian shield tholeiite in their trace element abundances and show variation consistent with derivation by partial

melting of garnet lherzolite (Chapter 3). The glasses have apparently escaped much of the shallow level processing that affects subaerially erupted lavas and offer the most direct constraint available on the composition of tholeiite primary magmas delivered to Kilauea volcano. They have constant Sr/Nd and Ti/Eu ratios which indicate that they have not undergone magma mixing with highly-fractionated liquids (Chapter 3). In addition, the glasses are almost in Fe/Mg exchange equilibrium with mantle olivine and require only minor correction for post-mantle segregation crystallization. High-MgO liquids are easily correctable for fractionation, since Hawaiian magmas have been shown to only crystallize olivine at MgO contents >7.5 wt.% (Helz, 1987; Helz and Thornber, 1987). Clague et al. (1991; 1995) correct for olivine fractionation and estimate the composition of tholeiite primary magmas delivered to Kilauea volcano. Herein, I determine the phase relations of their average tholeiite primary magma in a series of high-pressure melting experiments. The results are used to model the origin of Hawaiian tholeiite.

Previous experimental studies of tholeiite primary magmas

Experimental studies of primitive Hawaiian tholeiite compositions were performed by Green and Ringwood (1967), Green (1970) and Eggins (1992a). The experiments of Green and Ringwood (1967) and Green (1970) were performed on olivine tholeiites and picrites and showed that these compositions are not saturated with the phases of garnet lherzolite under any conditions, but are cosaturated on their liquidus with olivine and orthopyroxene between pressures of 1- and 2.2-GPa. The results of these experiments are of limited use because the experiments were conducted in Pt capsules, which results in Fe-loss from the silicate. Fe-loss in these experiments stabilizes orthopyroxene to lower pressures and increases the liquidus temperature. The experiments of Eggins (1992a) used a primary magma estimate based on a Kilauea Iki lava with 9.5 wt.% MgO, a much more evolved sample than the high-MgO glasses. The Eggins primary magma estimate (Table 1) was made by adding olivine to the lava composition until it was in Fe/Mg exchange equilibrium with $Fo_{90.5}$ olivine. The resulting composition is lower in SiO_2 and MgO and

higher in CaO, TiO_2, Na_2O and K_2O than the high-MgO glass-based primary magma estimate studied here. Eggins finds that the Kilauea Iki primary magma estimate is not saturated with the phases of garnet lherzolite under any conditions, but is cosaturated on its liquidus with olivine and orthopyroxene at 2.0-GPa.

EXPERIMENTAL AND ANALYTICAL METHODS

Starting Composition

The experimental starting composition (Table 1) is the *Kilauea primary tholeiitic melt* estimate of Clague et al. (1991). The composition was estimated by correcting for the low-pressure fractionation experienced by the high-MgO glasses. Clague et al. made a least squares fit to the glass data on an FeO-MgO variation diagram. The FeO and MgO contents of the liquid in equilibrium with $Fo_{90.7}$ olivine was then calculated assuming an Fe^{2+}/Fe^{tot} of 0.9 for the liquid and Fe/Mg exchange K_D of 0.3 for olivine. The remainder of the oxides were calculated by least square regression lines on MgO-variation diagrams. This estimate was later refined by Clague et al. (1995), who reported an error in their previous calculation and calculated both high- and low-FeO primary magma endmembers. Fortunately the estimate used for our starting material is very similar to the average of these (Table 1).

A synthetic mix of the estimated primary magma composition (Table 1) was prepared from high-purity elemental oxides and silicates. To ensure homogeneity, the mix was ground in an agate mortar under ethyl alcohol for 6 hours. 500-mg of the resulting powder was pressed into a pellet using Elvanol as a binding agent. The pellet was then hung on 0.004" Pt wire and conditioned in a 1-atm gas mixing furnace at an oxygen fugacity corresponding to the quartz-fayalite-magnetite buffer at 1075°C for 24-hours.

Experiments

Experiments were performed in 0.5" piston-cylinder apparatus, similar to the design of Boyd and England (1960), using $BaCO_3$ as the pressure medium (Appendix A) and the sample assembly described in Appendix B. 10-mg of conditioned starting material was placed in a graphite crucible and welded shut in a Pt outer-capsule. These capsules were placed in an alumina sleeve and positioned in the hotspot of a graphite heater with MgO spacers. The heater assembly was loaded into $BaCO_3$ pressure cells, which was surrounded by Pb-foil and placed in the pressure vessel. The piston-cylinder apparatus and sample assembly were calibrated for pressure against the transition of anorthite-gehlenite-corundum to Ca-Tschermak's pyroxene as determined by Hays (1965) (Appendix B). Temperature was monitored with $W_{97}Rh_3$–$W_{75}Rh_{25}$ thermocouples with no correction applied for pressure. The thermal gradient near the hotspot was measured at 20°C/0.1". Sample thickness is <0.05", resulting in a thermal gradient of <10°C. Experiments were pressurized cold to 1.0-GPa and then ramped up to 865°C at 100°C/minute where they were held for 6 minutes. They were then pumped to desired run pressure and ramped to final run temperature at 50°C/minute. Experiments were quenched by shutting of the power. Experiments were performed over a pressure range of 1- to 2.2-GPa with a temperature range to constrain the liquidus and subliquidus phase boundaries (Table 2). Experiments above 1.5-GPa were decompressed to 1.0-GPa immediately prior to quenching to prevent the formation of quench crystals in the liquid regions of the charge (Putirka et al., accepted 1995).

Analytical Methods

The experimental products were analyzed by electron microprobe at the Massachusetts Institute of Technology on a JEOL 733 Superprobe using wavelength-dispersive

techniques. Data were reduced using the correction scheme of Bence and Albee (1968) with the modifications of Albee and Ray (1970). Crystalline phases in the experiments were analyzed at 15-kV accelerating potential, 10-nA beam current and a spot size on the order of 2-μm. Spot size was increased to 10-μm for glass analyses in order to minimize diffusion of alkali elements away from the region of interest during the analysis. All observed primary phases were analyzed (Table 3). A materials balance calculation was used to estimate the phase proportions (Table 2) and determine whether the silicate charge had changed composition during the experiment. The silicate charge can lose Fe to the Pt capsules if fractures form in the graphite crucibles and allow the liquid phase to contact the Pt outer-capsule. Experiments where the materials balance calculation showed FeO loss of >1% relative were discarded.

EXPERIMENTAL RESULTS

The liquidus is cosaturated with olivine (ol) and low-Ca pyroxene (opx), the phases present in harzburgitic peridotite, at ~1.4-GPa and ~1425°C (Fig. 1). Below 1.4-GPa, ol is the liquidus phase and is followed down temperature by opx crystallization (Figs. 1 and 2). At 1.0-GPa, the liquid crystallizes ol until intersection of the ol-opx cotectic (point *a* in Fig. 2). Ol-opx crystallization drives the liquid towards the Diopside and Plagioclase apices of the normative projections (Fig. 2). The liquid would likely reach clinopyroxene saturation at ~1310°C based on the inferred cpx liquidus in Fig. 1. Between 1.0- and 1.5-GPa the ol-opx crystallization path shifts away from the Quartz apex towards the Olivine-Diopside and Olivine-Plagioclase joins, due the increasing proportion of opx in the crystallizing assemblage. Between 1.4- and 2.2-GPa, opx is the liquidus phase. At pressures between 1.4- and 2-GPa, the liquid crystallizes opx until intersection of the ol-opx cotectic (point *b* in Fig. 2). At 1.5-GPa, ol-opx crystallization drives the liquid across the Olivine-Diopside or -Plagioclase join, analogous to crossing *the critical plane of*

silica undersaturation of Yoder and Tilley (1962). This leads to saturation with sub-calcic-augite, whose composition is illustrated in Fig. 2. Sub-calcic augite (cpx) crystallization causes ol to the leave the assemblage—in the lowest temperature 1.5-GPa experiment, ol is only found as minor inclusions in opx. The crystallization path and phase boundaries at 1.8- and 2.0-GPa are similar to those at 1.5-GPa, but the opx-cpx cotectic is shifted towards the Olivine apex (Fig. 2) and the ol-opx-cpx multiple saturation point shifts back across the Olivine-Diopside and Olivine-Plagioclase boundary. In both cases, opx-cpx crystallization drives the liquid away from the Quartz apex and across the Olivine-Diopside and Olivine-Plagioclase boundary. At 2-GPa, the experiment at 1400°C has opx, cpx and trace amounts of ol phenocrysts. Olivine is not present in the 10° lower experiment indicating that the ol field is pinching out with increasing pressures (Fig. 1). At pressures >2-GPa, opx crystallization will likely lead directly to cpx crystallization without an interval of ol crystallization.

The experimental study of Eggins (1992a) on a Kilauea Iki parent magma found phase relations qualitatively similar to our own. The liquidus in their experiments is also saturated with ol and opx, but cosaturation occurred at ~2-GPa, ~0.6-GPa higher than this study. The pressure difference is likely due to the lower-SiO_2 content of Eggins' composition. Eggins also performed higher pressure experiments which show the transition in saturating liquidus phase from opx to cpx at 2.5-GPa.

DISCUSSION

The residual mineralogy of the source for Hawaiian tholeiites

Trace element constraints

Studies of Hawaiian tholeiite trace element abundances generally conclude that tholeiites are produced by variable degree partial melting of a source that contains garnet

and clinopyroxene. The strongest evidence for residual garnet in the tholeiite source comes from variations in their rare earth element (REE) abundances. Cogenetic suites of tholeiitic lavas have variable light REE abundances, but constant heavy REE abundances (e.g. Hofmann et al., 1984). The lack of variation in HREE abundances requires the source to have a bulk distribution coefficient (D) for the HREE approximately equal to unity. Garnet is the only common mantle phase with Ds for the HREE high enough to impart a D near unity for the source. The high-MgO glasses used to estimate the experimental starting composition also show variation in LREE abundances with nearly constant HREE abundances, consistent with their derivation from a garnet-bearing source (Chapter 3). The glasses also have a nearly constant Sm/Sr ratio which requires residual clinopyroxene in their source. Clinopyroxene is the only common mantle phase which can control the Sm/Sr ratio, since it is the only mantle phase in which Sm and Sr are moderately compatible and have similar Ds. Residual garnet and clinopyroxene in the Kilauea source is also supported by the source inversion modeling of Budahn and Schmitt (1985), who found that the Kilauea source contains up to 5 wt.% garnet and 30 wt.% clinopyroxene. Trace element abundance variations are not sensitive to the presence of olivine and orthopyroxene in the source since these phases have very low Ds for most of the trace elements. It is assumed that these phases are present in the source since they are the most refractory phases during lherzolite melting (e.g. Takahashi, 1986).

Experimental constraints

A magma produced by batch equilibrium partial melting of a multiphase source will show cosaturation on its liquidus with the phases present in its source at the pressure at which it formed (the multiple saturation hypothesis, BVSP, 1981). Kilauea tholeiite primary magma estimates are only cosaturated on their liquidus with ol and opx (Fig. 1 and Eggins, 1992a). Experimental studies have shown that ol and opx are the most refractory phases during lherzolite melting (e.g. Takahashi, 1986), and that an ol and opx

or harzburgitic residue would be produced by approximately 25% melting of a lherzolite source. Liquidus saturation with harzburgite thus supports tholeiite derivation from a source that has undergone much more melt extraction than the garnet lherzolite source indicated by trace element studies.

The contradiction between these results could be, but probably is not caused by the lack of dissolved volatiles in the experiments. Of the abundant volatiles (H_2O, CO_2 and S), H_2O will have the strongest effect on phase equilibria. Kushiro (1972) showed that the addition of water to basalt-peridotite systems expands the olivine phase volume to higher pressures. Experiments by Gaetani and Grove (1993, 1994) show that the addition of H_2O to basalt-peridotite systems also expands the stability of field of cpx and possibly garnet to lower pressures. The addition of H_2O to experiments on the tholeiite primary magma estimates offers the possibility of changing the phase relations such that the liquidus will become cosaturated with the phases of garnet lherzolite. However, the experiments of Kushiro (1972) and Gaetani and Grove (1993, 1994) contain >6 wt.% H_2O. The high-MgO glasses upon which our primary magma estimate is based are thought to have not degassed during eruption and have <0.35 wt.% H_2O (Clague et al., 1995); an order of magnitude lower H_2O content than is required to significantly affect the phase relations. Since lack of volatiles is probably not the cause of the contradiction in results, perhaps the multiple saturation hypothesis is not applicable to the generation of Hawaiian magmas. Evaluation this possibility requires discussion of the melt generation process in Hawaii.

The generation of melt beneath Hawaii

Magmatism in Hawaii is thought to result from decompression melting of the mantle as it ascends adiabatically in a buoyancy-driven plume. The temperature of the plume material decreases slowly during adiabatic ascent (0.3°C/km), while the solidus temperature

decreases an order of magnitude faster (approximately 3°C/km). Eventually the plume material intersects its solidus and begins to melt. Watson and McKenzie (1991) and Liu and Chase (1989; 1991) use the shape of the Hawaiian swell to estimate the temperature of the mantle plume. They calculate that the temperature of the plume would exceed the garnet lherzolite solidus at 120- to 130-km depth. Melting will continue until the plume stops its vertical ascent or the plume material is completely depleted in one of its phases, which will cause a step-function increase in the solidus temperature (Morse, 1980). The minimum depth of melting is approximately constrained by the lower stability field of garnet lherzolite, approximately 75-km depth. Melt segregation studies show that melts can segregate from their residue at extremely low-melt fractions, possibly 0.1% (Riley and Kolhstedt, 1992). Any melt that forms could decouple from the solid and percolate towards the surface in a process approximating near-fractional fusion. Erupted magmas, then, may represent aggregates of near-fractional polybaric melts rather than batch partial melts. The liquidus relations of aggregated liquids will depend on how the composition of garnet lherzolite melts change over the pressure range of melting.

The composition of melts of garnet lherzolite

If melt composition varies as a straight line in compositional space, aggregated liquids would be expected to fall on the line and the multiple saturation hypothesis should be valid. If, however, melt composition varies along a curved trajectory, aggregated liquids will fall off of the curve and will not be liquidus cosaturated with the phases present in their source. The composition of garnet lherzolite melts has been experimentally determined from 2.1- to 7.0-GPa in peridotite melting studies (Takahashi, 1986; Canil, 1992; and Walter, unpub. data) and other melting studies on non-peridotite compositions that crystallize the phases in garnet lherzolite (Wei et al., 1990; Kinzler, unpub. data). The data from these studies was compiled (Table 4, Figs. 3a,b) in an effort to deduce the effect of pressure and degree of melting on melt composition. The thick solid arrow in Figs. 3a,b schematically depicts the composition of near-solidus melts of

garnet lherzolite as a function of pressure. The variation in composition of the experimentally determined garnet lherzolite melts indicates that this boundary is likely curved. The tail of the arrow starts at the 1-GPa spinel lherzolite melts of Baker and Stolper (1994). Garnet lherzolite melts have higher normative Olivine contents than the spinel lherzolite melts and generally increase in their normative Olivine content from 2- to 7-GPa. Melts from 2- to 4-GPa are picritic (K-2.1, W-2.8 and W-3.0) and those from 5- to 7-GPa are komatiitic (Wei-5.6, W-7.0, C-5.5 and C-6.3). We conclude that garnet lherzolite melt composition will increase in normative Olivine content with pressure and have drawn the arrowhead pointing toward the Olivine apex.

The normative Quartz contents of the garnet lherzolite melts are a function of both pressure and degree of melting. Melts in the 2.1- to 5-GPa pressure range generally have zero to negative values for normative Quartz, with the exception of Canil's 4.5-GPa experiment. Melts above 5-GPa have positive normative Quartz. This shift from negative to positive normative Quartz suggests that the melt compositional boundary is curved and concave with respect to the Quartz apex, though its exact shape and position cannot be constrained. This curvature is consistent with the geometric prediction of O'Hara (1968) and the experiments of Walter and Presnall (1994) on the system CaO-MgO-Al_2O_3-SiO_2-Na_2O.

Using alkali content as an indicator of degree of melting, lower degree experimentally produced melts (those with the higher alkali contents—K-2.1, W-3 and W-5) are the most undersaturated in normative Quartz. Higher degree experimentally produced melts at similar pressures (those with the lowest alkali contents—T-3, W-4 and C-4.5) are Quartz normative. These results support the interpretation that lower degree melts will plot further from the Quartz apex than higher degree melts. The peridotite melting experiments plotted in Figs. 3a,b represent melt fractions of >15%, while geochemical evidence indicates that Hawaiian tholeiites form at melt fractions of <6.5% (e.g. Sims et al., 1995). Experimental liquids representing appropriate lower degree melts

would plot further from the Quartz apex than those available and the resulting mantle melting curve would plot even further from the Quartz apex than the curve depicted.

The composition of melts produced beneath Hawaii

The mantle melt compositional boundary can be used to approximate the composition of liquids and their aggregates produced by near fractional fusion in an upwelling mantle plume as in Hawaii. As a parcel of plume mantle rises, it will melt. When the amount of melt present exceeds approximately 1% of the total solid, the melt will segregate and rise faster than the surrounding matrix towards the surface. These instantaneous melts will vary in composition as a function of the height at which they are generated in the plume column, due to the effects of pressure and the extent of depletion of the mantle parcel. The deepest, initial plume melts will start near the head of the arrow in Figs. 3a,b. Shallower instantaneous melts will move towards the tail of the arrow as pressure decreases. Shallower melts will also be higher degree melts since the residue is continuously depleted by melting. The effect of increasing degree of melting will be to flatten the curve of the melt compositional boundary towards the Quartz apex.

For the purposes here, the exact shape of the melting curve is not important, but the curved geometry implies that an aggregate of liquids produced along this boundary will lie within the field defined by its concave side. Study of these aggregated liquid compositions in high pressure melting experiments will not show liquidus saturation with garnet lherzolite. Experimental study will show liquidus ol at pressures up to the lowest pressure at which garnet lherzolite melts are produced (~2.5-GPa), where the liquid will become cosaturated with opx. At higher pressures the saturating liquidus phase should change from opx to cpx, but this will depend on the how the position of the two phase boundaries shift with pressure. At pressures where the liquidus is two-phase saturated (ol-opx or opx-cpx), crystallization will drive residual liquids towards the melting curve and multiple saturation with the phases found in the residuum.

Kilauea primary magmas show distinct differences from melts of or aggregates of melts of garnet lherzolite. First, the Clague et al. (1995) and the Eggins (1992a) primary magma estimates plot outside of the field defined by the mantle melting boundary (grey field inside arrow in Figs. 3a,b). The Kilauea primary magma estimates are richer in normative Quartz than melts of or aggregates of melts of garnet lherzolite. This is a robust interpretation because the actual mantle melt compositional boundary would plot even further away from the Quartz apex than depicted if experimental results with lower and more relevant degrees of melting were used to estimate it. Second, the liquidus relations of the Kilauea primary magma estimate studied here are not similar to what would be expected of aggregated liquids. Our experiments show liquidus saturation with ol and opx at much lower pressures than an aggregated melt of garnet lherzolite could. Third crystallization in our or any other experimental study (e.g. Eggins, 1992a) does not lead to saturation with all of the mantle residual phases. Though our experiments have produced some liquids saturated with ol, opx and cpx, the cpx is sub-calcic augite (Fig. 2) and has much less Ca than clinopyroxene typically found in lherzolite samples. The ol and opx in these three phase saturated liquids are also notably more Fe-rich than typical mantle ol and opx.

We conclude that Hawaiian tholeiite primary magmas are displaced towards the Opx-Quartz join relative to melts of or polybaric aggregates of melts of garnet lherzolite. We propose that melt/wall-rock reaction processes in the plume top cause this displacement.

Melt/wall-rock reaction

Liquidus cosaturation with ol and opx implies that tholeiite primary magma estimates are in equilibrium with harzburgite. Experiments by Fisk (1986) showed that reaction of basaltic liquid with harzburgite increases the resultant liquid's SiO_2 content, consistent

with the higher normative Quartz contents of Kilauea primary magma estimates relative to melts of garnet lherzolite. Modeling of basalt/harzburgite interaction was further developed by Kelemen (1990a, b) who showed that basalts will assimilate opx and crystallize olivine when interacting with harzburgite. The dashed arrows in Figs. 3a,b show a reaction path that is similar to the one described by Kelemen that will produce Hawaiian tholeiite primary magmas from melts or aggregates of melts of garnet lherzolite. The reaction has two components. Component one involves the assimilation of opx and drives the aggregated garnet lherzolite melts directly towards Opx (Figs. 3a,b). Component two is olivine crystallization and drives liquids directly away from the Olivine apex. This reaction path is consistent with phase equilibria constraints. As high-pressure mantle melts decompress during ascent, the olivine phase volume expands (similar to the phase boundaries in Fig. 2) and melts will always be saturated with respect to olivine and undersaturated with respect to pyroxene. Liquids will assimilate pyroxene and crystallize olivine to get the heat. Field observations of a similar equilibration process have been made in the Trinity Peridotite (Quick, 1981 and Kelemen et al., 1992) where dunite is formed at melt pathways surrounded by progressively less depleted peridotites.

A plausible, physical model that forces Hawaiian primary magmas to interact with harzburgite was proposed by Eggins (1992b) . The model (Fig. 4) proposes that the central area of the plume is composed of harzburgite because it undergoes higher extents of melting than the plume edges. When the plume impinges the lithosphere, it will increase in diameter as its outer portions advect away laterally. The central region undergoes the most vertical ascent and subsequently achieves the highest degrees of melting, becoming harzburgite (*Garnet absent area,* Fig. 4). Melts decouple from the laterally advecting regions of the plume and continue to ascend vertically, passing through the central, depleted area of the plume head (Ribe and Smooke, 1987). Eggins suggested that these melts would react and equilibrate with the harzburgite zone in terms of major elements but maintain trace element abundance variations consistent with

derivation by melting of garnet lherzolite. He did not propose a mechanism by which melts would equilibrate. We develop this mechanism in the following sections. An alternative model is for harzburgite equilibration to take place within the lithosphere, likely depleted during formation at the East Pacific Rise. The model developed here will work regardless of where reaction takes place, though isotopic constraints discussed at the end support equilibration within plume material.

Proportions of reactants

We have constrained the proportions of components involved in the equilibration reaction (Table 5) by mass balancing Kilauea primary magma estimates against opx, olivine and polybaric aggregated melts of garnet lherzolite. Orthopyroxene composition is dependent on pressure and temperature, so we have used opx from experiment 37 (Table 3) which is near liquidus (3% crystallization) and just above the pressure of liquidus cosaturation with ol+opx. The parent magma estimate used in this study is in Fe/Mg exchange equilibrium with $Fo_{90.7}$ olivine. This choice is based on the composition of olivine microphenocrysts found in the high-MgO glass grains (Clague et al., 1991) and we assume the equilibration reaction will involve ol of this composition. The composition of the garnet lherzolite melt is difficult to constrain. Initial models (not reported) used melt compositions from a single experiment (batch melting model) and resulted in poor fits to the data. Subsequent models used polybaric, low- and high-FeO aggregated liquids (composition in Table 5, plotted as open circles in Figs. 3a,b) which were calculated from averages of the experimental melts. High-FeO aggregated liquid was produced by averaging the garnet lherzolite melts with the highest-FeO contents: Kinzler 2.1-GPa, Canil 4.5-GPa and Walter 5.0-GPa. Low-FeO liquid was produced by averaging predominantly lower pressure and lower-FeO melts: Walter 2.8-, 3.0- and 4.0-GPa and low pressure melt: Kinzler 2.1-GPa.

Mass balance was performed by multiple linear regression. In all cases we find that the equilibration reaction requires the crystallization of olivine and the assimilation of

opx, consistent with the phase relations. MgO, Al_2O_3 and SiO_2 are fit well in all of the mass balances while FeO, CaO and Na_2O show poorer fits. Lower degree melts, when available, will likely result in significantly better fits to the data. The liquids from the lherzolite melting experiments represent partial melts in excess of 15%, much higher than would be parental to Hawaiian tholeiites. Na_2O will be strongly affected by degree of melting and using lower degree partial melts will clearly improve the mass balance. FeO may also be negatively correlated with degree of melting in the garnet stability field—Walter's 2.8-GPa experiment has lower Na_2O, K_2O and FeO than the 3.0-GPa experiment. This is the opposite of the behavior of FeO in the spinel-field (Kinzler and Grove, 1993; Baker and Stolper, 1995).

Thermal Constraints

Kelemen et al. (1990b) showed that ol crystallization and opx assimilation is isenthalpic and for every unit of ol crystallized an equal unit of opx can be assimilated. The mass balance reactions are endothermic (Table 5), more opx is assimilated than olivine crystallized, and requires input of heat. In a mantle plume, where melts are ascending from deep, this excess heat could be in the form of superheat of the ascending liquid. The mantle solidus can be used to constrain the amount of superheat heat available and the feasibility of the proposed assimilation reactions.

The solid line in Fig. 5 shows the solidus for fertile garnet lherzolite of McKenzie and Bickle (1988). The plume will intersect this solidus at ~130 km (4.3-GPa, Fig. 5) based on geophysical studies of the Hawaiian swell (Liu and Chase, 1989; 1991). As the mantle melts, it's solidus temperature will increase above the fertile solidus. Kinzler and Grove (1992b) model this effect in the spinel stability field using a model of continuous melting with incomplete melt withdrawal. Melts form incrementally in 1% units for each 0.1-GPa of ascent with 90% of melt withdrawn at each step. Melts in Hawaii form from 4.3-GPa to 2.5-GPa (the lower stability of garnet lherzolite). This 1.8-GPa of decompression melting would result in a 35° increase in the solidus (Fig. 5) in the spinel

stability field and we assume a similar increase in the garnet stability field. Hawaiian melts segregating at an average depth of 3.4-GPa and would have a temperature of 1571°C. This is a minimum temperature constraint since the amount of melt produced per unit of adiabatic ascent decreases as melting proceeds, and melting would likely stop before 2.5-GPa due to loss of a phase.

The liquidus of the primary magma estimate studied here is cosaturated with ol and opx at 1.4-GPa. Adiabatic ascent of an average garnet lherzolite melt from 3.4- to 1.4-GPa would cool the melt from 1571°C to 1553°C (adiabatic ascent cools liquid at 9°/GPa), leaving the ascended melt 128° above the liquidus of the primary magma estimate (1425°C, Fig. 5). Using this temperature difference and the proportions from the mass balances, the thermal energy budget of the reactions can be determined (Table 6). Assuming C_p^{liquid}=0.3-cal/(°C*g) and the ΔH_f=100-cal/gram, superheat alone is almost sufficient to assimilate the amount of opx required by the reactions. There is more than enough heat to complete the reaction for all cases when superheat is combined with the heat available from ol crystallization. If assimilation took place in the relatively cool lithosphere, the excess heat could be used to thermally equilibrate the assimilated opx.

Mass constraints

The reactions in Table 5 require the assimilation of 24-44 wt.% of opx per unit of erupted liquid. The production of a Mauna Loa-sized shield (45,000-km^3) by these proportions requires a significant amount of opx in the source, which can be estimated by constraining the size of the reaction zone. Kilauea and Mauna Loa are approximately 30-km apart, yet clearly have distinct sources (Frey and Rhodes, 1993). Assuming the region through which magmas are generated approximates a cylinder, it would have a maximum radius of 15- to 20-km. We assume the vertical length over which assimilation takes place is 45-km, corresponding to the distance between our multiple saturation point and the base of the lithosphere in Hawaii (approximately 90-km). This region would need to contain 24 to 42 wt.% opx (Table 7) to produce parent magmas similar to the average of

the low- and high-FeO parents of Clague et al. (1995). The lower lithosphere could contain sufficient opx, but production of a Mauna Loa sized shield would completely deplete it in pyroxene and leave a dunitic residue.

Isotopic constraints, however, support equilibration in the plume top rather than the lithosphere. Hauri et al. (1994a,b) show that osmium isotopic ratios ($^{187}Os/^{186}Os$) of Kilauea tholeiites and picrites are substantially higher than those of the mid-oceanic ridge basalt source. Hauri et al. propose that the equilibration of Hawaiian melts with harzburgite must not involve significant amounts of lithospheric material or this geochemical signal would be lost. This result constrains the assimilation reaction to take place in the plume top and the amount of opx in the plume top can be constrained using garnet lherzolite melt reactions. Assuming plume material initially contained 21% opx, melting by the reaction:

1.67cpx+0.49gar+0.27ol=liquid+1.2opx (J. Longhi, pers. comm.)

would increase the source opx to 34% by 11% melting, while the reaction:

0.68cpx+0.63gar+0.19ol=liquid+0.5opx (Kinzler, 1992c)

would increase the source opx to 34% by 17% melting. Assuming 1% melting per 0.1-GPa of decompression (Ahern and Turcotte, 1979), decompression melting over a depth range of 130- to 70-km would result in approximately 20% melting of the source and sufficient opx can be produced by either reaction. This extent of melting would consume all of the source's garnet and cpx and leave a harzburgite residuum with sufficient opx to produce a Mauna Loa sized shield. Furthermore, the plume top will be continually replaced with new opx enriched material and would be form an undepletable reservoir.

Penetration of the lithosphere by the Hawaiian plume

The experiments show harzburgite equilibration at 1.4-GPa (Fig. 1). This pressure corresponds to 42-km depth, which is well within the estimated 90-km thick lithosphere beneath Hawaii (Detrick and Crough, 1978). This requires that the plume erode at least 48-km of lithosphere (illustrated in Fig. 4). This is a significant amount of lithospheric

thinning, but is consistent with some numerical simulations of plume-lithosphere interaction (Yuen and Fleitout, 1985). As mentioned earlier in the discussion, the incorporation of H_2O into our experimental study will likely result in a slight increase in the pressure of the ol-opx cosaturation point. This will reduce the amount of penetration of the plume into the lithosphere required. Hydrous experiments are planned to constrain the this exact point.

How can different pressure signatures of melt generation be maintained in tholeiite primary magmas if melts continually equilibrate with the wall-rock through which they ascend?

Throughout this paper it has been assumed that melts segregate by porous flow and that this forces chemical equilibrium to be achieved between the melts of garnet lherzolite produced in deeper regions of the plume with harzburgite in the plume top. The variation in FeO content of the tholeiite primary magma estimates of Clague et al. (1995) supports the generation of tholeiite primary magmas at different mean depths. Ascending liquids, then, must not continually equilibrate with the matrix in the garnet-present regions of plume material through which they ascend or else this chemical variation would be lost. Melt/wall-rock equilibration in the plume top, but not in deeper parts of the plume may be consistent with changes in mineral dissolution rates due to decompression of ascending melts. Mineral dissolution rate is a function of both temperature and the degree of departure from chemical equilibrium of the mineral/melt system. The higher temperatures in the deeper parts of the plume support higher dissolution rates there than in the shallower parts of the plume. However, the departure from equilibrium in the mineral/melt system will be greatest near the top of the plume. The dissolution rate of a mineral in a liquid is dependent on how close to saturation the liquid is with that mineral, shown experimentally by Brearley and Scarfe (1986). Liquids in deeper parts of the

plume will be surrounded with mineral phases with which they are saturated, so dissolution rates will be low. As melts ascend and decompress , the olivine primary phase volume will expand and melts will become saturated with olivine and increasingly undersaturated with pyroxene. This will result in an increase in the dissolution rate of opx near the plume top, consistent with an increased degree of chemical equilibration there rather than in the plume body.

CONCLUSIONS

We conclude that melt/wall rock reaction processes in the plume top play a major role in the formation of Hawaiian tholeiite. Experimentally produced melts of garnet lherzolite are much poorer in normative silica than estimated Hawaiian tholeiite primary magmas. Garnet lherzolite melts can become similar to tholeiite primary magmas by equilibrating with harzburgite in the plume top during melt/wall-rock reaction. The equilibration reaction involves orthopyroxene assimilation and olivine crystallization. This reaction is consistent with chemical, thermal and physical models of the mantle plume beneath Hawaii. Isotopic constraints require that the equilibration take place within plume, not lithospheric material, which requires a significant amount of erosion of the lithosphere by the mantle plume. Since melts of garnet lherzolite may be alkalic, changes in the melt/wall-rock reaction zone may play an important role in the transition between tholeiitic and alkalic volcanism in Hawaii.

FIGURE CAPTIONS

Figure 1. Pressure-temperature diagram showing the phase boundaries and experimental run products. Dashed boundaries are inferred. Highest temperature experiment at 2.0 GPa contains trace amounts of orthopyroxene crystals and is assumed to be near-liquidus.

Figure 2. Ternary projection of experimental liquids and phase boundaries in mineral normative units using the equations of Grove (1993). Solid lines are experimentally determined phase boundaries, dashed lines are inferred. Solid circle is the experimental starting composition from Table 1, solid squares are the experimental liquids from Table 3. Point 'a' denotes intersection of ol-opx cotectic after low pressure ol crystallization. Point 'b' denotes intersection of the ol-opx or opx-cpx cotectics after opx crystallization.

Figures 3a and b. Ternary projections of experimentally determined liquids in equilibrium with garnet lherzolite and proposed Kilauea primary tholeiites, in the same units as Fig. 2. Solid arrow shows the effect of increasing pressure on the composition of near solidus melts of garnet lherzolite. Field inside arrow is region where aggregates of melts along the arrow would plot. Dashed arrow shows the reaction path to go from garnet lherzolite melts to Kilauea primary magma estimates. *High- and low-Fe parents* are from Clague et al (1995) (Table 1). *Eggins parent* is from Eggins (1992a) (Table 1). Field labeled B-1 contains the spinel lherzolite melts of Baker and Stolper (1995). Composition of garnet lherzolite melts are reported in Table 4, labels correspond to the first initial of the author's name and the pressure of the experiment in GPa. C-Canil (1992); K-Kinzler (unpublished); T-Takahashi (1986), W-Walter (unpublished); Wei-Wei et al. (1990). Open circles show compositions of aggregated melts discussed in text.

Figure 4. Illustration of mantle plume and formation of melt beneath Hawaii, approximately to scale. Solid arrows are melt, dashed arrows are plume solids. Blank field is harzburgite zone in plume head. Plume head is drawn asymmetrically to account for effect of plate motion, indicated by arrow.

Figure 5. Mantle solidus beneath Hawaii showing effects of melting and adiabatic ascent on liquid temperatures.

FOOTNOTES TO TABLES

Table 1. '-' indicates concentration not reported.

Table 2. Experiments where phase proportions are not reported contained too much quench growth to analyze the glass. Phase abbreviations: ol-olivine, opx-orthopyroxene, cpx-sub-calcic augite.

Table 3. * indicates glass not analyzed due to presence of quench growth. '-' indicates concentration not determined. † indicates phase not analyzed. Phase abbreviations as in text.

Table 4. '-' indicates concentration not reported.

Table 5. Proportions were determined by multiple linear regression of orthopyroxene, olivine and an *Aggregated Liquid*. For the Clague et al. (1995) low-FeO parent, the low-FeO aggregated liquid was used. For the Clague et al. (1995) high FeO parent and the Eggins (1992a) parent, the high-FeO aggregated liquid was used.

Table 6. Heat calculated using the proportions from Table 5 assuming: C_p^{liquid}=0.3-cal/(°C*g) and the ΔH_f=100-cal/gram.

Table 7. Calculated assuming the density of basalt that makes up the Mauna Loa shield=2.9-g/cm^3 and the density of peridotite=3.3-g/cm^3.

REFERENCES

Ahern JL, Turcotte DL (1979). Magma migration beneath an ocean ridge. Earth Plan Sci Lett 45: 115-122

Albee AL, Ray L (1970). Correction factors for electron microprobe microanalysis of silicates, oxides, carbonates, phosphates and sulfates. Anal Chem 42: 1408-1418

Baker MB, Stolper EM (1995). Determining the composition of high-pressure mantle melts using diamond aggregates. Geochim Cosmochim Acta 58(13): 2811-2827

Bence AB, Albee AL (1968). Empirical corrections factors for the electron microanalysis of silicates and oxides. J Geol 76: 382-403

Boyd FR, England JL (1960). Apparatus for phase equilibrium studies at pressures up to 50 kbars and temperatures up to 1750°C. J Geophys Res 65: 741-748

Brearley M, Scarfe CM (1986). Dissolution rates of upper mantle minerals in an alkali basalt melt at high pressure: an experimental study and implication for ultramafic xenolith survival. J Petrol 27(5): 1157-1182

Budahn JR, Schmitt RA (1985). Petrogenetic modeling of Hawaiian tholeiitic basalts: A geochemical approach. Geochim Cosmochim Acta 49: 67-87

BVSP (1981). Basaltic volcanism on the terrestrial planets. New York, Pergamon Press, Inc.

Canil D (1992). Orthopyroxene stability along the peridotite solidus and the origin of cratonic lithosphere beneath southern Africa. Earth Plan Sci Lett 11: 83-95

Clague DA, Moore JG, Dixon JE, Friesen WB (in press, 1995). Petrology of submarine lavas from Kilauea's Puna Ridge, Hawaii. J Petrol

Clague DA, Weber WS, Dixon JE (1991). Picritic glasses from Hawaii. Nature 353: 553-556

Detrick RS, Crough ST (1978). Island subsidence, hotspots, and lithospheric thinning. J Geophys Res 83: 1236-1246

Eggins SM (1992a). Petrogenesis of Hawaiian tholeiites: 1, phase equilibria constraints. Contrib Mineral Petrol 110: 387-397

Eggins SM (1992b). Petrogenesis of Hawaiian tholeiites: 2, aspects of dynamic melt segregation. 110: 387-397

Feigenson MD (1986). Constraints on the origin of Hawaiian lavas. J Geophys Res 91: 9383-9393

Fisk MR (1986). Basalt magma interaction with harzburgite and the formation of high-magnesium andesites. Geophys Res Lett 13(5): 467-470

Frey FA, Rhodes JM (1993). Intershield geochemical differences among Hawaiian volcanoes: implications for source compositions, melting processes and magma ascent paths. Phil. Trans. R. Soc. Lond. 342: 121-136

Gaetani GA, Grove TL (1993). Effects of H2O on melting of mantle peridotite at 10 to 15 kbar. Trans Amer Geophys Union 74: 657

Gaetani GA, Grove TL (1994). Melting in the sub-arc mantle: the effects of H2O on primary magmas and the spinel-to-garnet transition. Mineral Mag 58A: 301-302

Green DH (1970). The origin of basaltic and nephelinitic magmas. Trans Leicester Lit Philos Society 64: 28-59

Green DH, Ringwood AE (1967). The genesis of basaltic magmas. Contrib Mineral Petrol 15: 103-190

Grove TL (1993). Corrections to expressions for calculating mineral components in "Origin of calc-alkaline series lavas at Medicine Lake volcano by fractionation, assimilation and mixing" and "Experimental petrology of normal MORB near the Kane Fracture Zone: 22°-25°N, mid-Atlantic ridge". Contrib Mineral Petrol 114: 422-424

Hauri EH, Kurz MD, Wagner TP (1994b). Tracing Plume-Lithosphere Interaction Beneath Hawaii: Constraints from the Osmium Isotope Systematics of Kilauea Tholeiites. Trans Amer Geophys Union 75(44): 723

Hauri EH, Wagner TP, Kurz MD (1994a). Melt generation and migration beneath Kilauea: constraints from Os isotopes and phase equilibra. Mineral Mag 58A: 392-393

Hays JF (1965). Lime-alumina-silica. Yearb Carnegie Inst Wash 65: 234-236

Helz RT (1987). Differentiation behavior of Kilauea Iki lava lake, Kilauea Volcano, Hawaii. Magmatic Processes: Physiochemical Principles Ed. B. O. Mysen. The Geochemical Society. 241-258

Helz RT, Thornber CR (1987). Geothermometry of Kilauea Iki lava lake, Hawaii. Bull Volcanol 49: 651-668

Hofmann AW, Feigenson MD, Raczek I (1984). Case studies in the origin of basalt: III. Petrogenesis of the Mauna Ulu eruption, Kilauea, 1969-1971. Contrib Mineral Petrol 88: 24-35

Kelemen PB (1990a). Reaction between ultramafic rock and fractionating basaltic magma I. phase relations, the origin of calc-alkaline magma series and the formation of discordant dunite. J Petrol 31(1): 51-98

Kelemen PB, Dick HJB, Quick JE (1992). Formation of harzburgite by pervasive melt/rock reaction in the upper mantle. Nature 358: 635-641

Kelemen PB, Joyce DB, Webster JD, Holloway JR (1990b). Reaction between ultramafic rock and fractionating basaltic magma II. Experimental investigations of reacton between olivine tholeiite and harzburgite at 1150-1050°C and 5kb. J Petrol 31(1): 99-134

Kinzler RJ (1992c). Mantle melting processes at the spinel-garnet transition (17-21Kb). EOS Trans. AGU 73(43): 615

Kinzler RJ, Grove TL (1992b). Primary magmas of mid-ocean ridge basalts 2. applications. J Geophys Res 97(B5): 6907-6926

Kinzler RJ, Grove TL (1993). Corrections and further discussion of the primary magmas of mid-ocean ridge basalts, 1 and 2. J Geophys Res 98(B12): 22339-22347

Kushiro I (1972). Effect of water on the composition of magmas formed at high pressures. J Petrol 13(2): 311-334

Liu M, Chase CG (1989). Evolution of midplate hotspot swells: numerical solutions. J Geophys Res 94(B5): 5571-5584

Liu M, Chase CG (1991). Evolution of Hawaiian basalts: a hotspot melting model. Earth Plan Sci Lett 104: 151-165

McKenzie D, Bickle MJ (1988). The volume and composition of melt generated by extension of the lithosphere. J Petrol 29: 625-679

Morse SA (1980). Basalts and phase diagrams. New York, Springer-Verlag

O'Hara MJ (1968). The bearing of phase equilibria studies in synthetic and natural systems on the origin and evolution of basic and ultrabasic rocks. Ann Rev Earth Plan Sci 4: 69-113

Putirka K, Johnson M, Kinzler RJ, Longhi J, Walker D (Accepted 1995). Thermobarometry of mafic igneous rocks based on clinopyroxene-liquid equilibria, 0 - 30 kb. Contrib Mineral Petrol

Quick JE (1981). Petrology and petrogenesis of the Trinity Peridotite, an upper mantle diapir in the eastern Klamath mountains, Northern California. J Geophys Res 86(B12): 11837-11863

Ribe NM, Smooke MD (1987). A stagnation point flow model for melt extraction from a mantle plume. J Geophys Res 92: 6437-6443

Riley GN, Kolhstedt DL (1991). Kinetics of melt migration in upper mantle-type rocks. Earth Plan Sci Lett 105: 500-521

Sims KWW, DePaolo DJ, Murrell MT, Baldridge WS, Goldstein SJ, Clague DA (1995). Mechanisms of magma generation beneath Hawaii and mid-ocean ridges: uranium/thorium and samarium/neodymium isotopic evidence. Science 267: 508-512

Takahashi E (1986). Melting of a dry peridotite KLB-1 to up to 14-GPa: Implications on the origin of peridotitic upper mantle. J Geophys Res 91: 9367-9382

Walter MJ, Presnall DC (1994). Melting behavior of simplified lherzolite in the system CaO-MgO-Al2O3-SiO2-Na2O from 7 to 35 kbar. J Petrol 35(2): 329-359

Watson S, McKenzie D (1991). Melt generation by plumes: a study of Hawaiian volcanism. J Petrol 32: 501-537

Wei K, Tronnes RG, Scarfe CM (1990). Phase relations of aluminum-undepleted and aluminum-depleted komatiites at pressures fo 4-12 GPa. J Geophys Res 95(B10): 15817-15827

Wright TL (1984). Origin of hawaiian tholeiite: A metasomatic model. J Geophys Res 89(B5): 3233-3252

Yoder HS, Tilley CE (1962). Origin of basaltic magmas: an experimental study of natural and synthetic rock systems. J Petrol 3: 342-532

Yuen DA, Fleitout L (1985). Thinning of the lithosphere by small-scale convective destabilization. Nature 313: 125-128

Figure 1

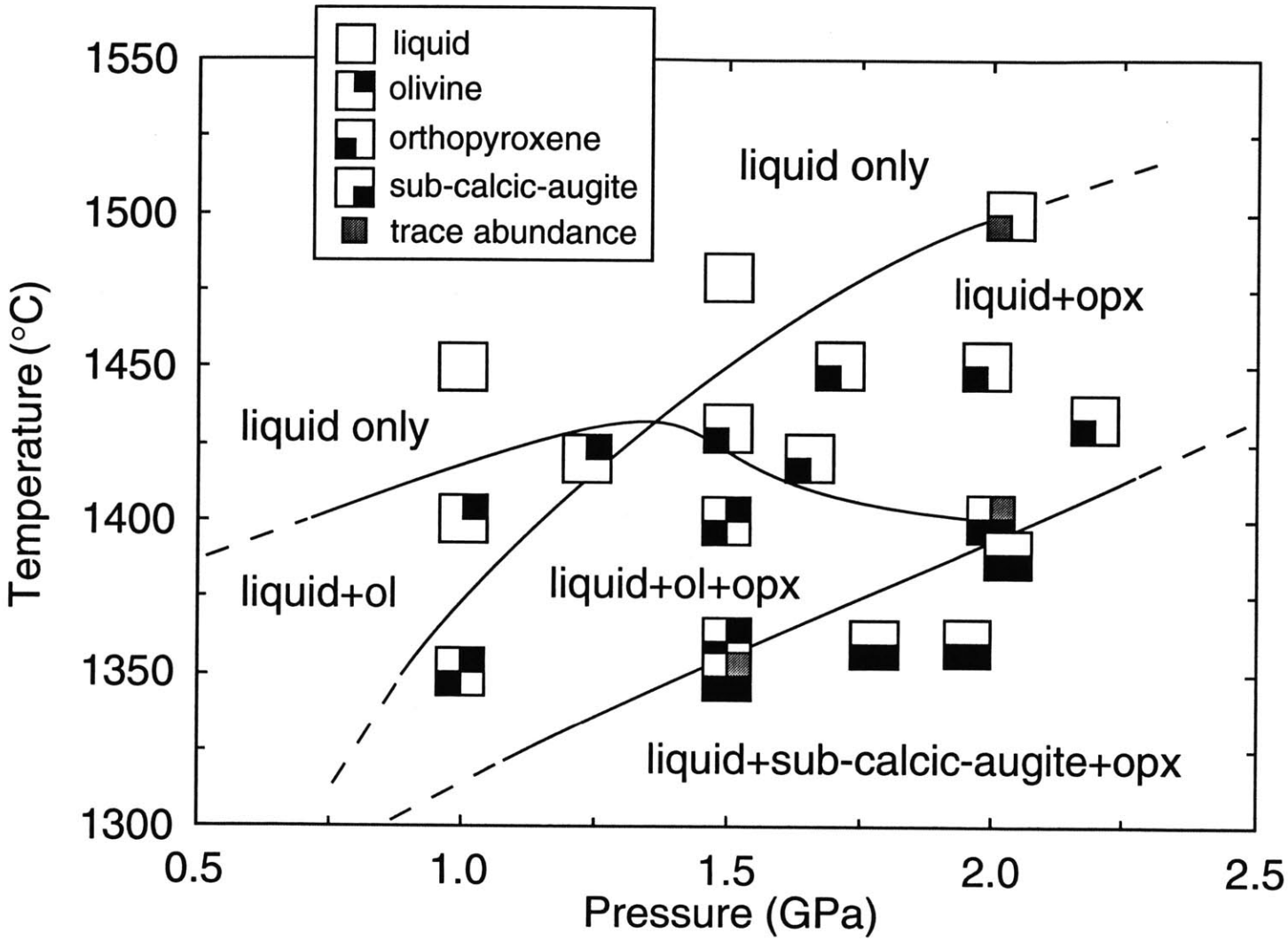
liquid
olivine
orthopyroxene
sub-calcic-augite
trace abundance
liquid only
liquid+opx
liquid only
liquid+ol
liquid+ol+opx
liquid+sub-calcic-augite+opx
1550
1500
1450
1400
1350
1300
Temperature (°C)
0.5
1.0
1.5
2.0
2.5
Pressure (GPa)

Figure 2

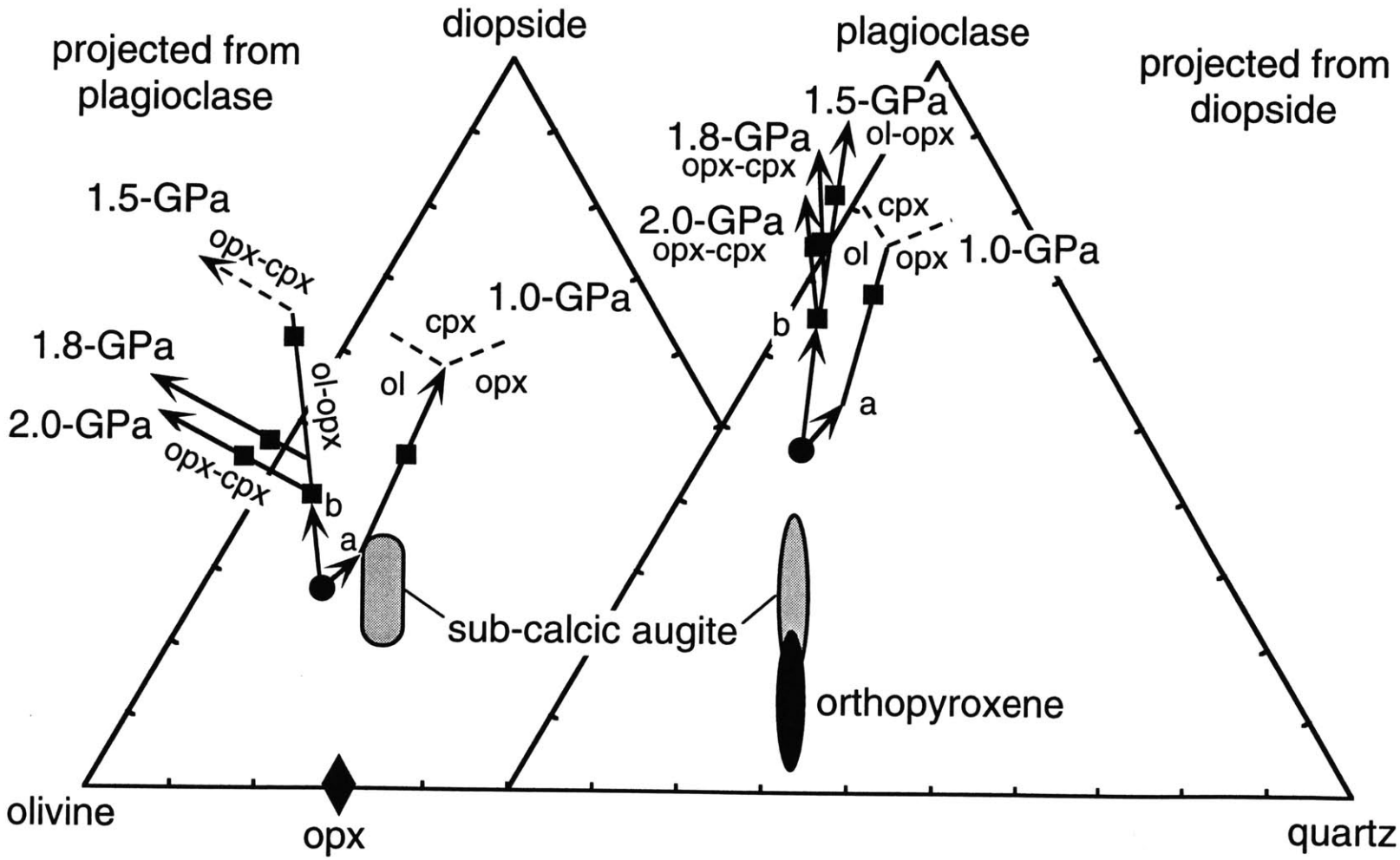
projected from plagioclase
diopside
plagioclase
projected from diopside
1.5-GPa
opx-cpx
1.8-GPa
2.0-GPa
opx-cpx
ol-opx
b
a
1.0-GPa
cpx
ol
opx
sub-calcic augite
1.8-GPa
opx-cpx
1.5-GPa
ol-opx
2.0-GPa
opx-cpx
cpx
ol
opx
1.0-GPa
b
a
orthopyroxene
olivine
opx
quartz

Figure 3a

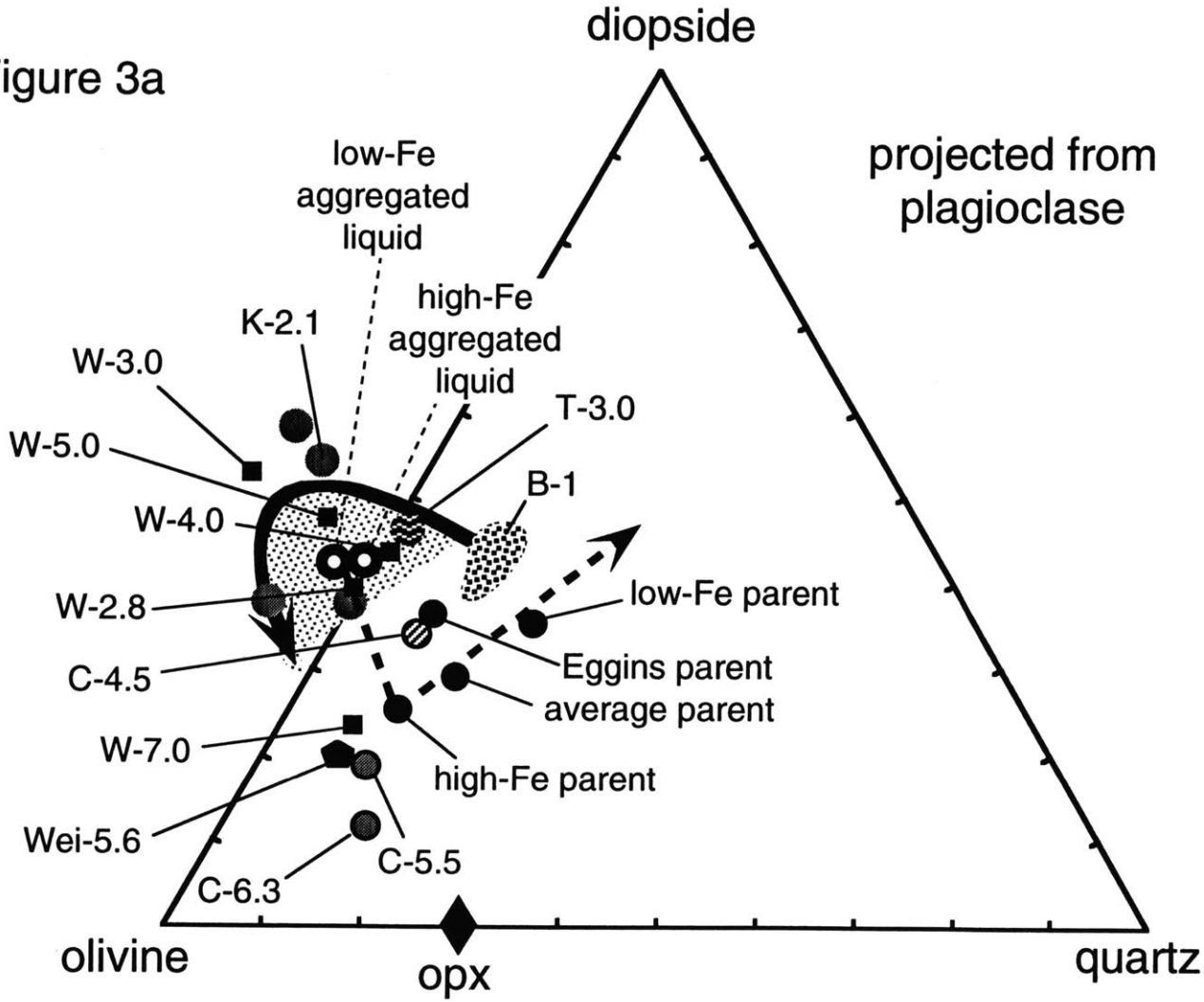
diopside
projected from
plagioclase
low-Fe
aggregated
liquid
high-Fe
aggregated
liquid
K-2.1
W-3.0
W-5.0
W-4.0
W-2.8
C-4.5
W-7.0
Wei-5.6
C-6.3
C-5.5
T-3.0
B-1
low-Fe parent
Eggins parent
average parent
high-Fe parent
olivine
opx
quartz

Figure 3b

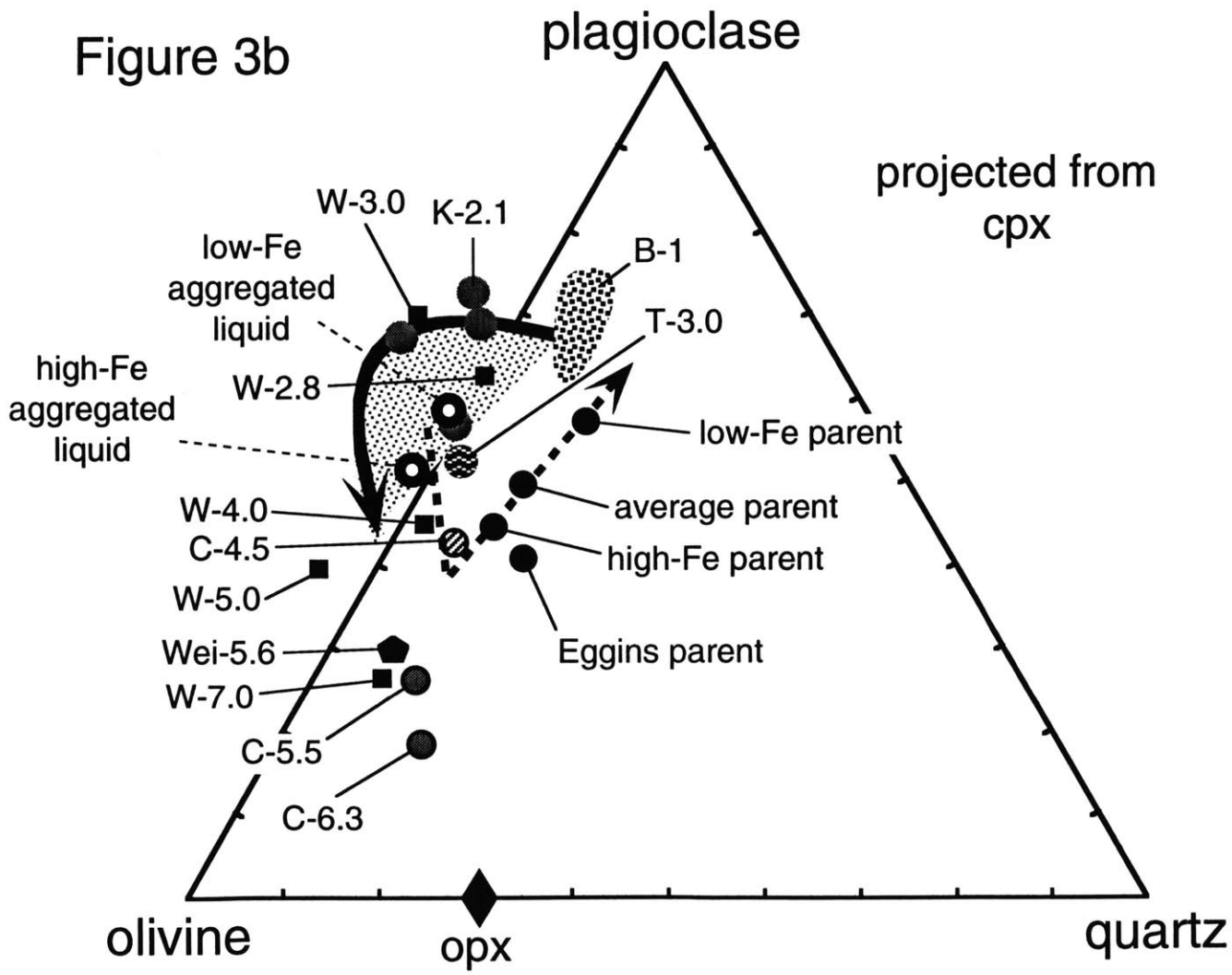
plagioclase
projected from cpx
W-3.0
K-2.1
low-Fe aggregated liquid
B-1
T-3.0
high-Fe aggregated liquid
W-2.8
low-Fe parent
average parent
W-4.0
C-4.5
high-Fe parent
W-5.0
Wei-5.6
Eggins parent
W-7.0
C-5.5
C-6.3
olivine
opx
quartz

Figure 4

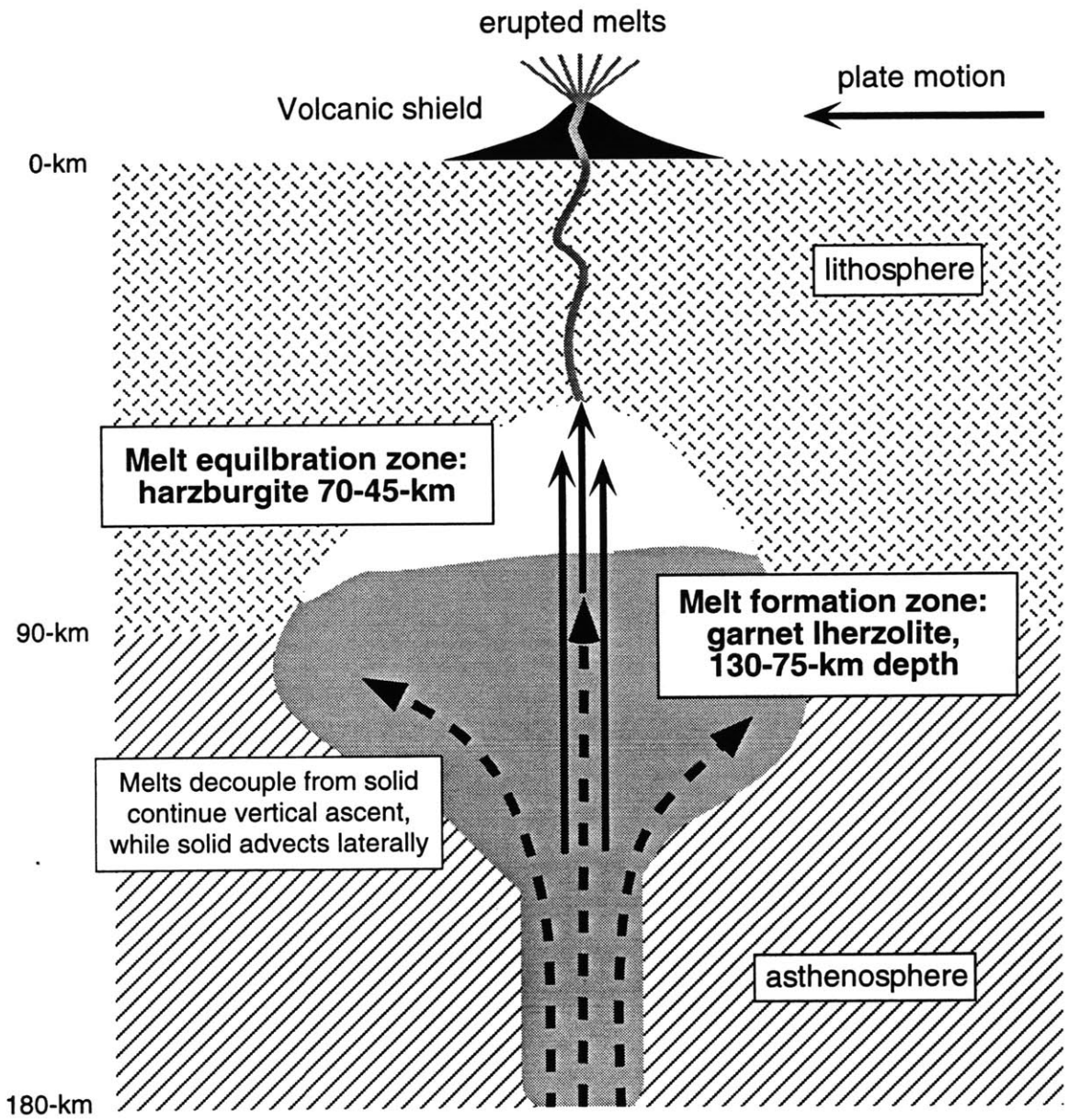
erupted melts
plate motion
Volcanic shield
0-km
lithosphere
Melt equilbration zone:
harzburgite 70-45-km
90-km
Melt formation zone:
garnet lherzolite,
130-75-km depth
Melts decouple from solid
continue vertical ascent,
while solid advects laterally
asthenosphere
180-km

Figure 5

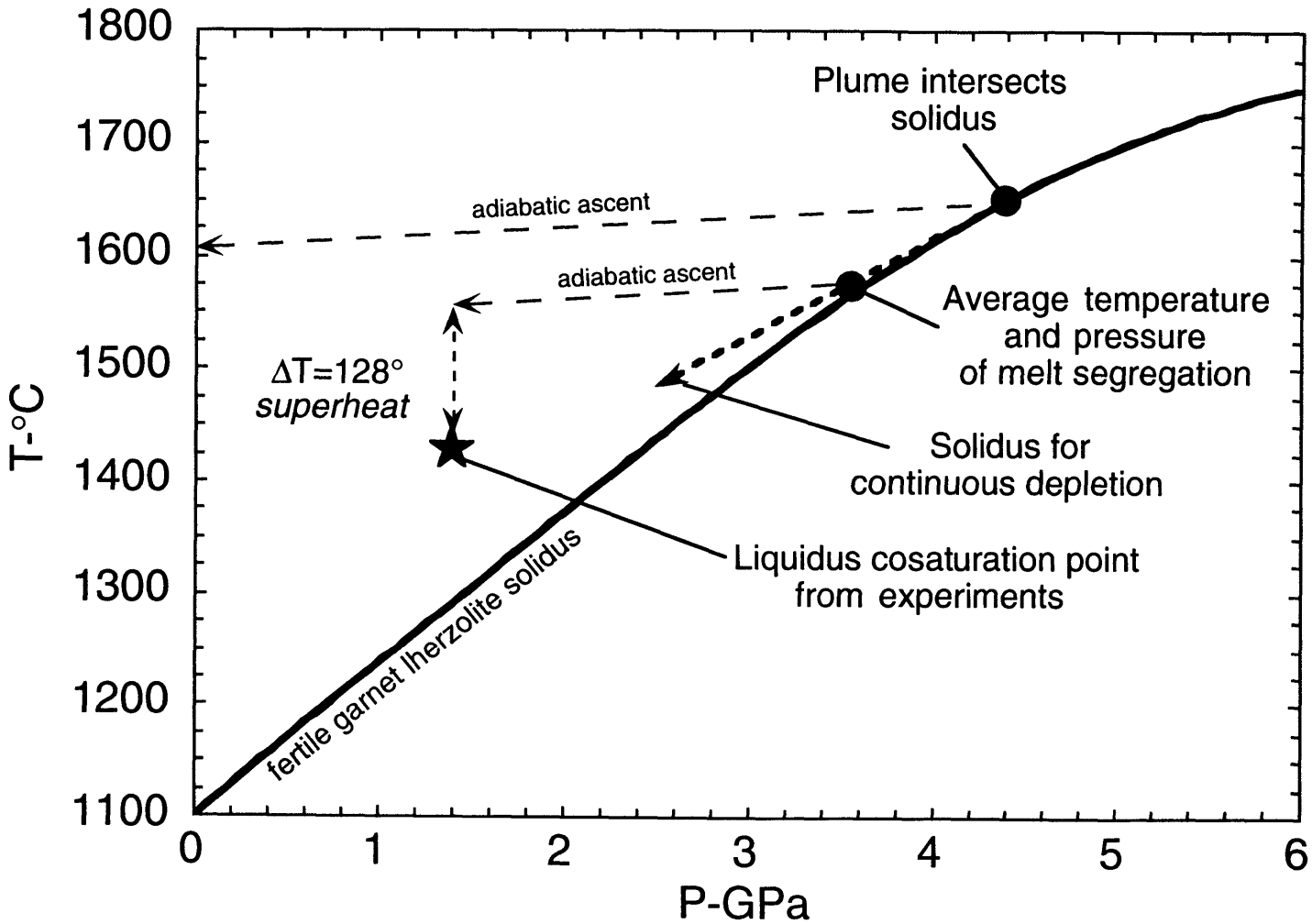
1800
1700
1600
1500
1400
1300
1200
1100
T-°C
0
1
2
3
4
5
6
P-GPa
Plume intersects solidus
adiabatic ascent
adiabatic ascent
Average temperature and pressure of melt segregation
ΔT=128° superheat
Solidus for continuous depletion
Liquidus cosaturation point from experiments
fertile garnet lherzolite solidus

Table 1. Experimental starting composition and Kilauea tholeiite primary magma estimates.

Composition	MgO	Al_2O_3	SiO_2	CaO	TiO_2	Cr_2O_3	MnO	FeO	P_2O_5	Na_2O	K_2O	NiO
	Estimate based on high-MgO glasses, Clague et al. (1991)											
Experimental starting composition	17.2	10.3	48.8	8.25	1.77	-	0.17	11.6	0.16	1.52	0.27	-
	Revised estimates based on high-MgO glasses, Clague et al. (1995)											
High-FeO	18.4	9.8	47.9	7.77	1.66	-	-	12.5	0.17	1.43	0.26	-
Low-FeO	13.4	12.3	51.0	9.72	2.08	-	-	9.1	0.21	1.86	0.33	-
Average	16.5	10.7	49.0	8.55	1.90	-	-	11.2	0.18	1.66	0.30	-
	Estimate based on Kilauea Iki lavas, Eggins (1992a)											
Kilauea Iki parent	16.0	10.5	47.8	9.26	2.09	0.13	0.15	11.6	0.20	1.79	0.43	0.10

Table 2. Experimental run conditions and products.

Run#	Pressure (GPa)	Temperature (°C)	Duration (min)	Phases present	Proportions	Σr^2
55	1.00	1450	20	glass	100	-
56	1.00	1400	40	glass+ol	93:7	0.2
57	1.00	1350	40	glass+ol+opx	70:12:18	0.06
38	1.23	1420	270	glass+ol	98:2	0.2
58	1.50	1480	18	glass	100	-
59	1.50	1430	38	glass+opx	96:4	1
61	1.50	1400	16	glass+ol+opx	-	-
60	1.50	1360	38	glass+ol+opx	57:4:39	4
62	1.50	1350	40	glass+opx(w/ol inclusions)+cpx	-	-
34	1.66	1420	720	glass+opx	77:23	0.2
37	1.71	1450	270	glass+opx	97:3	0.2
13	1.78	1360	1380	glass+opx+cpx	44:22:34	0.09
63	2.03	1500	16	glass+opx	100:trace	-
64	1.98	1450	32	glass+opx	-	-
65	2.00	1400	126	glass+ol(trace)+opx+cpx	-	-
11	2.03	1390	1620	glass+opx+cpx	63:19:18	0.2
9	1.95	1360	3060	glass+opx+cpx	35:12:53	0.03
147	2.20	1433	276	glass+opx	93:7	0.1

Table 3. Composition of experimental run products.

	Phase	#	MgO		Al_2O_3		SiO_2		CaO		TiO_2		Cr_2O_3		MnO		FeO		P_2O_5		Na_2O		K_2O		Total
BPC-9	glass	9	9.8	0.1	14.48	0.08	45.3	0.2	9.0	0.1	3.6	0.1	0.00	0.00	0.15	0.05	13.8	0.1	0.48	0.02	2.8	0.1	0.59	0.02	100.0
	opx	5	26.6	0.4	7.2	0.8	52.2	0.5	2.1	0.1	0.44	0.06	0.01	0.01	0.10	0.05	12.1	0.1	-	-	0.24	0.01	-	-	100.9
	cpx	4	20.1	0.5	8.2	0.5	51.3	0.8	9.2	0.5	0.74	0.06	0.05	0.02	0.15	0.06	10.3	0.2	-	-	0.87	0.04	-	-	101.0
BPC-11	glass	8	11.7	0.2	13.2	0.3	46.6	0.2	9.7	0.3	2.4	0.1	0.07	0.04	0.20	0.03	12.7	0.2	0.33	0.03	2.1	0.1	0.34	0.03	99.5
	opx	9	28.7	0.4	5.1	0.8	54.2	0.5	2.6	0.2	0.26	0.04	0.00	0.00	0.16	0.01	9.6	0.2	-	-	0.15	0.02	-	-	100.8
	cpx	8	23.3	0.7	5.6	0.6	53.4	0.4	8.2	0.8	0.37	0.04	0.01	0.01	0.15	0.01	9.3	0.3	-	-	0.50	0.06	-	-	100.9
BPC-13	glass	9	9.6	0.1	14.2	0.1	45.4	0.6	9.4	0.1	3.08	0.08	0.01	0.01	0.20	0.06	13.1	0.1	0.41	0.03	2.8	0.1	0.48	0.03	98.7
	opx	6	26.9	0.4	6.1	1.1	52.5	0.8	2.1	0.2	0.37	0.08	0.04	0.06	0.16	0.04	11.30	0.07	-	-	0.18	0.05	-	-	99.6
	cpx	4	20.0	0.7	7.7	0.6	50.7	0.5	10.5	0.7	0.62	0.09	0.08	0.02	0.16	0.04	9.5	0.3	-	-	0.70	0.05	-	-	99.9
BPC-34	glass	6	13.5	0.2	12.30	0.05	47.4	0.1	10.0	0.1	2.19	0.06	0.02	0.02	0.18	0.04	12.2	0.1	0.30	0.04	1.88	0.08	0.29	0.02	100.1
	opx	5	30.0	0.6	3.7	0.6	55.2	0.9	2.35	0.09	0.22	0.09	0.12	0.01	0.17	0.01	8.8	0.1			0.10	0.03			100.7
BPC-37	glass	6	16.82	0.08	10.73	0.06	49.3	0.2	8.3	0.1	1.80	0.04	0.02	0.02	0.22	0.03	11.71	0.07	0.22	0.02	1.6	0.1	0.25	0.02	100.9
	opx	3	32.4	0.1	1.8	0.1	56.9	0.1	1.53	0.09	0.13	0.02	0.11	0.05	0.09	0.05	7.31	0.02	-	-	0.08	0.02	-	-	100.3
BPC-38	glass	6	16.86	0.09	10.61	0.06	49.7	0.2	8.2	0.1	1.79	0.06	0.02	0.02	0.20	0.05	11.6	0.2	0.19	0.02	1.59	0.09	0.24	0.01	101.0
	ol	3	47.6	0.5	0.11	0.01	40.8	0.2	0.27	0.02	0.09	0.01	0.07	0.06	0.10	0.04	11.6	0.2	-	-	-	-	-	-	100.7
BPC-55	glass	7	17.4	0.1	10.23	0.09	48.8	0.3	7.8	0.2	1.74	0.03	0.01	0.01	0.11	0.03	11.3	0.1	0.21	0.01	1.5	0.1	0.22	0.02	99.4
BPC-56	glass	7	15.1	0.1	10.8	0.1	49.5	0.2	8.5	0.1	1.88	0.03	0.01	0.01	0.12	0.05	11.32	0.08	0.20	0.03	1.6	0.1	0.24	0.01	99.2
	ol	5	47.5	0.3	0.1	0.1	39.9	0.3	0.28	0.00	0.04	0.03	0.00	0.00	0.14	0.02	12.03	0.16	0.01	0.00	-	-	-	-	100.1
BPC-57	glass	7	9.3	0.5	14.0	0.2	48.9	0.4	10.8	0.2	2.44	0.05	0.01	0.02	0.19	0.06	11.6	0.2	0.29	0.04	2.1	0.1	0.31	0.02	99.8
	ol	4	44.8	0.2	0.10	0.02	39.2	0.2	0.39	0.00	0.11	0.01	0.01	0.01	0.10	0.01	16.36	0.08	0.00	0.00	-	-	-	-	101.1
	opx	6	30.7	0.4	3.1	0.5	55.1	0.4	2.3	0.2	0.38	0.03	0.06	0.02	0.16	0.01	9.4	0.1	-	-	0.02	0.03	-	-	101.1
BPC-59	glass	6	16.5	0.2	10.8	0.2	49.6	0.3	8.1	0.4	1.94	0.06	0.00	0.01	0.15	0.05	11.3	0.2	0.23	0.01	1.48	0.08	0.26	0.02	100.5
	opx	4	32.0	0.5	2.8	0.3	56.0	0.1	1.7	0.1	0.26	0.03	0.00	0.00	0.08	0.00	7.5	0.2	-	-	0.05	0.01	-	-	100.3
BPC-60	glass	5	6.6	1.2	14.8	0.8	47.0	0.3	10.0	0.3	2.7	0.1	0.02	0.03	0.17	0.05	14.2	0.6	0.39	0.05	3.3	0.3	0.50	0.06	99.7
	ol	3	44.7	0.3	0.18	0.03	39.3	0.3	0.38	0.01	0.07	0.04	0.01	0.02	0.17	0.00	16.3	0.2	0.02	0.02	-	-	-	-	101.2
	opx	4	29.4	0.5	5.2	1.6	53.9	0.5	2.3	0.2	0.37	0.07	0.00	0.00	0.14	0.01	9.61	0.09	-	-	0.09	0.02	-	-	101.1
BPC-61	glass	*																							
	ol	2	45.2	0.4	0.19	0.02	39.7	0.1	0.37	0.01	0.05	0.05	0.00	0.00	0.11	0.01	14.12	0.01	0.01	0.00	-	-	-	-	
	opx	4	31.0	0.5	3.5	0.6	55.2	0.9	2.1	0.2	0.29	0.07	0.00	0.00	0.10	0.00	8.7	0.2	-	-	0.05	0.01	-	-	101.0
BPC-62	glass	*																							
	opx	4	29.7	0.5	3.9	1.1	54.5	0.5	2.5	0.4	0.31	0.06	0.00	0.00	0.11	0.00	9.7	0.1	-	-	0.10	0.01	-	-	100.7
	cpx	3	25.3	0.8	4.1	0.9	53.1	0.7	6.5	0.8	0.46	0.03	0.00	0.00	0.15	0.02	9.4	0.2	-	-	0.3	0.1	-	-	99.4
BPC-63	glass	6	16.7	0.9	10.9	0.7	49.3	0.4	8.5	0.3	2.0	0.2	0.01	0.02	0.177	0.07	11.8	0.2	0.19	0.04	1.6	0.2	0.25	0.03	101.5
	opx	3	32.4	1.6	3.4	1.8	55.9	1.6	1.5	0.2	0.4	0.2	0.02	0.01	0.10	0.03	7.3	0.5	-	-	0.06	0.04	-	-	101.0
BPC-64	glass	*																							
	opx	4	29.9	0.1	4.5	0.2	55.1	0.2	2.59	0.08	0.28	0.01	0.00	0.00	0.14	0.01	8.77	0.06	-	-	0.14	0.01	-	-	101.3
BPC-65	glass	*																							
	ol	1	46.2	-	0.36	-	40.6	-	0.52	-	0.13	-	0.00	-	0.10	-	12.9	-	0.03	-	-	-	-	-	100.7
	opx	3	27.8	0.3	6.54	0.98	53.2	0.2	2.62	0.15	0.43	0.04	0.02	0.01	0.15	0.01	10.3	0.10	-	-	0.17	0.01	-	-	101.3
	cpx	†																							
B-147	glass	7	16.06	0.09	10.93	0.06	48.5	0.3	8.55	0.13	1.72	0.05	0.01	0.01	0.09	0.03	11.78	0.13	0.23	0.01	1.59	0.06	0.22	0.01	99.7
	opx	3	31.9	0.7	3.08	0.50	55.6	0.7	1.88	0.29	0.22	0.04	0.01	0.01	0.13	0.01	7.95	0.29	-	-	0.07	0.02	-	-	100.8

Table 4. Experimental melts of garnet lherzolite.

Study-Run #	Pressure (kbars)	MgO	Al_2O_3	SiO_2	CaO	TiO_2	Cr_2O_3	MnO	FeO	P_2O_5	Na_2O	K_2O
Kinzler 1995-L69	19	14.3	16.3	45.4	11	0.48	0.03	0.06	8.95	0.11	2.16	0.08
Kinzler 1995-L58	21	12	14.4	44.4	11.7	0.48	0	0.11	10.7	0.06	2.21	0.07
Takahashi 1986-L43	30	19.2	11.0	46.9	12.2	0.9	0.4	0.2	7.8	-	1.2	
Walters (unpublished)	28	16.6	14.5	45.4	11.53	1.33	-	-	8.25	-	1.21	0.44
Walters (unpublished)	30	16.5	12.7	43.0	10.65	1.79	-	-	9.67	-	1.56	1.47
Walters (unpublished)	40	20.7	9.44	46.9	11.8	0.63	-	-	9.97	-	0.74	0.30
Walters (unpublished)	50	22.3	6.52	42.0	10.7	0.92	-	-	11.6	-	0.69	0.56
Walters (unpublished)	70	27.1	6.08	46.5	7.45	0.59	-	-	11.0	-	0.55	0.31
Canil 1992	45	19	9.7	45.9	10.4	-	0.5	-	10.4	-	0.7	-
Canil 1992	55	25.9	6.7	46.6	6.7	-	0.6	-	10.2	-	0.6	-
Canil 1992	63	29	5.5	47.3	5.1	-	0.4	-	9.4	-	0.3	-
Wei et al 1992-AUK	56	26.4	7.97	45.9	7.74	0.41	-	0.21	11.07	-	0.43	0.09

Table 5. Reaction models.

Parent Composition	Reference	MgO	Al_2O_3	SiO_2	CaO	FeO	Na_2O	Lq	Oliv	Opx	Σr^2
Estimated Kilauea primary magmas and models								*Proportions*			
Glass-based, Low-FeO	Clague et al. (1995)	13.8	12.6	52.4	9.98	9.33	1.91				
Model (using low-Fe agg. lq)		13.840	12.116	52.408	10.740	9.056	1.315	85.85	-30.64	44.29	1.2
Glass-based, High-FeO	Clague et al. (1995)	18.8	10.0	49.0	7.94	12.7	1.46				
Model (using high-Fe agg. lq)		19.142	9.368	49.043	9.956	10.586	1.071	83.45	-9.12	24.79	9.2
Kilauea Iki	Eggins (1992a)	16.5	10.9	49.3	9.55	12.0	1.85				
Model (using high-Fe agg. lq)		16.684	10.296	49.327	10.941	10.835	1.182	92.33	-16.65	23.54	4.1

Reactants							
High-FeO aggregated liquid		18.7	10.7	46.4	11.5	11.5	1.26
Low-FeO aggregated liquid		17.0	13.2	46.5	11.8	10.0	1.49
Olivine	Clague et al. (1991)	49.3	0.00	41.5	0.22	9.03	0.00
Orthopyroxene	This study, exp 37	32.4	1.77	56.9	1.53	7.31	0.08

Table 6. Thermal energy calculations for reaction models.

Clague et al. 1995, low-FeO primary magma estimate

Heat available (cal)		Heat required (cal)
Superheat Lq	Ol Xlization	Opx Assim
+3291	+3069	-4432

Balance=+1928

Clague et al. 1995, high-FeO primary magma estimate

Heat available (cal)		Heat required (cal)
Superheat Lq	Ol Xlization	Opx Assim
+3210	+911	-2463

Balance=+1658

Eggins 1992a primary magma estimate

Heat available (cal)		Heat required (cal)
Superheat Lq	Ol Xlization	Opx Assim
+3535	+1678	-2375

Balance=+2838

Table 7. Percentage of orthopyroxene required in source to produce a Mauna Loa sized shield.

weight of orthopyroxene assimilated

vol of Mauna Loa (km^3)	% opx assimilated	density of magma (kg/km^3)	kg of opx
45,000	0.34	2.9E+12	4.44E+16

% orthopyroxene required in source region

source radius (km)	source length (km)	volume (km^3)	density peridotite (kg/km^3)	kg of peridotite	wt. % opx
40	45	226195	3.3E+12	7.46E+17	0.06
20	45	56549	3.3E+12	1.87E+17	0.24
15	45	31809	3.3E+12	1.05E+17	0.42

Chapter Three

Trace element abundances of high-MgO glasses from Hawaii

ABSTRACT

The trace element abundances of high-MgO glass grains from the Hawaiian volcanoes, Kilauea, Mauna Loa and Haleakala have been determined by ion-microprobe. The Kilauea glasses are the main focus of the study; seven high-MgO (10 to 15 wt.%) and two low-MgO (6.8 wt.%) glasses were analyzed. Four glasses from Mauna Loa and five glasses from Haleakala with moderately high-MgO (8 to 11 wt.%) contents were also analyzed. The glasses have trace element abundance characteristics that are similar to typical Hawaiian tholeiite, e.g. $(La/Yb)_{C1}$ ratio of the glasses varies between 2.5 and 3.7. The Sr/Nb, Zr/Nb, and Rb/Sr ratios of the glasses vary between characteristic Kilauea and Mauna Loa values and indicate a range of primary magma compositions. The overall geochemical similarity of the glasses to typical Hawaiian shield tholeiites supports the use of the glasses for estimating Hawaiian primary magma compositions and constraining characteristics of the melt generation process. The glasses have undergone minor, but variable amounts of olivine fractionation. Major elements were brought into Fe/Mg equilibrium with $Fo_{90.7}$ olivine by olivine addition. Fractionation corrected incompatible elements and CaO are positively correlated with the Ce/Yb ratio. This incompatible behavior for CaO is the opposite of that inferred from experimental studies of spinel lherzolite melting, but is consistent with the trends observed in Kilauea and Mauna Loa shield lavas (Frey and Rhodes, 1993). Fractionation corrected Yb and Dy abundances of the Kilauea glasses are nearly constant, while La and Ce show 25% relative variation. Inversion of the Kilauea glass trace element abundances using the techniques of Hofmann and Feigenson (1983) shows that their source is flat relative to C1 chondrites and has a much higher bulk D for the HREE than the LREE. The constant abundances and higher source D for the HREE are consistent with the formation of the glasses by partial melting of garnet lherzolite. Chapter 2, however, shows that the primary magma estimate based on these glasses is in equilibrium with depleted harzburgite, not garnet lherzolite. Chapter 2 proposes that Hawaiian magmas react and equilibrate with harzburgite in the plume top. This chapter investigates the effect of this equilibration reaction on trace element abundances and finds that they are all generally diluted by reaction with LREE abundances diluted slightly more than the HREE abundances due to the higher concentrations of the HREE in orthopyroxene.

INTRODUCTION

Tholeiitic basalt is the basic building block of the Hawaiian islands, comprising over 95% of each individual volcanic shield (Clague and Dalrymple, 1987). If these lavas are derived by melting within a mantle plume, as commonly postulated, their compositions can be used to infer the composition and mineralogy of the plume and important characteristics of the melting process. The first step in understanding tholeiite origin is identifying primary magmas, lava samples that are liquids and have been minimally modified since segregation from their source. Most subaerially-erupted lavas do not meet this criteria because their compositions are affected by crystal fractionation, crystal entrainment, magma mixing and assimilation in shallow-level plumbing systems. Basaltic liquids decrease in MgO-content as they crystallize, hence lavas with higher MgO-contents are considered to be closer to primary magma compositions. Samples that are glass are quenched liquids and thus high-MgO glasses are the ideal samples for studying the characteristics of tholeiite primary magmas.

This study reports the trace element abundances of high-MgO glasses from Kilauea, Mauna Loa and Haleakala volcanoes. The trace element abundance data is used to establish the relationship between high-MgO glasses and typical Kilauea and Mauna Loa shield lavas. The data is also used to gain insight into the general Hawaiian melt generation process and the nature of the Kilauea source. In Chapter 2, a primary magma estimate based on the Kilauea glasses was subjected to a series of high-pressure melting experiments. The results of these experiments showed that Hawaiian magmas must equilibrate with depleted harzburgite during segregation from the mantle. The effect of harzburgite equilibration on trace element abundances is modeled and discussed at the end of this chapter.

DESCRIPTION OF GLASS GRAINS

All of the samples are fragments of tholeiitic basalt glass (100 to 300 μm across). The Kilauea samples occur as sand grains in a turbidite deposit near Kilauea's submarine east rift zone, the Puna Ridge (Clague et al., 1991). Their compositional characteristics, interpretation and relation to other Puna Ridge lavas are discussed in Clague et al. (1995). The glasses were submarine-erupted from the rift within the last few thousand years. They are unique in that they have up to 15.0 wt.% MgO, the highest magnesia contents reported for volcanic glass from Hawaii (Clague et al., 1991 and Frey, 1991). Microphenocrysts of forsteritic olivine, up to $Fo_{90.7}$, are present in some grains. Overall, the glasses have higher SiO_2 and lower TiO_2, K_2O and P_2O_5 contents than typical subaerially-erupted Kilauea lavas. They show significant variation in FeO content, up to 30% relative at constant MgO. Clague et al. (1995) conclude that the compositional variation in the glasses with >10 wt.% MgO is produced by olivine fractionation of different parent magmas related through variations in the partial melting process. The glasses selected for ion-microprobe analysis have nearly constant FeO contents (11-12 wt.%). Most have >10 wt.% MgO (Table 1).

The Mauna Loa and Haleakala glasses have moderately high-MgO contents, 8 to 11 wt.%. No phenocrysts are present in the grains. The Mauna Loa glasses were found in a sand core off Mauna Loa's submarine southwest rift. The glasses are derived from both subaerially-erupted airfall and submarine-eruptions like the Kilauea glasses. The Haleakala samples were found in a Mn-cemented sandstone sampled by dredge #43 of Moore et al. (1990).

ANALYTICAL METHODS

Glasses were mounted in polished thin sections and analyzed for trace element abundances (Table 1) by secondary ion mass spectrometry using the Cameca IMS 3f ion microprobe at the Woods Hole Oceanographic Institution. Rare earth elements (La, Ce, Nd, Sm, Eu, Dy, Er, and Yb) and Hf were analyzed using a 1- to 2-nA primary beam of O^- ions focused to a spot size of 20- to 30-μm. Other trace elements (Sc, Ti, V, Cr, Sr, and Zr) were analyzed using a 0.2-nA primary beam, focused to a spot size of 8- to 15-μm. Positive secondary ions were collected and counted by an electron multiplier, molecular interferences excluded by energy filtering using ±10-V energy window, a -35 to -60V offset for REEs, and a -90V offset for other trace elements (Shimizu and Hart, 1982). One sigma uncertainties based on counting statistics are approximately 4-7% relative for the REE. Europium uncertainties are 10-14% relative due to the correction factors applied for BaO interferences. Erbium has NdO, SmO and BaO_2 interferences which can result in positive Er anomalies. Neither Eu or Er data were used in the subsequent modeling. The other trace elements have uncertainties based on counting statistics of <2% relative with the exception of Nb and Rb which have uncertainties of 10% relative due to their low abundances. Kilauea glass sample KL-2 (Newsom, 1986) was used as a standard. Replicate analyses of KL-2 and high-MgO Kilauea glass 57-7 show precision that is similar to that calculated from counting statistics.

RESULTS

All of the glasses have $(LREE/HREE)_{C1}>1$, similar to other Hawaiian tholeiites (Fig. 1). At a given MgO content the glasses show a wide range of Ce/Sm and Ce/Yb ratios (Fig. 2). The Ce/Yb and Ce/Sm ratios are generally good discriminants between historical Kilauea and Mauna Loa shield lavas, but apparently are not for these glasses. The Kilauea

glasses show a positive correlation of Ce/Sm and Ce/Yb with MgO content and range from low, Mauna Loa-like values to higher, Kilauea-like values. The Mauna Loa glasses show similar variation and two of the three glasses have higher Ce/Sm than the historical Mauna Loa shield lavas. These trends have not been observed in the historical shield lavas. The Ce/Sm and Ce/Yb ratios of the Haleakala glasses are similar to historical Mauna Loa shield lavas.

The Sr/Nb, Zr/Nb and Rb/Sr ratios are very good discrimants between Kilauea and Mauna Loa shield lavas (Fig. 3, Frey and Rhodes, 1993) and this is consistent most of the glass data. The Sr/Nb and Zr/Nb ratios of the Kilauea glasses are both negatively correlated with the Ce/Yb ratio (Fig. 4). Unlike the Ce/Yb and Ce/Sm ratios, the Sr/Nb and Zr/Nb of the Kilauea glasses are similar to Kilauea shield lavas (Fig. 3a,b). Two Kilauea glasses (57-35 and 57-27) and two Haleakala glasses are at the boundary of the Kilauea and Mauna Loa shield lavas due to their low-Nb contents. The Mauna Loa glasses have Kilauea shield-like Sr/Nb and Zr/Nb and are at the boundary for the REE ratios. All of the Kilauea glasses have Rb/Sr (Fig. 3c) in the Kilauea shield lava field, most are similar to the Puna Ridge lavas. Two glasses, 57-13 and 57-35, have Rb/Sr ratios near the highest reported for Kilauea lavas due to their high-Rb contents. The Haleakala glasses are split between the fields in Rb/Sr, while the Mauna Loa glasses are in the Mauna Loa shield lava field.

The La/Ce ratio is 0.39±0.02 for the Kilauea, Mauna Loa and Haleakala glasses. This value is identical to that of C1 chondrites (Anders and Grevesse, 1989) and primitive mantle (PM) estimates (Sun and McDonough, 1989). The Nb/La ratio of the Kilauea glasses is ~1.1 times C1 or PM estimates, while the Nb/La ratio of the Mauna Loa and Haleakala glasses is higher, but more variable at ~1.3 times C1 or PM estimates. These values are consistent with historical Kilauea and other Kea range lavas, but higher than Mauna Loa or Loa range lavas (McDonough, in prep). The K/La ratio of the Kilauea

glass is 0.83 times PM, more depleted than the other incompatible element ratios. The K/La ratio of the Mauna Loa and Haleakala glasses is slightly higher and more variable than the K/La of the Kilauea glasses, but it is also relatively depleted at 0.92 times PM. The Ti/Eu and Sm/Sr ratios are constant for the Kilauea glasses. The Ti/Eu is near C1 and PM values and the Sm/Sr ratio is 0.9 times C1 and 0.8 times PM.

DISCUSSION

Significance of the glasses

Figures 1, 2 and 3 show that the glasses have similar chemical characteristics to typical, low-MgO Hawaiian tholeiites. Their high-MgO nature, then, is not the result of an anomalous melting event and they are likely produced by the same processes that produce most Hawaiian tholeiitic magmas. Use of the glass major element concentrations for making primary magma estimates is thus justified. The trace element ratios of the glasses (Fig. 2 and 3) are not uniquely like Kilauea or Mauna Loa shield lavas, but share some characteristics of each. This may indicate that a range of primary magmas are delivered to each volcano and that high-MgO glasses are samples of these liquids prior to a mixing event which obscures this signal.

Post-mantle segregation effects in the glasses

The glasses have variable MgO contents and Fe/Mg ratios. This implies that some processing has taken place since segregation from their source. The presence of olivine microphenocrysts in the glasses suggests that crystallization occurred. Studies of Kilauea Iki lava lakes (Helz, 1987 and Helz and Thornber, 1987) show that at low pressures magnesian Kilauea magmas crystallize only olivine until they reach ~7.5 wt.% MgO.

Clague et al. (1995) show that the high-MgO Kilauea glasses follow similar olivine fractionation curves. Magma mixing is another possible cause of chemical variation. Mixing of a highly evolved liquid with a primitive liquid could result in a range of MgO contents and trace element abundances. However, mixing with highly evolved liquids would strongly affect the Sm/Sr and Ti/Eu ratios, which are sensitive indicators of plagioclase and Fe-Ti oxide fractionation, respectively. These ratios are nearly constant for the Kilauea high-MgO glasses and indicate such mixing has not occurred. The glasses can thus be corrected to their pre-fractionation major and trace element abundance levels using olivine addition calculations.

Olivine fractionation correction

All glass compositions with >8.7 wt.% MgO were corrected to be in Fe/Mg equilibrium with $Fo_{90.7}$ olivine through olivine addition (Table 2). $Fo_{90.7}$ was selected because it is the most magnesian olivine composition found in the Kilauea glasses. The compositions were corrected using the MORBFRAC program described in Grove et al. (1992). Briefly, major element concentrations of glasses were normalized to 100%, volatile free. Fe^{2+}/Fe^{Total} was assumed to be 0.9, based on the wet chemical determination of Moore (1965) for the glassy rim of a Puna Ridge lava. Olivine was added in 0.25 wt.% increments as stoichiometric $(Mg, Fe)_2SiO_4$. Fe/Mg ratio of the added olivine was recalculated at each step to maintain equilibrium with the liquid assuming an exchange $K_D^{Fe\text{-}Mg}$ of 0.3 (Roeder and Emslie, 1970). The glasses required the addition of 5 to 24 wt.% olivine to equilibrate with $Fo_{90.7}$. Trace element abundances were corrected to reflect the olivine addition calculation assuming complete incompatibility in olivine (dilution factors in Table 2).

Fractionation corrected major element concentrations

The fractionation correction reduces much of the variation in glass major element data. FeO^T and Na_2O contents (Fig. 5) are nearly constant with the exception of Kilauea glass 57-13 which has higher FeO^T and lower Na_2O. This could indicate that 57-13 is derived from a deeper melt (Kinzler and Grove, 1992, 1993 and Langmuir et al., 1992). Corrected K_2O, CaO and TiO_2 (not shown) concentrations of the Kilauea glasses are variable and show strong positive correlations with the Ce/Yb ratio (Fig. 5).

Implications for differences between Kilauea and Mauna Loa

Frey and Rhodes (1993) note that Mauna Loa shield lavas have distinctly lower CaO, TiO_2 and K_2O and higher SiO_2 contents than Kilauea shield lavas. The Mauna Loa high-MgO glasses (Fig. 5) similarly have lower K_2O contents than the Kilauea glasses, but have higher CaO and lower SiO_2 (not shown) than the Kilauea glasses. The trace element ratios (Fig. 3) show that the Mauna Loa glasses also have Sr/Nb and Zr/Nb ratios similar to Kilauea shield lavas and Rb/Sr ratios similar to typical-Mauna Loa. The Kilauea glasses also show contrasting characteristics and have Ce/Yb ratios (Fig. 2) similar to Mauna Loa shield lavas, but have Sr/Nb and Zr/Nb ratios similar to Kilauea lavas. These results imply that a range of primary magmas are delivered to each volcano. These variations may be obscured in typical shield lavas by mixing processes.

The CaO contents of the fractionation corrected high-MgO glass compositions are well correlated with the Ce/Yb ratio (Fig. 5). This correlation indicates that CaO content should decrease as extent of melting increases; i.e. Ca behaves like an incompatible element. This behavior for CaO is the opposite of that observed in experimental studies of spinel lherzolite melting (Kinzler, 1992b). The behavior of CaO during melting of garnet lherzolite is unknown; the CaO contents of experimentally produced melts of garnet lherzolite compiled in Chapter 2 are too heterogeneous to constrain its behavior. Frey and Rhodes (1993) note that Kilauea shield tholeiites have higher CaO and incompatible

element abundances than Mauna Loa shield tholeiites. The strong CaO-Ce/Yb correlation of the high-MgO glasses is consistent with the inference that Kilauea shield tholeiites form by lower mean extents of melting that Mauna Loa shield tholeiites. This interpretation is also supported by the correlations of glass Zr/Nb and Sr/Nb with Ce/Yb ratio (Fig. 4).

Fractionation corrected trace element abundances and the mineralogy of the Kilauea tholeiite source

The variations in REE abundances of the Kilauea glasses can be used to constrain the mineralogy of their source. After correction for olivine fractionation, the Dy and Yb abundances of the Kilauea glasses show less than 8% relative variation, almost within the analytical uncertainty. However, the La and Ce abundances show 25% relative variation that is positively correlated with TiO_2 and K_2O. The REE variations are illustrated in Fig. 6, where the La and C1 normalized REE abundances are plotted against corrected La abundances. The slopes of regression lines through the elements increase with increasing atomic mass of the REE (Fig. 6, Table 3). Since the Yb and Dy abundances do not vary significantly, the La/(Yb or Dy)$_{C1}$ ratio varies dramatically and forms a steeply sloped line. Since Ce covaries with La, the (La/Ce)$_{C1}$ ratio forms a nearly horizontal line.

Variable LREE abundances with nearly constant HREE abundances have been observed and discussed previously (e.g. Shimizu and Arculus, 1975; Frey et al., 1980; Hofmann et al. 1984). The conclusion reached in these studies is that the variations in LREE abundances reflect variations in the degree of melting, while the lack of variation in the HREE abundances reflect their high compatibility in the source due to the presence of residual garnet. These conclusions can be illustrated using equation 15 of Shaw (1970) for batch equilibrium partial melting:

$$C^L/C_O=1/(D_O+F(1-P)), \qquad (1)$$

where C^L is the concentration in the melt, C_O is the initial concentration in the solid, D_O is bulk solid/liquid distribution coefficient, F is the degree of melting and P is the weighted partition coefficient based on the proportion of minerals entering into the liquid. For the HREE to maintain constant concentration under the varying F indicated by the LREE variations, P must approach unity. This reduces equation 1 to $C^L/C_O=1/D_O$ and concentration in the liquid is independent of F. This is also true for Shaw's equation for aggregated fractional melts. Alternatively, if D_O is large compared to F(1-P), as could be the case for low F and elements with moderate to high compatibilities, melting could appear to be independent of F, but this again requires phases with Ds approaching unity. The Ds for the REE in the common mantle minerals olivine, orthopyroxene, clinopyroxene, spinel and plagioclase (noted exception of Eu) are all less than one. For P to equal one, a phase such as garnet with Ds greater than unity for the HREE, must be present. Frey et al. (1980) and Hofmann et al. (1984) have shown that accessory phases with high-Ds for the HREE, such apatite and amphibole, cannot produce the observed variations. We conclude that variations in glass trace element abundances require residual garnet in the glass source. This conclusion is also supported by inversion models for the bulk D of the source, developed in the Inversion Models section below.

Evidence for residual clinopyroxene

The Sm/Sr ratio of the Kilauea glasses is nearly constant while Sm and Sr each show variation in abundance (Fig. 7). Element pairs that maintain constant ratios, while individually showing variation in abundance, have partition coefficients that are either identical or negligibly small for the residual mineralogy of the source (Hofmann et al. 1984). Sr and Sm abundances are not correlated with the highly incompatible elements which implies that the controlling phase must have at least moderately high Ds for Sr and Sm. Olivine and opx have similar Ds for Sr and Sm, but Ds that are too low. The D for Sr in garnet is very low (~0.01) and results in $D^{Sm}/D^{Sr}=111$ (Hauri et al., 1994), which is too

high to buffer the Sm/Sr ratio. Clinopyroxene (cpx) has a D^{Sm} of 0.46 and a D^{Sr} of 0.16, yielding a D^{Sm}/D^{Sr} of ~3 (Hofmann et al, 1984; Hauri et al., 1994). Clinopyroxene, then, is the only phase that could control the Sm/Sr ratio must be in the glass residuum.

The variation in trace element abundances of the high-MgO Kilauea glasses are consistent with derivation by partial melting of source that retained garnet and clinopyroxene. We now use inversion modeling to constrain the trace element abundances and bulk distribution coefficients of this source.

INVERSION MODELS

Source trace element abundances

The Kilauea glass data were inverted to constrain their source abundances and partition coefficients relative to La using the techniques of Minster and Allegre (1978), as simplified by Hofmann and Feigenson (1983). Corrected data were plotted on a process identification diagram similar to that of Treuil and Joron (1975) using La as the highly incompatible element (Fig. 6). Rb is a better choice from the point of incompatibility, but the analytical uncertainties are higher. Interelement diagrams similar to those of Hanson (1989) identified La as the most incompatible element of the remaining choices. Samples related through partial melting should form linear trends in Fig. 6 (Treuil and Joron 1975; Minster and Allegre 1978), and the Kilauea glass data satisfies this criterion. The y-intercept of the each element's regression line (Fig. 6, Table 3) determines its abundance in the source relative to La, using equation (7') of Hofmann and Feigenson (1983):

$$C^i_o/C^H_o=(1-P^i)/I^i, \qquad (2)$$

where C_o is the source concentration of the element (i denotes the element of interest; H denotes the highly incompatible element, which is La in this case), P is the weighted partition coefficient of the melting reaction and I is the y-intercept value of the regression

line for the element of interest. I is a near zero value for the HREE regression lines, and this result greatly magnifies uncertainties in the determined values of P. Hofmann et al. (1984) solved for P iteratively by assuming the source had a smooth pattern for the HREE, and then solved for the melt reaction from P assuming 1) only cpx and garnet are involved in the melt reaction and 2) the reaction involves the maximum amount of cpx consistent with the P. Assumption 1 is valid because the Ds for olivine/liquid and orthopyroxene/liquid are low enough that their addition to either side of the melting reaction has little effect on the inversion results. Assumption 2 is also valid because the inversion results are relatively insensitive to large variations in the melting reaction. Hofmann et al. calculate that cpx and garnet enter the melt in a ratio of 81:19.

The uncertainties on our I values for Dy and Yb preclude our solving for P using this same technique. Instead, we used the Hofmann et al. melt reaction to get an initial estimate of the source abundances. The light and middle REE form a smooth, flat pattern at ~1, similar to the pattern shown in Fig. 8. If we assume that the relatively flat pattern of the LREE supports a flat overall source pattern, we can assume that the source has $C^{Yb}_o/C^{La}_o=1$. Calculation of P from eq. 2 using I=-0.017 yields a P value of 1.017. Using the same assumptions as Hofmann et al, this value of P constrains the melt reaction to 85.23cpx:14.77garnet. The inversion results plotted in Fig. 7 use this melt reaction. The inversion results indicate that the Kilauea source is nearly chondritic, similar to the results of other inversion studies of Kilauean lavas (e.g. Hofmann et al., 1984).

Recent experimental studies indicate that melting of garnet lherzolite involves a reaction relationship of garnet+cpx+olivine melting to produce opx+liquid (Herzberg et al. 1990; Kinzler 1992c). In the garnet lherzolite melting reaction of Kinzler (1992c):

$$0.19\text{olivine} + 0.68\text{cpx} + 0.63\text{garnet} = 1.0\text{liquid} + 0.50\text{opx}$$

cpx and garnet enter the melt in nearly equal proportions. This reaction was determined near the spinel to garnet transition. The much higher cpx/garnet ratio entering the melt estimated in the inversion could reflect the effect of increasing pressure on the mantle

melting reaction. Increasing pressure could increase the stability of garnet and lower the proportion of it entering the melt.

The element pairs in the glasses that show variation in abundance, but constant ratios give the source ratio. There are slight differences between these values and those of the inversion. The Nd/Zr ratio of the inverted source is 1.1*C1, similar to the 1.2*C1 value of the glasses. The Sm/Sr of the inverted source is 1.1*C1, higher than the 0.9*C1 value of the glasses. The Nb/La ratios show the most significant differences: 0.8*C1 for the inverted source and 1.1*C1 in the glasses. The uncertainties on the inversion for Nb are very high and the value from the glasses is likely more correct. Isotopic data can also be used to constrain the relative abundances of the source. Nd isotopic data from Hawaiian volcanics (e.g. DePaolo and Wasserburg, 1976; O'Nions et al., 1977; Chen and Frey, 1985) and specifically from Kilauea tholeiites (e.g. Hofmann et al. 1984; Stille et al. 1986) reflect derivation from sources with a time averaged Sm/Nd ratio greater than the chondritic value, indicating a LREE depleted source. The results of our and other inversions of the REE abundances of Hawaiian lavas (e.g. Albarede 1983; Feigenson et al. 1983; Hofmann et al. 1984) conclude that the sources have flat to slightly LREE enriched REE patterns relative to C1, inconsistent with the isotopic data. This has generally been interpreted to mean that the source has recently been enriched in highly incompatible elements.

Source bulk distribution coefficients

The La-normalized distribution coefficients were calculated using equation (10) of Hofmann and Feigenson (1983):

$$D^i_o/C^H_o=S^i(1-P^i)/I^i, \qquad (3)$$

where D^i_o is the bulk partition coefficient for element i in the source and S^i is the slope the regression line from Fig. 6 (other variables as for equation 1). The results of the inversions (Fig. 8) show a distinct increase in D^{Dy} and D^{Yb} relative to the other elements. The uncertainties on this inversion are greater than the small spikes displayed by adjacent elements, e.g. $D^{Dy}>D^{Yb}$ and $D^{Eu}<D^{Sm}$, but smaller than the large increase in source D^{Dy} and D^{Yb}. The higher Ds for the HREE are consistent with the interpretation that garnet is a residual phase in the glass source.

The trace element abundance variations of the high-MgO Kilauea glasses thus support their derivation from a garnet lherzolite source, identical to the inferred source for the Kilauea shield lavas (e.g. Hofmann et al., 1984; Budahn and Schmitt, 1985). The phase equilibria experiments of Chapter 2 show that the glass-based primary magma estimate is not in equilibrium with garnet lherzolite at any pressure, but is in equilibrium with harzburgite at lithospheric depths. Chapter 2 proposes that the contradiction between results of the geochemical and experimental studies supports a model for the formation of Hawaiian tholeiite wherein melts of garnet lherzolite from deep parts of the plume react and equilibrate with harzburgite in the plume top. We now explore the effect of this reaction on trace element abundances.

Effect of harzburgite equilibration on trace element abundances

The equilibration of melts of garnet lherzolite with harzburgite involves assimilation of opx and crystallization olivine. The Ds for the HREE in opx approach 0.1, and opx assimilation may fractionate the HREE relative to the LREE. The effect of the equilibration reaction on melt REE abundances was calculated using the AFC equations of DePaolo (1981), where mass assimilated is greater than the mass crystallized. For simplicity, we used the trace element abundances of 57-13 as an initial melt of garnet

lherzolite. This is clearly not correct since we propose in Chapter 2 that the glasses come from primary magmas that have already undergone harzburgite equilibration. This exercise is simply a means of exploring the effect of the equilibration reaction on trace element abundances.

Models were calculated for the three separate reactions modeled in Table 5-Chapter 2, based on three different primary magma estimates. The final liquid after reaction is listed under the Models section of Table 4. The Δ in Table 4 reports the percentage change between the initial liquid, 57-13, and the final liquid for each individual model. Olivine is the only crystallizing phase during reaction, Ds in Table 4). The trace element abundances of the opx assimilant are critical to determining the relative fractionation of HREE relative to the LREE, so two endmember cases for opx were used. The first model, *Depleted opx assimilant* (Table 4), uses an opx produced by 30% melting of garnet lherzolite assuming a slightly depleted, but near chondritic source using the melt reaction of Kinzler (1992c). The second model, *Enriched opx assimilant* (Table 4), uses an opx that is in equilibrium with 57-13 using the opx Ds in Table 4. F in Table 4 denotes the percentage of magma mass increase during the equilibration reaction. It was calculated by normalizing the proportions of reactants in Table 5-Chapter 2 to the amount of initial liquid, F equal to the new proportion of final liquid. Ma/Mc in Table 4 denotes the ratio of mass assimilated to mass crystallized. These values were also calculated using the proportions of reactants in Table 5-Chapter 2, normalized to the amount of initial liquid.

Results

The REE abundances of the liquid are generally diluted by reaction. The dilutions of LREE abundances are independent of the opx composition, while the HREE abundances are slightly less diluted during assimilation of the enriched opx. This effect, however, is small enough that it is difficult to display graphically. When the depleted opx composition is used for the assimilant, the LREE and HREE abundances are diluted in almost identical proportions: Yb is diluted at 0.96-0.98 times La. The fraction of dilution

is similar to the fraction of magma mass increase. When the enriched opx composition is used, the ratio of LREE to HREE dilution is a function of the Ma/Mc ratio. When the Ma/Mc=1.4, Yb is diluted at 0.72 times La. When the Ma/Mc=2.7, Yb is diluted at 0.87 times La. Thus, assimilation of the enriched opx will have a slight flattening effect on the REE pattern and slightly decrease the La/Yb ratio. A. W. Hofmann (pers. comm.) has reported that HREE abundances from different Hawaiian volcanoes show ±3% variation when corrected for olivine fractionation. The melt reactions required to produce the high and low-Fe extreme parents of Clague et al. (1995) have ratios of Ma/Mc that differ by a factor of 2. These large differences in reaction produce a 4% difference in post-reaction abundance of Yb. This would produce overall variation of ±2%, similar to the amount of variation observed by Hofmann.

CONCLUSIONS

Picritic glass grains from Hawaiian volcanoes have trace element abundances and ratios similar to more abundant shield lavas. This similarity supports the generation of picritic glasses from the same sources and by the same mechanisms that produce more typical Hawaiian tholeiite. These glasses can thus be used to estimate the composition of Hawaiian primary magmas. The Kilauea and Mauna Loa glasses show that liquids with a variety of overlapping chemical characteristics are delivered to both volcanoes. The correlation of the glasses' fractionation corrected CaO contents with their Ce/Yb ratio supports the inference that Kilauea shield lavas are produced by lower mean extents of melting than Mauna Loa shield lavas (Frey and Rhodes, 1993). The variations in trace element abundances of the Kilauea glasses indicate that their source contained garnet and clinopyroxene. A tholeiite primary magma estimate based on the Kilauea glasses does not show liquidus saturation with a peridotitic residue containing garnet and cpx (Chapter 2), but does show saturation with harzburgite. Chapter 2 proposes that this contradiction

reflects equilibration of melts of garnet lherzolite from deeper regions of the plume with harzburgite in the plume top. The effect of the equilibration reaction is to dilute most trace element abundances. HREE abundances will be diluted slightly less than the LREE, resulting in a slight flattening of the overall REE pattern. The magnitude of this effect is dependent on the concentration of trace elements in the assimilated opx.

Figure Captions

Figure 1. Comparison of Kilauea glass trace element abundances to published Kilauea and Mauna Loa abundances. Glass data from Table 1. Abundances normalized to C1 of Anders and Grevesse (1989). Data for Kilauea and Mauna Loa fields as follows: Kilauea field from BVSP (1981); Hofmann et al. (1984); Mauna Loa field from BVSP (1981); Budahn and Schmitt (1985).

Figure 2. Ratios of REE showing differences between Kilauea and Mauna Loa. Glass data from Table 1. 1 sigma error bars, 14% relative. Error bars are left off all glasses except Mauna Loa in the interest of clarity. References as in Fig. 1.

Figure 3. Trace element ratios plotted against MgO in wt.%. Data for ratios from Table 1. MgO in wt.%, also reported in Table 1. Data for Kilauea and Mauna Loa as in Fig. 1 except for Kilauea/Mauna Loa dividing lines which are approximated from Frey and Rhodes (1993). 1 sigma error bars.

Figure 4. Trace element ratios plotted against Ce/Yb ratio. 1 sigma error bars.

Figure 5. Major element abundances corrected for olivine fractionation plotted against Ce/Yb ratio. 1 sigma error bars.

Figure 6. Process identification diagram similar to that of Treuil and Joron (1975). La (horizontal axis) corrected for olivine fractionation. Vertical axis normalized to C1 of Anders and Grevesse (1989). 1 sigma error bars.

Figure 7. Sm/Sr plotted against fractionation corrected Sr abundance in ppm for high-MgO Kilauea glasses. Error bars are 5% based on uncertainty in ion probe analyses.

Figure 8. La-normalized source concentrations and bulk distribution coefficients after inversion using the equations of Hofmann and Feigenson (1983). Vertical axis shows concentrations in mantle source normalized to source concentration of La and C1 chondrite. Solid line shows best value based on inversion. Dashed lines are maximum and minimum values based on uncertainties in regression coefficients (Table 3). Dy is not plotted because inversion equations became undefined for uncertainty in regression coefficients.

Footnotes to Tables

Table 1. Rare earth element and other trace element abundances. MgO in wt.% from Clague et al (1995). All other elemental abundances in parts per million.

Table 2. Major element abundances corrected to be in equilibrium with $Fo_{90.7}$ olivine. Original analyses reported in Clague et al (1995). Olivine was added in 0.25 weight % increments, details in the text. Dilution factor equals 0.9975^N, where N is the "No. Steps" of olivine addition.

Table 3. Linear regressions for lines in Fig. 6. r^2 is sum of the squared residuals.

Table 4. All trace element abundances normalized to C1-chondrite of Anders and Grevesse (1989). F, Ma and Mc as defined in DePaolo (1981).

REFERENCES

Albarede F (1983). Inversion of the batch melting equations and the trace element pattern of the mantle. J Geophys Res 88: 10573-10583

Anders E, Grevesse N (1989). Abundances of the elements: Meteoritic and solar. Geochim Cosmochim Acta 53: 197-214

Budahn JR, Schmitt RA (1985). Petrogenetic modeling of Hawaiian tholeiitic basalts: A geochemical approach. Geochim Cosmochim Acta 49: 67-87

BVSP (1981). Basaltic volcanism on the terrestrial planets. New York, Pergamon Press, Inc.

Chen C, Frey FA (1985). Trace element and isotopic geochemistry of lavas from Haleakala volcano, East Maui, Hawaii: implications for the origin of Hawaiian basalts. J Geophys Res 90(B10): 8743-8768

Clague DA, Dalrymple GB (1987). The Hawaiian-Emperor volcanic chain Part I Geologic evolution. Volcanism in Hawaii, Volume 1, Professional Paper 1350 Eds. R. W. Decker, T. L. Wright and P. H. Stauffer. Denver, U.S. Geological Survey. 5-54

Clague DA, Moore JG, Dixon JE, Friesen WB (in press 1995). Petrology of submarine lavas from Kilauea's Puna Ridge, Hawaii. J Petrol

Clague DA, Weber WS, Dixon JE (1991). Picritic glasses from Hawaii. Nature 353: 553-556

DePaolo DJ (1981). Earth Plan Sci Lett 53: 189-202

DePaolo DJ, Wasserburg GJ (1976). Inferences about magma sources and mantle structure from variations of $^{143}Nd/^{144}Nd$. Geophys Res Lett 3: 743-746

Feigenson MD, Hofmann AW, Spera FJ (1983). Case studies on the origin of basalt II. The transition from tholeiitic to alkalic volcanism on Kohala volcano, Hawaii. Contrib Mineral Petrol 84: 390-405

Frey FA (1991). Mantle yields its secrets. Nature 353: 500

Frey FA, Rhodes JM (1993). Intershield geochemical differences among Hawaiian volcanoes: implications for source compositions, melting processes and magma ascent paths. Phil. Trans. R. Soc. Lond. 342: 121-136

Frey FA, Roden MF, Zindler A (1980). Constraints on mantle source compositions imposed by phosphorous and the rare-earth elements. Contrib Mineral Petrol 75: 165-173

Grove TL, Kinzler RJ, Bryan WB (1992). Fractionation of mid-ocean ridge basalt (MORB). Mantle flow and melt generation at mid-ocean ridges Eds. J. Phipps Morgan, D. K. Blackman and J. M. Sinton. Washington, D.C., American Geophysical Union. 361

Hanson GN (1989). An approach to trace element modeling using a simple igneous system as an example. Geochemistry and mineralogy of the rare earth elements Eds. B. R. Lipin and G. A. McKay. Washington, D.C., Mineralogical Society of America. 79-97

Hauri EH, Wagner TP, Grove TL (1994). Expermental and natural partitioning of Th, U, Pb and other trace elements between garnet, clinopyroxene and basaltic melts. Chemical Geology 117: 149-166

Helz RT (1987). Differentiation behavior of Kilauea Iki lava lake, Kilauea Volcano, Hawaii. Magmatic Processes: Physiochemical Principles Ed. B. O. Mysen. The Geochemical Society. 241-258

Helz RT, Thornber CR (1987). Geothermometry of Kilauea Iki lava lake, Hawaii. Bulletin of Volcanology 49: 651-668

Herzberg CT, Gasparik T, Sawamoto H (1990). Origin of mantle peridotite: constraints from melting experiments to 16.5 GPa. J Geophys Res 95(B10): 15779-15803

Hofmann AW, Feigenson MD (1983). Case studies on the origin of basalt I. Theory and reassessment of the Grenada basalts. Contrib Mineral Petrol 84: 382-389

Hofmann AW, Feigenson MD, Raczek I (1984). Case studies in the origin of basalt: III. Petrogenesis of the Mauna Ulu eruption, Kilauea, 1969-1971. Contrib Mineral Petrol 88: 24-35

Kinzler RJ (1992c). Mantle melting processes at the spinel-garnet transition (17-21Kb). EOS Trans. AGU 73(43): 615

Kinzler RJ, Grove TL (1992b). Primary magmas of mid-ocean ridge basalts 2. applications. J Geophys Res 97(B5): 6907-6926

Kinzler RJ, Grove TL (1993). Corrections and further discussion of the primary magmas of mid-ocean ridge basalts, 1 and 2. J Geophys Res 98(B12): 22339-22347

Langmuir CH, Klein EM, Plank T (1992). Petrological systematics of mid-ocean ridge basalts: constraints on melt generation beneath ocean ridges. Mantle flow and melt generation at mid-ocean ridges Eds. J. Phipps-Morgan, D. K. Blackman and J. M. Sinton. Washington, D.C., American Geophysical Union. 183-280

McDonough WF (in prep). Mantle plume dynamics in Hawaii.

Minster JF, Allegre CJ (1978). Systematic use of trace elements in igneous processes. Part III: Inverse problem of batch partial melting in volcanic suites. Contrib Mineral Petrol 68: 37-52

Moore et al. (1990). Subsidence and volcanism of the Haleakala Ridge, Hawaii. Journal of Volcanology and Geothermal Research 42: 273-284

Moore JG (1965). Petrology of deep-sea basalt near Hawaii. American Journal of Science 263: 40-52

Newsom HE (1986). Oceanic Basalts. Earth Plan Sci Lett 80: 299

O'Nions RK, Hamilton PJ, Evensen NM (1977). Variations in 143Nd/144Nd and 87Sr/86Sr ratios in oceanic basalts. Earth Plan Sci Lett 34: 13-22

Roeder PL, Emslie RF (1970). Olivine liquid equilibrium. Contrib Mineral Petrol 29: 275-289

Shaw DM (1970). Trace element fractionation during anatexis. Geochim Cosmochim Acta 34: 237-243

Shimizu N, Arculus RJ (1975). Rare earth element concentrations in a suite of basanitoids and alkali olivine basalts from Grenada, Lesser Antilles. Contrib Mineral Petrol 50: 231-240

Shimizu N, Hart SR (1982). Applications of the ion microprobe to geochemistry and cosmochemistry. Ann Rev Earth Plan Sci 10: 483-526

Stille P, Unruh DM, Tatsumoto M (1986). Pb, Sr, Nd, and Hf isotopic constraints on the origin of Hawaiian basalts and evidence for a unique mantle source. Geochim Cosmochim Acta 50: 2303-2319

Sun SS, McDonough WF (1989). Chemical and isotopic systematics of oceanic basalts: Implications for mantle composition and processes. Magmatism in ocean basins Eds. A. J. Saunders and M. J. Norry. London, Geologic Society Special Publications. 313-345

Treuil M, Joron JL (1975). Utilisation des elements hygromagmatophiles pour la simplification de la modelisation quantitative des processes magmatiques. Exemples de l'Afar de la dorsale medio-Atlantique. Soc Italiana Minerel Petrol 31: 125-174

Figure 1

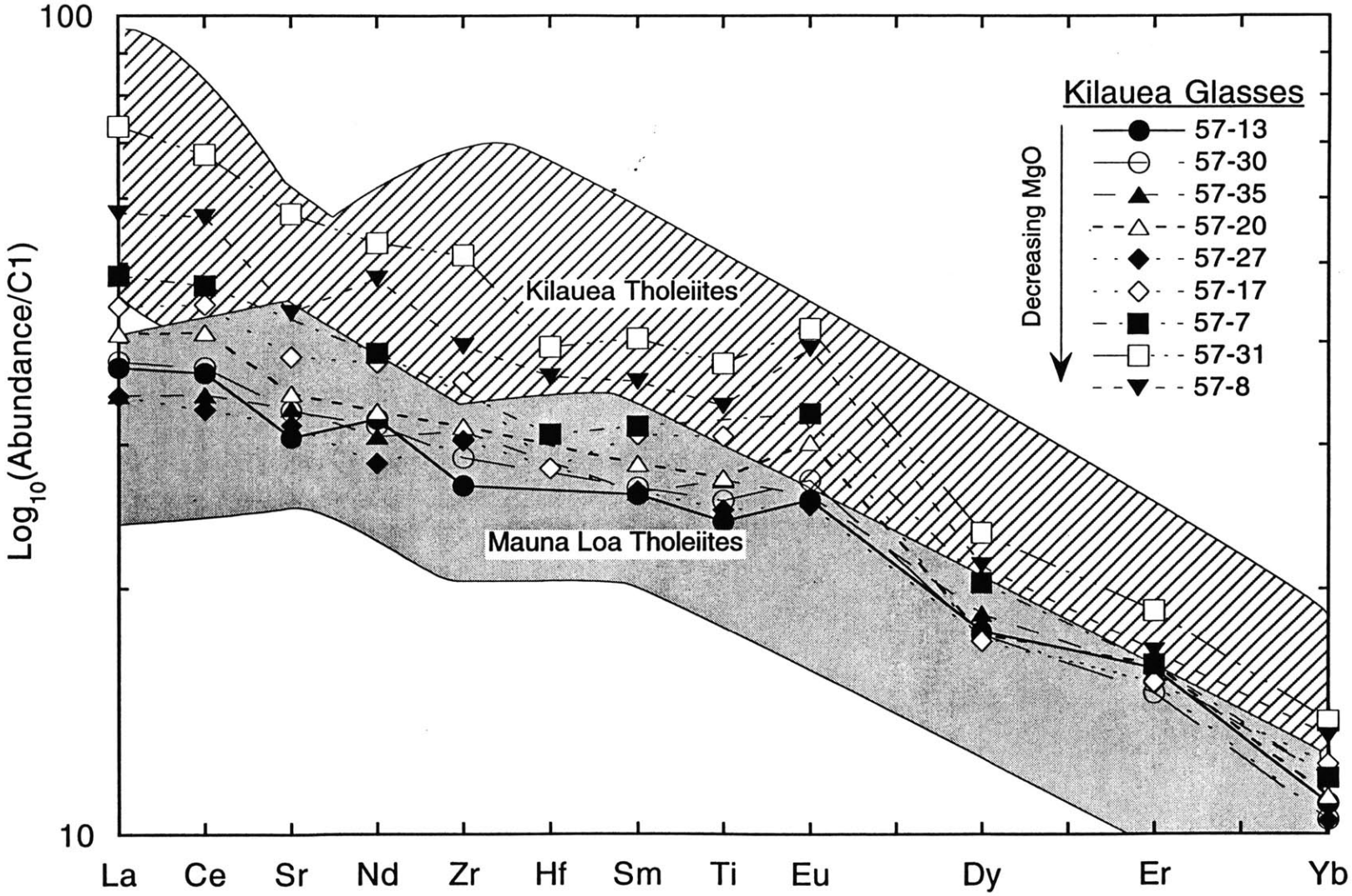
100
10
Log_{10}(Abundance/C1)
La
Ce
Sr
Nd
Zr
Hf
Sm
Ti
Eu
Dy
Er
Yb
Kilauea Tholeiites
Mauna Loa Tholeiites
Kilauea Glasses
57-13
57-30
57-35
57-20
57-27
57-17
57-7
57-31
57-8
Decreasing MgO

Figure 2

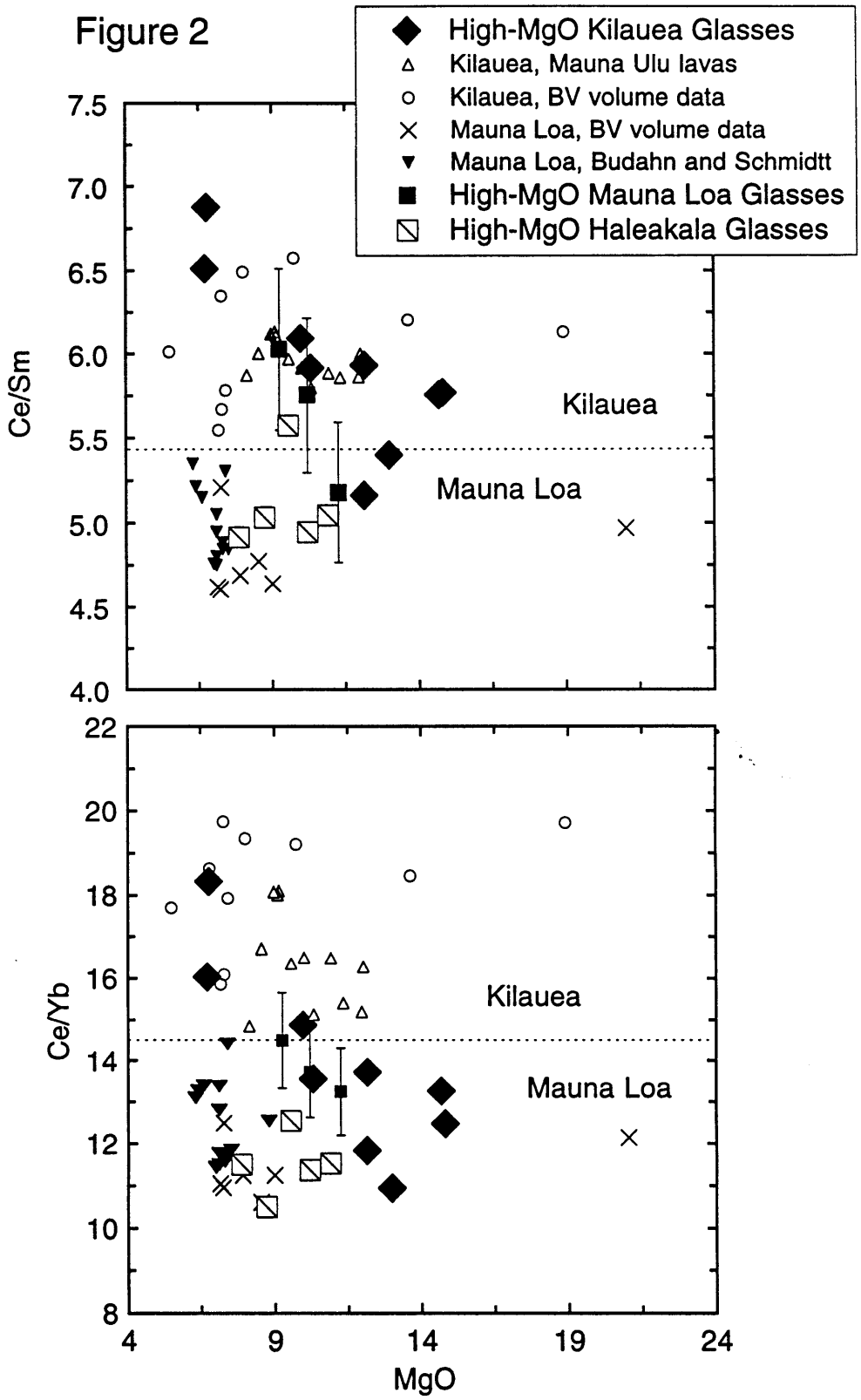
High-MgO Kilauea Glasses
Kilauea, Mauna Ulu lavas
Kilauea, BV volume data
Mauna Loa, BV volume data
Mauna Loa, Budahn and Schmidtt
High-MgO Mauna Loa Glasses
High-MgO Haleakala Glasses
Ce/Sm
7.5
7.0
6.5
6.0
5.5
5.0
4.5
4.0
Kilauea
Mauna Loa
Ce/Yb
22
20
18
16
14
12
10
8
Kilauea
Mauna Loa
4
9
14
19
24
MgO

Figure 3

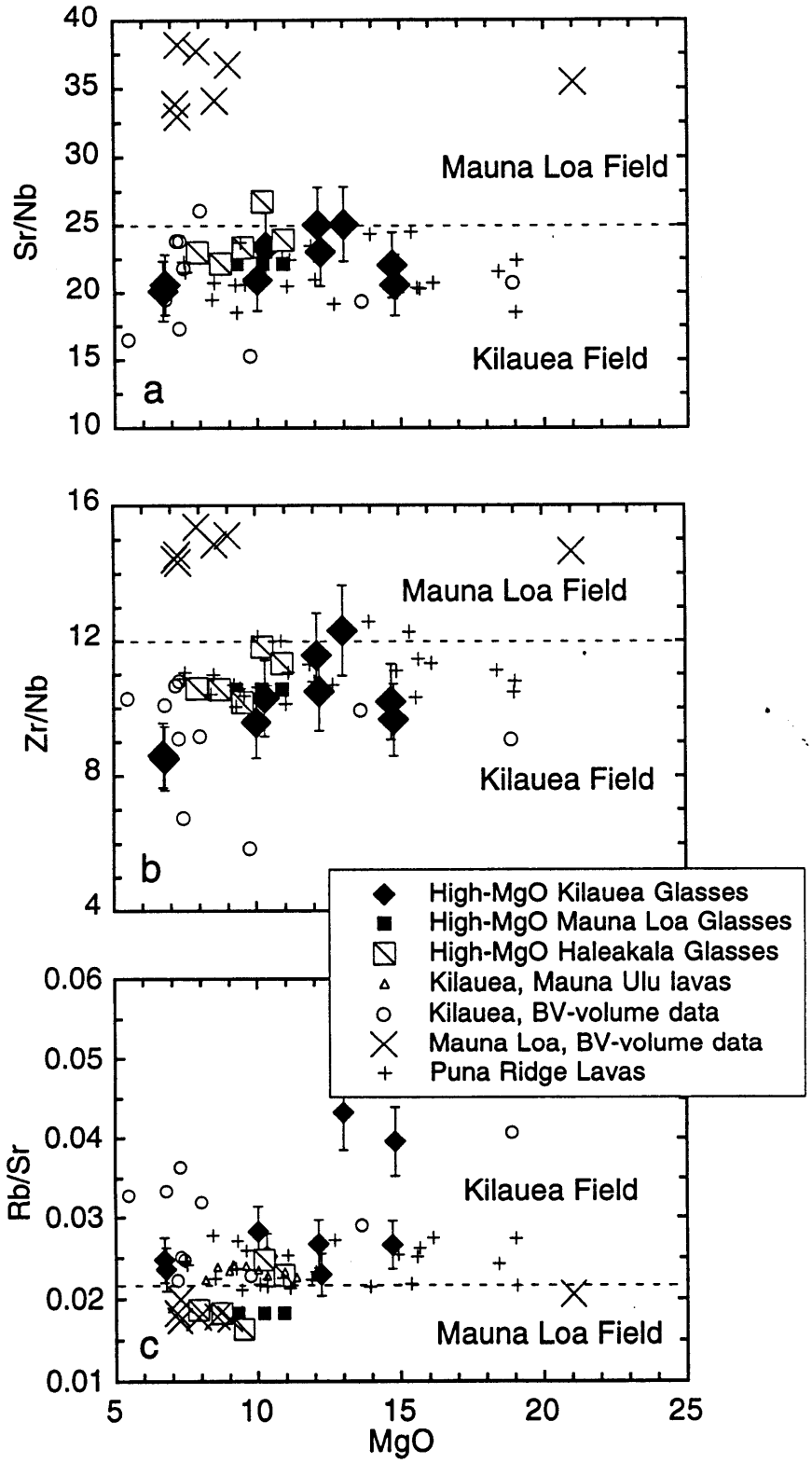
Sr/Nb
Mauna Loa Field
Kilauea Field
a
Zr/Nb
Mauna Loa Field
Kilauea Field
b
Rb/Sr
Kilauea Field
Mauna Loa Field
c
MgO
High-MgO Kilauea Glasses
High-MgO Mauna Loa Glasses
High-MgO Haleakala Glasses
Kilauea, Mauna Ulu lavas
Kilauea, BV-volume data
Mauna Loa, BV-volume data
Puna Ridge Lavas

Figure 4

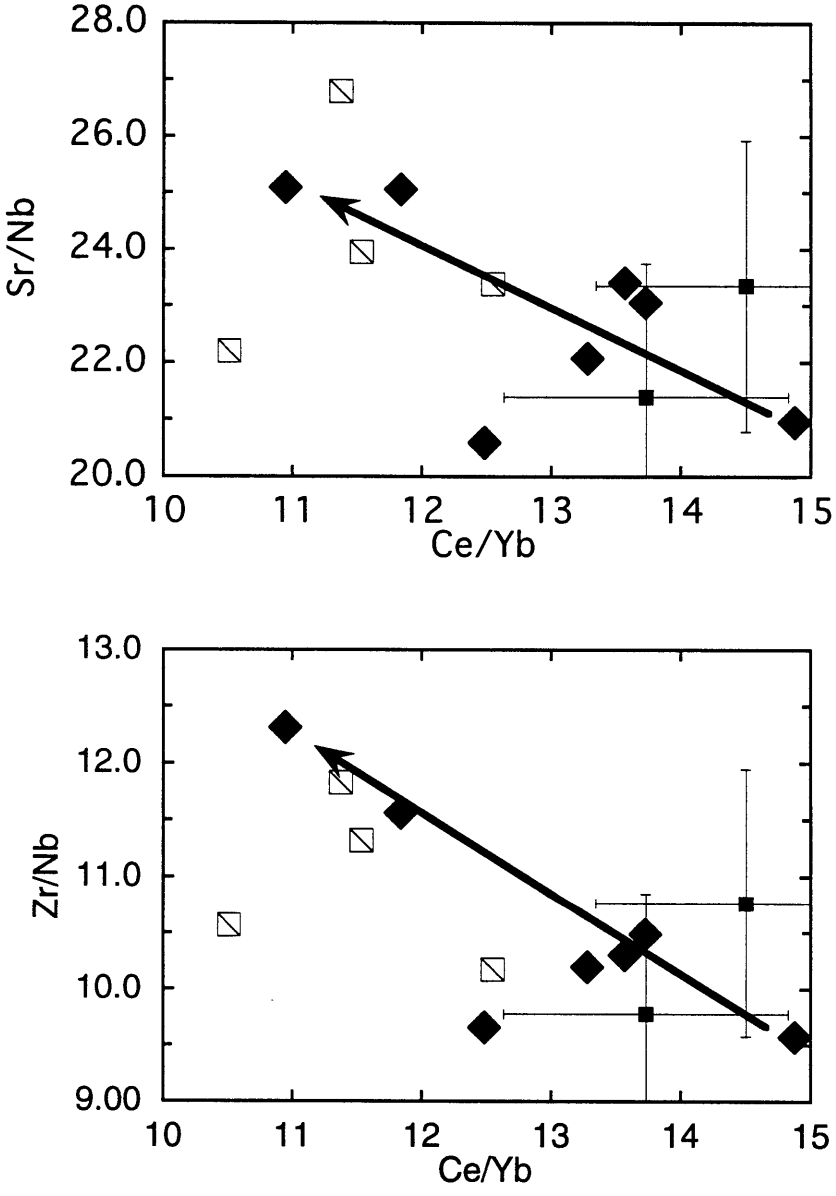
28.0
26.0
24.0
22.0
20.0
Sr/Nb
10
11
12
13
14
15
Ce/Yb
13.0
12.0
11.0
10.0
9.00
Zr/Nb
10
11
12
13
14
15
Ce/Yb

Figure 5

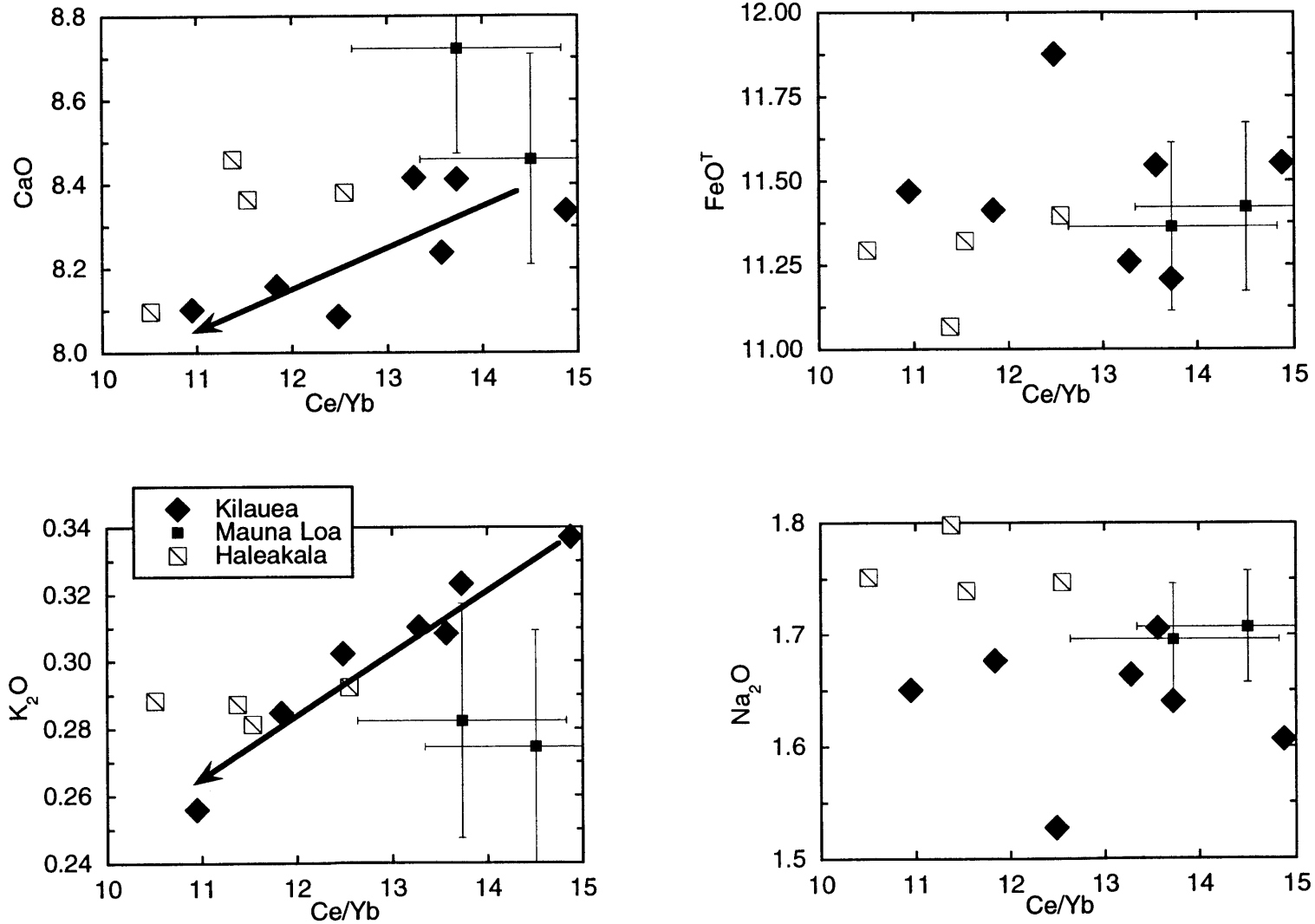
CaO
8.8
8.6
8.4
8.2
8.0
10
11
12
13
14
15
Ce/Yb
FeO^T
12.00
11.75
11.50
11.25
11.00
Ce/Yb
Kilauea
Mauna Loa
Haleakala
K_2O
0.34
0.32
0.30
0.28
0.26
0.24
Ce/Yb
Na_2O
1.8
1.7
1.6
1.5
Ce/Yb

Figure 6

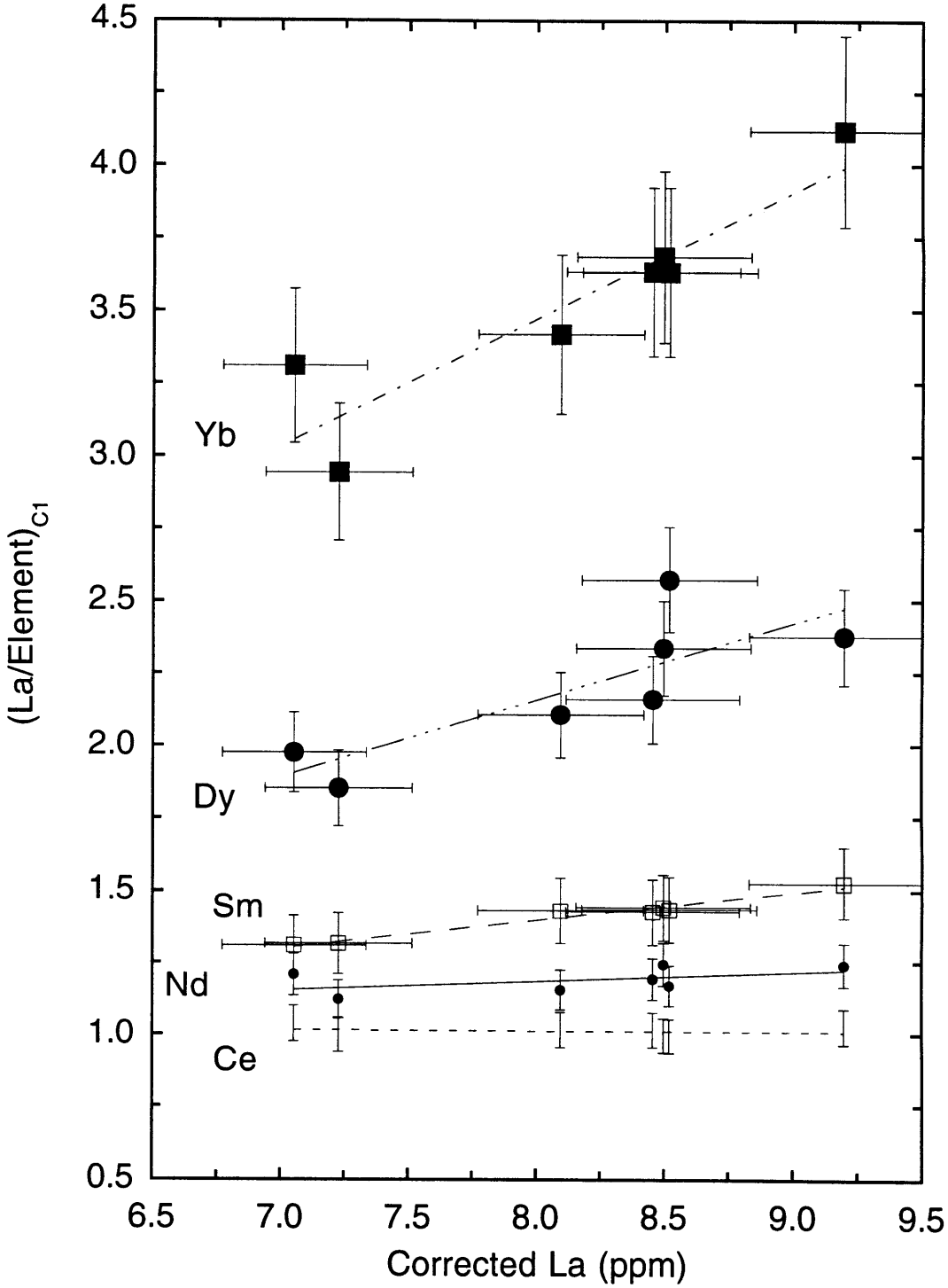
4.5
4.0
3.5
3.0
2.5
2.0
1.5
1.0
0.5
(La/Element)C1
Yb
Dy
Sm
Nd
Ce
6.5
7.0
7.5
8.0
8.5
9.0
9.5
Corrected La (ppm)

Figure 7

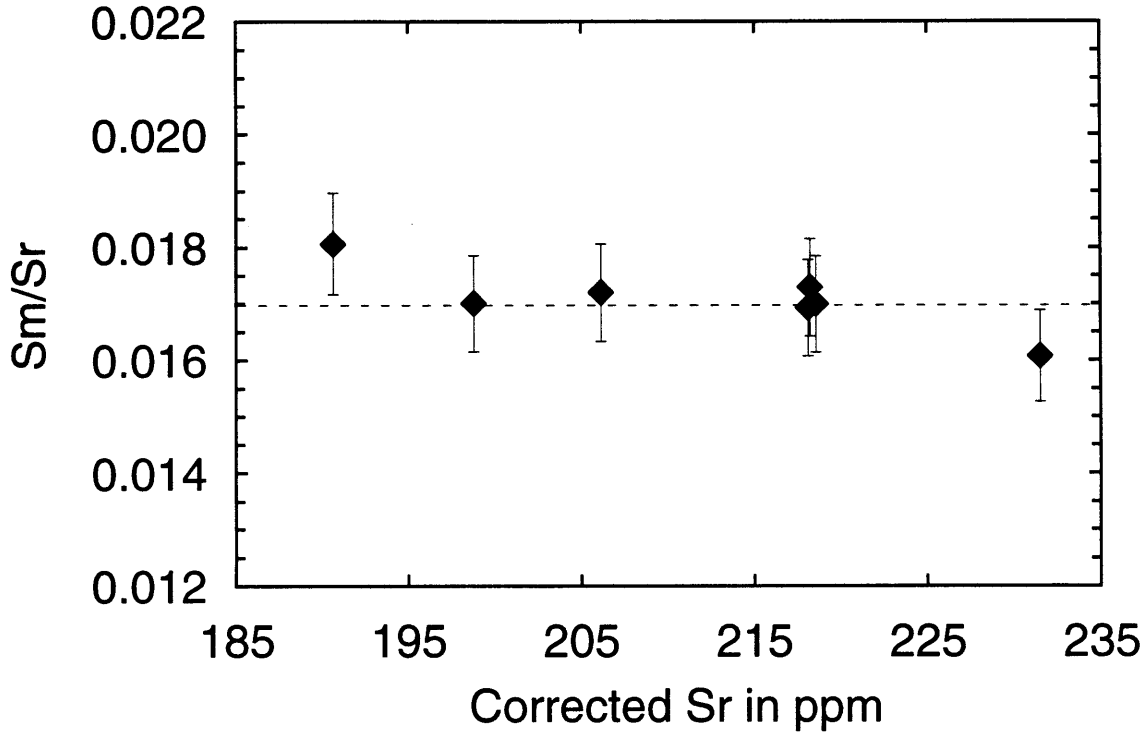
0.022
0.020
0.018
0.016
0.014
0.012
Sm/Sr
185
195
205
215
225
235
Corrected Sr in ppm

Figure 8

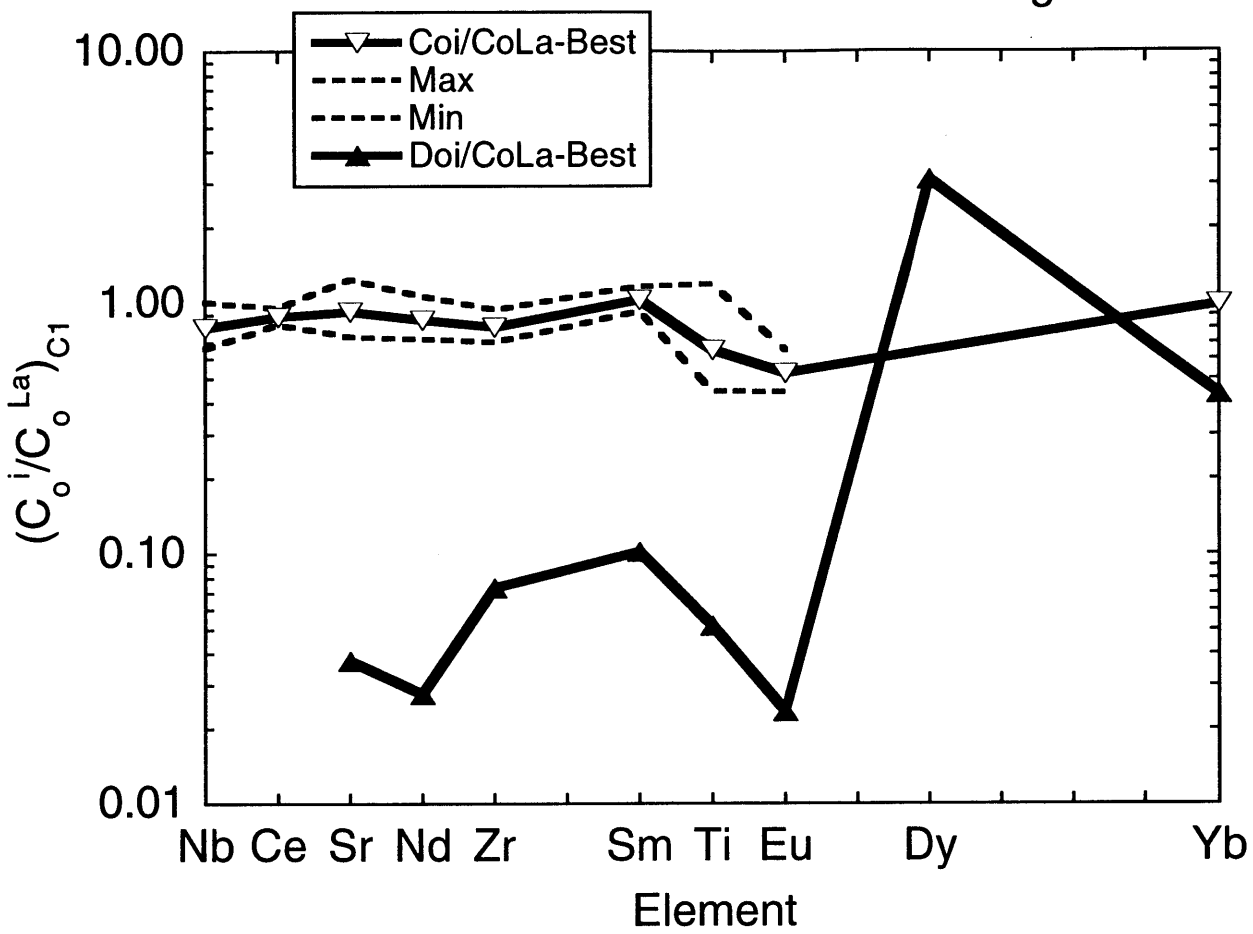
Coi/CoLa-Best
Max
Min
Doi/CoLa-Best
10.00
1.00
0.10
0.01
$(C_o^i/C_o^{La})_{C1}$
Nb Ce Sr Nd Zr Sm Ti Eu Dy Yb
Element

Table 1. Trace element abundances of high-MgO glasses from various Hawaiian volcanoes.

Sam. #	MgO	La	Ce	Nd	Sm	Eu	Dy	Er	Yb	Rb	Nb	Sr	Zr	Hf	Ti	Sc	V	Cr
Kilauea Glasses																		
57-13	14.8	8.7	22.1	14.6	3.8	1.43	4.3	2.5	1.77	8.81	10.8	223	105	-	10997	26.1	214	1235
57-30	14.7	8.9	22.5	14.4	3.9	1.52	4.3	2.37	1.7	6.12	10.4	230	106	-	11128	26.1	216	1163
57-35	13.0	8.1	20.8	13.9	3.9	1.5	4.5	2.5	1.9	9.23	8.5	213	105	-	11172	25.7	213	970
57-20	12.2	9.6	24.8	14.9	4.2	1.7	4.3	2.6	1.81	5.68	10.7	247	112	-	11726	25.7	234	924
57-27	12.1	8.1	20.0	12.9	3.9	1.41	4.2	2.4	1.69	6.08	9.1	228	105	-	11076	25.8	214	857
57-17	10.3	10.4	26.8	17.1	4.5	1.8	4.2	2.4	2.0	7.12	12.1	282	124	2.9	14185	27.4	276	731
57-7	10.0	11.3	28.3	17.6	4.6	1.8	4.9	2.6	1.9	7.60	12.8	269	123	3.2	13171	27.7	248	621
57-31	6.77	17.2	40.9	23.9	5.9	2.32	5.7	3.0	2.23	10.31	21.2	436	180	4.1	17651	31.3	314	331
57-8	6.71	13.5	34.3	21.7	5.3	2.20	5.17	2.7	2.14	8.17	16.4	330	141	3.8	15671	27.5	270	265
Mauna Loa Glasses																		
S6/T5	10.2	8.1	21.1	12.8	3.7	1.34	3.43	1.98	1.54	6.13	12.3	263	120	-	12534	28.3	236	620
T-22	9.25	8.5	22.2	13.5	3.7	1.32	3.57	1.77	1.53	6.02	10.4	243	112	-	11554	25.7	223	460
T-21	10.90	-	-	-	-	-	-	-	-	5.68	8.1	271	110	-	10855	25.1	235	368
T16	11.3	8.1	20.0	14.2	3.9	1.52	3.21	1.92	1.51	-	-	-	-	-	-	-	-	-
Haleakala Glasses																		
3a	10.2	8.2	20.6	14.7	4.2	1.54	4.08	2.08	1.81	6.39	9.6	258	114	-	12153	27.0	242	638
3b	10.9	7.7	19.3	14.1	3.8	1.32	3.60	2.23	1.67	5.68	10.3	248	117	-	12589	27.5	249	719
1	8.73	8.0	19.3	14.1	3.8	1.55	3.79	2.02	1.84	4.97	12.2	271	129	-	13445	27.7	260	450
9	9.5	8.3	20.9	13.7	3.8	1.42	3.55	2.13	1.67	4.26	11.1	259	113	-	12017	27.7	238	523
11	7.86	9.5	24.2	17.3	4.9	1.91	4.54	2.50	2.10	6.39	14.8	340	157	-	15879	29.0	267	326

Table 2. Major elements corrected to be in equilibrium with $Fo_{90.7}$ olivine.

Sam #	No. Steps	% Dilution	SiO_2	Al_2O_3	TiO_2	FeO^T	P_2O_5	MgO	CaO	Na_2O	K_2O
Kilauea Glasses											
57-13	31	0.925	48.5	10.3	1.77	11.8	0.18	17.6	8.09	1.53	0.30
57-30	20	0.951	49.0	10.6	1.89	11.2	0.18	16.7	8.42	1.67	0.31
57-35	45	0.893	48.9	10.8	1.74	11.4	0.17	17.0	8.11	1.65	0.26
57-20	50	0.882	49.0	10.9	1.83	11.1	0.20	16.6	8.42	1.64	0.32
57-27	54	0.874	49.2	10.6	1.71	11.3	0.16	16.9	8.17	1.68	0.29
57-17	79	0.821	48.6	10.5	1.91	11.4	0.20	17.1	8.26	1.71	0.31
57-7	83	0.812	48.6	10.5	1.89	11.4	0.16	17.1	8.36	1.61	0.34
Mauna Loa Glasses											
S6	82	0.814	48.5	10.3	1.85	11.4	0.18	17.2	8.72	1.70	0.28
22	94	0.790	48.6	10.3	1.75	11.4	0.20	17.3	8.46	1.71	0.27
21	77	0.825	48.5	10.3	1.81	11.5	0.20	17.4	8.33	1.64	0.29
Haleakala Glasses											
3a	75	0.829	48.7	11.0	1.80	11.1	0.16	16.7	8.46	1.80	0.29
3b	72	0.835	48.7	10.5	1.81	11.3	0.17	17.1	8.36	1.74	0.28
1	97	0.784	48.8	10.6	1.81	11.3	0.19	17.2	8.10	1.75	0.29
9	90	0.798	48.6	10.4	1.77	11.4	0.17	17.2	8.38	1.75	0.29
11	113	0.754	46.6	11.0	2.00	11.6	0.20	17.6	8.60	2.07	0.33

Table 3. Linear regression results for Kilauea high-MgO glasses.

Regression Line	Slope	Std. error	Intercept	Std. error	r^2
Ce	-0.003	0.010	1.038	0.080	0.020
Nd	0.032	0.022	0.930	0.182	0.294
Sm	0.099	0.008	0.606	0.069	0.965
Dy	0.266	0.084	0.029	0.689	0.666
Yb	0.436	0.086	-0.017	0.705	0.837
Nb	-0.039	0.032	1.234	0.259	0.271
Sr	0.040	0.030	0.935	0.241	0.310
Zr	0.091	0.012	0.647	0.095	0.936
Ti	0.079	0.045	0.791	0.360	0.438

Table 4. Effect of harzburgite equilibration reaction on trace element abundances.

Constants

Element	Initial Melt Conc./C1 57-13	Crystallizing Phase Ds Ol Ds	Opx Ds
La	34.2	4.30E-05	0.0004
Ce	34.2	0.0001	0.0007
Nd	29.6	0.0001	0.0025
Zr	25.0	0.0011	0.0181
Sm	24.1	0.0002	0.0082
Eu	24.1	0.0002	0.0109
Ti	22.2	0.0074	0.1194
Dy	16.7	0.0014	0.0332
Er	14.8	0.0031	0.0503
Yb	10.2	0.0082	0.0860

	F	Ma/Mc
Low-FeO Parent	1.16	1.4
High-FeO Parent	1.18	2.7
Eggins Parent	1.08	1.4

Models

Depleted opx assimilant

Element	Assimilant Depleted opx	Low-FeO Parent Lq	Low-FeO Parent Δ	High-FeO Parent Lq	High-FeO Parent Δ	Eggins Parent Lq	Eggins Parent Δ
La	1.49E-31	29.5	13.8	29.0	15.3	31.7	7.4
Ce	3.31E-26	29.5	13.8	29.0	15.3	31.7	7.4
Nd	6.93E-16	25.5	13.8	25.1	15.3	27.4	7.4
Zr	1.52E-06	21.5	13.8	21.2	15.3	23.1	7.4
Sm	6.54E-09	20.7	13.8	20.4	15.3	22.3	7.4
Eu	2.22E-07	20.7	13.8	20.4	15.3	22.3	7.4
Ti	0.056	19.1	13.9	18.8	15.3	20.5	7.5
Dy	0.004	14.3	13.8	14.1	15.3	15.4	7.4
Er	0.032	12.8	13.8	12.5	15.2	13.7	7.4
Yb	0.162	8.82	13.3	8.66	14.9	9.45	7.1

Enriched opx assimilant

Element	Enriched opx	Lq	Δ	Lq	Δ	Lq	Δ
La	0.013	29.5	13.8	29.0	15.2	31.7	7.4
Ce	0.025	29.5	13.8	29.0	15.2	31.7	7.4
Nd	0.074	25.6	13.7	25.1	15.2	27.4	7.3
Zr	0.452	21.7	13.0	21.3	14.8	23.2	7.0
Sm	0.196	20.8	13.4	20.4	15.1	22.3	7.2
Eu	0.262	20.9	13.3	20.4	15.0	22.3	7.1
Ti	2.651	20.4	8.3	19.4	12.4	21.2	4.4
Dy	0.553	14.6	12.2	14.2	14.5	15.6	6.6
Er	0.744	13.1	11.5	12.7	14.1	13.9	6.2
Yb	0.875	9.2	9.9	8.8	13.2	9.6	5.3

Chapter Four

Experimental constraints on the origin of high-Ti lunar magmas

ABSTRACT

Phase equilibria and dissolution rate experiments are used to develop an assimilation model for the origin of high-Ti lunar ultramafic glasses. The near-liquidus phase relations of the most Ti-rich ultramafic lunar glass (Apollo 14 black glass) were determined to 2.2-GPa. The liquidus is saturated with Cr-spinel at 1-atm, olivine between ~0.5- and 1.5-GPa, and low-Ca pyroxene+Cr-spinel above 1.5-GPa. The lack of ilmenite on this composition's liquidus at any pressure implies that high-Ti ultramafic glasses are not produced by melting of an ilmenite bearing source. The combined results of phase equilibria studies of ultramafic glass compositions show that TiO_2 content and temperature of liquidus cosaturation with olivine+low-Ca pyroxene are inversely correlated. This evidence supports high-Ti magma formation by an assimilation process. We show via mass balance calculations that a high-Ti black glass magma can be produced from a low-Ti green glass primary magma by assimilating ilmenite and high-Ca pyroxene in a 2:1 ratio by volume. Heat for assimilation can be provided by adiabatic ascent of low-Ti primary magmas from the deep lunar interior. The dissolution rate of ilmenite was measured in both low- and high-Ti lunar magmas. Ilmenite dissolves approximately two times faster than high-Ca pyroxene (Zhang et al., 1989), which matches the 2:1 ratio of ilmenite/cpx assimilation dictated by mass balance. The concurrence of the phase equilibria, mass balance and dissolution rate results strongly supports formation of high-Ti lunar magmas by an assimilation mechanism. This mechanism can produce high-Ti magmas with the lunar magma ocean cumulates in their initial stratigraphic positions, as opposed to melting models which require large-scale lunar overturn (e.g. Hess and Parmentier, 1994).

INTRODUCTION

Lunar magmas, as represented by the lunar ultramafic glasses, show 50-fold variation in TiO_2-content (Fig. 1). The sheer magnitude of this variation implies that the moon's upper mantle has large compositional heterogeneities, which is consistent with the formation of the lunar interior by crystallization of a moon-wide magma ocean. Nevertheless, understanding the details by which these compositionally diverse magmas are generated offers constraints on evolution of the lunar mantle after magma ocean crystallization.

The crystallization sequence of the lunar magma ocean would have been olivine and low-Ca pyroxene, followed by plagioclase (Taylor and Jakes, 1974). This would lead to Ti and Fe enrichments in the residual liquid, similar to the trends observed in large terrestrial igneous bodies, and ilmenite would probably precipitate during the final stages of crystallization. The ilmenite-bearing layer is proposed to exist at approximately 100-km depth in the moon, sandwiched between the plagioclase-rich lunar crust and the deep olivine and low-Ca pyroxene cumulates. Models of high-Ti magma formation generally involve the ilmenite-bearing layer, but differ in how it is involved. The different models of high-Ti magma formation have dramatically different implications for the evolution of the lunar mantle. It was initially proposed that this layer might melt directly to produce high-Ti magmas (Walker et al., 1975b), but this model proved inconsistent with experimental studies of the lunar ultramafic glasses. An assimilation model was then proposed where low-Ti magmas, formed by melting the deep lunar interior, assimilate the ilmenite-bearing layer en route to the surface (Hubbard and Minear, 1975). This model was rejected by Ringwood and Kesson (1976) based on suppositions of the proportions of assimilants and the thermal energy budget of the reaction. Lacking an adequate model in a static moon, Ringwood and Kesson (1976) proposed the dynamic overturn model where the ilmenite-bearing layer sank into the lunar interior. This sinking event mixed the high- and low-Ti parts of the cumulate pile and formed hybridized source zones, melting of which could

produce magmas with a wide range of Ti contents. Subsequently, physical models of the moon predicted overturn of the magma ocean cumulate pile (e.g. Herbert, 1980). A number of variations of the overturn and source mixing model have been proposed by Hess and coworkers (1991-1994) that produce high-Ti magmas and a lunar core.

Herein, I critically reevaluate the assimilation model for the formation of lunar high-Ti magmas by modeling the chemical variation between the low- and high-Ti extremes of the lunar ultramafic glasses. These glasses chemically resemble high-Mg mare basalts (e.g. Ridley et al., 1973) and are the best candidates for primary magmas found on the moon (Delano, 1986). They were erupted in volatile charged, fire-fountain events (Reid et al., 1973 and Heiken et al., 1974) and form dark-mantle deposits detected throughout the lunar surface (Head, 1974). Extensive study of the ultramafic glasses by Delano (1986) has lead to the identification of 25 primitive endmembers. These picritic glasses have higher Mg, Ni and molar Mg/(Mg+Fe) than non-cumulate mare basalts, and are the best choices available for lunar primary magmas.

The near-liquidus phase relations of the most Ti-rich ultramafic glass, the Apollo 14 black glass (Fig. 1), were determined in a series of high pressure melting experiments. The results of these experiments are combined with mass balance calculations to show that the black glass can be produced from the lowest-Ti ultramafic glass, the Apollo 15 green glass (Fig. 1), by assimilation of ilmenite and clinopyroxene. The thermal energy budget of this reaction is constrained using the results of phase equilibria experiments. The feasibility of this reaction is then evaluated by experimental determination of the dissolution rate of ilmenite in lunar magmas and comparing it the dissolution rate of clinopyroxene reported in other studies.

EXPERIMENTAL AND ANALYTICAL METHODS

Phase equilibria experiments

The near-liquidus phase relations of Apollo 14 black glass (AP 14 black) were determined in a series of melting experiments from 1-atm to 2.2-GPa. The composition used is that reported by Delano (1986). A synthetic analog of the glass was prepared from high-purity oxides and silicates (Table 1). To ensure homogeneity, the mix was ground in an agate mortar under ethyl alcohol for 6 hours.

1-atm experiments

Each 1-atm experiment was conducted using approximately 50-mg of AP 14 black powdered mix, pressed into a pellet using Elvanol as a binding agent. The pellet was sintered to an 0.8-mm diameter, Fe-Pt loop fabricated to minimize Fe-exchange with the silicate melt. The loop was hung in the hotspot of a Deltech DT31VT vertical quenching furnace. All experiments were performed at an oxygen fugacity corresponding to Fe-FeO using constant mixing proportions of H_2 and CO_2 gases with flow rates of approximately 0.1-ml/s. Oxygen fugacity was monitored using a ZrO_2-CaO electrolyte cell calibrated at the Fe-FeO buffer. Temperature was monitored with Pt-$Pt_{90}Rh_{10}$ thermocouples calibrated against the melting points of NaCl, Au, and Pd on the IPTS 1968 temperature scale. Experiments were drop-quenched into water. Temperature was varied to constrain the liquidus temperature and first crystalline phase appearance.

High pressure experiments

Starting material for the high pressure experiments was prepared by pressing 500-mg of powdered mix into a pellet using Elvanol as a binding agent. The pellet was hung on 0.004" Pt wire and conditioned at an oxygen fugacity corresponding to the Fe-FeO buffer at 1075°C for 24-hours using the same furnace and techniques employed for the 1-atm experiments. 10-mg of conditioned starting material was placed in a graphite crucible and

welded shut in a Pt outer-capsule. These capsules were placed in an alumina sleeve and positioned in the hotspot of a graphite heater with MgO spacers. Experiments were performed in 0.5" piston-cylinder apparatus, similar to the design of Boyd and England (1960), using $BaCO_3$ as the pressure medium (thesis Appendix A). Pressure was calibrated against the transition of anorthite-gehlenite-corundum to Ca-Tschermak's pyroxene as determined by Hays (1965) (thesis Appendix B). Temperature was monitored with $W_{97}Rh_3$–$W_{75}Rh_{25}$ thermocouples with no correction applied for pressure. The thermal gradient near the hotspot was measured at 20°C/0.1". Sample thickness is <0.05", resulting in a thermal gradient of <10°C. Runs were cold pressurized to 1.0-GPa and then ramped up to 865°C at 100°C/minute where they were held for 6 minutes. They were then pumped to desired run pressure and ramped to final run temperature at 50°C/minute. Experiments were quenched by shutting off the power. Experiments above 1.5-GPa were decompressed to 1.0-GPa immediately prior to quenching to prevent the formation of quench crystals in the liquid regions of the charge (Putirka et al., Accepted 1995).

Experiments were performed over a pressure range of 1- to 2.2-GPa and a temperature range that spanned the liquidus and subliquidus phase boundaries (Table 2). All observed primary phases were analyzed (Table 3). A materials balance calculation was used to estimate the phase proportions (Table 2) and determine whether the silicate charge had changed composition during the experiment. The silicate charge can lose Fe to the Pt capsules if fractures form in the graphite crucibles and allow the liquid phase to contact the Pt outer-capsule. Experiments where the materials balance calculation showed FeO loss of >1% relative were discarded.

Ilmenite dissolution experiments

Starting materials

The dissolution rate of ilmenite was determined in both low- and high-Ti lunar magmas. The compositions of all materials are listed in Table 1. The ilmenite portion of the charge was cut from a homogeneous ilmenite megacryst from the Frank Smith kimberlite mine, South Africa. The megacryst is polycrystalline but completely unaltered, which is rare for large ilmenite samples. Trace amounts of sulfide are present along some grain boundaries.

Four different magma compositions were selected to allow for near-liquidus experiments to be performed at a variety of temperatures and TiO_2 contents. Synthetic analogs of the lunar magma compositions (Table 1) were prepared and conditioned at an oxygen fugacity corresponding to the Fe-FeO buffer using the techniques discussed in the phase equilibria section. Most experiments between 1350° and 1550°C use low-Ti, Apollo 15 green glass group C (Delano, 1986), which contains 0.26 wt.% TiO_2. One experiment at 1450°C used the high-Ti, AP 14 black glass composition used for the phase equilibria experiments. Experiments at 1270°C were performed using mare basalt compositions with lower liquidus temperatures than the ultramafic glasses. Two experiments at 1270°C use the low-Ti, Luna 24 ferrobasalt composition from Grove (1978). It contains 0.88 wt.% TiO_2. One experiment at 1270°C used the high-Ti, Apollo 11 high-K basalt 10072 of Grove and Beaty (1980). It contains 12 wt.% TiO_2.

Experiments

All experiments were performed in a piston cylinder device at 1-GPa pressure using the techniques described for the phase equilibria experiments and in thesis Appendix A. The run assembly (Fig. 2) differs from that used for the phase equilibria experiments in that a slightly larger graphite capsule was used and no Pt outer capsule was used. Within the graphite capsule, an ilmenite disk was sandwiched between equal sized layers of lunar magma composition. This sandwich technique was developed by Zhang et al. (1989) to

impede convection within the charge. The ilmenite disk and capsule are sized to form a tight fit with each other to prevent movement of the disk during the experiment. The ilmenite disks were prepared by coring the megacryst with a diamond coring bit with an inside diameter of 0.11". The resulting core was sliced into disks using a low-speed diamond wafering saw. Disks were polished on 600-grit sandpaper. Disks prepared by this technique varied in thickness by <±30μm.

Experiments were run at a variety of temperatures and durations to determine the temperature and time dependence of dissolution rate (conditions in Table 4). Most experiments used low-Ti magma compositions as the liquid portion of the charge. One experiment at 1450°C and one at 1270°C were performed with high-Ti liquid compositions to constrain the compositional dependence of dissolution rate. Most experimental products consisted of liquid plus ilmenite disk. A few also contained Cr-ulvospinel, olivine or pigeonite, listed in Table 4. Analyses of some of these phases are reported in Table 5.

Analytical methods

The experimental products were analyzed by electron microprobe at the Massachusetts Institute of Technology on a JEOL 733 Superprobe using wavelength-dispersive techniques. Data were reduced using the correction scheme of Bence and Albee (1968) with the modifications of Albee and Ray (1970). Crystalline phases in the experiments were analyzed at 15-kV accelerating potential, 10-nA beam current and a spot size on the order of 2-μm. Spot size was increased to 10-μm for glass analyses in order to minimize diffusion of alkali elements away from the region of interest during the analysis. The thickness of the ilmenite disk in the dissolution rate experiments was determined using a Zeiss reflected light microscope with an ocular scale accurate to ±10-μm.

EXPERIMENTAL RESULTS

Results of Phase Equilibria Experiments

The liquidus of AP 14 black glass (Fig. 3) was determined to 2.2-GPa. It is cosaturated with olivine (ol), low-Ca pyroxene (opx) and chrome-spinel (Cr-sp) at 1.5-GPa and 1430°C. At pressures above 1.5-GPa, the liquidus is saturated with opx and Cr-sp. Below 1.5-GPa, the liquidus is saturated with ol and at 1-atm it is saturated with Cr-sp. The liquidus is notably lacking ilmenite.

Results of ilmenite dissolution experiments

The results of the ilmenite dissolution rate experiments are shown in Fig. 4. Ilmenite dissolution rate increases with temperature and decreases with increased run duration and TiO_2 content of the liquid portion of the charge. In the super-liquidus, 1550°C experiment, the ilmenite disk completely dissolved in low-Ti AP 15 green liquid in only 480-seconds. The reported dissolution rate is a minimum value, indicated by the vertical arrow and question mark in Fig. 4. Small chromium-ulvospinel (Cr-usp) phenocrysts are present in the bottom of the charge, similar in composition to those found in runs 51 and 54 (Table 5). Three experiments were performed at 1450°C. Two experiments of varying duration were performed using low-Ti AP 15 green glass liquids, one for 255- and another for 1800-seconds. The dissolution rate of ilmenite at 255-seconds is approximately 4 times that at 1800-seconds. This decrease in dissolution rate with time is consistent with a diffusion controlled dissolution mechanism (Zhang et al., 1989). Time-independent dissolution rates would imply that convection was occurring within the charge. In the 1800-second experiment, over 65% of the disk dissolved. The disk lost contact with the sides of the capsule and sank to the bottom (Fig. 5). Minor amounts of Cr-usp and olivine crystallized in this experiment (Table 5). The Cr-usp phenocrysts are ~10-μm in size and are found

suspended in a thin layer (~100-μm) around the ilmenite disk (Fig. 5). Olivine phenocrysts are found in a thin layer near the top of the charge. Olivine is Fo_{84} and its floatation indicates that the melt had a density >3.37-g/cm^3.

The third experiment performed at 1450°C used high-Ti AP 14 black glass liquid. This experiment was run for 1800-seconds and has a slightly slower (Fig. 4) dissolution rate than the equivalent experiment with low-Ti AP 15 green glass liquid. Dissolution in the black glass liquid experiment proceeded to a similar extent to that in the green glass liquid experiment. In the black glass liquid experiment, the ilmenite disk sank to the bottom of the charge and a few Cr-usp phenocrysts (Table 5) precipitated in a layer around it. The liquids in both of the 1800-second, 1450°C experiments (green and black glass liquids) vary in TiO_2 content from 32 wt.% near the ilmenite disk to 24 wt.% near the upper part of the charge (Fig. 6, chapter Appendix 1).

Dissolution experiments at sub-liquidus temperatures for AP 15 green glass liquid contained the ilmenite disk and minor olivine crystals at 1400°C and olivine and pigeonite crystals at 1350°C. Experiments performed at 1270°C using low- and high-Ti mare basalts were near liquidus and contained no crystalline phases aside from the ilmenite disk. The results of the 1270°C experiments show similar relations to the higher temperature experiments: shorter duration—faster dissolution rate and higher initial liquid Ti-content—slightly slower dissolution rate. The data points from all of the experiments were fit with an Arrhenius relationship:

$$\text{Dissolution rate}=(1.5432*10^{-17})*e^{(0.019763*\text{Temperature})};\ R^2=0.64541.$$

This equation does not take into account the complexities of dissolution rate from run duration and composition, but is useful for testing the assimilation model developed below.

DISCUSSION

The nature of the lunar interior and sources of lunar magmas

Evidence of a lunar magma ocean

The lunar upper mantle and crust are thought to have formed by crystallization of a moon-wide magma ocean 4.2 to 4.4 billion years ago (reviewed in Warren, 1985). The magma ocean model was proposed early in the Apollo program by Smith et al. (1970) and Wood et al. (1970) to explain the presence of the thick anorthositic crust that encircles the moon. The presence of this much fractionated crustal material requires the crystallization of a large magma body, presumed to be a magma ocean. The magma ocean model also offers explanation of the complementary Eu-anomalies of the highland anorthosites and mare basalts (reviewed in Taylor, 1982) and is consistent with the isotopic fractionations required in the mare basalt source regions (Lugmair et al., 1975; Tera and Wasserburg, 1975).

Crystallization of the lunar magma ocean

Taylor and Jakes (1974) presented a magma ocean crystallization model that produces compositionally distinct crystal cumulate zones within the lunar upper mantle. This model has been modified by others since its inception (e.g. Walker et al., 1975a; Snyder et al., 1992), discussed below, but all models produce the same range of cumulates. The Taylor and Jakes' magma ocean was initially 1000-km deep. A depth of 400-km has been suggested by studies of the thermal properties of the moon (Solomon and Chaiken, 1976), but the order of cumulate crystallization is not dependent on this depth. The magma ocean initially crystallized olivine, which sank to its base, forming a dunite layer. The ocean surface formed a frozen crust that was continually broken up and remixed by meteoric bombardment. Progressive olivine crystallization lead to opx saturation and the precipitation of harzburgite at 250-300-km depth. Taylor and Jakes (1974) and Walker et

al. (1975a) suggested that melting of this region produced low-Ti mare basalts and low-Ti ultramafic glasses. Walker et al. (1975a) pointed out that this region might be lherzolitic due complex crystallization effects that could take place during cumulate sinking. In either case, the residual liquid would be continually enriched in Al and Ca and eventually reach plagioclase stability. Plagioclase floated upward and combined with some of the frozen crust to form the lunar highlands. The segregation of plagioclase resulted in a negative Eu anomaly in the mare basalt source and a complementary positive one in the crust. Continued differentiation caused crystallization of higher-Ca pyroxenes between 250- and 100-km and the enrichment of Fe and Ti in the residual liquid caused the crystallization of ilmenite at 100-km depth. Taylor and Jakes (1974) and Walker et al. (1975b) suggested that remelting of the ilmenite-bearing region produced high-Ti lunar magmas. At the end of crystallization, an incompatible element-rich, KREEP-type liquid was trapped beneath the base of the highlands crust and the upper part of the cumulate pile.

Experimental constraints on lunar magma sources

Experimental petrology of lunar mare basalts was used to determine the mineralogy and depth of the mare basalt sources by using the *multiple saturation hypothesis*. This hypothesis states that the liquidus of a primary magma will be multiply saturated with the phases present in its source at the pressure at which it formed (discussed in BVSP, 1981). It assumes that magmas form by partial melting of a multi-phase source at a single depth, and that the studied magma composition is a primary magma, that is a magma that has not been altered since segregation from its source. Experimental studies of low- and high-Ti mare basalts showed liquidus saturation with magma ocean cumulate phases at pressures consistent with the depths of these phases according to the Taylor and Jakes (1974) magma ocean crystallization model. Low-Ti mare basalts showed liquidus cosaturation with ol+opx at pressures indicating depths of 200 to 400-km (Green et al., 1971 and Grove et

al., 1973), consistent with the mafic cumulates thought to reside there. High-Ti mare basalts showed liquidus cosaturation with cpx, ilmenite and spinel at pressures indicating depths of ~100-km (Longhi et al., 1974), similar to the depth of the proposed ilmenite-bearing layer. These results supported the generation of mare basalts by simple remelting of the magma ocean cumulates at different depths.

However, the simple cumulate remelting model proved inconsistent with experimental studies of high-Ti ultramafic glass compositions. The liquidus relations of the high and low-Ti ultramafic glasses are summarized in Table 6. The high-Ti ultramafic glasses are not saturated with ilmenite or another phase rich enough in Ti to be produced by melting. The AP 15 red glass has 13.8 wt.% TiO_2, a higher TiO_2 content than highest-Ti mare basalts, but does not show liquidus or near-liquidus saturation with ilmenite at any pressure (Kesson, 1975; Delano, 1980). The red glass is liquidus cosaturated with ol+opx at 2.5-GPa and has Cr-sp as a sub-liquidus phase. The AP 14 black glass studied here is the most Ti-rich ultramafic glass discovered. It has 16.2 wt.% TiO_2, 2.5 wt.% more than the red glass, and has liquidus relations similar to the red glass, but shifted to lower pressures (Fig. 3). The AP 14 black glass is not near saturation with ilmenite, but has Cr-sp with 10-15 wt.% TiO_2 on its liquidus at low and high pressure. If this Cr-sp were present in the residuum, its Ti content would be too low to produce a black or red glass type liquid by partial melting. The spinel also has 30 wt.% Cr_2O_3 and is probably not a reasonable saturating phase in the residuum. The dissolution rate experiments show that the AP 14 black glass composition is very far from saturation with ilmenite. Liquids with over 30 wt.% TiO_2 (run #54, Fig. 6) were produced that are not ilmenite saturated.

Both low- and high-Ti ultramafic glass compositions are liquidus cosaturated with ol and opx in the pressure range of 1.5 to 2.5-GPa, with no relationship between TiO_2 content and pressure of multiple saturation (Table 6). The similar pressures of ol+opx cosaturation could indicate that both low- and high-Ti magmas are derived from melting of the same deep, mafic magma ocean cumulates at depths between 300-500-km. This depth

is well below the 100-km depth predicted for the late stage, ilmenite-bearing cumulate layers. There is a strong correlation between TiO_2 content and temperature of liquidus saturation with ol+opx (Fig. 7). The black and red glasses have the lowest liquidus temperatures, but define the low- and high-pressure extremes of ol-opx liquidus saturation (Table 6). If low- and high-Ti ultramafic glass magmas are produced at a similar depth within the moon, this would indicate large vertical temperature anomalies in the lunar mantle.

Assimilation

Alternatively, some process besides melting could take place during the formation of lunar magmas. If the lunar magma source is at 300-500-km depth, magmas must travel much further through the moon to erupt than terrestrial magmas travel through the earth. It is possible that some processing takes place en route that alters lunar magma compositions. If this process is responsible for generating the range in TiO_2 contents observed in lunar magmas, its characteristics are as follows: 1) increase liquid TiO_2 content; 2) lower liquidus temperature; and 3) produce liquids that are not in equilibrium with a very high-Ti phase. Assimilation of the Ti-rich, ilmenite-bearing cumulates by low-Ti primary magmas is compatible with all of these characteristics. Assimilation of Ti-rich cumulates would increase magmatic TiO_2 content, while decreasing liquidus temperature due to the heat required for assimilation. The assimilating liquid would not have to come into equilibrium with the ilmenite assimilant and thus may not be near saturation with it in experimental studies.

An assimilation origin for high-Ti mare basalts was initially proposed by Anderson (1971), who suggested that high-Ti magmas are derived from low-Ti primary magmas that assimilate armalcolite at subcrustal depths. This model proved inconsistent with studies of armalcolite stability (Kesson and Lindsley, 1976). The assimilation model was revived by Hubbard and Minear (1975) who proposed that high-Ti magmas were produced as hybrid liquids from selective assimilation of the ilmenite- and clinopyroxene-bearing magma ocean

cumulates by low-Ti primary magmas. Ringwood and Kesson (1976) rejected this model based on erroneous assumptions of the assimilation reaction. Ringwood and Kesson assumed that the ilmenite and cpx cumulates would be assimilated in the proportion in which they are present. They speculated that cpx and ilmenite would be present in a 2:1 ratio, and that compositional and thermal energy constraints were not consistent with an assimilation model. Ringwood and Kesson in turn proposed the cumulate overturn model where the ilmenite-bearing layer sinks into the basal mafic cumulates and equilibrates with it. Melting of this mixed source zone, they proposed, would produce magmas with a wide range of Ti-contents.

We reevaluate the assimilation model in light of our experimental studies and show that an assimilation origin for high-Ti magmas is not only plausible, but is favored by available evidence.

Assimilation model for high-Ti magma genesis

Compositional constraints on assimilation

This bulk assimilation assumption of Ringwood and Kesson (1976) is not necessarily valid since assimilation will be controlled by kinetic factors, i.e. the relative dissolution rates of ilmenite and cpx. We have constrained the assimilation reaction through mass balance calculations (Table 7) that model the relationship between the high- and low-Ti extremes of the lunar ultramafic glasses. The model uses the lowest-Ti ultramafic glass, the AP 15 green (Fig. 1), as a primary melt from the lunar interior and the most Ti-rich ultramafic glass, the AP 14 black (Fig. 1), as the liquid after assimilation. Assimilation is assumed to take place by dissolution of ilmenite and cpx, allowing for the crystallization of olivine. The proportions of reactants were determined by multiple linear regression of Apollo 15 green glass, ilmenite, cpx and ol against the Apollo 15 black glass. The olivine composition is in equilibrium with the green glass, from experiments of Green and

Ringwood (1973). The ilmenite composition is from a highly evolved mare basalt from Apollo 17, sample 70125 reported in Dymek et al. (1975). Clinopyroxene composition is an average from the crystallization experiments of Grove and Beaty (1980) on the Apollo 11 high-K basalts.

The simple model does a remarkably good job of recovering the AP 14 black glass composition (Table 7). The reaction requires the assimilation of ilmenite and cpx in the weight proportions of 3:1, and minor crystallization of olivine. These results are consistent with the liquidus relations of Fig. 3, which show that the AP 14 black glass liquid is saturated with olivine below 1.5-GPa, the depths at which assimilation is likely to take place. More complex models allowing for the incorporation of pigeonite and KREEP-type liquid were also developed, but did not result in an appreciably better fit to the data. KREEP liquid is certainly incorporated into high-Ti magmas as evidenced by the very high trace element abundances of the Ti-rich ultramafic glasses (Shearer and Papike, 1992).

Thermal energy constraints on the assimilation model

The proportions of reactants (Table 7) were used to estimate the thermal energy budget of the assimilation reaction, results in Table 8. Assuming the ΔH_f=100-cal/gram for all phases, ilmenite and cpx assimilation requires 40-cal/gram of black glass liquid produced. Olivine crystallization of the assimilating liquid produces 0.8-cal/gram, which is not enough heat for the assimilation reaction. Additional heat is available from the superheat of the primary liquid. The AP 15 green glass liquidus (T.L. Grove, unpublished) is approximately 100° higher than the AP 14 black glass liquidus (Fig. 8). We assume that the green glass-type primary magma segregates from its source at the temperature and pressure at which it is multiply saturated with ol and opx, 2-GPa (400-km) and 1550°C. This melt adiabatically ascends to the ilmenite and cpx cumulate layer at 100-km depth (~0.5-GPa pressure, Fig. 8). At this point the liquid is 160° hotter than the black glass liquidus (Fig. 8). Assuming the C_p^{liquid}=0.3-cal/(°C*g) this provides 29.3-cal/gram of superheat for

assimilation. Superheat plus the heat of olivine crystallization provides 75% of the heat necessary for reaction. This is very close considering the uncertainties involved in estimating the reaction, the depth of the ilmenite layer, and the depth of formation of the low-Ti primary magma. Low-Ti primary magmas may be segregated at higher pressures than indicated by their ol+opx cosaturation point. Longhi (1992) has proposed that green glass type liquids are produced by near-fractional decompression melting of the lunar mantle starting at depths >1000-km (5-GPa). He suggests that the ol and opx cosaturation point is an artifact of aggregation of these liquids. Segregation of the low-Ti parent from the mean depths proposed by Longhi would provide more than enough heat for the assimilation reaction.

Kinetic constraints on the assimilation model

The mass balance results (Table 7) show that formation of high-Ti, AP 14 black glass-type magmas from low-Ti, AP 15 green glass-type magmas requires assimilation of ilmenite and clinopyroxene in a 3:1 ratio. A simple, kinetic test of this model is to compare the relative dissolution rates of ilmenite and cpx to see if they are consistent with the assimilation ratio. More complex modeling is not possible because the relative proportions of ilmenite and other minerals in the lunar upper mantle are unknown. The dissolution rate of cpx has been determined by Brearley and Scarfe (1986) and Zhang et al. (1989). There is a lot of uncertainty associated with comparing these results for cpx dissolution to our own for ilmenite dissolution because dissolution rate is a function of temperature, composition and time (in the diffusion limited case). Both the Brearley and Scarfe (1986) and Zhang et al. (1989) studies were conducted at temperatures well above the liquidus, while our experiments were conducted at liquidus to subliquidus temperatures. Zhang et al. (1989) developed and used the disk-sandwich technique, employed here (Fig. 2), to study the dissolution of end-member diopside in andesitic liquid. The dissolution rate of diopside is approximately one third that of ilmenite in Zhang et al.'s experiments of similar duration

to our own (Table 9, Fig.4). Zhang et al.'s shortest duration experiment shows a diopside dissolution rate similar to the dissolution rate of ilmenite at this temperature. Brearley and Scarfe (1986) determined the dissolution rates of natural, mantle cpx in alkali olivine basalt. These experiments use spheres surrounded by melt to measure dissolution rate. The dissolution rates in these experiments were independent of time, probably due to convection in the experimental assembly. Brearley and Scarfe (1986) ran their experiments 25 to 125° above the liquidus with run times similar to the ones in this study. Their dissolution rates for cpx at 1.2-GPa are 2 to 14 times slower than our ilmenite dissolution rates.

We conclude that the dissolution rate of ilmenite is likely to be significantly faster than that of cpx in lunar magmas, consistent with the proportions dictated by mass balance. In the mass balance reaction from Table 7, ilmenite and cpx are assimilated in 3:1 ratio by weight or a 2:1 ratio by volume. The average ratio of our ilmenite and Zhang et al.'s cpx dissolution rate data (Table 9) is 2:1, which matches the ilmenite/cpx volume dissolution ratio from mass balance.

CONCLUSIONS

Model of high Ti-magma genesis

The high-Ti ultramafic glasses may be produced by assimilation of ilmenite and clinopyroxene into low-Ti ultramafic primary magmas. This model is consistent with compositional, thermal and kinetic aspects of the assimilation reaction. Assimilation could take place in the shallow lunar mantle where ilmenite and clinopyroxene would be present according to models of lunar magma ocean crystallization (e.g. Taylor and Jakes, 1974). The parental, low-Ti ultramafic magmas may be generated by polybaric, near-fractional fusion of the lunar interior during adiabatic decompression, as proposed by Longhi (1992). We do not know if this assimilation reaction is the mechanism by which the high-Ti mare

basalts also form, because a clear genetic link between the ultramafic glasses and the mare basalts has yet to be established (Longhi, 1987).

Constraints on Lunar overturn

The assimilation model developed here produces high-Ti magmas with the initial magma ocean cumulate stratigraphy in the lunar upper mantle intact. Other models of high-Ti magma genesis require overturn of the cumulate pile to mix the ilmenite-bearing layer (Ringwood and Kesson, 1976) or melts of the ilmenite-bearing layer (Hess and Parmentier, 1994) with the low-Ti magma source. A number of physical models of the magma ocean cumulate pile support this large-scale overturn event (Herbert, 1980; Spera, 1992; Hess and Parmentier, 1993; and Parmentier and Hess, 1995). There are a number of arguments against the cumulate overturn models. The first is that the physical models of the cumulate pile that show overturn require that the ilmenite-bearing layer is very thick, 5 to 10% of the total magma ocean (Spera, 1992; Hess and Parmentier, 1993) . Snyder et al. (1992) argue that this is unreasonably thick because ilmenite precipitation would likely initiate small, localized convection. The density anomaly of an ilmenite-bearing layer would thus be smeared out across a thicker, less dense layer than that required by overturn models. Another argument against the overturn models is the strong correlation between TiO_2 content and temperature of liquidus saturation with ol+opx (Fig. 7). The AP 14 black and AP 15 red glasses have the lowest liquidus temperatures, but define the low- and high-pressure extremes of ol-opx liquidus saturation (Table 6). If the overturn model were correct, this would indicate large vertical temperature anomalies in the lunar mantle which does not seem probable.

The final argument against formation of high-Ti magmas by the lunar overturn model is that the high compressibilities and densities of high-Ti magmas would prevent their eruption if they were produced at similar depths to the low-Ti magmas. Delano (1990)

proposed that high-Ti compositions might become denser than their crystalline surroundings at relatively modest pressures. Agee and Circone (1995) have experimentally confirmed this result and show that Apollo 14 black glass liquids would become denser than olivine and low-Ca pyroxene cumulates at 200- to 300-km depth. Consequently, if the ilmenite layer sank and enriched the source in Ti, melts of these regions would sink into the deep lunar interior rather than erupt on the surface. Hess (1991) proposed a way to overcome this problem through partial crystallization and entrainment of high-Ti liquid in ascending diapirs.

Clearly the processes that can occur in a magma ocean cumulate pile are complex. In showing that high-Ti magmas may be produced without lunar overturn, we have not excluded the lunar overturn model, but rather have shown that an alternative model is as, if not more, consistent with the available data.

Figure Captions

Figure 1. Plot of TiO_2 in wt.% against Mg# (molar Mg/Mg+Fe) of pristine lunar glasses. Data from Delano (1986).

Figure 2. Sample assembly for dissolution rate experiments. Remainder of sample assembly as in Appendix B.

Figure 3. Phase diagram of Apollo 14 black glass. Data from Table 2.

Figure 4. Results of dissolution rate experiments. All experiments performed on low-Ti liquids except those noted. Clinopyroxene dissolution rate data from Brearley and Scarfe (1986) and Zhang et al. (1989).

Figure 5. Picture of experiment 51, dissolution of ilmenite in Apollo 15 green glass liquid.

Figure 6. TiO_2 content of liquid in dissolution rate experiments as a function of distance from the ilmenite disk.

Figure 7. Plot of TiO_2 in wt.% against the temperature of liquidus cosaturation with olivine and low-Ca pyroxene. Data from this study, Green et al. (1975); Delano (1980); Chen et al. (1982); Chen and Lindsley (1983)

Figure 8. Plot of the liquidi of Apollo 14 black glass (this study) and Apollo 15 green glass (T.L. Grove, unpublished data).

Footnotes to Tables

Table 1. Oxide values in wt.%. Compositions of Apollo 14 black and Apollo 15 green glasses from Delano (1986). Ilmenite was provided by Dr. Nobu Shimizu and is from the Frank Smith mine, South Africa. Apollo 11 high K basalt composition from Beaty et al. (1979). Luna 24 composition from Grove (1978).

Table 2. Phase proportions determined by multiple linear regression of analyzed phases (Table 3) against staring composition (Table 1). 'tr' indicates trace abundance. '-' not determined.

Table 3. Oxide values in wt. %. Reported value is average of 'N' points, number after oxide is 1 standard deviation on average. '-' indicates concentration not determined.

Table 4. All experiments at 1-GPa

Table 5. Values in wt. %.

Table 6. Temperature and pressure of olivine and opx multiple saturation for ultramafic glass compositions. Data: 1-T.L. Grove, unpublished, 2-Chen and Lindsley (1983), 3-Chen et al. (1982), 4-Green et al. (1975), and 5-Delano (1980).

Table 7. Model and proportions were determined by multiple linear regression of Initial liquid and Reactants against the Resultant liquid, Apollo 14 black glass composition. Glass data is from Delano (1986). Olivine composition is from the experiments of Green and Ringwood (1973). Ilmenite is from 70125, reported in Dymek et al. (1975). Cpx (high-Ca pyroxene) is the average of the experimental cpxs from Grove and Beaty (1980).

Table 8. Calculated based on proportions from Table 7. C_p^{liquid}=0.3-cal/(°C*g) and the ΔH_f=100-cal/gram. ΔT is the difference in adiabatically ascending green glass liquid temperature and black glass liquidus temperature at 0.5-GPa from Fig. 8.

Table 9. Data from Table 4, Brearley and Scarfe (1986) and Zhang et al. (1989).

Appendix 1. Values in wt. %. First measurement was taken ~75-μm from the edge of the disk to avoid quench growth.

References

Agee CB, Circone S (1995). Crystal-liquid density inversions in high-TiO2 lunar basalt. Lunar and Planetary Science Conference Abstracts 26: 5-6

Albee AL, Ray L (1970). Correction factors for electron microprobe microanalysis of silicates, oxides, carbonates, phosphates and sulfates. Anal Chem 42: 1408-1418

Anderson AT (1971). Exotic armalcolite and the origin of Apollo 11 ilmenite basalts. Geochim Cosmochim Acta 35: 969-973

Beaty DW, Hill SMR, Albee AL, Ma M-S, Schmitt RA (1979). The petrology and chemistry of basaltic fragments from the Apollo 11 soil, part I. Proc Lun Plan Sci Conf 10: 41-75

Bence AB, Albee AL (1968). Empirical corrections factors for the electron microanalysis of silicates and oxides. J Geol 76: 382-403

Boyd FR, England JL (1960). Apparatus for phase equilibrium studies at pressures up to 50 kbars and temperatures up to 1750°C. J Geophys Res 65: 741-748

Brearley M, Scarfe CM (1986). Dissolution rates of upper mantle minerals in an alkali basalt melt at high pressure: an experimental study and implication for ultramafic xenolith survival. J Petrol 27(5): 1157-1182

BVSP (1981). Basaltic volcanism on the terrestrial planets. New York, Pergamon Press, Inc.

Chen H-K, Delano JW, Lindsley DH (1982). Chemistry and phase relations of VLT volcanic glasses from Apollo 14 and Apollo 17. J Geophys Res 87: A171-A181

Chen H-K, Lindsley DH (1983). Apollo 14 very low-titanium glasses: Melting experiments in iron-platinum alloy capsules. J Geophys Res 88: B335-B342

Delano JW (1980). Chemistry and liquidus relations of Apollo 15 red glass: implications for the deep lunar interior. Proc Lun Plan Sci Conf 11: 251-288

Delano JW (1986). Pristine lunar glasses: Criteria, data, and implication. J Geophys Res 91(B4): D201-D213

Delano JW (1990). Buoyancy-driven melt segregation in the earth's moon, I. Numerical results. Proc Lun Plan Sci Conf 20: 3-12

Dymek RF, Albee AL, Chodos AA (1975). Comparative mineralogy and petrology of Apollo 17 mare basalts: Sample 70215, 71055, 74255 and 75055. Proc Lun Plan Sci Conf 6: 49-77

Green DH, Ringwood AE (1973). Significance of a primitive lunar basaltic composition present in Apollo 15 soils and breccias. Earth Plan Sci Lett 19: 1-8

Green DH, Ringwood AE, Hibberson WO, Ware NG (1975). Experimental petrology of the Apollo 17 mare basalts. Proc Lun Plan Sci Conf 11: 871-893

Green DH, Ringwood AE, Ware NG, Hibberson WO, Major A, Kiss E (1971). Experimental petrology and petrogenesis of Apollo 12 basalts. Proceedings of the 2nd Lunar and Planetary Science conference : 601-615

Grove TL (1978). Cooling histories of the Luna 24 very low Ti (VLT) basalts: an experimental study. Proc Lun Plan Sci Conf 9: 565-584

Grove TL, Beaty DW (1980). Classification, experimental petrology and possible volcanic histories of the Apollo 11 high-K basalts. Proc Lun Plan Sci Conf 11: 149-177

Grove TL, Walker D, Longhi J, Stolper EM, Hays JF (1973). Petrology of rock 12002 and origin of picritic basalts at Oceanus Procellarum. Proc Lun Plan Sci Conf 4: 995-1011

Hays JF (1965). Lime-alumina-silica. Yearb Carnegie Inst Wash 65: 234-236

Head JW (1974). Lunar dark mantle deposits: possible clues to the distribution of early mare deposits. Proc Lun Plan Sci Conf 5: 207-222

Heiken GH, McKay DS, Brown RW (1974). Lunar deposits of possible pyroclastic origin. Geochim Cosmochim Acta 38: 1704-1718

Herbert F (1980). Time dependent lunar density models. Proc Lun Plan Sci Conf 11: 2015-2030

Hess PC (1991). Diapirism and the origin of high TiO2 mare glasses. Geophys Res Lett 18: 2069-2072

Hess PC (1993). The ilmenite liquidus and depths of segregation for the high-Ti picrite glasses. Lunar and Planetary Science Conference Abstracts 24: 649-650

Hess PC, Parmentier EM (1993). Overturn of magma ocean ilmenite cumulate layer: implications for lunar magmatic evolution and formation of a lunar core. Lunar and Planetary Science Conference Abstracts 24: 651-652

Hess PC, Parmentier EM (1994). Overturn of magma ocean ilmenite cumulate layer (II): implications for lunar thermal and magmatic evolution. Abstracts of the Lunar and Planetary Science conference 25: 541-542

Hubbard NJ, Minear JW (1975). A chemical and physical model for the genesis of lunar rocks: Part II. Mare basalts. Lunar Science VI : 405-407

Kesson SE (1975). Mare basalts: melting experiments and petrogenetic interpretations. Proc Lun Plan Sci Conf 6: 921-941

Kesson SE, Lindsley DH (1976). The effects of Al3+, Cr3+, and Ti3+ on the stability of armalcolite. Proc Lun Plan Sci Conf 6: 921-941

Longhi J (1987). On the connection between mare basalts and picritic volcanic glasses. Proceedings of the 17th Lunar and Planetary Science conference in the Journal of Geophysical Research 92: E349-E360

Longhi J (1992). Origin of picritic green glass magmas by polybaric fractional fusion. Proc Lun Plan Sci Conf 22: 343-353

Longhi J, Walker D, Grove TL, Stolper EM, Hays JF (1974). The petrology of the Apollo 17 mare basalts. Proceeding of the Lunar and Planetary Science Conference 5: 447-469

Lugmair GW, Scheinin NB, Marti K (1975). Sm-Nd age of Apollo 17 basalt 75075: Two stage igneous processes in mare basalt genesis. Lunar Science 6: 531-533

Parmentier EM, Hess PC (1995). Spatial and temporal scales of lunar differentiation: implications for subsequent thermal and chemical evolution of the moon. Abstracts of the Lunar and Planetary Science conference 26: 1107-1108

Putirka K, Johnson M, Kinzler RJ, Longhi J, Walker D (Accepted 1995). Thermobarometry of mafic igneous rocks based on clinopyroxene-liquid equilibria, 0 - 30 kb. Contrib Mineral Petrol :

Reid AM, Lofgren GE, Heiken GH, Brown RW, Moreland G (1973). Apollo 17 orange glass, Apollo 15 green glass and Hawaiian lava fountain glass. EOS Trans AGU 54: 606-607

Ridley WI, Reid AM, Warner JL, Brown RW (1973). Apollo 15 green glasses. Physics of Earth and planetary interiors 7: 133-136

Ringwood AE, Kesson SE (1976). A dynamic model for mare basalt petrogenesis. Proc Lun Plan Sci Conf 7: 1697-1722

Shearer CK, Papike JJ (1992). Relationship between Apollo 12 high-Ti, red picritic glass and high-Ti basaltic magmatism. Proc Lun Plan Sci Conf 23: 1281-1282

Smith JV, Anderson AT, Newton RC, Olsen EJ, Wyllie PJ, Crewe AV, Isaacson MS, Johnson D (1970). Petrologic history of the moon inferred from petrography, mineralogy, and petrogenesis of Apollo 11 rocks. Proceedings of the Apollo 11 lunar science conference : 897-825

Snyder GA, Taylor LA, Neal CR (1992). A chemical model for generating the sources of mare basalts: combined equilibrium and fractional crystallization of the lunar magmasphere. Geochim Cosmochim Acta 56: 3809-3823

Solomon SC, Chaiken J (1976). Thermal expansion and thermal stress in the moon and terrestrial planets: clues to early thermal history. Proc Lun Plan Sci Conf 7: 3229-3243

Spera FJ (1992). Lunar magma transport phenomena. Geochim Cosmochim Acta 56: 2253-2265

Taylor SR (1982). Planetary Science: A lunar perspective. Houston, Lunar and Planetary Institute

Taylor SR, Jakes P (1974). The geochemical evolution of the moon. Proc Lun Plan Sci Conf 5: 1287-1305

Tera F, Wasserburg GJ (1975). The evolution and history of mare basalts as inferred from the U-Th-Pb systematics. Lunar Science 6: 807-809

Walker D, Longhi J, Hays JF (1975a). Differentiation of a very thick magma body and implications for the source regions of the mare basalts. The sixth lunar and planetary science conference, Houston, Pergammon

Walker D, Longhi J, Stolper EM, Grove TL, Hays JF (1975b). Origin of titaniferous lunar basalts. Geochim Cosmochim Acta 39: 1219-1235

Warren PH (1985). The magma ocean concept and lunar evolution. Ann Rev Earth Plan Sci 13: 201-240

Wood JA, Dickey JS, Marvin UB, Powell BN (1970). Lunar anorthosites and a geophysical model of the moon. Proceedings of the Apollo 11 lunar science conference : 965-988

Zhang Y, Walker D, Lesher CE (1989). Diffusive crystal dissolution. Contrib Mineral Petrol 102: 492-513

Figure 1

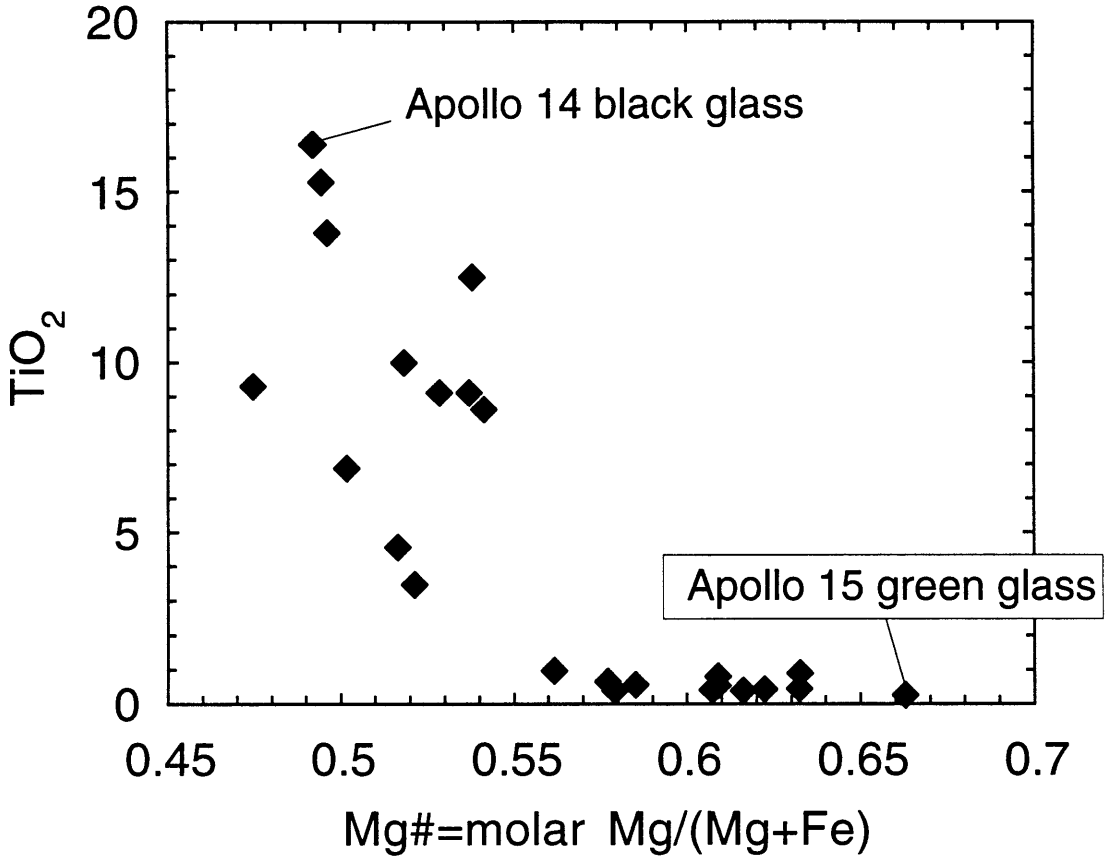
Apollo 14 black glass
Apollo 15 green glass
TiO_2
20
15
10
5
0
0.45
0.5
0.55
0.6
0.65
0.7
Mg#=molar Mg/(Mg+Fe)

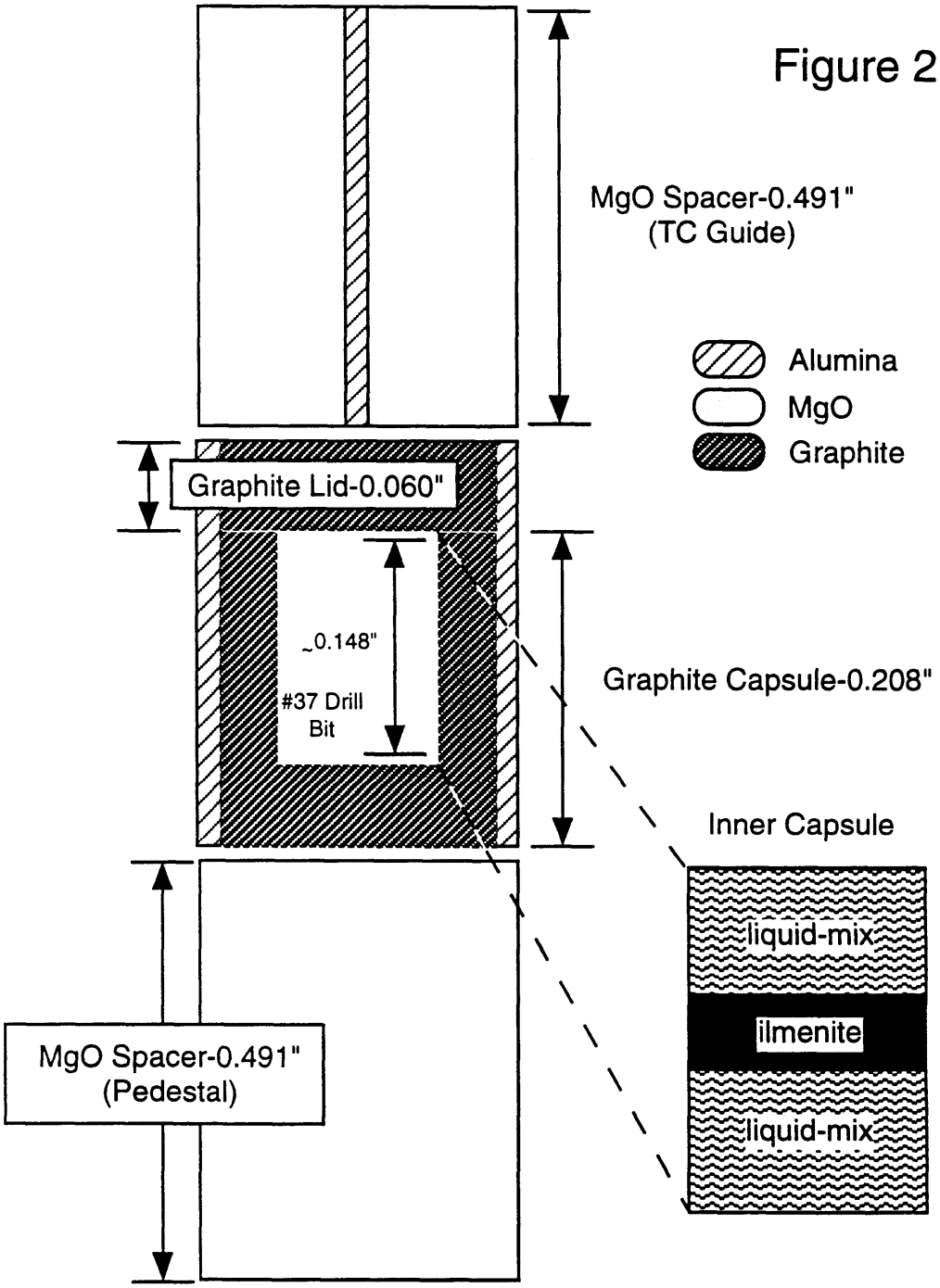
Figure 2
MgO Spacer-0.491"
(TC Guide)
Alumina
MgO
Graphite
Graphite Lid-0.060"
~0.148"
#37 Drill
Bit
Graphite Capsule-0.208"
Inner Capsule
liquid-mix
ilmenite
liquid-mix
MgO Spacer-0.491"
(Pedestal)

Figure 3

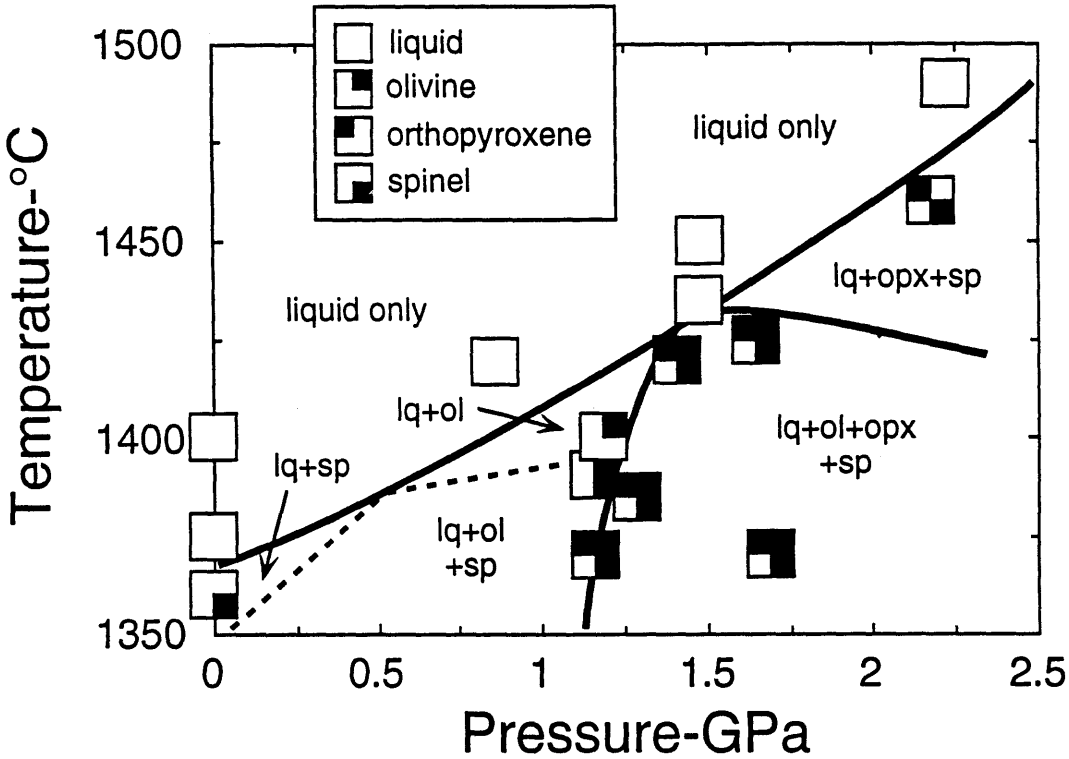
liquid
olivine
orthopyroxene
spinel
liquid only
liquid only
lq+opx+sp
lq+ol
lq+sp
lq+ol+opx
+sp
lq+ol
+sp
1500
1450
1400
1350
0
0.5
1
1.5
2
2.5
Temperature-°C
Pressure-GPa

Figure 4

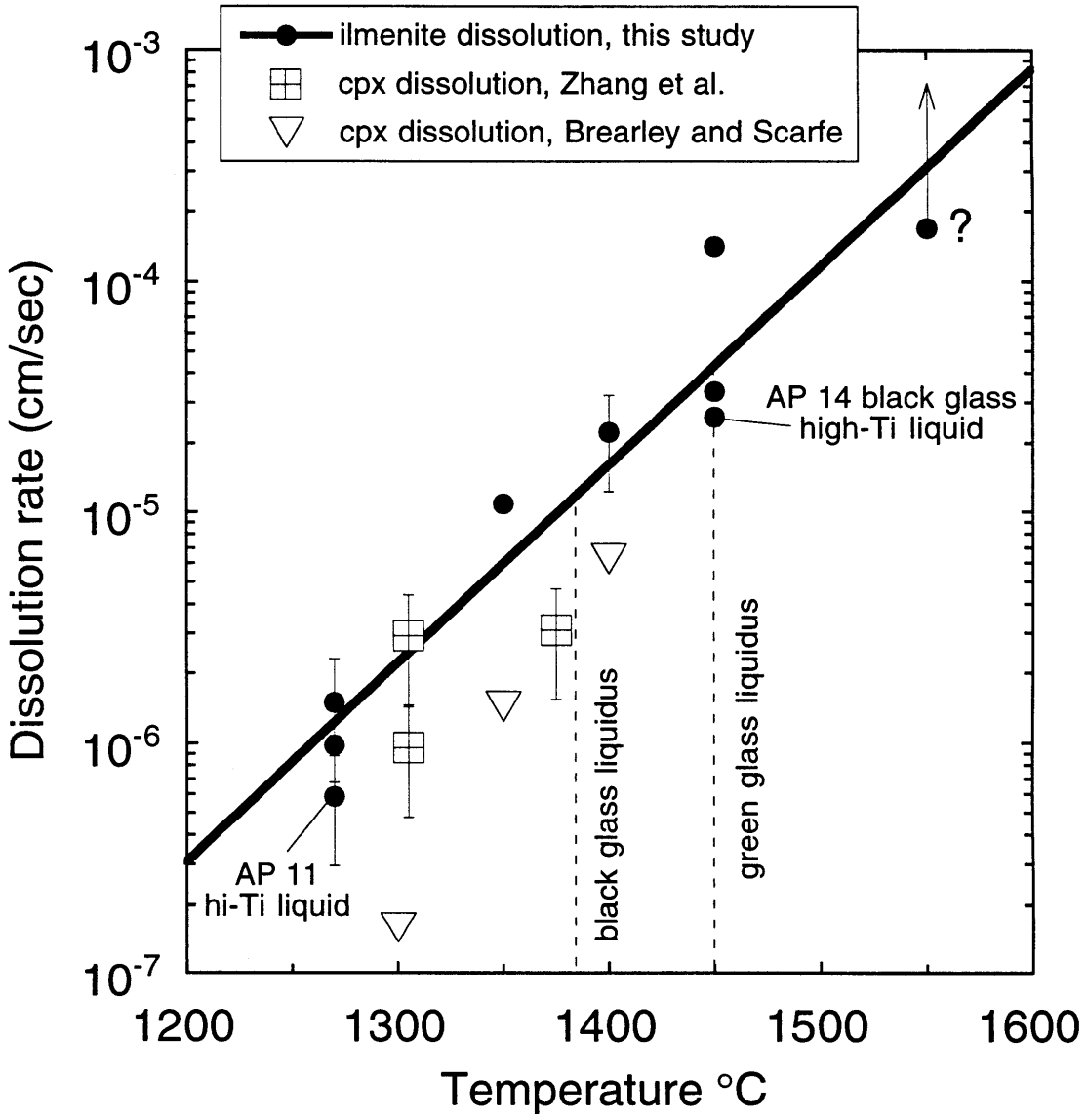
ilmenite dissolution, this study
cpx dissolution, Zhang et al.
cpx dissolution, Brearley and Scarfe
Dissolution rate (cm/sec)
10-3
10-4
10-5
10-6
10-7
1200
1300
1400
1500
1600
Temperature °C
?
AP 14 black glass
high-Ti liquid
AP 11
hi-Ti liquid
black glass liquidus
green glass liquidus

Figure 5 Experiment #51

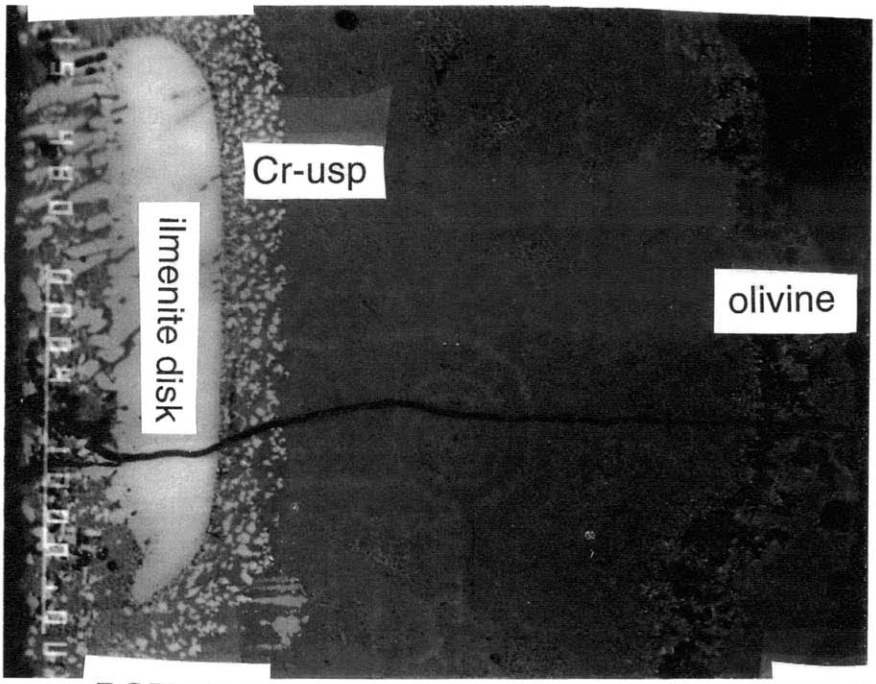

BOTTOM TOP

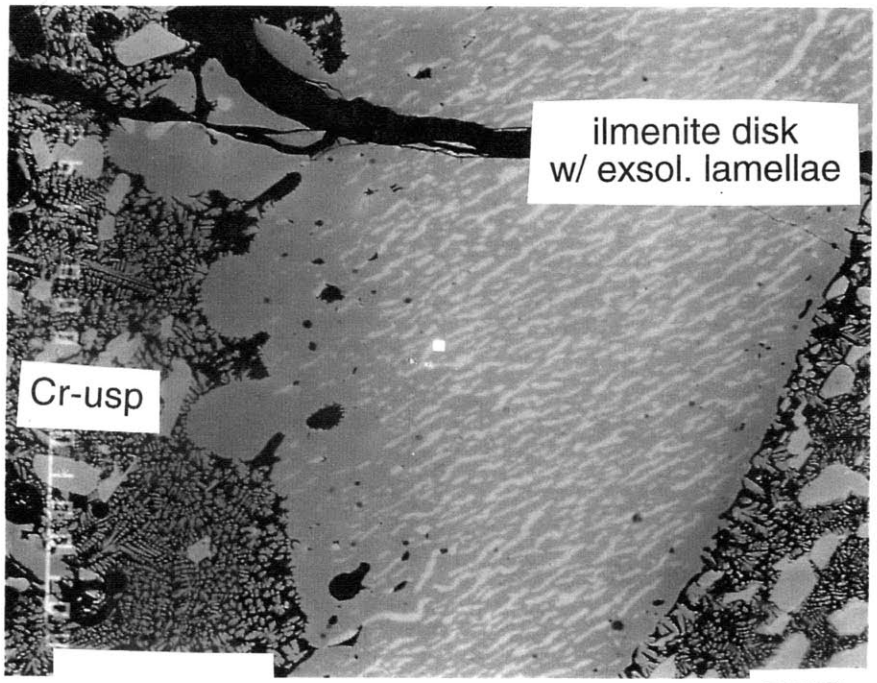

BOTTOM TOP

Figure 6

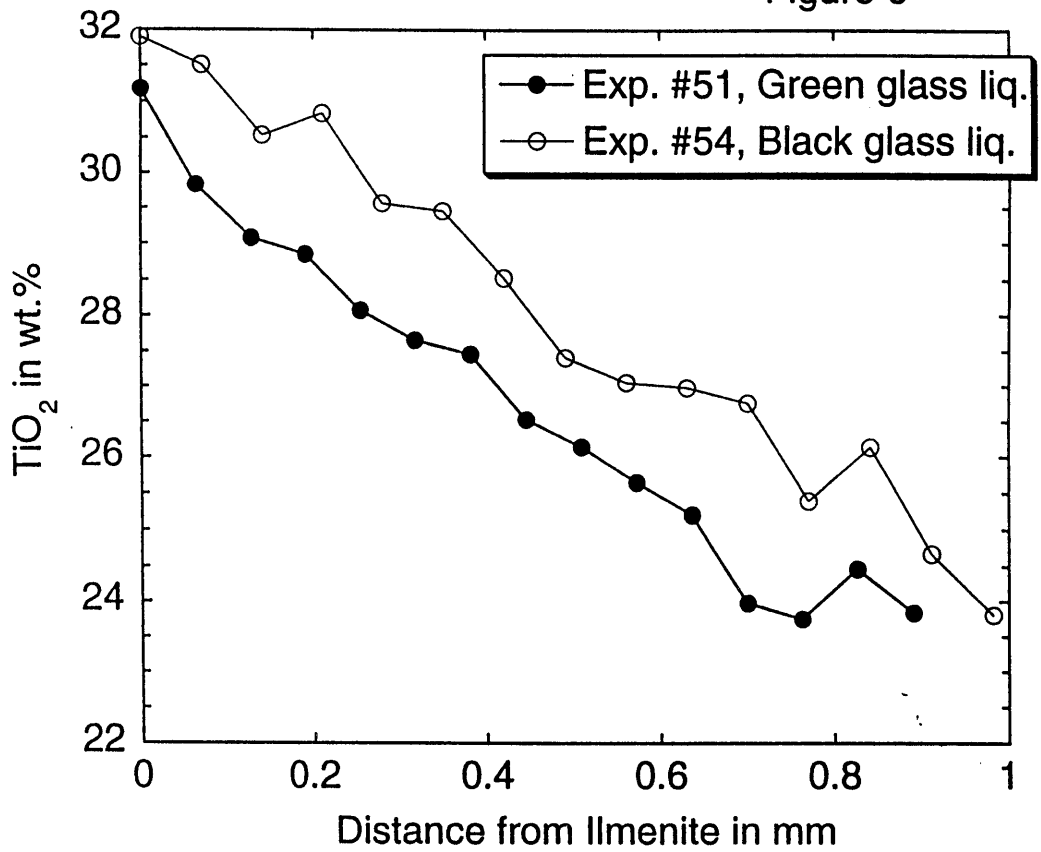
Exp. #51, Green glass liq.
Exp. #54, Black glass liq.
32
30
28
26
24
22
TiO_2 in wt.%
0
0.2
0.4
0.6
0.8
1
Distance from Ilmenite in mm

Figure 7

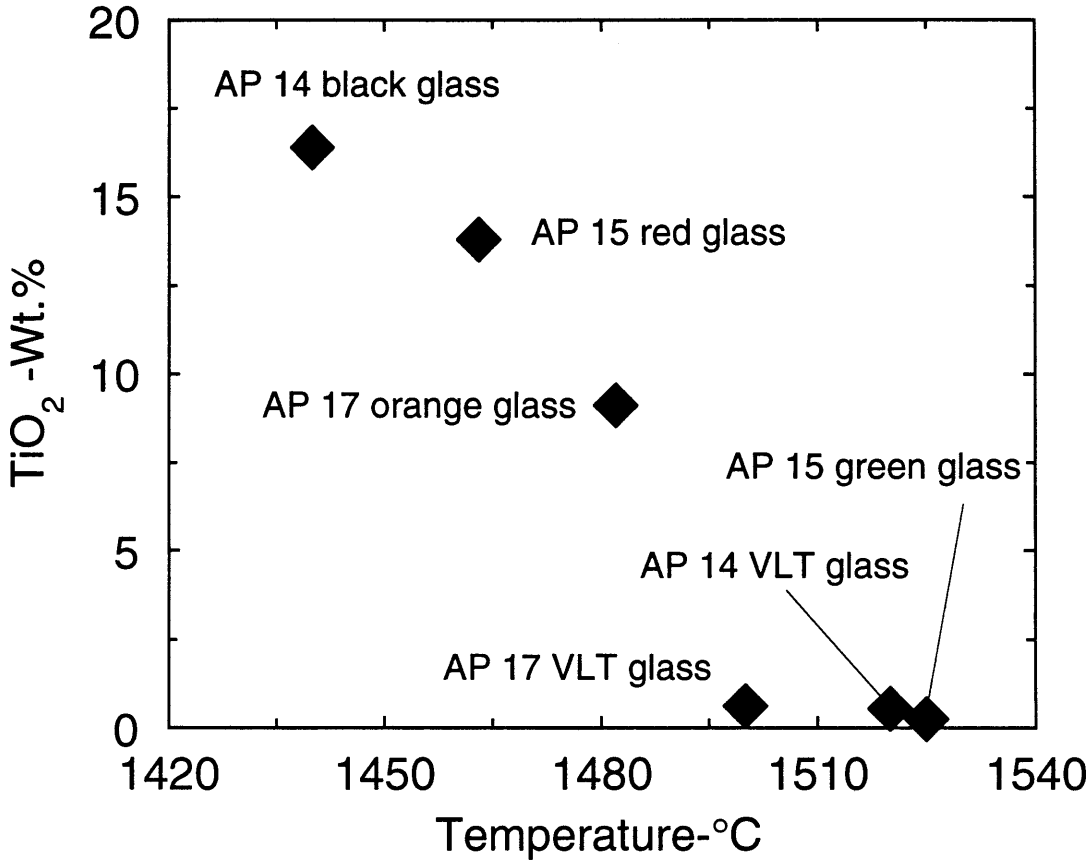
20
15
10
5
0
1420
1450
1480
1510
1540
TiO2 -Wt.%
Temperature-°C
AP 14 black glass
AP 15 red glass
AP 17 orange glass
AP 15 green glass
AP 14 VLT glass
AP 17 VLT glass

Figure 8

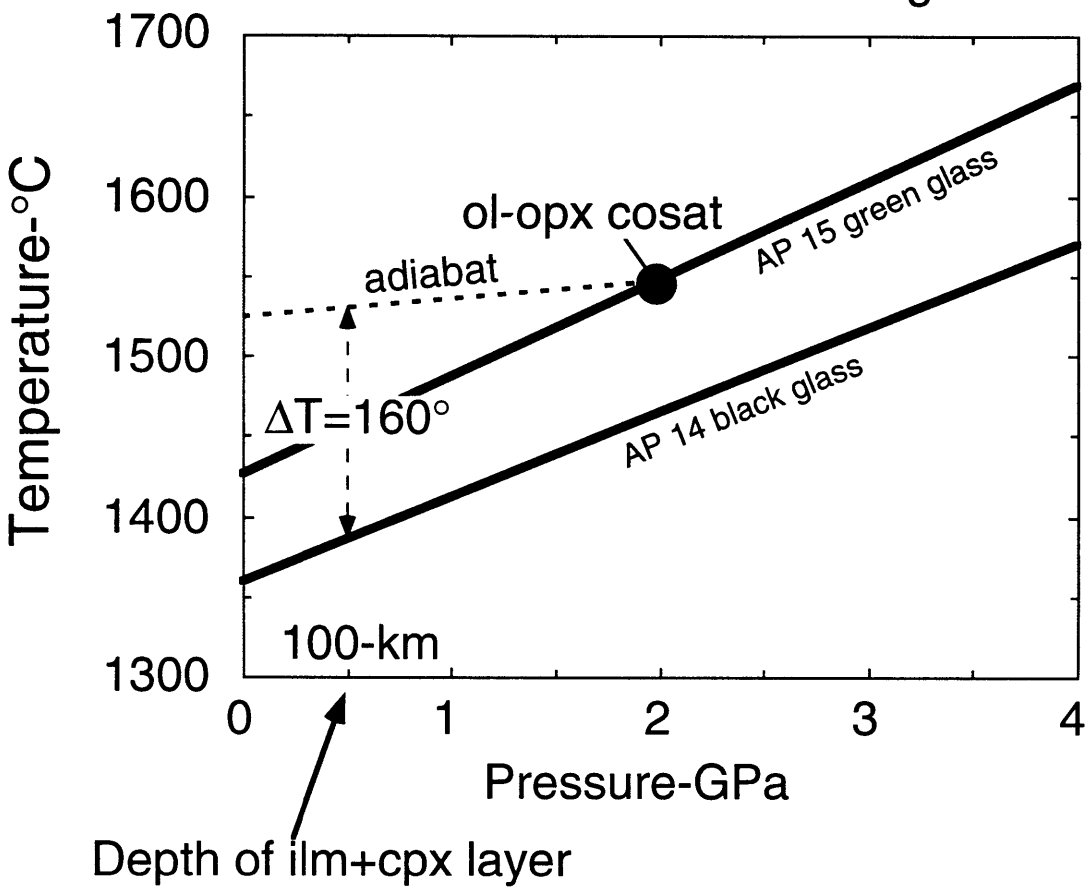
1700
1600
1500
1400
1300
Temperature-°C
ol-opx cosat
adiabat
AP 15 green glass
AP 14 black glass
ΔT=160°
100-km
0
1
2
3
4
Pressure-GPa
Depth of ilm+cpx layer

Table 1. Starting materials used in experiments.

Sample	MgO	Al_2O_3	SiO_2	CaO	TiO_2	Cr_2O_3	MnO	FeO	Na_2O	K_2O	Ni	P_2O_5
Phase equilibria study												
Apollo 14 black glass	13.3	4.6	34.0	6.9	16.4	0.92	0.31	24.5	0.23	0.16	-	-
Ilmenite dissolution rate study												
Ilmenite, Frank Smith Mine	11.4	0.64	0.13	0.07	51.8	1.70	0.17	33.2	-	-	0.22	-
Apollo 15 green glass, group C	18.2	7.74	48	8.57	0.26	0.57	0.19	16.5	-	-	-	-
Apollo 11 high-K basalt, 10072	7.64	7.89	41.2	10.5	12	0.28	0.24	19.4	0.34	0.27	-	0.19
Luna-24 ferrobasalt	6.31	12.6	47.1	12.8	0.88	0.23	0.25	20.2	0.2	0.02	-	-

Table 2. Conditions and results of phase equilibria experiments on Apollo 14 black glass.

Run #	Pressure-GPa	Temperature-°C	Duration (h)	Phases present	Proportions	Σr^2
B-162	2.18	1460	13	gl,opx,sp	1:tr:tr	-
B-166	1.70	1370	84	gl,ol,opx,sp	75:7:14:5	0.5
B-167	1.17	1370	22	gl,ol,opx,sp	87:10:2:1	0.4
B-169	1.19	1400	31	gl,ol	94:5	1
B-170	1.29	1385	44	gl,ol,opx,sp	91:9:tr:tr	0.2
B-171	1.66	1425	14	gl,ol,opx,sp	94:4:2:tr	0.2
B-172	1.41	1420	18	gl,ol,opx,sp	90:7:3:tr	0.5
B-175	1.48	1450	5.5	gl	-	-
B-176	2.22	1490	8.5	gl	-	-
BPC-17	1.16	1390	24	gl,ol,sp	95:4:1	0.4
B-181	0.86	1420	24	gl	-	-
B-182	1.48	1435	15	gl	-	-
1	0.0001	1360	4.5	gl,sp	1:tr	-
2	0.0001	1375	3.5	gl	-	-
3	0.0001	1400	3	gl	-	-

Table 3. Composition of run products in phase equilibria experiments on Apollo 14 black glass.

Run #	phase	N	MgO		Al_2O_3		SiO_2		CaO		TiO_2		Cr_2O_3		MnO		FeO		Na_2O		K_2O		Total
B-162	glass	7	13.4	2.4	5.1	0.5	33.9	2.6	7	1	16.4	2.7	0.94	0.2	0.33	0.06	23.2	1.5	0.15	0.08	0.11	0.06	100.2
	opx	8	27.5	0.4	2.9	0.3	53.2	0.5	1.64	0.06	0.95	0.1	1.12	0.1	0.21	0.02	13.4	0.1	0.03	0.03	-	-	100.9
	spin	3	10.8	0.3	11.9	0.1	0.31	0.01	0.13	0.03	11.5	0.4	34.4	0.8	0.25	0.00	31.5	0.7	-	-	-	-	100.7
B-163	glass	7	11.1	0.2	5.41	0.05	32.4	0.3	8.2	0.1	19.1	0.1	0.89	0.03	0.27	0.04	21.0	0.3	0.21	0.04	0.13	0.01	98.7
	opx	4	27.5	0.3	3.0	0.3	52.5	0.5	1.66	0.02	0.9	0.1	1.10	0.07	0.22	0.01	13.4	0.3	0.04	0.01	-	-	100.4
	spin	3	10.1	0.2	12.6	0.1	0.28	0.02	0.07	0.00	9.3	0.2	38.0	0.6	0.27	0.01	30.1	0.5	-	-	-	-	100.7
B-166	glass	7	9.3	0.1	5.82	0.05	31.5	0.1	8.95	0.06	18.2	0.1	0.42	0.04	0.33	0.05	24.6	0.3	0.27	0.03	0.14	0.00	99.6
	ol	3	37.2	0.09	0.11	0.03	37.7	0.1	0.31	0.01	0.22	0.03	0.21	0.01	0.28	0.03	24.8	0.2	-	-	-	-	100.9
	opx	5	25.6	0.3	3.2	0.5	51.9	0.7	2.3	0.1	1.1	0.1	0.8	0.1	0.26	0.02	15.2	0.1	0.06	0.00	-	-	100.5
	spin	3	8.5	0.1	1.64	0.03	0.06	0.00	0.11	0.01	52.1	0.2	6.1	0.2	0.25	0.01	33.1	0.3	-	-	-	-	101.9
B-167	glass	7	9.9	0.07	5.39	0.08	33.3	0.1	7.82	0.07	17.8	0.1	0.58	0.05	0.26	0.04	24.7	0.2	0.15	0.04	0.12	0.01	100.0
	ol	4	38.7	0.08	0.07	0.01	37.8	0.0	0.24	0.01	0.24	0.02	0.24	0.02	0.24	0.01	23.9	0.1	-	-	-	-	101.4
	opx	6	27.4	0.1	2.2	0.2	52.4	0.3	1.56	0.04	1.19	0.07	0.91	0.04	0.22	0.05	14.4	0.1	0.02	0.01	-	-	100.3
	spin	4	10.0	0.3	8.8	0.2	0.13	0.03	0.08	0.03	16.7	0.2	29.5	0.2	0.30	0.01	35.9	0.2	-	-	-	-	101.4
B-169	glass	7	11.3	0.1	5.16	0.05	34.33	0.20	7.32	0.05	16.5	0.1	0.81	0.07	0.24	0.04	24.0	0.2	0.18	0.05	0.11	0.01	99.7
	ol	4	39.7	0.2	0.08	0.05	38.05	0.04	0.22	0.01	0.17	0.01	0.26	0.01	0.22	0.03	22.4	0.2	-	-	-	-	101.1
B-170	glass	7	10.7	0.4	5.34	0.03	33.9	0.1	7.60	0.08	17.4	0.3	0.71	0.03	0.34	0.03	24.3	0.2	0.19	0.05	0.11	0.01	100.2
	ol	4	38.6	0.2	0.08	0.00	37.9	0.2	0.25	0.01	0.16	0.02	0.27	0.05	0.20	0.04	23.6	0.1	-	-	-	-	101.0
	opx	4	27.0	0.2	2.45	0.06	52.6	0.2	1.62	0.03	1.14	0.02	1.00	0.08	0.21	0.00	14.2	0.1	0.02	0.02	-	-	100.3
	spin	4	9.8	0.08	9.19	0.07	0.22	0.07	0.08	0.02	16.0	0.1	32.8	0.2	0.28	0.01	33.4	0.3	-	-	-	-	101.8
B-171	glass	7	11.7	0.08	5.06	0.03	33.1	0.1	7.29	0.02	16.8	0.1	0.75	0.05	0.25	0.05	24.7	0.2	0.20	0.03	0.13	0.01	99.5
	ol	7	40.3	0.1	0.09	0.01	37.9	0.2	0.23	0.01	0.25	0.01	0.29	0.01	0.25	0.01	21.3	0.3	-	-	-	-	100.7
	opx	4	28.2	0.3	2.3	0.4	52.6	0.4	1.46	0.04	1.06	0.12	1.01	0.15	0.18	0.01	13.1	0.1	0.01	0.01	-	-	99.9
	spin	2	11.0	0.10	10.0	0.1	0.26	0.00	0.13	0.00	12.9	0.1	34.0	0.0	0.26	0.01	31.5	0.0	-	-	-	-	100.1
B-172	glass	7	10.8	0.04	5.24	0.04	33.2	0.2	7.62	0.05	17.4	0.1	0.64	0.04	0.26	0.07	25.1	0.3	0.26	0.05	0.13	0.01	100.2
	ol	3	39.1	0.3	0.08	0.02	38.1	0.1	0.23	0.00	0.17	0.03	0.23	0.02	0.23	0.02	22.9	0.1	-	-	-	-	101.1
	opx	5	27.7	0.2	2.34	0.09	52.7	0.2	1.46	0.01	1.09	0.05	1.04	0.05	0.20	0.01	13.7	0.2	0.00	0.00	-	-	100.2
	spin	3	10.1	0.10	9.10	0.07	0.00	0.00	0.14	0.00	15.2	0.1	31.2	0.0	0.37	0.01	34.4	0.0	-	-	-	-	100.4
BPC-17	glass	7	12.0	0.08	5.02	0.04	34.1	0.2	7.25	0.05	16.4	0.1	0.64	0.04	0.28	0.07	24.3	0.2	0.20	0.04	0.12	0.01	99.9
	ol	3	40.1	0.1	0.07	0.02	38.3	0.3	0.22	0.01	0.17	0.03	0.29	0.02	0.23	0.04	21.4	0.1	-	-	-	-	100.8
	spin	3	10.3	0.1	7.35	0.07	0.00	0.00	0.14	0.00	14.5	0.1	35.5	0.0	0.35	0.01	32.3	0.0	-	-	-	-	100.4

Table 4. Conditions and results of ilmenite dissolution rate experiments.

Exp#	Liquid composition	Temperature °C	Initial length (cm)	Final length (cm)	Duration (sec)	Dissolution rate (cm/sec)	Phases present
49	Apollo 15 green glass	1450	0.074±3	0.038±1	255	1.41E-04	lq+ilm
50	Apollo 15 green glass	1400	0.107±3	0.099±3	375	2.23E-05	lq+ilm
51	Apollo 15 green glass	1450	0.086±4	0.026±2	1800	3.35E-05	lq+ilm+Cr-usp+ol
52	Apollo 15 green glass	1350	0.070±1	0.050	1800	1.09E-05	lq+ilm+Cr-usp+ol+pig
53	Apollo 15 green glass	1550	0.081±1	0.000	480	1.69E-04	lq+Cr-usp
54	Apollo 14 black glass	1450	0.074±4	0.027±1	1800	2.59E-05	lq+ilm+Cr-usp
66	Apollo 11 high-K	1270	0.077±4	0.074±4	5700	5.88E-07	lq+ilm
67	Luna 24	1270	0.156±4	0.148±8	5580	1.49E-06	lq+ilm
68	Luna 24	1270	0.076±1	0.058±2	18960	9.78E-07	lq+ilm

Table 5. Crystalline phases in some ilmenite dissolution rate experiments.

Phase	MgO	Al_2O_3	SiO_2	CaO	TiO_2	Cr_2O_3	MnO	FeO	NiO
				Experiment #51					
olivine	43.6	0.07	39.3	0.20	0.29	0.25	0.07	15.0	0.23
chrome-spinel	15.9	4.82	0.11	0.08	31.8	11.0	0.10	36.0	0.39
chrome-spinel	15.8	4.80	0.15	0.07	31.8	11.0	0.20	36.3	0.34
ilmenite disk	13.5	0.78	0.03	0.06	58.3	1.70	0.13	26.2	0.17
exsolution lamellae	13.6	1.78	0.15	0.02	38.4	2.57	0.23	44.2	0.25
				Experiment #54					
chrome-spinel	14.8	3.71	0.17	0.05	30.0	15.4	0.23	35.7	0.17
ilmenite disk	12.7	0.65	0.04	0.07	57.8	2.72	0.16	26.8	0.13

Table 6. Temperature and pressure of liquidus saturation with olivine and low-Ca pyroxene.

Mission	Glass type	TiO_2 (wt.%)	Temperature °C	Pressure (GPa)	Reference
Apollo 15	green	0.26	1525	2.0	1
Apollo 14	VLT	0.55	1520	2.2	2
Apollo 17	VLT	0.63	1500	1.8	3
Apollo 17	orange	9.12	1482	2.2	4
Apollo 15	red	13.8	1463	2.5	5
Apollo 14	black	16.4	1430	1.5	This study

Table 7. Mass balance calculation.

	Initial liquid	Reactants			Resultant liquid	
Oxide	Apollo 15 green	olivine	ilmenite	cpx	Model	Apollo 14 black
MgO	18.3	40.3	3.54	16.4	13.514	13.3
Al_2O_3	7.80	0.10	0.01	2.50	5.010	4.61
SiO_2	48.4	39.3	0.04	50.5	34.203	34.1
CaO	8.63	0.40	0.00	15.0	6.746	6.92
TiO_2	0.26	0.10	54.4	2.58	16.880	16.4
FeO	16.6	19.8	42.0	13.0	23.959	24.6
Proportions	0.6103	-0.0086	0.3027	0.0988	1	Σr^2=0.89
unc.	0.07	0.02	0.008	0.06		

Table 8. Thermal energy budget for assimilation reaction per gram of black glass liquid produced.

Heat available		Heat required
Superheat of liquid (ΔT=160°)	Olivine crystallization	Ilmenite and cpx assimilation
+29.3 cal/gram	+0.8 cal/gram	-40.0 cal/gram

Balance=-9.9 (25% short)

Table 9. Results of experimental studies of the dissolution rate of cpx.

Press. (kb)	Temp. °C	µm diss.	Time (seconds)	Diss. rate (cm/s)	Ilm. Diss. Rate	Ratio ilm/cpx diss
			Zhang et al. 1989			
21.5	1375	56	1810	3.1E-06	9.5E-06	3.1
10.5	1305	40	4190	9.5E-07	2.4E-06	2.5
10.5	1305	26	890	2.9E-06	2.4E-06	0.8
					Average	2.1
			Brearley and Scarfe 1986			
5	1250			1.1E-06	8.1E-07	0.7
5	1300			4.8E-06	2.2E-06	0.4
12	1300			1.6E-07	2.2E-06	13.6
12	1350	Time independent		1.4E-06	5.8E-06	4.0
12	1400			6.3E-06	1.6E-05	2.5
30	1450			9.1E-07	4.2E-05	46.4
30	1500			2.5E-05	1.1E-04	4.5
					Average	7.3

Appendix 1. Composition of liquid as a function of distance from the interface.

Distance (mm)	MgO	Al_2O_3	SiO_2	CaO	TiO_2	Cr_2O_3	MnO	FeO	P_2O_5	Na_2O	K_2O	Σ
					BPC-51							
0	13.5	3.88	21.4	4.09	31.2	0.46	0.16	25.0	0.05	0.00	0.00	99.7
0.064	13.5	4.00	22.0	4.46	29.8	0.62	0.09	24.5	0.06	0.05	0.02	99.1
0.127	14.1	4.07	21.7	4.21	29.1	0.49	0.14	25.0	0.00	0.08	0.00	98.8
0.191	14.5	3.89	22.6	4.26	28.8	0.43	0.28	24.3	0.10	0.05	0.00	99.3
0.255	14.4	3.98	23.5	4.42	28.1	0.50	0.14	24.3	0.06	0.00	0.03	99.4
0.318	14.4	4.03	23.2	4.32	27.7	0.49	0.13	24.0	0.05	0.06	0.02	98.4
0.382	14.6	4.33	23.7	4.48	27.5	0.51	0.18	24.3	0.09	0.13	0.00	99.8
0.446	14.9	4.34	24.4	4.55	26.5	0.60	0.11	23.8	0.02	0.11	0.01	99.5
0.509	15.0	4.30	24.7	4.49	26.1	0.46	0.07	23.8	0.04	0.05	0.00	99.0
0.573	15.0	4.48	25.0	4.72	25.7	0.48	0.20	23.6	0.03	0.00	0.01	99.2
0.636	14.8	4.38	25.3	4.52	25.2	0.46	0.08	23.0	0.11	0.08	0.00	97.9
0.700	15.9	4.40	26.7	4.72	24.0	0.40	0.13	22.6	0.08	0.11	0.00	99.0
0.764	15.3	4.59	26.6	4.78	23.8	0.46	0.13	22.5	0.04	0.07	0.02	98.3
0.827	16.6	3.95	25.1	4.17	24.5	0.52	0.16	23.6	0.07	0.08	0.03	98.7
0.891	14.2	5.06	27.4	5.07	23.8	0.42	0.20	23.1	0.06	0.13	0.02	99.5
					BPC-54							
0	12.5	3.07	20.0	4.28	31.9	0.65	0.20	26.7	0.08	0.09	0.08	99.5
0.070	13.4	2.88	20.0	4.10	31.5	0.66	0.18	26.7	0.12	0.12	0.08	99.7
0.140	12.6	3.07	20.9	4.33	30.5	0.56	0.21	26.2	0.09	0.07	0.08	98.6
0.210	12.4	3.21	21.0	4.33	30.8	0.75	0.24	26.3	0.08	0.11	0.08	99.3
0.281	12.6	3.09	21.3	4.49	29.6	0.71	0.12	25.8	0.08	0.09	0.08	98.0
0.351	13.0	3.18	22.1	4.53	29.5	0.62	0.14	26.2	0.09	0.12	0.07	99.5
0.421	13.0	3.12	23.3	4.55	28.5	0.74	0.25	25.7	0.10	0.16	0.10	99.6
0.491	13.2	3.28	24.4	4.70	27.4	0.60	0.19	25.4	0.10	0.17	0.07	99.5
0.561	13.6	3.13	24.0	4.72	27.1	0.64	0.25	25.4	0.08	0.19	0.10	99.2
0.631	13.5	3.24	23.5	4.29	27.0	0.74	0.24	25.9	0.06	0.20	0.10	98.7
0.701	13.7	3.26	24.1	4.77	26.8	0.51	0.25	25.8	0.07	0.14	0.11	99.5
0.772	13.9	3.41	25.1	4.72	25.4	0.69	0.27	25.2	0.10	0.05	0.10	99.0
0.842	13.9	3.42	25.7	4.81	26.1	0.49	0.16	24.3	0.08	0.10	0.10	99.2
0.912	14.2	3.41	27.3	5.18	24.7	0.45	0.10	23.9	0.07	0.21	0.12	99.5
0.982	14.3	3.56	27.8	5.37	23.8	0.50	0.19	23.2	0.10	0.19	0.10	99.1

Appendix A

Construction of the Piston-Cylinder

Overview

This appendix describes the design and construction of the end-loaded piston-cylinder device constructed to perform the experiments of Chapters 2 and 4. This device can be used to perform experiments in the pressure range of 1- to 3-GPa and the temperature range of 400 to 2000°C. My hope is that this document will be useful to users of the MIT devices as well as those who want to build their own. It is the guide I would have liked to have had when starting out.

The material is presented as general guide for the construction of piston-cylinder subsystems and contains descriptions and diagrams of the pumping, heating and cooling systems. These systems can be constructed entirely from off-the-shelf parts from the suppliers listed at the end. A discussion of the components of a piston-cylinder stack is also included. Emphasis is placed on component function, rather than design, since complex pieces like the pressure-vessel will likely be purchased pre-built. Parts of the MIT stacks were designed and modified by the author, but a detailed discussion of stack design is beyond the scope and intent of this work. The appendix is divided two major sections. Section one describes the pressure generating system including the press frame, stack and pumping system. Section two describes the temperature control system including the heating and cooling systems.

Pressure Generating System

The Press Frame

The press or load frame holds the entire apparatus together. Press frames are available in a variety of strengths and styles (3-post, 4-post, H-Frame) and can be purchased pre-built. The most important criteria for frame selection is tons of force the frame can withstand. This will be based on the pressure which the user would like achieve. For a 0.5" piston device (standard size) to achieve 3-GPa of sample pressure requires 43-tons of force. Above 2-GPa, three times as much end-load force should be applied as sample force, so the press frame should be at least 128-ton for 3-GPa experiments. Frames of this strength are available as a stock item from Enerpac corporation. The MIT press frame is three-post configuration with the end-load ram built into the base. Its strength is unknown, but it has been taken to 90-tons by the author without failure. The three-post configuration works well because it is useful to load various parts of the stack from the side. This may be a problem with H-frames.

The Stack

The stack is the business end of the device, where pressure is generated and the experiment is performed. It requires machinists skills to construct and some parts need to be purchased from companies specializing in their production.

Parts of the stack The stack (end on view in Fig. 1) consists of number of steel plates, each of which has a specific function. The *TC-line-feed-plate* allows the thermocouple (TC) leads to pass from the center of the stack to the temperature controller through a slot cut in the plate (side view in Fig. 2). The *TC-guide-plate* lines the TC up with the experiment and holds the sample assembly inside the *pressure-vessel,* where the sample-

assembly undergoes pressurization. The sample-assembly (discussed in appendix B) includes the pressure-media, heater and sample. The *bridge* provides space within the stack for the *sample-ram* to pump up and apply pressure to the *piston* and sample-assembly. The *end-load-ram* compresses the stack. *Spacer-plates* take up any daylight between the stack and the press frame and minimize the amount of pumping required on the *end-load-ram.* Also in the stack are mylar sheets which provide electrical insulation and force current through the heater instead of the press frame (electrical circuit described below). The O-rings (Fig. 2) on the *TC-guide-plate* and *bridge* keep cooling water from leaking out between the plates. The O-rings should be made of Viton™ instead of butyl rubber to prevent breakdown during high-temperature experiments or China-syndrome-type accidents (accidental cooling water shut-off). High temperature silicon cement (General Electric Red RTV 106) can be used to hold the O-rings in place

The tungsten-carbide (WC) pieces in Figs. 1 and 2 are the load-bearing portions of the system. The *piston* applies pressure directly to the sample-assembly and is subject to very high pressures and temperatures. The *puck* is the link between the *piston* and *sample-ram.* The *TC-guide-plate, bridge and pressure-vessel* have WC-cores due to the high loads placed on them. The *pressure-vessel* is the most complex part of the design. It is formed interference fit rings of different material. At the center is the WC-core. Though WC has a lot of strength under compression, it has little strength under tension. The WC-core is interference fit into two rings of hardened steel which tightly compress it. The cores used on our laboratory are under 3-GPa of confining pressure and purchased from Rockland Research Corp. A soft steel safety ring is placed around the outside of the rings in the event of failure of the core and hardened rings. The WC pieces should be grade C-2 and can be purchased from a technical ceramics company (Chand Associates Inc.) that specializes in hot-isostatic pressing (HIPing). Most of the other pieces of the stack can be made by a machinist out of tool steel.

Warnings: 1) When setting up the stack, the slot in the *TC-line-feed-plate* should be oriented away from the user. In the event of core failure during an experiment superheated-gas may escape out this slot and severely burn the user. During core failure, high-temperature, low-pressure conditions may be produced in sample-assembly and may cause the $BaCO_3$ pressure media to de-carbonate. The super-heated CO_2 gas will vent through the thermocouple feeds and come out through the slot in the *TC-line-feed-plate.* 2) The mylar sheets should be replaced whenever cuts or tears begin to appear. The primary cause of core failure at MIT is arcing between the *TC-guide-plate* and *pressure-vessel* core causing small cracks which nucleate larger cracks. 3) Cooling water will quickly rust the steel plates. They should be covered anti-rust agent such as Permalex high temperature Anti-Seize Lubricant (NAPA # 765-1674) available from auto parts distributors. An anti-corrosive fluid could also be added to the cooling water.

The Pumping System

This part of the system can be constructed entirely from off-the-shelf parts by someone with good mechanical skills. The stack described above requires two pumping systems, one to drive the *end-load-ram* and another to drive the *sample-ram.*

Ram and pump selection The ram (or hydraulic-cylinder) is the first important choice. There are number of low-cost hydraulic rams and pumping systems available that go to 10,000-psi, which is the pressure standard for use in the vehicle repair industry. We chose the RR-1502 hydraulic cylinder from Enerpac corporation based on its size and heavy load capacity. It has a piston diameter of 6.25" and can be pumped to 10,000-psi. When driving a 0.5" piston it can theoretically achieve sample pressures of 10.7-GPa, well above the limit of available pressure-vessels. Enerpac (and a number of other companies) make hand-powered and electrical pumps that go to 10,000-psi. We used the

P-39, hydraulic hand pump from Enerpac. It can achieve 10,000-psi and has a 43-cubic-inch volume which is more than sufficient.

Pumping system design The pumping system we designed is very simple (Fig. 3) and consists of a pump, valve and gauge. Hand pumps are inexpensive (~$150) enough that it is cheaper to design two independent systems for the two rams than to add an extra valve and use one pump. Between the valve and pump, a pressure sensitive *blow-out* device (Autoclave Engineering Inc.) was added to keep the user from over-pumping the system. The *blow-out* consists of a metal disk (Inconel) which is set up on one end of a standard three-way connector. The pressure at which the disk will rupture is set by the torque on the nut which holds it in place.

Tubing The use of 10,000-psi tubing also allows the use swage-type fittings. Swagelok™ (Swagelok Corp.) and Speed-bite™ (Autoclave Engineering Inc.) are the two common brands. These fittings allow the user to cut tubing, place it in the fitting and simply tighten to make the connection. This is orders of magnitude easier than cone-seat type fittings required for pressure applications >10,000-psi. We use 1/4" stainless-steel tubing and fittings throughout the laboratory. Its inner diameter easily accommodates the oil volumes required for piston-cylinder applications. Swagelok and Autoclave recommend fully annealed, high quality seamless or welded and drawn 316 SS tubing, ASTM A269 or A213 or equivalent. For 10,000-psi 1/4" stainless steel tubing to be used with swage fitting, the tubing should have a wall thickness of 0.065" and a hardness of Rb80 or less. The slightly softer hardness is required to make the proper swage at the fitting (this also means the tubing is much easier to bend than typical high pressure tubing!). If possible, a tubing bender should be used to bend the tubing. This will assure that all bends exceed the minimum radius of curvature for the tubing and make the system stronger.

Valves A variety of inexpensive valves are available in this pressure range. We used the stainless steel, Whitey SS-3HNBS4 for severe service (Swagelok Corp.). This valve has a ball-tip stem and seat and holds up well under repeated use.

Pressure gauges The selection of the end-load-ram pressure gauge is not of critical importance. The end-load does affect the sample pressure and a reading of ±5-10% is acceptable. The sample-ram pressure gauge is important for reproducing pressure in the experiment and should be very precise. We use a Heise bourdon-tube gauge. Note should be taken to purchase a gauge in the correct range!

Temperature Control

Temperature control has two goals. Goal one is to heat and maintain the experiment at the desired temperature. This is accomplished through the heating system which controls the temperature in the experiment by monitoring temperature and varying the amount of current sent to the heater. Goal two is to keep the outer parts of the system cool to prevent their failure. This accomplished by running cooling water through parts of the stack and a refrigerated water recirculator. Both the heating and cooling systems can be constructed from off-the-shelf parts with the same level of mechanical skills required to build the pumping system and basic knowledge of electricity.

The Heating System

Piston-cylinder devices commonly use graphite heaters. During the course of the experiment the characteristics these heaters change such that a sophisticated temperature controlling device is required for precision temperature control. This device can be purchased from a number of vendors. The remainder of the system can be made of stock parts from an electrical supply house.

Temperature control We selected the Eurotherm 818s temperature controller and use it to run a Eurotherm 470 true power controller. The 818s is easily programmed to accept different thermocouple types. It also allows easy programming of multiple temperature ramps and ramp rates. Both of these features have proven very useful. The 470 controls power, as opposed to just current or voltage (hence the name, *true* power controller), and can easily adjust to the changing resistance conditions in the graphite heater. This system controls the heater to within ±1° at temperatures above approximately 400°C. It is, however, a difficult system to trouble shoot. Even when wired incorrectly it can

compensate and work well for long periods of time, but will eventually break and require repair and calibration at the factory.

System design The temperature control circuit is shown in Fig. 4. The 818s measures the temperature in the sample assembly through the TC-line (shielded coaxial cable) and controls the power output of the 470. The 470 puts out a ~240-VAC signal which is run through a 20:1 step-down transformer to convert it to 12-VAC and a LOT of amps. The transformer is connected to the stack such that current is forced through the heater in the sample assembly. The high-amperage requires a large diameter conductor. We use 4x0 welding-cable. Welding-cable has very low resistance due to the high number of strands in it and is also relatively flexible and easy to manipulate.

Current (Fig. 4) goes from the transformer to the TC-guide-plate, where it is blocked by mylar insulators from passing through everything except the graphite heater in the sample-assembly. The current exits via the piston and bridge and back to the transformer. The circuit is isolated by the transformer such that current must return to the transformer. You should not be able to be shocked by touching the device and a ground out of the circuit. However, current will flow between a point between the mylar sheets and any other point on the device (e.g. press frame, pump handles). For example, if a tool touches the TC-guide plate and one of the press-frame posts, CURRENT WILL ARC ACROSS, which is not good for you or the controller.

Warnings: 1) Never touch or attempt to hook up the power leads with the temperature control system plugged in. 2) Always ground leads before working with them by touching them to the press frame. The 818s has a bug in its *output-power-reading*. There are certain conditions such that the 818s will read zero output power, but the power leads are LIVE and if you touch them you could be killed. In addition, the 470 has a large inherent capacitance. If the controller was powered down incorrectly, the 470 will have a large amount of stored current that it will let loose on start-up. Example: previous run crashed due to thermocouple failure or was quenched by pulling the plug rather than using the

controller to quench. Old run is removed and a new one set up. As the system is plugged in, the temperature will shoot up to about 300°C then fall back down to room temperature. That could have been you!

The Cooling System

The high-temperatures and long durations of silicate melting experiments require that the piston-cylinder stack be cooled throughout the experiment. This is accomplished by running refrigerated water through parts of the stack.

System design The system must continually flow cool water across the top and bottom of the pressure-vessel. The TC-guide-plate and bridge have wells cut into them between their outer edge and the WC cores, on the side adjacent to the pressure-vessel (not shown in figures). When pressed against the pressure-vessel these wells provide pathways for water to flow through the compressed stack, following the arrows in Fig. 5. Water flows from the cold water source to a port on the TC-guide-plate, across the top of the pressure vessel and out a port on the opposite side. It then flows through a short hose to a port on the side of the bridge, across the bottom of the pressure-vessel, out a port on opposite side and back to the water source. The water source in Fig. 5 is a Neslab CFT model 33 refrigerating recirculator. This unit breaks regularly and its purchase is not recommended. The system is rated to cool at 3751 BTU/hour at 20°C. It can keep the water temperature at 30°C for a typical experiment (water flowing at 45-psi through 3/8" fittings). At this cooling water temperature, the stack and end-load-ram heat up for the first 10-15hrs of the run, resulting in a slight pressure increase in the experiment. The valves in Fig. 5 are for purging water in the apparatus at the end of an experiment. The water is blown out by closing the valve on the H_2O supply side and opening the valve to the compressed air. The quick-connect on the H_2O-return side of the recirculator must be opened to prevent the compressed air from blowing out plumbing in the water recirculator.

Valves, fittings and tubing The water recirculation system is low-pressure, 40 to 60-psi at most. The compressed air system is somewhat higher (we use building air). 3/8" brass valves and fittings are used throughout with standard air-compressor type quick-connectors on the stack and in-line with the return-side of the water recirculator. Tubing is rubber, 300-psi rated braided hose by Boston Perfection. It is connected to standard hose connectors and cinched down with metal hose clamps. We initially used Tygon™ tubing through the system but the temperatures and pressures caused it to stress and fail.

Warnings Even with cooling, the stack will heat up. This can cause a number of problems, not the least of which is ruining pressure control during the experiment. As the stack heats up, the oil in the sample-load-ram also heats up and expands, causing perpetual pressure increases in the experiment. If the water is maintained at 30°C, the stack should complete its heat-up cycle within 12- to 15-hrs. This is acceptable for long duration, multi-day experiments but should be figured in for shorter duration runs. If the stack is not cooled during a typical silicate melting experiment (1100° to 1600°C) it will get too hot to touch within 15 to 20 minutes and exceed the melting point of butyl rubber in approximately 30 minutes. This has happened in cases where the cooling water was accidentally turned off or never turned on. When this happens, the O-rings on the TC-guide-plate and the bridge will melt and need to be replaced. The high temperatures will also ruin the oil-seals in the sample- and end-load-rams if ignored too long. The small screen filter inside the water recirculator should be cleaned regularly (every 15 experiments).

Figure Captions

Figure 1. Piston-cylinder stack, end on view. The sample assembly would be located in the center of the pressure vessel.

Figure 2. Piston-cylinder stack, top-down view of individual plates.

Figure 3. Pumping system for both sample- and end-load-rams. *Wagner Power Pumper* is in no way related to a Wagner Power Painter™.

Figure 4. Heating system showing electrical components and connections to the stack.

Figure 5. Cooling system showing connections to stack.

Suppliers

Autoclave Engineering Inc.
2930 West 22nd Street
Erie PA 16512-9989
814-838-3806

Local Supplier: Power & Process Inc.
P.O. Box 7117
1168 Farmington Ave
Kensington, CT 06037
203-828-9976

Chand Associates Inc.
2 Coppage Dr.
Worcester, MA 01603-1252
508-791-9549

Enerpac Corporation

Local Supplier: Toomey Associates
1101 Russell Rd
P.O. Box 577
Westfield, MA 01086-0577
1-800-762-5192

Eurotherm Corporation
11485 Sunset Hills Road
Reston, VA 22090
703-471-4870

Local Supplier: PTSystems
565 Carriage Shop Rd
P.O. Box 3288
East Falmouth, MA 02536
508-457-9055

Neslab Instruments
P.O. Box 1178
Portsmouth, NH 03802-1178
(800)-258-0830

Swagelok Company
Solon, Ohio 44139

Local Supplier: Cambridge Valve and Fitting Inc.
50 Manning Rd
Billerica, MA 01821
617-272-8270

Rockland Research Corporation
16 Tompkins Ave
West Nyack, NY 10994
914-353-4686

Figure 1

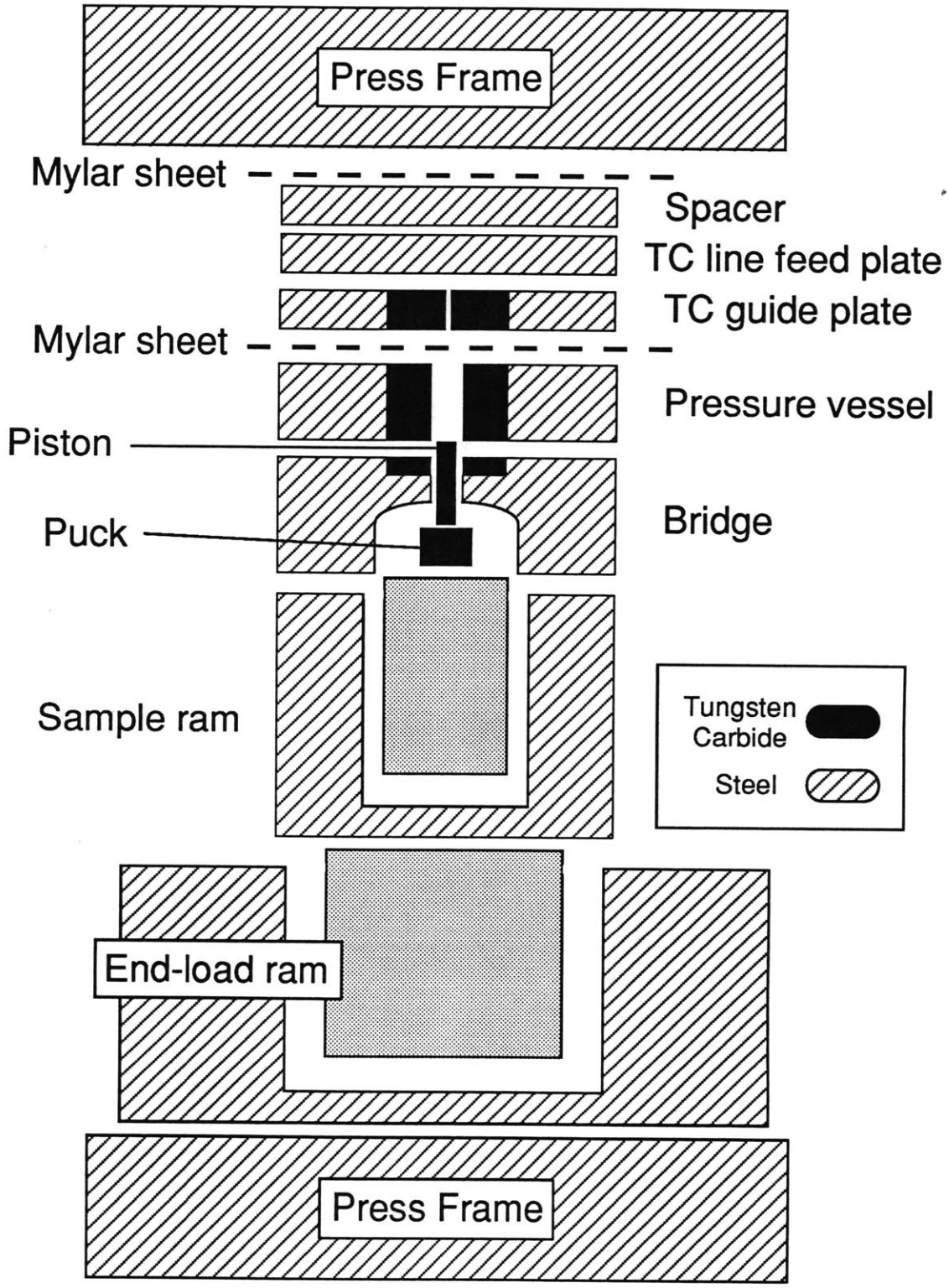
Press Frame
Mylar sheet
Spacer
TC line feed plate
TC guide plate
Mylar sheet
Pressure vessel
Piston
Puck
Bridge
Sample ram
Tungsten Carbide
Steel
End-load ram
Press Frame

Figure 2

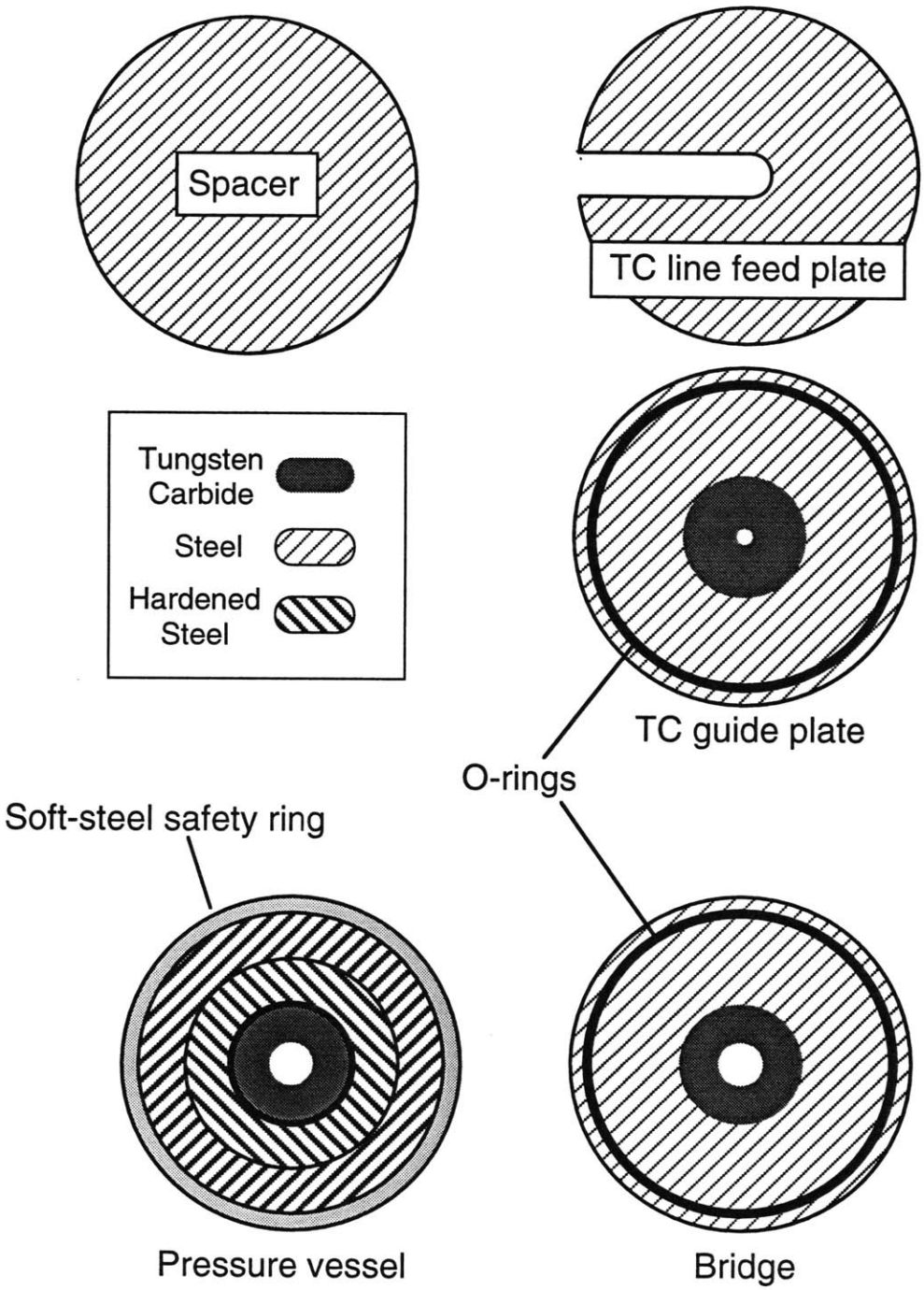
Spacer
TC line feed plate
Tungsten Carbide
Steel
Hardened Steel
TC guide plate
O-rings
Soft-steel safety ring
Pressure vessel
Bridge

Figure 3

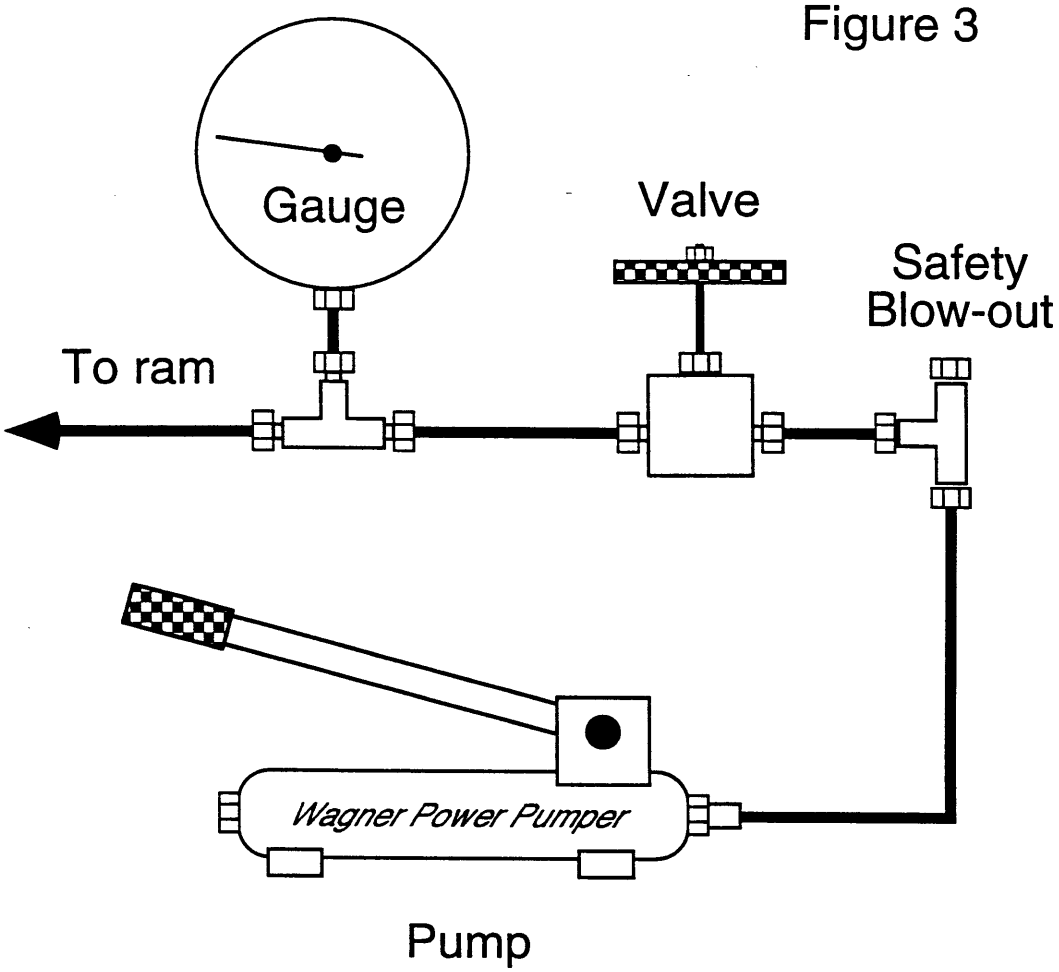

Figure 4

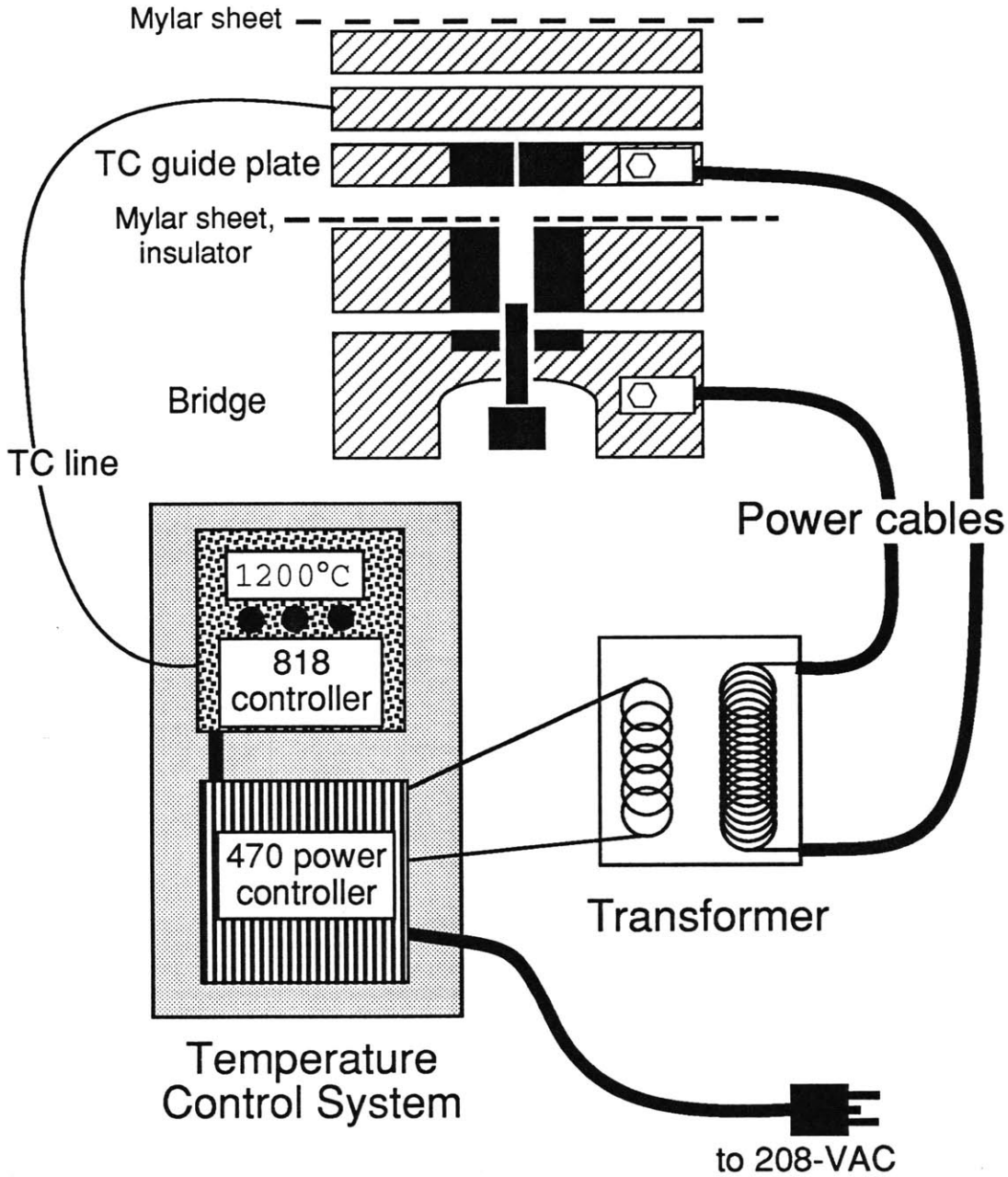
Mylar sheet
TC guide plate
Mylar sheet, insulator
Bridge
TC line
Power cables
1200°C
818 controller
470 power controller
Transformer
Temperature Control System
to 208-VAC

Figure 5

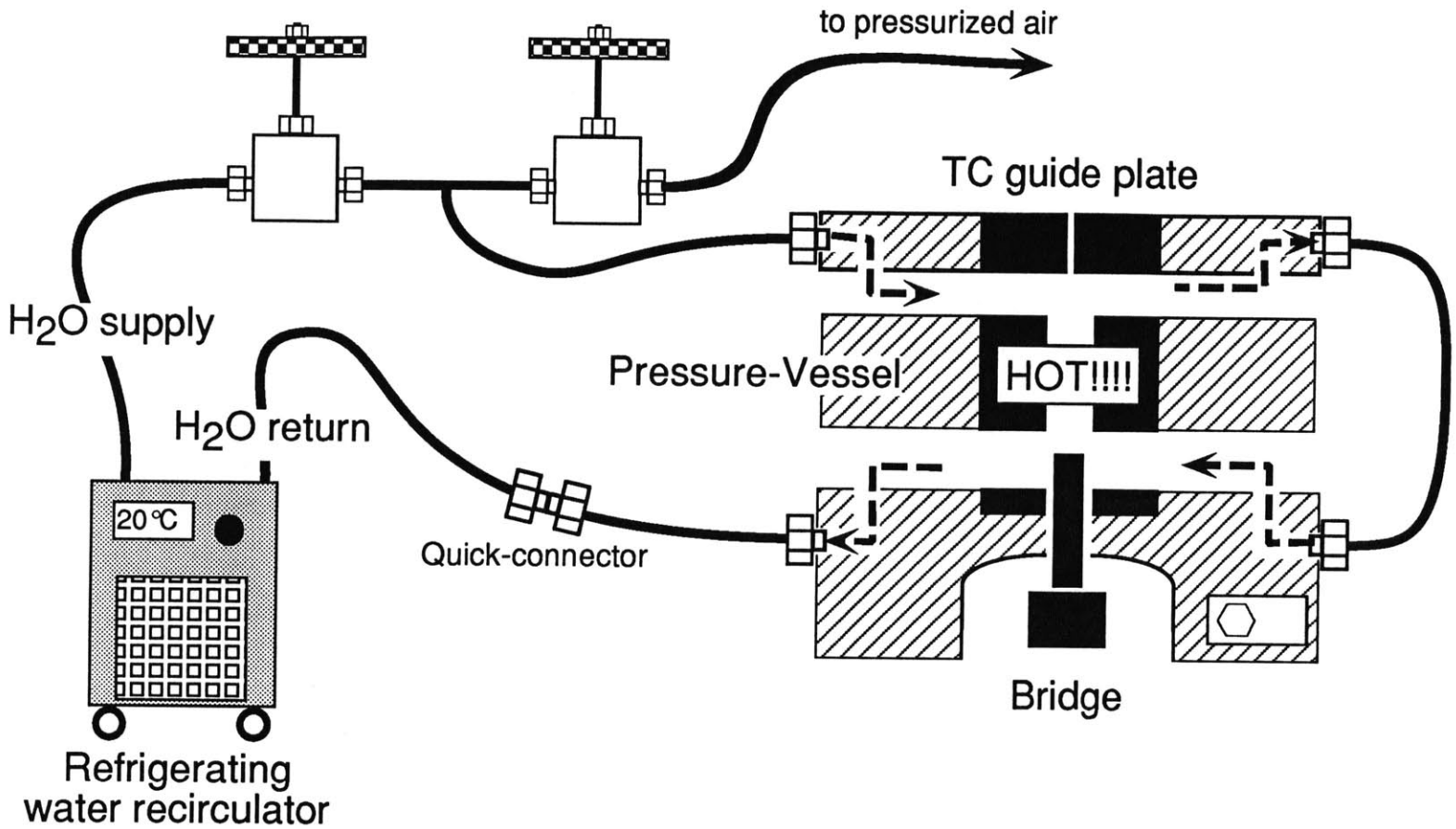
to pressurized air
TC guide plate
H_2O supply
Pressure-Vessel
HOT!!!!
H_2O return
20 ℃
Quick-connector
Bridge
Refrigerating
water recirculator

Appendix B

Piston-Cylinder Sample-Assembly and Calibration

Overview

This section describes the sample-assembly and calibration of the piston-cylinder apparatus described in appendix A. Pressure corrections for piston-cylinder devices are dependent on the small uncertainty associated with the device and the large uncertainty associated with the friction-correction. The friction-correction depends on the characteristics of the sample assembly, primarily on the material used as the pressure media. This appendix is divided into two parts. Part one is a description of the sample assembly with detailed instructions on making $BaCO_3$ pressure-cells. Part two describes the calibration procedure.

Sample Assembly

Description of parts

The sample assembly (Fig. 1, Table 1) is designed to heat and accurately measure temperature to 2000°C, be non-reactive to molten silicate and maintain its geometry while being crushed under enormous forces. It is an engineering marvel. The material of interest (silicate in Fig. 1) is placed inside a graphite capsule which is welded into a Pt outer capsule. This capsule is placed inside an Al_2O_3 sleeve and then positioned in the center of a graphite heater with MgO spacers. The thermocouple ($W_{97}Rh_3$–$W_{75}Rh_{25}$) is threaded into an electrically insulating Al_2O_3 ceramic. The ceramic is fed through a hardened steel plug and the MgO spacer towards the top of the Pt capsule. The steel plug is surrounded by a thin pyrophyllite gasket. The bottom of the assembly is a graphite disk that makes a strong electrical contact between the heater and piston. The $BaCO_3$ cell surrounds the graphite heater and maintains hydrostatic stresses throughout the assembly. A thin layer of Pb-foil is wrapped around the $BaCO_3$.

$BaCO_3$ cell preparation

Pressure media selection There are a variety of materials that can be used for the pressure media, all of which have advantages and disadvantages. $BaCO_3$ is the most stable pressure media in common use. It is, however, toxic to animals. NaCl is non-toxic, but allows horizontal movement within the sample assembly and causes thermocouple failures. In over 200 runs with $BaCO_3$ cells, I have yet to have a failure due to thermocouple failure. Talc is also non-toxic (unless you are a zinc miner), but contains H_2O which can contaminate the charge. Fluorite offers a possible alternative that should be investigated.

Cell preparation The cell is made by pressing the $BaCO_3$ into a hollow cylinder and sintering it in a furnace. Cells are made from granular, calcined $BaCO_3$, mixed with

photocopy-machine toner that acts as a binder. Each cell requires 7.3-g of $BaCO_3$ and 0.2-g of toner (Table 2). Mix enough material to make 10 cells in a container with a tight cap. Mix the contents by rapid agitation of the container. Weigh out 7.5-g of mix and pour it into the cell press (Fig. 2, specifications in Table 3). The inside of the cell press should be lubricated with MoS_2, G-n Metal Assembly Paste™ (Dow-Corning Company). Pressurize the powder with 10-tons of force. Maintain it at pressure for 1-minute and press out. The resulting cells should be approximately 1.23" in length (Table 2). Cells should be fired in a furnace at 700°C for 30 minutes. Upon firing the toner (finely chopped plastic) will ignite, so firing must be performed under a hood. After firing cell will be 1.25".

Warnings: $BaCO_3$ is the active ingredient in rat poison. It is clear from the Material Safety Data Sheet (MSDS) that little is known about its affect on humans. According to the sheet, it will probably not hurt you in small doses but will kill you in large doses. Good housekeeping measures are recommended during its use. I cover all areas where it will be used with paper. I also wash all the parts I've touched including the balance etc. The material we use is granular so it does not create much dust when weighed out, but could be weighed out under a hood to prevent unnecessary exposure.

Calibration

Thermal gradient measurement

The thermal gradients in the sample assembly were measured while carrying out a series of differential thermal analysis experiments using two thermocouples (TCs) offset in the heater. In these experiments, a notch was cut in the side of the 4-holed alumina TC ceramic 0.1" from the end, such that two of the holes were exposed. A $W_{97}Rh_3$ TC leg was run through one of these holes and out to the bottom of the ceramic, leaving an exposed area at the notch. A $W_{75}Rh_{25}$ leg was run through the other exposed hole. At the notch, the end of this leg was bent and looped under the $W_{97}Rh_3$ leg, forming a complete TC circuit. A $W_{75}Rh_{25}$ leg was then run through one of the remaining unexposed holes and used to form a TC circuit with the $W_{97}Rh_3$ leg at the bottom of the ceramic. The length of the sample assembly pieces were altered such that the longer TC was located in the center of the furnace and the shorter leg was located 0.1" above the hotspot. The temperature difference between these thermocouples was measured in a number of experiments above 1000°C and is approximately 20°.

Pressure calibration

The piston-cylinder device and $BaCO_3$ sample-assembly were pressure-calibrated against the transition of anorthite-gehlenite-corundum to Ca-Tschermak's pyroxene (CaTs) as determined by Hays (1965). Differential thermal analysis measurements were also carried out using Au and NaCl. We found this technique to be more difficult to perform and less reproducible than the CaTs synthesis experiments.

Starting material A synthetic mix of $CaAl_2SiO_6$, Ca-Tschermak's pyroxene, was prepared from high-purity synthetic oxides. This mix was ground in agate mortar for 6-hours to ensure homogeneity.

Method The phase diagram for $CaAl_2SiO_6$ was determined by Hays (1965). This composition forms anorthite-gehlenite-corundum (an-geh-cor) at low pressures and CaTs at higher pressures. The phase boundary was determined over a wide range of temperatures by Hayes and is described by the equation:

$$\text{Pressure} = 12500+9.9*(\text{Temperature}-1250) \quad (1)$$

where Pressure is in bars and Temperature is in Centigrade. The reaction is strongly dependent on pressure, as opposed to temperature, which makes it a good choice for a pressure calibration.

Starting material was loaded into Pt capsules and run in an assembly identical to Fig. 1, minus the graphite capsule. $CaAl_2SiO_6$ will not react with the Pt so the graphite is unnecessary. All experiments were performed at 1300°C, where the phase boundary between CaTs and an-geh-cor is 1.3-GPa (equation 1). Runs were cold pressurized to 1.0-GPa and then ramped up to 865°C at 100°C/minute where they were held for 6 minutes. They were then pumped to desired run pressure (1- to 1.6-GPa) and ramped to 1300°C at 50°C/minute. Experiments were quenched by shutting of the power. The reaction kinetics were previously determined in a series of CaTs synthesis experiments. The synthetic powder converts to CaTs or anorthite-gehlenite-corundum in under 4-hrs. Calibration experiments were all performed at a minimum of twice this value, one run near the transition point was held for 68-hrs.

Results Our results (Table 4) show the boundary at 1.3-GPa, indicating that there is almost no correction required for this device using the $BaCO_3$ assembly. This result was surprising. Pressure calibrations of other piston-cylinder devices using the $BaCO_3$ assembly in our lab, as well as at the University of Chicago and Columbia University

laboratories, yielded pressure corrections of ~0.3-GPa. The friction correction between different laboratories is likely somewhat variable due to differences in the technique of cell preparation, but the inter-laboratory corrections are too similar for there to be much dependence on this variable. Determining the force exerted by the ram on the sample requires knowledge of the ram-radius and a measurement of ram-oil pressure. The uncertainty, then, must lie somewhere in this estimation.

Oil pressure is measured by a new, factory-calibrated, Heise bourdon-tube gauge. We are only running within the lower third of the gauge's range, so there is likely some uncertainty in the oil-pressure measurement, but not enough to account for 0.3-GPa uncertainty. This device uses a very-large capacity sample-ram (Enerpac RR-1502, discussed in appendix A). The piston radius of this ram is 6.25", nearly twice that of the average piston-cylinder sample-ram. Enerpac states in their catalog that specifications are subject to change without notice. Calls to Enerpac yielded decidedly vague answers with regards to specific details of the ram specifications, likely because some of the oil-seal technology is proprietary. In any case, the device is now accurately calibrated. This has been independently confirmed by the comparing phase assemblages in silicate melting experiments performed in this device and the other calibrated MIT device.

References

Hays JF (1965). Lime-alumina-silica. Yearb Carnegie Inst Wash 65: 234-236

Figure Captions

Figure 1. The sample assembly.

Figure 2. The $BaCO_3$ cell press. All pieces should be made of hardened steel. The short piston should be used to pressurize the cell. The long piston should be used to push it out. Piston dimension are given in Table 3.

Figure 1

Not to scale

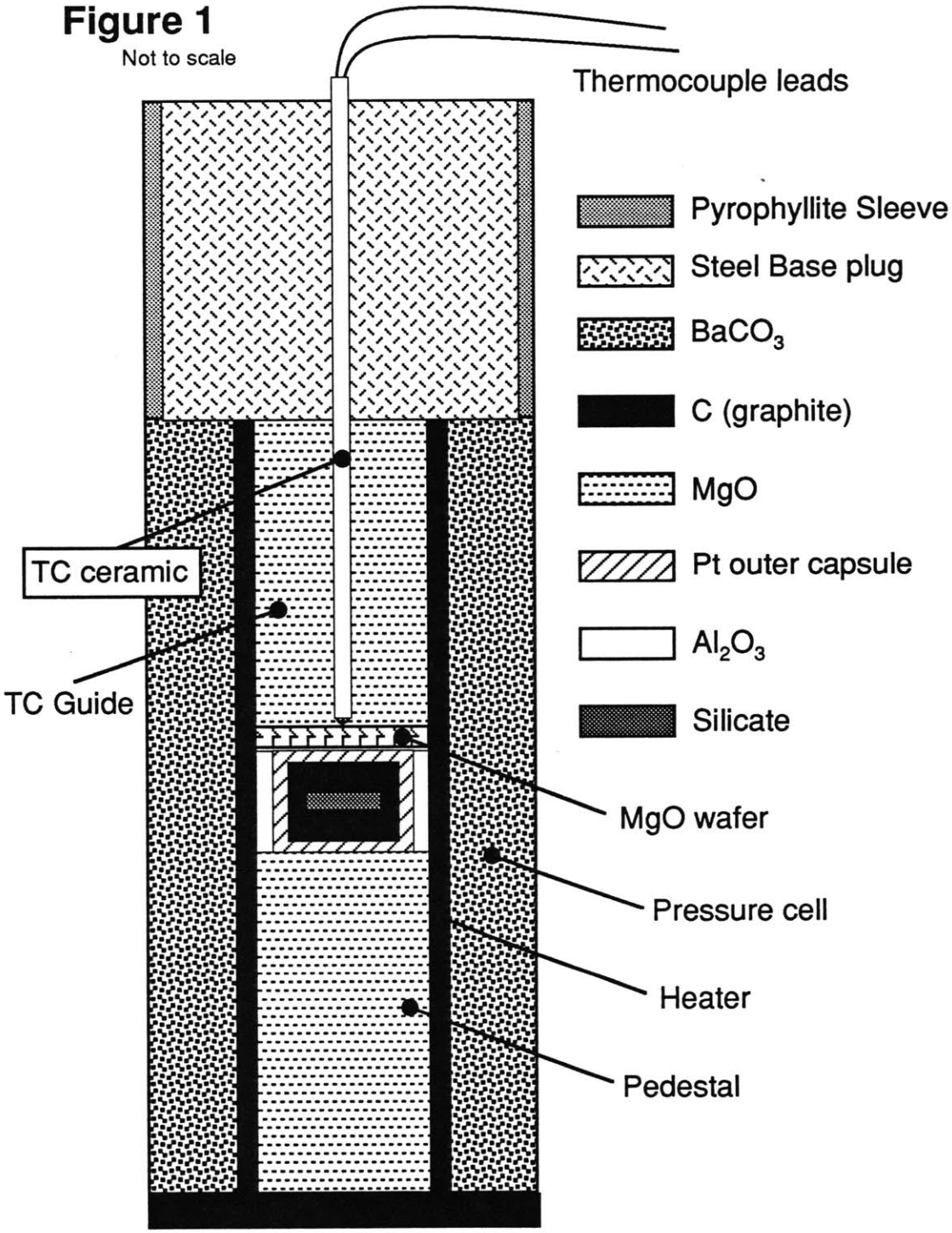

size specifications in Table 1

Figure 2
1:1 scale

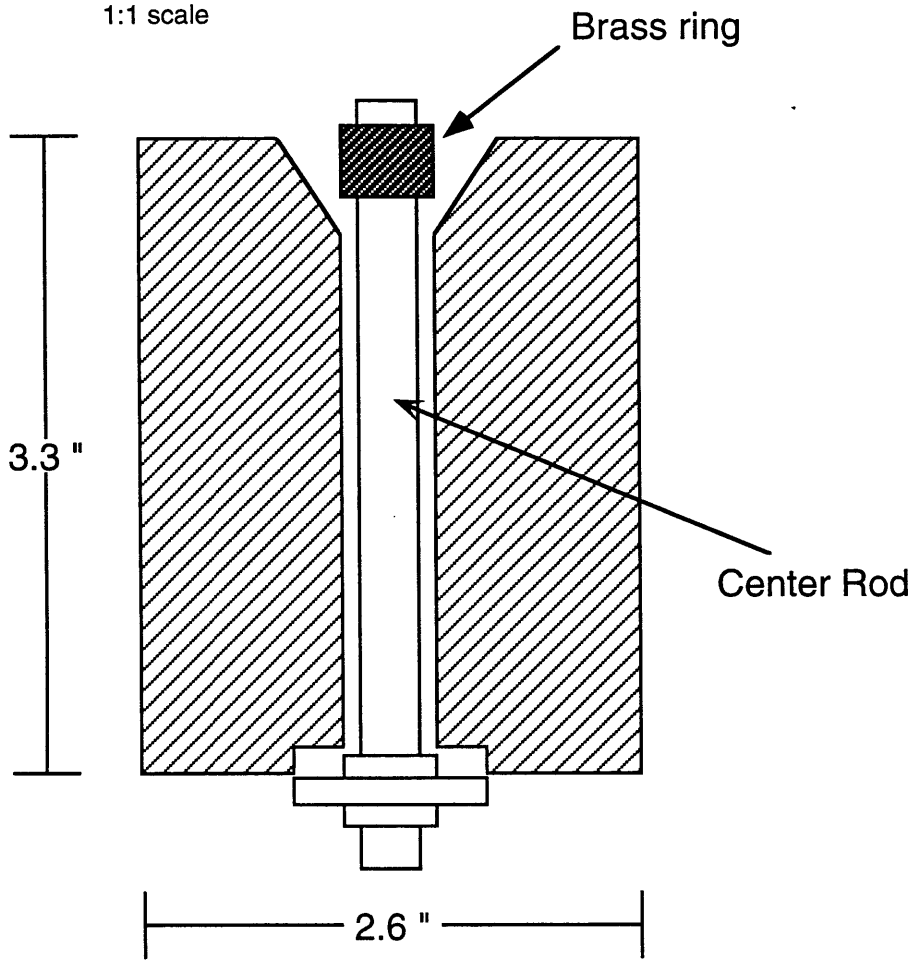

All other parts are hardened steel!

size specifications in Table 3

Table 1. Specifications for sample assembly parts.

Piece	Length	OD	ID	Depth
Capsule-Bottom	0.105	0.168	0.880	0.055
Capsule-Lid	0.050	0.168	0.850	0.020
TC Ceramic-4-hole	2.030	0.064	-	-
Base plug	0.498	0.437	0.070	-
Pyrophyllite	0.498	0.497	0.437	-
Heater	1.250	0.312	0.250	-
Graphite disk	0.060	0.494	-	-
MgO spacers	-	-	-	-
TC Guide	0.500	0.247	0.067	-
Wafer	0.625-0.5*(x)	0.247	-	-
Pedestal	0.125-0.5*(x)	0.247	-	-

where x=capsule length

	Inital length	OD	ID
Pt tubing	0.375	0.180	0.170

	Thickness
Pb Foil	0.001

All measurements in inches.

Table 2. Specifications for $BaCO_3$ cells

Mix Parameters	$BaCO_3$	Toner
Mix proportions	7.3 grams	0.20 grams
Total per cell	7.5 grams	

Pressurize to approx 20,000-psi

Firing Parameters	Length	Tol.
Pre-Firing	1.230"	
Post-Firing	1.250"	0.003?

Fire at 700°C for 30 minutes.

Table 3. Specifications for $BaCO_3$ cell press

Part	Height	OD	ID
Pressure vessel	3.3	2.6	0.485
Center rod	4.0	0.310	-
Brass piece	0.370	0.480	0.315
Piston	3	0.470	-
Piston	2	0.470	-

All measurements in inches.

Table 4. Pressure calibration experiments.

Pressure (GPa)	Duration (h)	Result
1.08	19	Gehl+An+Cor
1.23	68	Gehl+An+Cor
1.28	5.5	Gehl+An+Cor
1.31	9	CaTs+Gehl+An+Cor
1.38	17	CaTs+An (trace)
1.63	8	CaTs+An (trace)